NASA Contractor Report 168197

STAGNATION REGION GAS FILM COOLING - EFFECTS OF DIMENSIONLESS COOLANT TEMPERATURE

M. A. Bonnice and M. R. L'Ecuyer

Purdue University
West Lafayette, Indiana 47907

July 1983

Prepared for

NATIONAL AERONAUTICS AND SPACE ADMINISTRATION
Lewis Research Center
Under Grant NSG-3071

FOREWORD

The study reported herein was conducted under the sponsorship of the National Aeronautics and Space Administration, Grant No. NSG 3071, with technical cognizance of Mr. F.S. Stepka, NASA Lewis Research Center, Turbine Cooling Branch. The experimental apparatus used was fabricated with partial support from the Office of Naval Research, Power Program, Contract No. N00014-75-C-0873.

A previous study using the same apparatus (see Reference [1]) was conducted under the sponsorship of the Office of Naval Research, Power Program, Contract No. N00014-7 C-0873, with technical cognizance of Mr. James R. Patton, Jr.

The authors express their appreciation for the support provided by the aforementioned agencies. The authors also wish to acknowledge the assistance of Dr. B.A. Reese, Chief Scientist, AEDC (AFSC), formerly Professor and Head, School of Aeronautics and Astronautics, Purdue University. The authors are indebted to Ms. T. Wetli and Ms. B. Gick, Thermal Sciences and Propulsion Center, for their assistance in preparing the manuscript.

TABLE OF CONTENTS

Page

NOMENCLATURE

A	area, or half the length of the minor axis of the coolant hole exit area
B	half the length of the major axis of the coolant hole exit area
c_p	specific heat at constant pressure
C_f	friction coefficient (Appendix A)
C	tunnel blockage factor
d_o	coolant hole diameter
D	cylinder diameter, or coolant hole diameter (Appendix B)
Ec	Eckert number, $V_\infty^2/c_p(T_\infty - T_w)$
f	friction factor
F_s	surface force due to friction
h	local heat transfer coefficient
I	momentum flux ratio $(\rho_c V_c^2)/(\rho_\infty V_\infty^2)$
k	thermal conductivity
K	roughness height
K_s	sand grain roughness
L	length of coolant hole
$\dot{m}$	mass flow rate
M	blowing ratio $(\rho_c V_c)/(\rho_\infty V_\infty)$
Ma	Mach number
Nu	Nusselt number, hD/k
P	pressure, or spacing of rows of film coolant holes
Pr	Prandtl number, $\mu c_p/k$

NOMENCLATURE (Cont'd)

q"	local heat flux
Re	Reynolds number based on mean film temperature
Re^*	Reynolds number based on freestream density and film viscosity, $\rho_\infty V_\infty D/\mu_f$
R	gas constant
S	coolant hole center-to-center spacing along a row of holes
St	Stanton number, $q''/(\rho c_p V)_\infty (T_\infty - T_w) = h/(\rho c_p V)_\infty$
SNR	Stanton Number Reduction, $1 - St_{FC}/St_o$
STR	Stanton Number Ratio, St_{FC}/St_o
t	time dependent component of temperature
T	temperature, or time averaged temperature
u	time dependent component of velocity
V	velocity, or time averaged velocity
x	distance in streamwise direction downstream of coolant holes
x^+	dimensionless distance parameter, (L/D)/(RePr)
y	vertical distance
z	spanwise or lateral distance along the surface, normal to the flow direction

GREEK

α	coolant hole angle measured along surface relative to the x-axis, or a parameter in coolant mass flow distribution (Appendix A)
β	coolant injection angle measured from the surface tangent

NOMENCLATURE (Cont'd)

GREEK (cont'd)

γ	specific heat ratio, c_p/c_v
δ^*	boundary layer displacement thickness
ϵ	property exponent (i.e., $k \propto T^{\epsilon}$)
θ	angular position along a cylinder relative to stagnation, or dimensionless temperature
θ_c	dimensionless coolant temperature, $\frac{T_c - T_\infty}{T_{w,nom} - T_\infty}$
θ_i	angular position of row of coolant holes relative to stagnation line
μ	dynamic viscosity
ρ	density

SUBSCRIPTS

AVG	spanwise averaged
b	bulk temperature
c	coolant condition at exit of coolant hole
D	based on cylinder diameter
f	mean film temperature, $T_f = (T_\infty + T_w)/2$ or $T_f = (T_b + T_w)/2$
FC	with film cooling
i	at injection, or denoting the i^{th} element, or inlet condition
j	denoting the j^{th} element
m	average along the length of the coolant hole
MAX	spanwise maximum SNR, at a fixed blowing ratio, M, and downstream distance, x/d_o

NOMENCLATURE (Cont'd)

SUBSCRIPTS (con't)

nom	nominal wall temperature, $T_{w,nom}$, computed as an average of the temperatures from the 47 wall thermocouples in the film cooled region
o	without film cooling, or outlet condition
p	plenum condition
ROW	spanwise averaged wall temperature for a row of thermocouples
SEG	temperature of drop-in segment
T	total or stagnation condition
TOTAL	total coolant flowrate supplied to plenum
w	wall condition
x	parameter is a function of x-coordinate
∞	local freestream condition around the test cylinder
∞,o	freestream condition upstream of the test cylinder

SUPERSCRIPTS

*	Reynolds number based on freestream density and film viscosity
$\overline{\quad}$	average quantity

I. INTRODUCTION

To meet the demands for improved gas turbine engine performance, turbine inlet gas temperatures have been progressively increased. This has required a continuous evolution of improved materials and more effective methods of cooling turbine vane and blade surfaces.

Typical methods of cooling include: (a) internal convection, where internal heat removal is enhanced by flow through labyrinth channels, pin fins and impingement flow, and (b) external film cooling, where external heat transfer to the surface is reduced by ejection of coolant onto the vane surface through discrete slots or rows of holes. In regions of high thermal load (e.g., the leading edge of a turbine vane), the maintenance of allowable metal temperatures frequently requires the use of closely spaced multiple rows of holes (i.e. full-coverage film cooling) to obtain the necessary combination of external film cooling and internal convection (within the holes).

This study is the second part of an experimental investigation conducted to determine the effects of full-coverage film cooling for turbine vane leading edge applications. In the first part of the investigation, Luckey and L'Ecuyer [1] reported the results of film cooling for a range of coolant hole configurations, with the coolant temperature equal to the test surface wall temperature. The purpose of the study reported herein was to examine the effects of film cooling with the coolant temperature less than the wall temperature.

I.A. Definition of Film Cooling Parameters

The geometric and flow parameters used to describe multiple row film cooling are illustrated in Figure 1. The film coolant is injected onto the surface through holes of diameter, d_o, with center-to-center hole spacing, S, and row spacing, P. The origin of the coordinate system is located at the center of the coolant hole with (x) defining the direction of the freestream flow and (z) the lateral or spanwise direction. Non-dimensional coordinates x/d_o and z/S are used for convenience.

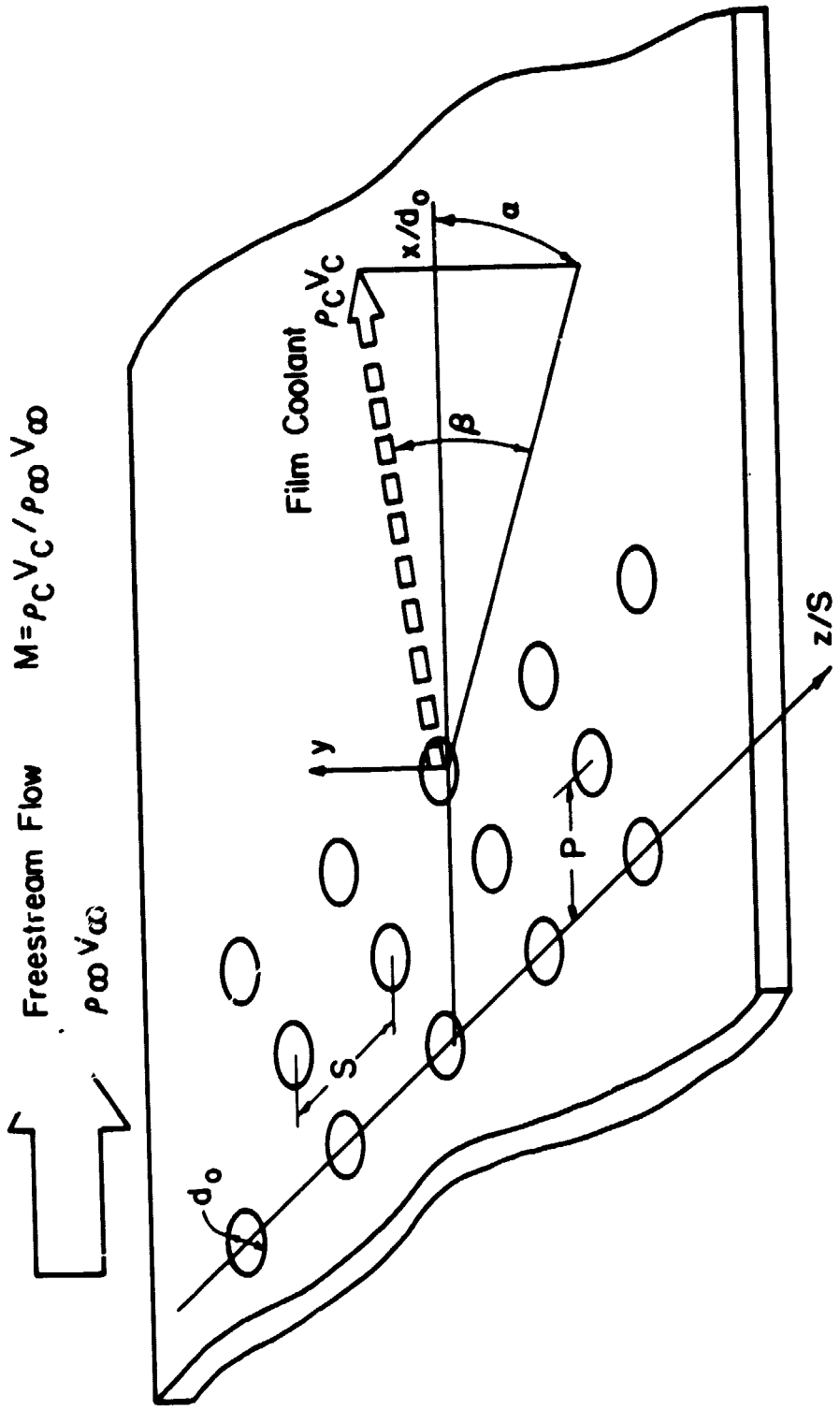

Figure 1. Film Cooling Geometric and Flow Parameters

The orientation of the coolant hole is defined by the angle α, with respect to the streamwise (x) direction, and the angle β, with respect to the local surface tangent. An angle $\alpha=0°$ corresponds to streamwise coolant injection, while $\alpha=90°$ and $0°<\alpha<90°$ are referred to as spanwise and compound injection, respectively. Due to the angle limitations imposed by surface curvature in the leading edge region, all experiments in this study and in part one of the investigation [1] were performed with spanwise injection ($\alpha=0°$).

The film cooling performance is governed by the mass flux ($\rho_c V_c$) and temperature (T_c) of the coolant injected onto the surface. It is common to characterize the injected mass flux by the blowing ratio defined as

$$M = \frac{\rho_c V_c}{\rho_\infty V_\infty} \tag{1}$$

where $\rho_\infty V_\infty$ denotes the local freestream mass flux at the point of injection. In the leading edge region, there is a large variation of $\rho_\infty V_\infty$ along the surface.

The temperature of the coolant leaving the hole may be characterized by a dimensionless coolant temperature defined as

$$\theta_c = \frac{T_c - T_\infty}{T_w - T_\infty} = \frac{(T_c/T_\infty) - 1}{(T_w/T_\infty) - 1} \tag{2}$$

The hydrodynamic behavior of the injected coolant also depends on the following related parameters.

density ratio

ideal gases of constant molecular weight, constant pressure

$$\frac{\rho_c}{\rho_\infty} = \frac{T_\infty}{T_c} = \left[1 + \theta_c\left(\frac{T_w}{T_\infty} - 1\right)\right]^{-1} \tag{3}$$

velocity ratio

$$\frac{V_c}{V_\infty} = M\left[1 + \theta_c\left(\frac{T_w}{T_\infty} - 1\right)\right] \tag{4}$$

momentum flux ratio

$$I = \frac{\rho_c V_c^2}{\rho_\infty V_\infty^2} = M^2 \left[1 + \theta_c \left(\frac{T_w}{T_\infty} - 1 \right) \right] \tag{5}$$

I.B. Discussion of the Literature

A comprehensive review of the film cooling literature has been prepared by Goldstein [2]. In addition, subsequent reviews of the literature may be found in [1], [3] and [4] documenting the influence of numerous variables governing film cooling performance. The purpose of the present discussion is to review the features of film cooling models important to the subject study. Of particular interest is the modeling of film cooling conditions characteristic of the gas turbine environment wherein large values of gas-to-wall temperature ratio and coolant-to-freestream density ratio exist.

An examination of the film cooling literature reveals two methods that have been developed for the analysis of film cooling performance. The adiabatic effectiveness method is based on a sequence of two experiments. First, the temperature distribution for an adiabatic film cooled wall is used to determine the adiabatic effectiveness distribution which is taken to be independent of coolant temperature. Separately, the hydrodynamic influence of coolant blowing on the heat transfer coefficient is determined. This information then enables the prediction of the actual heat flux for a specified (non-adiabatic) film cooled wall temperature. (See [1] for more discussion.)

The adiabatic effectiveness method has been used widely. The adiabatic wall condition usually is achieved using wall materials of very low thermal conductivity and using wall-to-coolant temperature differences that are small. In this context, the investigation of the influence of the gas-to-wall temperature ratio is very limited. The influence of coolant-to-freestream density ratio has been investigated by using a coolant gas of high molecular weight, measuring impermeable wall effectiveness, and applying the mass transfer analogy.

An alternate approach to film cooling performance analysis is the direct heat flux (or isothermal wall) method based on the linear superposition model of Choe, Kays, and Moffat [5]. Their analysis of the energy equation for the thermal boundary layer for isothermal wall, constant property flow yields a temperature field that is linearly dependent on the film coolant dimensionless temperature, θ_c. Utilizing the Stanton number defined as

$$St = \frac{q_w''}{(\rho\, c_p\, V)_\infty\, (T_\infty - T_w)} \tag{6}$$

the linear temperature field results in a linear dependence of St on θ_c given as

$$St = St_1 + (\theta_c - \theta_{c1}) \frac{St_2 - St_1}{\theta_{c2} - \theta_{c1}} \tag{7}$$

Direct heat flux measurements, for an isothermal film cooled wall, yield St_1 and St_2 for two different film coolant temperatures, θ_{c1} and θ_{c2}. Equation (7) then enables the prediction of the heat flux (St) for any other specified coolant temperature, θ_c.

To test the validity of the model, Choe, Kays and Moffat [5] performed experiments on a flat, isothermal test surface to measure the heat flux (St) at constant blowing ratio for selected coolant temperatures (θ_c). Sample results for the Stanton number change (ΔSt) for M=0.52 are shown in Figure 2. Using experimental data for $\theta_{c1} = 0.057$ and $\theta_{c2} = 1.13$, values for ΔSt were predicted (eqn (7)) for $\theta_c = 1.395$ and are shown to be in good agreement with measured values.

The linear superposition model is based on the assumption of constant fluid properties. Certainly, for the experiments of [5], with the free-stream air at room temperature and the surface temperature 10° to 20°K higher, the constant properties model shows excellent agreement with experimental results.

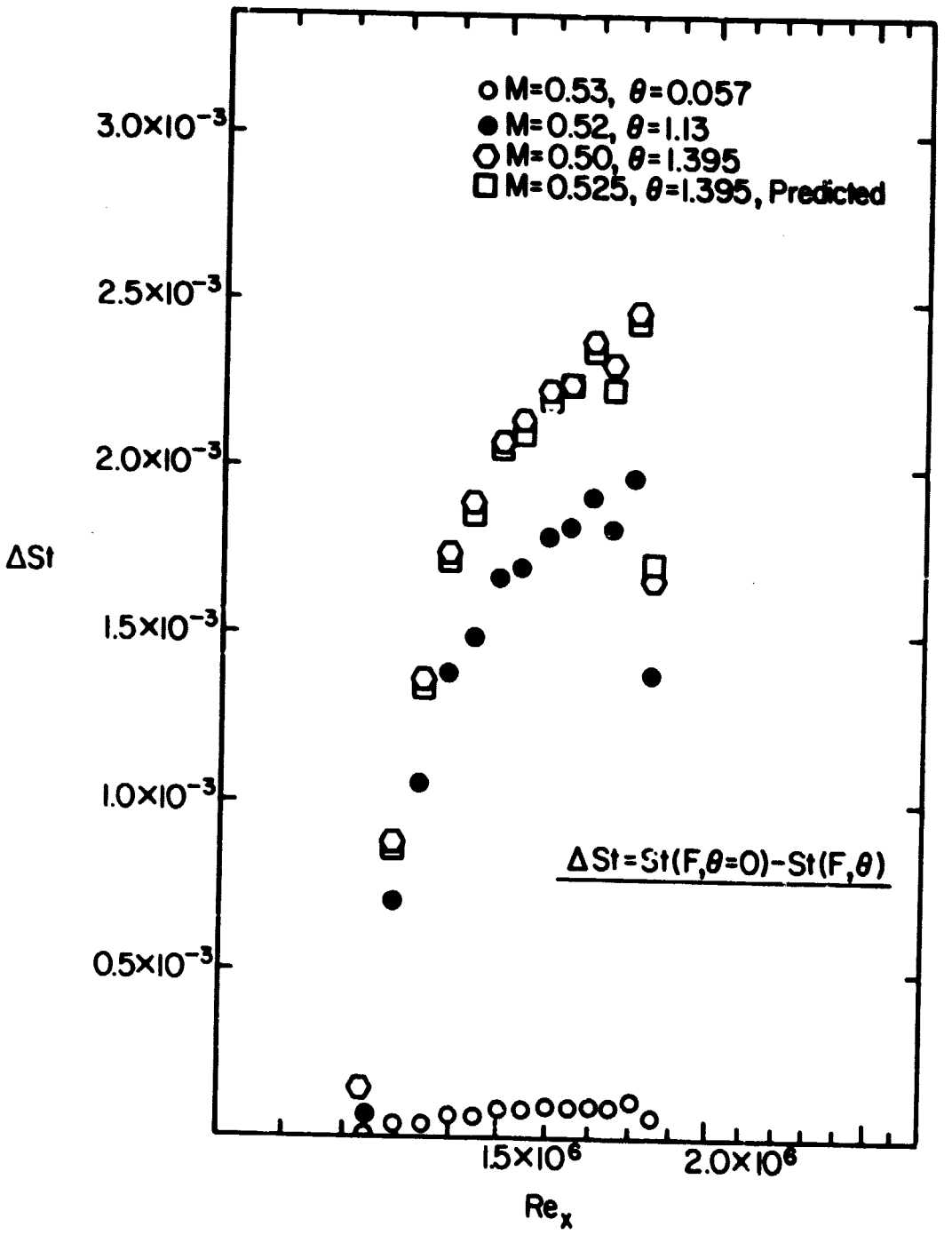

Figure 2. Effect of Dimensionless Coolant Temperature on Stanton Number (Choe, Kays, and Moffat [5])

Also implied in the constant properties model is the assumption that the flow field with coolant injection is unaffected by changes in the coolant temperature (θ_c). For the experiments of [5], with T_w/T_∞ = 1.067 and M = constant, the variation of θ_c from 0.0 to 1.4, corresponding to a 9% variation in the momentum flux, velocity, and density ratios (see eqns (3) - (5)), should have little affect on the flow field. However, for gas turbine applications (T_∞/T_w ~ 1.5 - 2.0), the influence of θ_c on property variations and the flow field has not been investigated.

The foregoing discussion illustrates the difficulty in modeling the film cooling performance characteristic of the gas turbine environment wherein the importance of large values of gas-to-wall temperature ratio and coolant-to-freestream density ratio is uncertain. In the present study, the direct heat flux method was selected to permit the inclusion of those parameters in the investigation of film cooling characteristic of the turbine vane leading edge.

I.C. Scope of the Investigation

An experimental program was initiated to investigate multiple row film cooling configurations typical of turbine vane leading edge applications. Simulation of the gas turbine environment was accomplished using the stagnation region of a cylindrical, film cooled test surface in a crossflow of heated air with Re_D ~ 9 x 10^4 and T_∞/T_w ~ 1.7. Film cooling experiments were conducted with spanwise angled holes (α = 90°, β = 25°, see Fig. 1) using miniature heat flux sensors to measure the local heat flux. The film cooling performance was determined by the Stanton Number Reduction ($1 - St_{FC}/St_o$) due to film coolant injection.

In the first part of the investigation, Luckey and L'Ecuyer [1] reported the results for coolant hole configurations varying the hole-to-hole spacing, row-to-row spacing, number of rows, and the location of rows relative to the stagnation line. All experiments in the first part were conducted with the coolant temperature equal to the wall temperature, θ_c = 1.

In the second part of the investigation, reported herein, experiments were conducted using the same cylindrical test surface and instrumentation to determine the influence of coolant temperature on Stanton Number

Reduction for the range $1.18 \leq \theta_c \leq 1.56$. Experiments were performed with a single row of spanwise angled holes ($\alpha = 90°$, $\beta = 25°$) with a hole-to-hole spacing of $S/d_o = 5$. Film cooling data were obtained with the row of holes at three locations ($\theta_i = 5.0°$, $22.9°$, and $40.8°$) relative to stagnation covering the same range of coolant blowing ratio ($0.25 \leq M \leq 10.25$) used in the first part of the investigation [1]. Results are presented to show the influence of θ_c on the local and spanwise averaged Stanton Number Reduction.

II. EXPERIMENTAL INVESTIGATION

II.A. Introduction

The objective of the research program was to investigate multiple row film cooling under conditions characteristic of the leading edge of a turbine vane. To model the leading edge region, geometric similarity was obtained using the front stagnation region of a circular cylinder in crossflow. Initially, an extensive study was conducted by Luckey and L'Ecuyer [1] using a film coolant temperature equal to the wall temperature, $\theta_c = 1.0$. In the subject study, experiments were conducted to determine the influence of film coolant temperature on the film cooling performance using $T_c < T_w$, $\theta_c > 1.0$. The experimental apparatus was essentially the same as that used in [1] with modifications of the film coolant supply to produce reduced coolant temperatures in the range $1.18 \leq \theta_c \leq 1.56$.

Effective modeling of the convective heat transfer environment for the leading edge region requires the simulation of important dimensionless parameters that govern the flow and heat transfer phenomena. A dimensional analysis of the governing conservation equations [3] shows that the Nusselt number can be expected to depend upon the following parameters:

$$Nu = f(x, z, Re_D, Pr, Ec, \epsilon, T_\infty/T_w).$$

With film cooling along the surface, dimensional analysis shows [6] that the Nusselt or Stanton number is also a function of the following film cooling parameters:

$$St = f(M, \theta_c, \rho_c/\rho_\infty, \delta^*/d_0, \alpha, \beta).$$

In this investigation (the subject study and [1]), experiments were conducted to simulate the values of Re_D, T_∞/T_w, M, θ_c, ρ_c/ρ_∞, δ^*/d_0, α, and β, typical of the leading edge of a film cooled turbine vane.

II.B. Description of Experimental Apparatus

The investigation of multiple row film cooling typical of a turbine vane leading edge was conducted using a cylindrical test surface exposed to a crossflow of air heated by a gas turbine combustor. A brief description of the experimental apparatus is presented in the following sections. A more detailed description is given in [1].

II.B.1. Flow System

Figure 3 is a simplified schematic of the overall flow system used in conducting this investigation. A blow-down facility provided an air flow permitting a continuous run time of approximately one hour. The air entered a gas turbine combustor, where methyl alcohol was burned to provide the nominal freestream temperature of T_∞ ~ 500K.

Downstream of the combustor the flow was dumped into a large settling chamber to provide some control of the turbulence intensity passing through the test flow channel. The hot flow from the combustor was directed against the dome end of the chamber and passed through three stainless steel fine mesh screens. The flow accelerated through a 2:1 area contraction to the chamber exit.

At the entrance to the flow channel, a stainless steel honeycomb flow straightener was maintained in position by a fine screen. The flow channel sections, shown in Figure 3, had an open area of 0.46m by 0.30m. A turbulence screen could be inserted between any two flow channel sections.

Upstream of the test section holding the cylinder, a special flow channel section was positioned to allow the insertion of probes into the flow stream. A traversing mechanism attached to the outside of the flow section allowed a probe to be traversed across the entire depth or width of the flow field.

Downstream of the traversing probe, the test cylinder was held in the flow channel with circular flanges. Each flange consisted of two separate pieces which were held together by machine screws. As the machine screws were tightened, o-rings between the two flange pieces provided a pressure seal around the cylinder. By loosening the machine screws holding the flange together, it was possible to rotate the cylinder with respect to the flow channel.

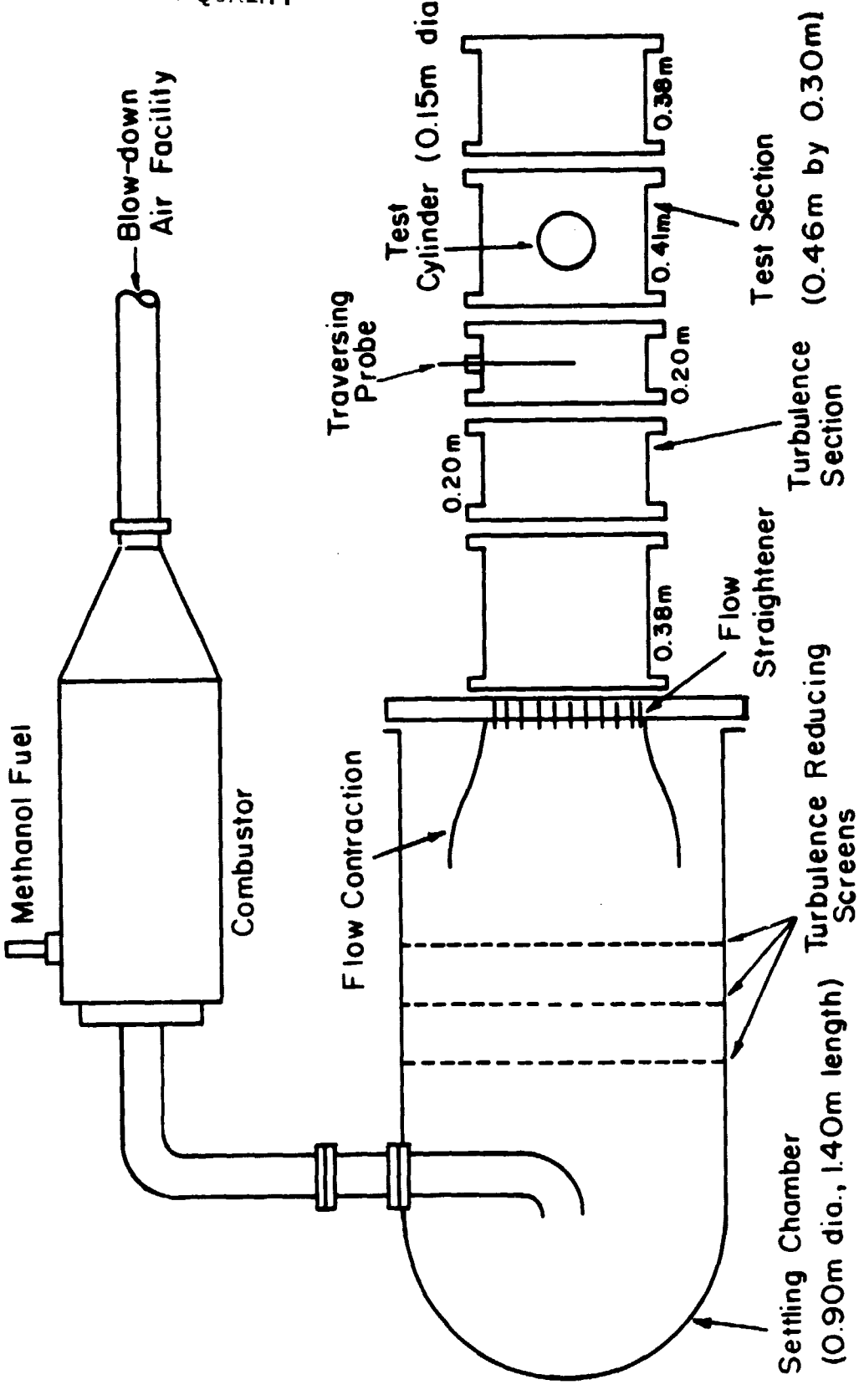

Figure 3. Schematic of the Flow System

The hot freestream flow passed over the test cylinder and was exhausted to the atmosphere.

II.B.2. Test Cylinder

A schematic drawing of the test cylinder is shown in Figure 4. The 0.15m diameter cylinder, also shown in the photograph in Figure 5, was a scaled-up model of the leading edge of a turbine vane. The large increase in size enabled the use of film coolant holes that were large relative to the instrumentation which measured the surface heat flux and temperature. This was the same test cylinder used in the first part of the investigation [1].

Three concentric cylinders were used to construct the 0.41m long test cylinder. The inner, stainless steel cylinder was machined with channels to provide for internal cooling of the test cylinder. The second stainless steel cylinder was slipped over the inner cylinder, sealing the cooling channels. Tubes were installed at both ends of the cooling channels to allow for the flow of water coolant. The outer cylinder was a thin skin of beryllium-copper slipped over, and brazed to, the stainless steel cylinder.

Film coolant holes were located in removable drop-in segments which fit into five slots milled into the test cylinder. The coolant holes were drilled with a hole-to-hole spacing of $S/d_0 = 5$, and the segments were installed with a row-to-row spacing of $P/d_0 = 5$. Figure 6 shows the test cylinder with two of the five drilled segments installed. The experiments of the present study were performed with film coolant supplied to a single row of holes (Row 1 in Figure 4). The holes in the remaining four rows were plugged inside the test cylinder.

Figure 7 shows a schematic of the segment used in Row 1. The eleven coolant holes were counterbored from the bottom of the segment and a short length of copper tubing was inserted into each hole. The copper tubes were used to support thermocouples measuring the temperature of the coolant entering the segment.

Coolant lines were connected to each of the eleven copper tubes in the segment to supply air film coolant to each coolant hole. In this study, the coolant supply lines were made of thick-wall rubber tubing.

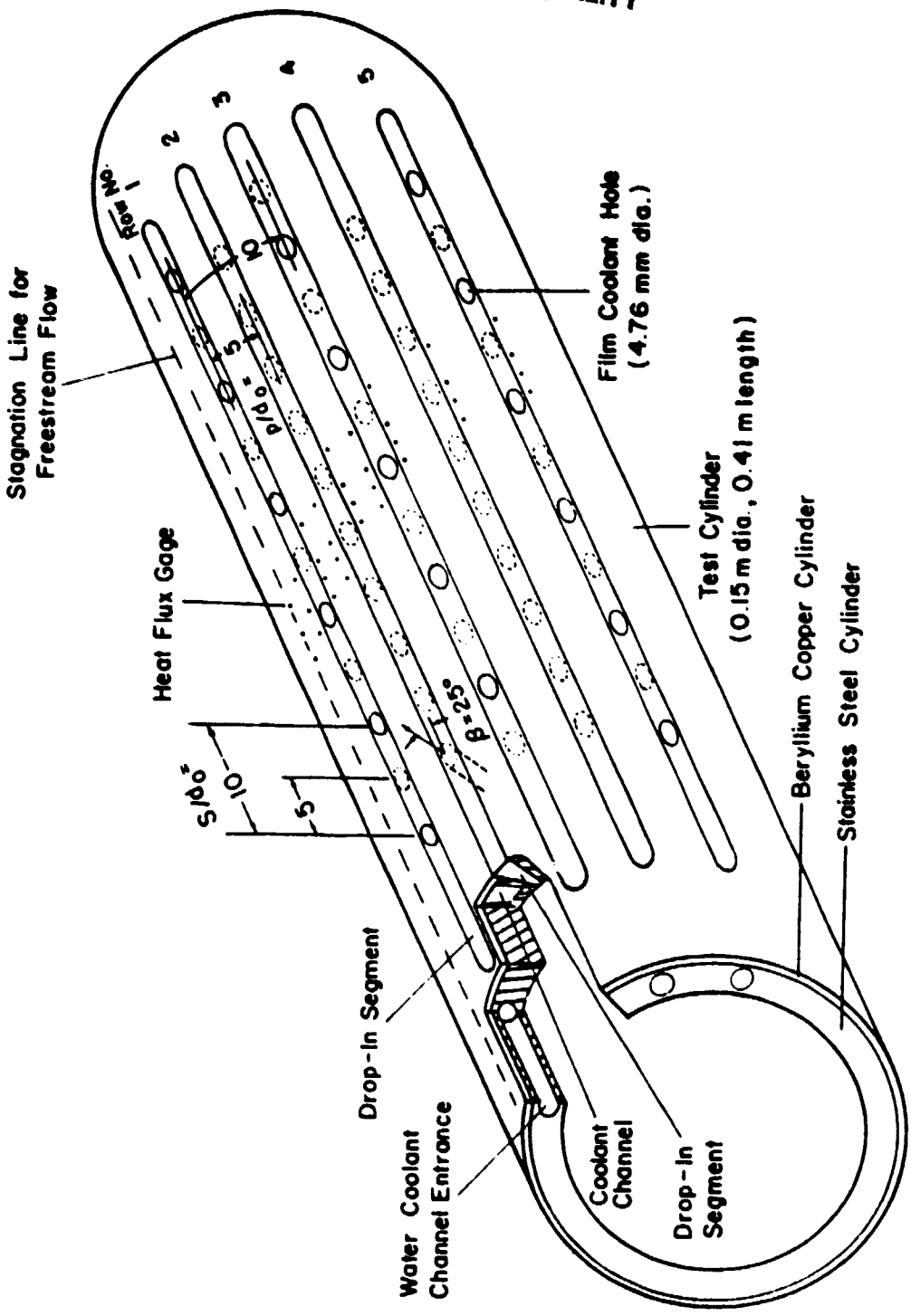

Figure 4. Schematic of the Test Cylinder

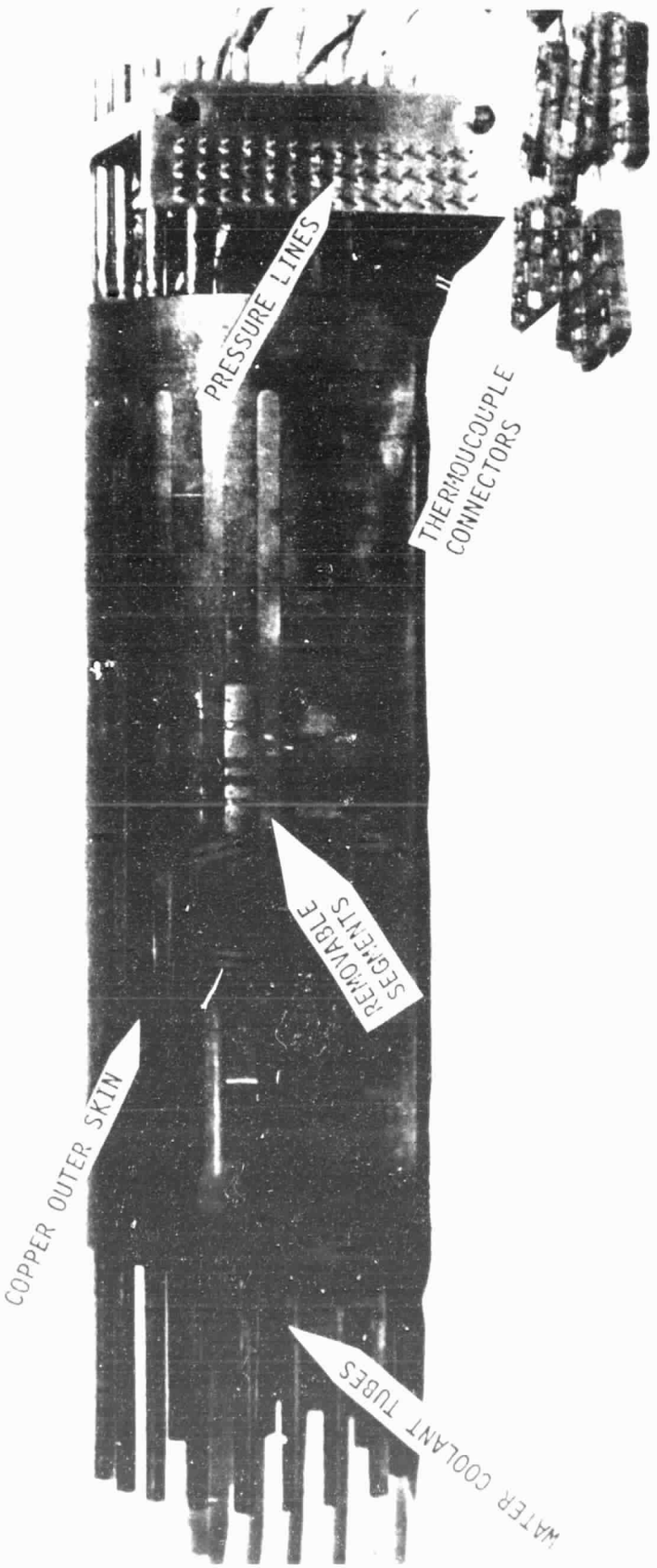

Figure 5. Photograph of the Test Cylinder

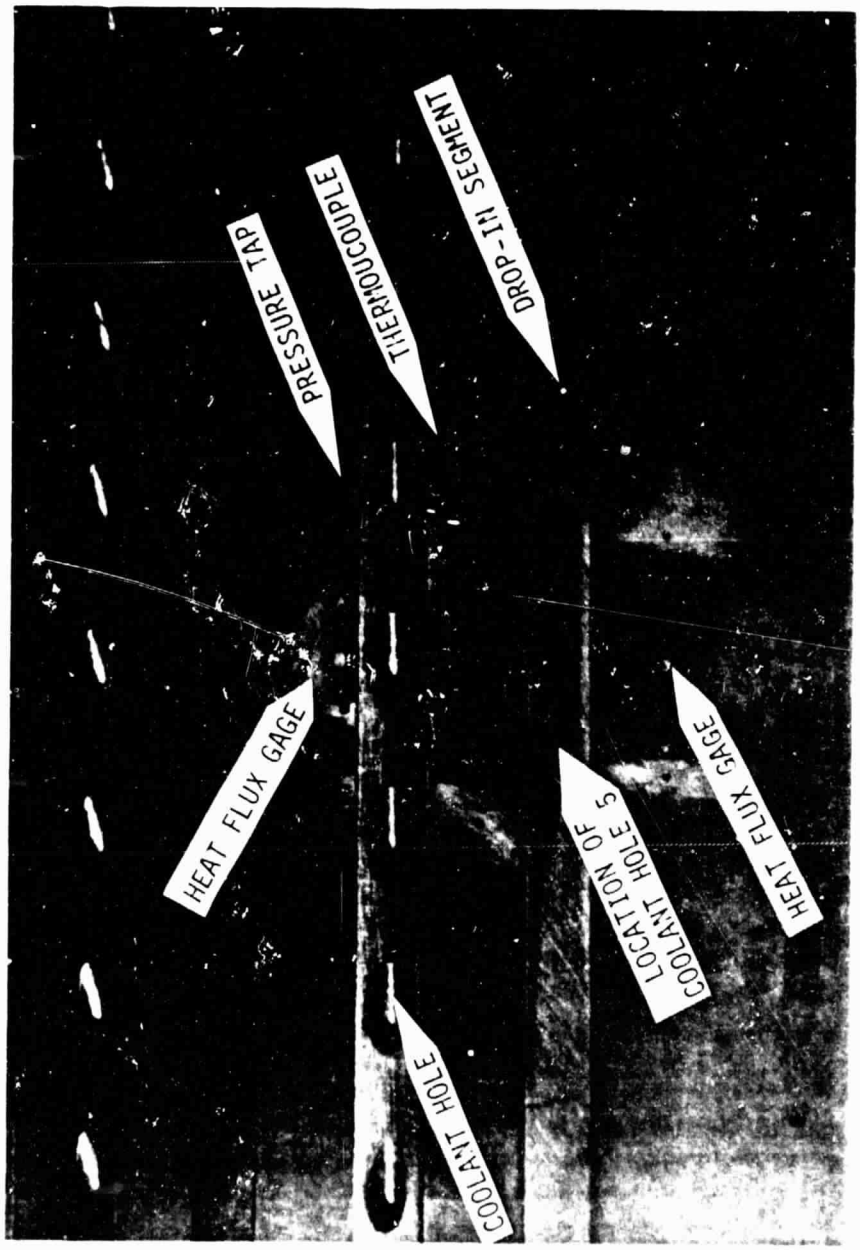

Figure 6. Photograph of the Instrumented Region of the Test Cylinder

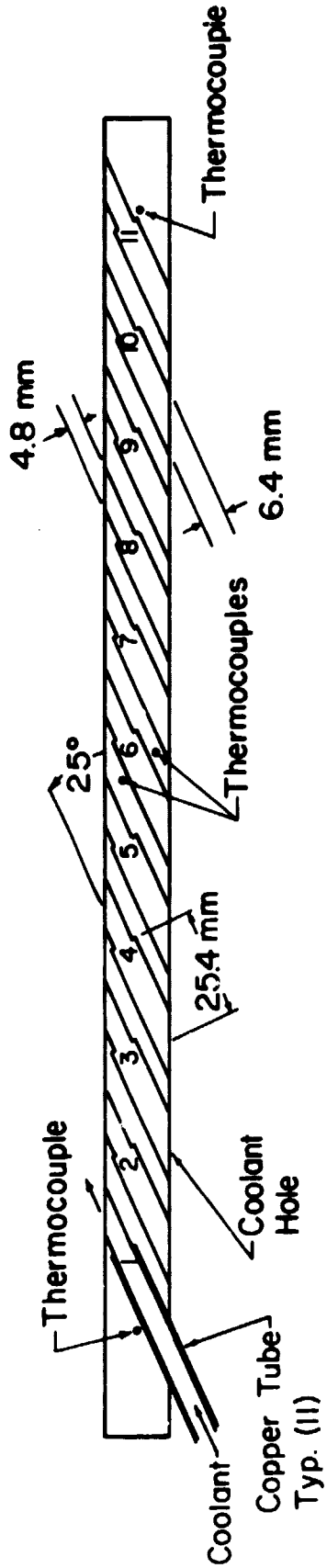

Figure 7. Schematic of a Drop-in Segment (Row 1)

In the previous study [1], the coolant supply lines were thin-wall vinyl tubing.

II.B.3. Film Coolant Supply System

The experimental apparatus described in the previous sections was the same for both the present study and the first part of the investigation [1], with the exception of the film coolant supply system. This sytem was modified to produce reduced coolant temperatures yielding $T_c < T_w$, $\theta_c > 1.0$.

Figure 8 is a schematic diagram of the film coolant supply system. Air from the blow-down facility was split and routed to two separate film coolant flow paths leading to the test cylinder. Path A supplied the Primary Plenum with five lines delivering coolant to holes No. 4 through 8 in the drop-in segment for Row 1 (see Fig. 7). Path B supplied the Secondary Plenum with six lines delivering coolant to holes No. 1, 2, 3, 9, 10, 11 (see Fig. 7). Each of the eleven coolant holes in Row 1 was fed by a distinct delivery-supply line.

For each of the two flow paths, the coolant flow rate was controlled with fine needle valves and was measured with hot-film mass flow meters. The metered air flow was routed to the coils of a methanol heat exchanger.

The methanol heat exchanger consisted of a dry-ice/methanol mixture (stable bath temperature of 178K) in which coils of tubing (length = 6.1m, i.d. = 10.8mm, L/D = 560) were submerged. The methanol heat exchanger was used to remove moisture from the film coolant air to prevent icing and plugging of the small diameter tubes downstream.

The film coolant air for the two flow paths was dumped into plenums at the exit of each heat exchanger coil. Five coolant delivery lines were connected to the primary plenum and six coolant delivery lines were connected to the secondary plenum. The plenums served to apply a uniform pressure at the inlet of the coolant delivery lines. The measured plenum air pressure and temperature were used in calculating the coolant mass flow rate through each coolant line.

The coolant delivery lines were connected from the primary and secondary plenums to the air inlet side of the nitrogen heat exchanger illustrated schematically in Figure 9. Eleven tubes passed through the

shell of the heat exchanger, one for each film coolant delivery-supply line. Liquid nitrogen was supplied to the shell of the nitrogen heat exchanger in a counter-flow arrangement. The nitrogen heat exchanger was constructed entirely of brass, with all parts joined by silver-solder. The shell measured 76mm o.d., wall thickness 3.2mm, length 0.20m. The air cooler tubing measured 3.2mm o.d., 1.6mm i.d., length 0.66m, L/D ~ 410.

Liquid nitrogen was forced into the nitrogen heat exchanger through copper tubing by pressurizing one or two liquid nitrogen storage dewars. The number of dewars and the dewar pressure were selected to provide a nitrogen flow rate which produced the desired film coolant temperature.

The chilled film coolant air was routed from the nitrogen heat exchanger to the test cylinder drop-in segment (Row 1) through the rubber coolant supply lines.

As shown in Figure 8, the film coolant supply was split into two paths (A and B) with the five coolant delivery-supply lines fed by the primary plenum routed to the primary coolant holes (No. 4 - 8) located in the instrumented region of the test cylinder. The five primary coolant lines were selected to minimize the hole-to-hole variation in the film coolant flowrate and exit temperature in the instrumented region.[1] The six remaining lines, fed by the secondary plenum, were routed to film coolant holes No. 1, 2, 3, 9, 10, 11 to maintain a uniform temperature in the drop-in segment.

II.C. Instrumentation and Measurements

The mass flow rates of the combustion air and fuel were measured using flat-plate orifices with pressure transducers to measure the differential and static pressures. The freestream flow conditions (T_T, P_T, P) were measured 0.23m upstream of the leading edge of the test cylinder. Measurements were made with a wedge-shaped pitot-static pressure and total temperature probe.

---

[1] Preliminary tests were conducted to select those five delivery-supply lines with nearly equal pressure and temperature drop characteristics to supply the five primary coolant holes.

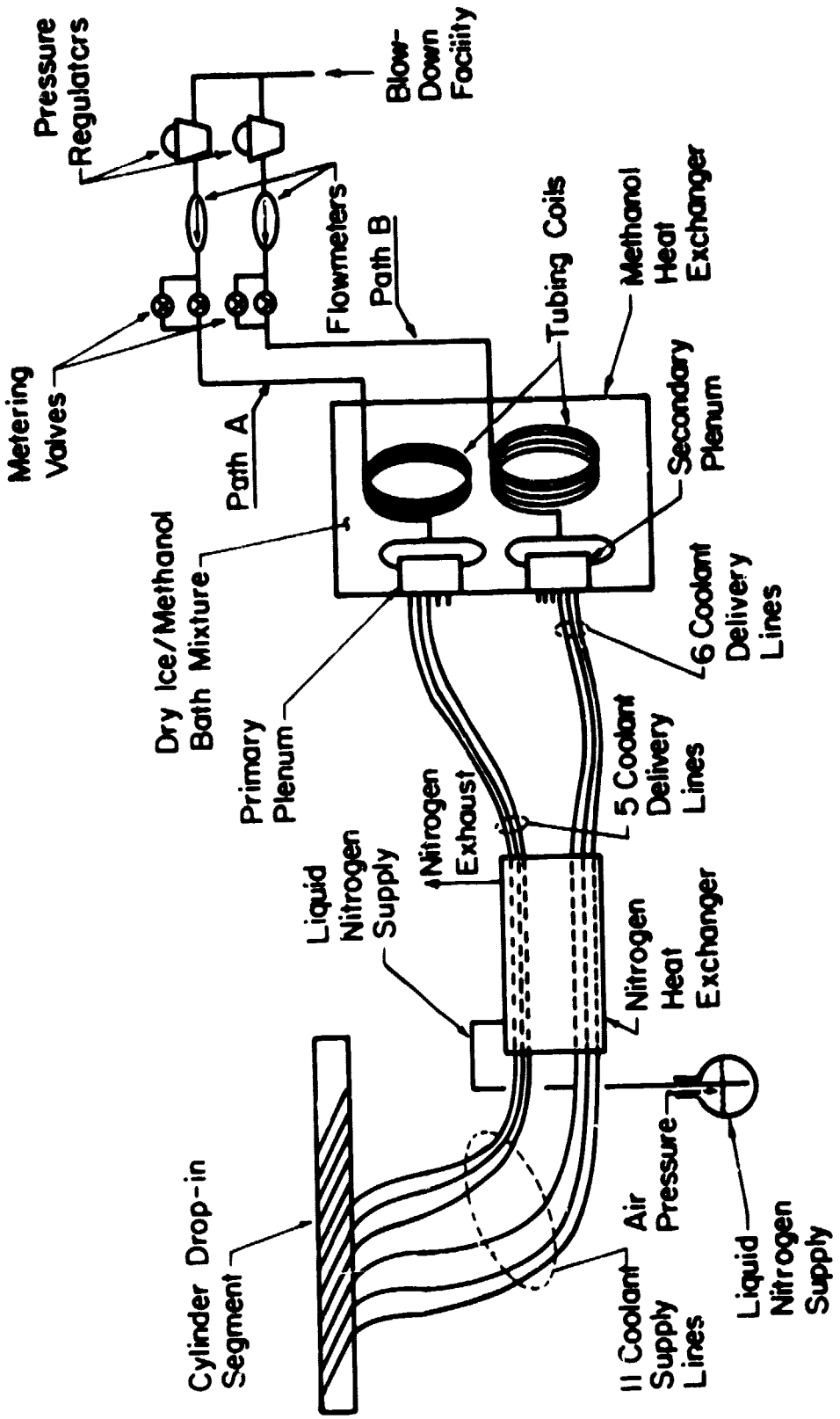

Figure 8. Schematic of the Film Coolant Supply System

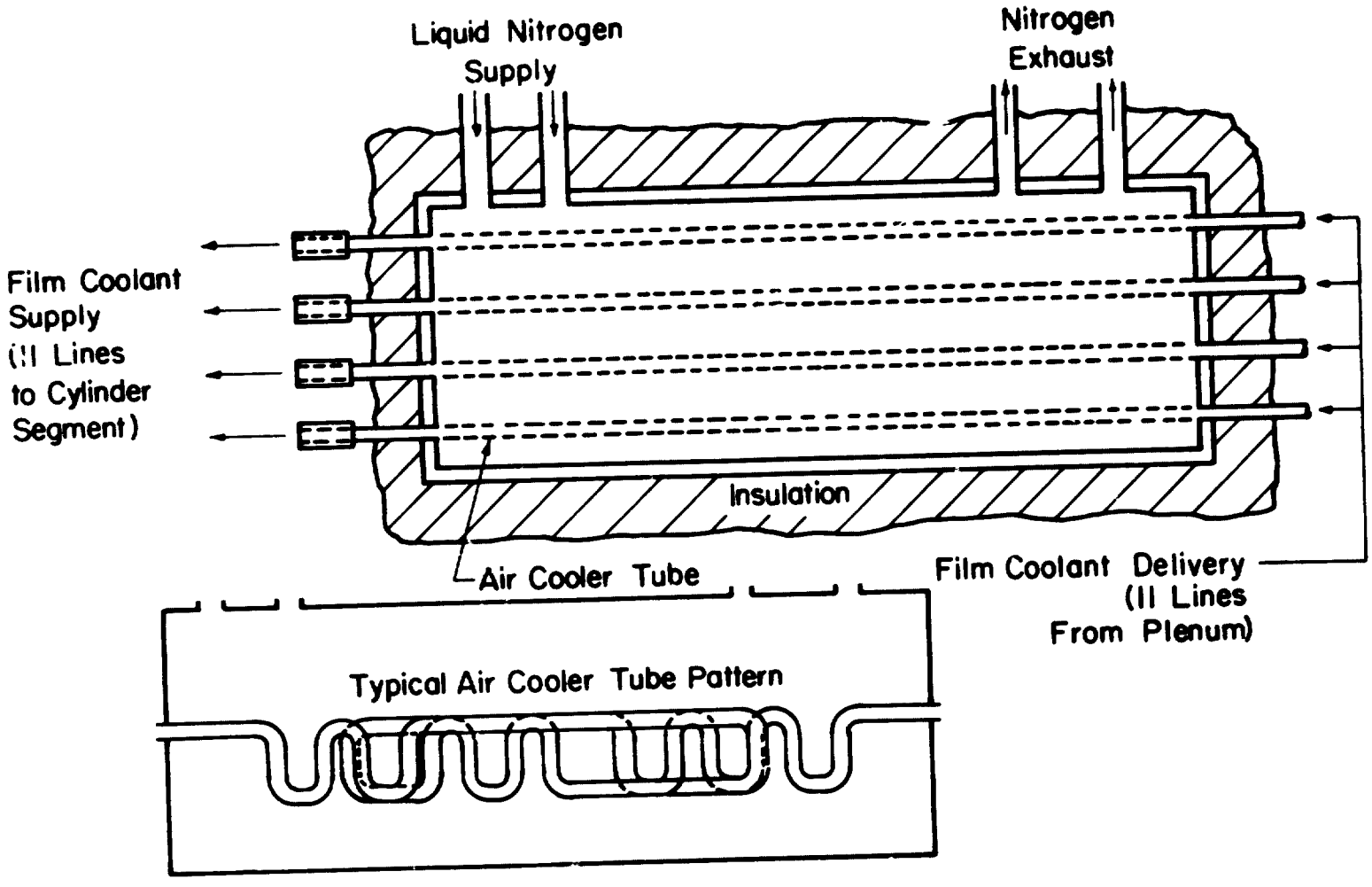

Figure 9. Schematic of the Nitrogen Heat Exchanger

A view of the instrumentation installed in the film cooled region of the test cylinder is shown in the photograph of Figure 6. In the schematic diagram, Figure 10, the instrumentation and coolant holes in the film cooled region of the test cylinder are shown to scale. The coolant holes represented by solid outlines (Row 1) are those through which coolant was ejected. All other holes (dashed outlines) were plugged inside the test cylinder in the present study. The hole and row spacing shown in Figure 10 is $S/d_o = 5$, $P/d_o = 5$.

The location of the instrumentation (Figure 10) is given in terms of the dimensionless streamwise coordinate (x/d_o) relative to Row 1 for each of the nine rows of heat flux gages (see right margin). The dimensionless spanwise coordinate (z/S) is shown with the origin (z/S = 0) at the center of coolant hole No. 5. The angular position along the left margin shows the position relative to the stagnation line when Row 1 is located 5.0° from stagnation. Table 1 lists the streamwise and spanwise coordinates for all heat flux gages. The repeatability of operational heat flux gages is discussed in Section III.F.

The test cylinder was instrumented for surface static pressure and wall temperature measurements. Thermocouples (copper-constantan)) were placed on either side of each heat flux gage to determine the streamwise and spanwise wall temperature distribution.

Table 1. Heat Flux Gage Locations

Gage Number	x/d_o	z/S	Gage Number	x/d_o	z/S
* 1	-3.50	0.00	* 18	6.50	1.83
* 2	-3.50	0.50	19	8.50	0.50
3	-3.50	0.00	20	8.50	0.83
4	-1.50	0.00	21	8.50	1.17
* 5	-1.50	0.50	22	8.50	1.83
6	-1.50	0.00	23	11.50	0.00
7	1.50	0.00	24	11.50	0.33
8	1.50	0.33	25	11.50	0.67
9	1.50	0.67	26	11.50	1.33
10	1.50	1.33	27	16.50	0.50
11	3.50	0.00	28	16.50	0.83
12	3.50	0.33	29	16.50	1.17
13	3.50	0.67	30	16.50	1.83
14	3.50	1.33	31	21.50	0.00
15	6.50	0.50	32	21.50	0.33
16	6.50	0.83	33	21.50	0.67
17	6.50	1.17	34	21.50	1.33

*Gage not operational. See Section III.F.

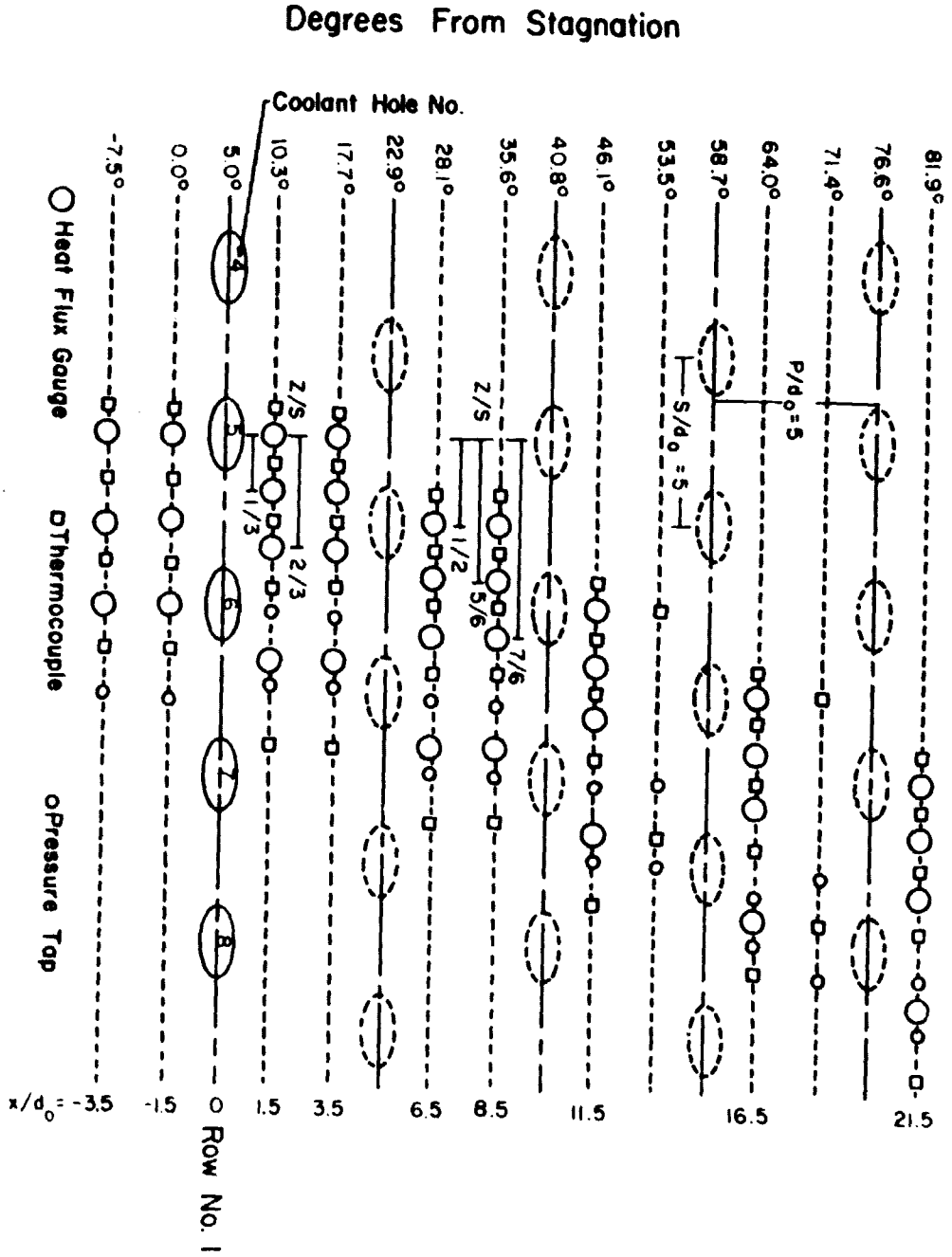

Figure 10. Schematic of the Instrumented Region of the Test Cylinder

Direct measurement of the surface heat flux was made using miniature, Gardon type, thin foil heat flux gages. Due to the small size of the gages used, a microvolt signal was produced. Therefore, each gage was matched with an operational amplifier to provide a millivolt signal proportional to the heat flux.

The mass flow rate of film coolant air to the primary and secondary plenums in the methanol heat exchanger was measured with hot film mass flowmeters. The static pressure and temperature in the plenums were measured to determine the mass flow rate of coolant delivered to each coolant hole.

The reader is referred to [1] for a more detailed descriptiton of the test cylinder instrumentation.

In the subject study, the temperature of the film coolant supplied to the coolant holes in the drop-in segment was measured using the thermocouple fixture illustrated in Figure 11. A copper-constantan thermocouple was sealed into a short length of copper tubing. A screen was attached to the inlet of the tube to promote uniformity of the coolant velocity and temperature profiles. The copper tube thermocouple fixture was installed into the drop-in segment film coolant hole as shown in Figure 12. The film coolant supply line was attached to the copper tube to deliver film coolant from the nitrogen heat exchanger. Each of the five primary coolant holes, No. 4 through 8 (see Figures 8 and 10), was equipped with the copper tube thermocouple fixture to measure the film coolant temperature supplied to the primary holes in the drop-in segment. The secondary coolant holes, No. 1, 2, 3, 9, 10, 11, were supplied by a copper tube identical to that shown in Figure 11 but with no thermocouple installed.

The wall temperature distribution in the drop-in segment was measured using four embedded copper-constantan thermocouples as shown in Figure 8.

During an experiment, the voltage output from all heat flux gages and thermocouples was periodically scanned and recorded with a 96 channel data acquisition system.

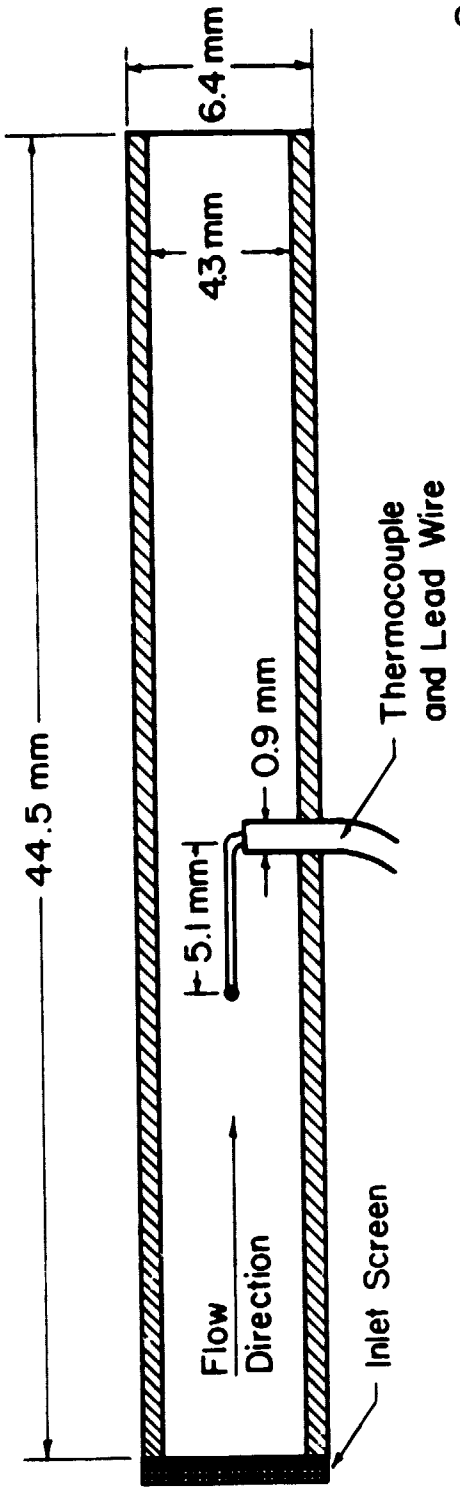

Figure 11. Copper Tube Thermocouple Fixture

Figure 12. Installation of the Thermocouple Fixture in the Drop-in Segment

II.D. Description of the Experiment

This experimental program was conducted to investigate the reduction in the local heat flux due to film cooling from multiple row injection on the leading edge of a cylindrical test surface with flow conditions chosen to simulate the film cooling typical of the leading edge of a turbine vane. To ensure that the experiment modeled representative leading edge conditions, a survey of turbine engine companies was made to determine flow conditions and coolant hole geometry typical of current and future leading edge designs. Table 2 shows the range of parameters important in film cooling the leading edge of turbine vanes and the specific values of each parameter being matched in this investigation.

A Reynolds number of 9×10^4 based on the leading edge diameter was chosen to match typical engine conditions. In the present study, a moderate freestream gas temperature (~500K) and water cooling of the test cylinder to maintain the surface near room temperature (~294K), provided a freestream-to-wall temperature ratio of 1.7. The use of a copper skin helped maintain an approximately isothermal wall condition.

The experiments of this study were performed with a clear wind tunnel (no turbulence generating screens) with the turbulence intensity approaching the leading edge of the cylinder measured to be in the range 4 - 8%.

In the subject study, the coolant hole injection angle of 25° and the spanwise hole-to-hole spacing of $S/d_o = 5$ were chosen for direct comparison with the results of the previous study [1]. Experiments were conducted with a single row of film cooling holes, placed at angular locations, θ_i = 5.0°, 22.9°, and 40.8°, corresponding to injection locations used in the previous study [1].

Experiments were performed with the dimensionless coolant temperature in the range $1.18 \leq \theta_c \leq 1.56$. Values for the blowing ratio were chosen to cover the range used in [1]. Table 3 summarizes the values of θ_c and M used in the subject study.

Table 2. Turbine Gas Stream and Film Cooling Heat Transfer Parameters

	Typical Leading Edge Conditions[1]	Purdue Investigation
Freestream Conditions		
Reynolds Number (Re_D)	4×10^4 - 1×10^5	9×10^4
T_∞/T_w	1.4 - 1.9	1.7
Turbulence Intensity	7 - 20%	4 - 8%
Mach number	0.1 - 0.2	0.03
Coolant Hole Geometry		
Spanwise Angle	15° - 45°	25°
Hole Spacing (S/d_o)	4 - 10	5
Injection Location (θ_i)	0 - 90°	5,0°, 22.9°, 40.8°
Coolant Flow Conditions		
Blowing Ratio (M) $(\rho_c V_c/\rho_\infty V_\infty)$	0.5 - 2.0	0.25 - 10.25
Coolant Temperature (θ_c)	1.4 - 2.0	1.18 - 1.56

[1] Information collected from a survey of engine companies to determine conditions typical of current and future leading edge designs.

Table 3. Range of Conditions Simulated in the Present Study

$\theta_i = 5.0°$

M	2.01	2.99	5.17	10.23
θ_c	1.29	1.29	1.32	1.38

$\theta_i = 22.9°$

M	0.25	0.74	1.23	2.07	2.45
θ_c	1.18	1.33	1.30	1.29	1.29
		1.45	1.56	1.36	1.39

$\theta_i = 40.8°$

M	0.51	0.74	0.95	1.14	1.58
θ_c	1.36	1.34	1.38	1.40	1.36
	1.50				

II.E. Data Reduction

During each experimental run, the following measurements were recorded:

(a) freestream total temperature
(b) freestream total pressure and total-to-static pressure difference
(c) cylinder surface and segment temperatures and surface heat flux distributions
(d) film coolant flowrate to the primary and secondary plenums
(e) coolant pressure and temperature in the primary and secondary plenums
(f) film coolant temperatures at the inlet to the primary film coolant holes (No. 4 through 8)

These measurements were used to compute the film cooling performance parameters.

The freestream total temperature and total-to-static pressure ratio were used to determine the freestream velocity ($V_{\infty,0}$) and static temperature. The Reynolds number was calculated based on the cylinder diameter. Following convention in the gas turbine industry, a mean film temperature, $T_f = (T_\infty + T_{w,nom})/2$, was used to determine the density and viscosity in the Reynolds number. The perfect gas law was used to compute the freestream density ($\rho_{\infty,0}$) and other physical properties of the freestream (μ, k, γ, Mol.Wt.) were determined from Ref. [7].

The local freestream velocity around the cylinder, V_∞, was computed from incompressible potential flow theory. The expression for a cylinder in an infinite freestream was corrected to account for tunnel blockage effects, yielding

$$V_\infty = C\ 2V_{\infty,0} \sin\theta.$$

The tunnel blockage correction, C, calculated from incompressible potential flow theory (see [1]) had the values

Degrees from Stagnation, θ_i =	5.0°	22.9°	40.8°
Correction Factor, C =	1.089	1.091	1.093

Because of the low freestream Mach number ($Ma_{\infty,0} \simeq 0.03$), incompressible freestream flow was assumed such that $\rho_\infty V_\infty = \rho_{\infty,0} V_\infty$.

The surface heat flux for each gage was measured first with film coolant flow (q''_{FC}), immediately followed (allowing for thermal equilibrium) by measurements of the heat flux without film coolant flow (q''_o). The Stanton number with film cooling and without (i.e. dry wall) were computed as

$$St_{FC} = \frac{q''_{FC}}{\left[(\rho V c_p)_\infty (T_\infty - T_w)\right]_{FC}}$$

$$St_o = \frac{q''_o}{\left[(\rho V c_p)_\infty (T_\infty - T_w)\right]_o}$$

Repetitive measurements, to ensure constant flow conditions, were made to obtain four values for St_{FC} and St_o. The average values for St_{FC} and St_o were used to compute the Stanton Number Reduction

$$SNR = 1 - \frac{St_{FC}}{St_o}$$

The Stanton Number Reduction gives the fractional change in surface heat transfer due to film coolant flow. To ensure reproducibility, data are only reported for experiments in which the four measured values of St_{FC} were within ± 5% of the average, and the four measured values of St_o were within ± 3% of the average value.

A nominal cylinder wall temperature, $T_{w,nom}$, was calculated as the average of the wall temperatures at the 47 thermocouple locations shown in Figure 10.

The coolant mass flow rate supplied to the primary plenum was measured, along with the temperature and pressure of the coolant air in the primary plenum. The coolant temperature entering each of the five primary coolant holes in the drop-in segment was measured. These measurements provided for the calculation of the coolant blowing ratio (M) and dimensionless coolant temperature (θ_c).

For each of the primary coolant holes, the mass flow rate and coolant exit temperature were calculated by the method of Appendix A.[1] The coolant mass flux for each primary hole was calculated as the coolant mass flow rate divided by the coolant hole cross-sectional area. The blowing ratio (M) was calculated as the ratio of the average coolant mass flux for the five primary coolant holes to the local freestream mass flux ($\rho_\infty V_\infty$).

The value of the coolant dimensionless temperature (θ_c) was calculated from the freestream temperature, $T_{\infty,o}$, the nominal wall temperature, $T_{w,nom}$, and the average of the coolant exit temperatures for the five primary coolant holes, T_c. Thus,

$$\theta_c = \frac{T_c - T_{\infty,o}}{T_{w,nom} - T_{\infty,o}}$$

The coolant-to-freestream density ratio was determined by assuming ideal gas behavior, equal coolant exit and freestream pressures, and using the average of the coolant exit temperatures for the five primary coolant holes (T_c). Thus,

$$\frac{\rho_c}{\rho_\infty} = \frac{T_{\infty,o}}{T_c}$$

The coolant-to-freestream velocity ratio (V_c/V_∞) and momentum flux ratio ($\rho_c V_c^2/\rho_\infty V_\infty^2$) were computed from the values of M and ρ_c/ρ_∞.

---

[1] The method used to calculate the mass flow rate and coolant exit temperature was based on a combination of the momentum equation and a convection correlation for temperature rise in the film coolant hole (Appendix B).

The raw data indicate the following uncertainties in the film cooling parameters:

Blowing ratio, M:	± 5%
Dimensionless Coolant Temperature, θ_c:	± 6%
Stanton Number Reduction, SNR: (and Stanton Number Ratio, STR)	± 0.05 in SNR (STR) units

III. PRELIMINARY EXPERIMENTS

III.A. Introduction

The experimental investigation reported herein was conducted to examine the effects of dimensionless coolant temperature on leading edge film cooling. The flow system used in the subject experiment was identical to that used in the initial study [1]. Preliminary experiments to qualify the test apparatus included profiles of freestream velocity, temperature, and cold flow turbulence intensity and test cylinder pressure and temperature distributions. These results were reported in [1] and were not repeated in the subject study. However, to ensure repeatability of the data, some preliminary experiments were conducted in this study to measure cylinder heat transfer with and without film cooling under conditions similar (i.e. $\theta_c = 1$) to those used in the previous study [1]. Additional preliminary experiments were performed to determine the hot flow freestream turbulence intensity and to define the hole-to-hole distributions of coolant blowing ratio and dimensionless coolant temperature pertinent to the subject film cooling experiments with $\theta_c > 1.0$.

III.B. Freestream Conditions

In the initial study [1], freestream velocity, temperature and cold flow turbulence intensity profiles in the wind tunnel were reported. Results showed that the velocity profile was uniform within 3% of the centerline value, and the total temperature profile was uniform within 2% of the centerline value in the region of the test cylinder. Under cold flow, with a clear wind tunnel (no turbulence screens), the turbulence intensity in the region of the cylinder was 4.4% ± 0.3%.

Measurements were made in the subject study to determine the centerline turbulence intensity in the clear wind tunnel (no turbulence screens) with hot flow. The results for hot flow, performed in a manner similar to the cold flow measurements [1] indicated a value for "apparent turbulence intensity" higher than the 4.4% found for cold flow turbulence

intensity. This was attributed to the hot wire probe response to both freestream velocity and temperature fluctuations.

Experiments were conducted to isolate the contributions of velocity and temperature fluctuations by (a) determining the anemometer sensitivity to velocity (V_∞ = 11.3, 14.6, 17.7 m/s) at constant freestream temperature (T_∞ = 501, ± 1°K) and (b) determining the anemometer sensitivity to temperature (T_∞ = 467, 501, 534°K) at constant freestream velocity (V_∞=14.7,±0.2m/s). Unfortunately, due to scatter in the data, it was not possible to accurately isolate the probe sensitivities to velocity and temperature fluctuations. The results did show consistently that the ratio of velocity fluctuation to temperature fluctuation had a value

$$\frac{\sqrt{(\overline{u^2})}/V_{\infty,0}}{\sqrt{(\overline{t^2})}/T_{\infty,0}} = 1.75$$

An estimate of the turbulence intensity (due to velocity fluctuations) for the hot flow showed (a) a lower bound of 2.7 - 4.1% using the above ratio (1.75) to extract the temperature influence, and (b) an upper bound of 6.3 - 8.1% assuming the influence of temperature fluctuations is negligible.[1] These results show that the hot flow film cooling experiments in the subject study and the previous study [1] were exposed to a turbulent freestream rms velocity fluctuation at least of the order of 4% and a turbulent freestream combined rms velocity and temperature fluctuation of approximately 6 to 8%. While the hydrodynamics of film cooling is expected to be primarily influenced by the freestream velocity fluctuations, the surface heat flux is most likely influenced by the combined velocity and temperature fluctuations.

III.C. Cylinder Pressure Distribution

Test cylinder surface static pressure measurements were reported in [1]. The measurements were made with solid segments installed in the test cylinder (no film coolant holes). It was found that the pressure distribution indicated a supercritical flow with boundary layer separation at

[1] For more details see Appendix C, reference [8].

about 90° to 100° from stagnation. The cylinder pressure distribution was found to be unchanged when turbulence screens were inserted in the wind tunnel or when coolant holes were present in the cylinder surface [1]. Thus, for the present study, with a clear wind tunnel and coolant holes in the cylinder surface, there existed an orderly development of the boundary layer for the entire film cooled region ($0 \leq \theta_i \leq 90°$).

III.D. Cylinder Temperature Distribution

The temperature distribution of the surface of the test cylinder was measured with thermocouples embedded flush with the surface. To arrive at a nominal wall temperature, $T_{w,nom}$, the indicated temperatures of the 47 thermocouples (see Figure 10) were averaged. At each streamwise row of temperature instrumentation, an average temperature also was calculated and denoted T_{ROW}. The streamwise variation of T_{ROW} is shown in Figure 13 for a representative film cooling experiment (θ_i = 5.0°, M = 2.03, θ_c = 1.29). In this experiment, the maximum value for $(T_{ROW} - T_{w,nom})/T_{w,nom}$ was -2.5% (ie. - 7°K). The distribution of wall temperature (Figure 13) was similar for all experimental tests, with the maximum value of $(T_{ROW} - T_{w,nom})/T_{w,nom}$ equal to -3.2% (ie. = -9°K).

In a given row (at a particular angular location) the maximum-to-minimum variation in local temperature was typically 3°K to 5°K. The largest maximum-to-minimum variation of temperature in a row of thermocouples was found directly behind the coolant holes and was 17°K.

In the first drop-in segment, the temperature was measured at four spanwise locations. Across the span of this segment, the temperature variation was small, typically 2 - 3°K. At the highest values of blowing ratio and θ_c, the average temperature of this segment was 18°K lower than the nominal wall temperature.

For the remaining four segments, the temperature was measured at one location per segment. The temperatures of these segments were usually 7 - 9°K lower than the nominal wall temperature. The segment temperatures (T_{SEG}) are plotted in Figure 13 for the representative case.

ORIGINAL PAGE IS
OF POOR QUALITY

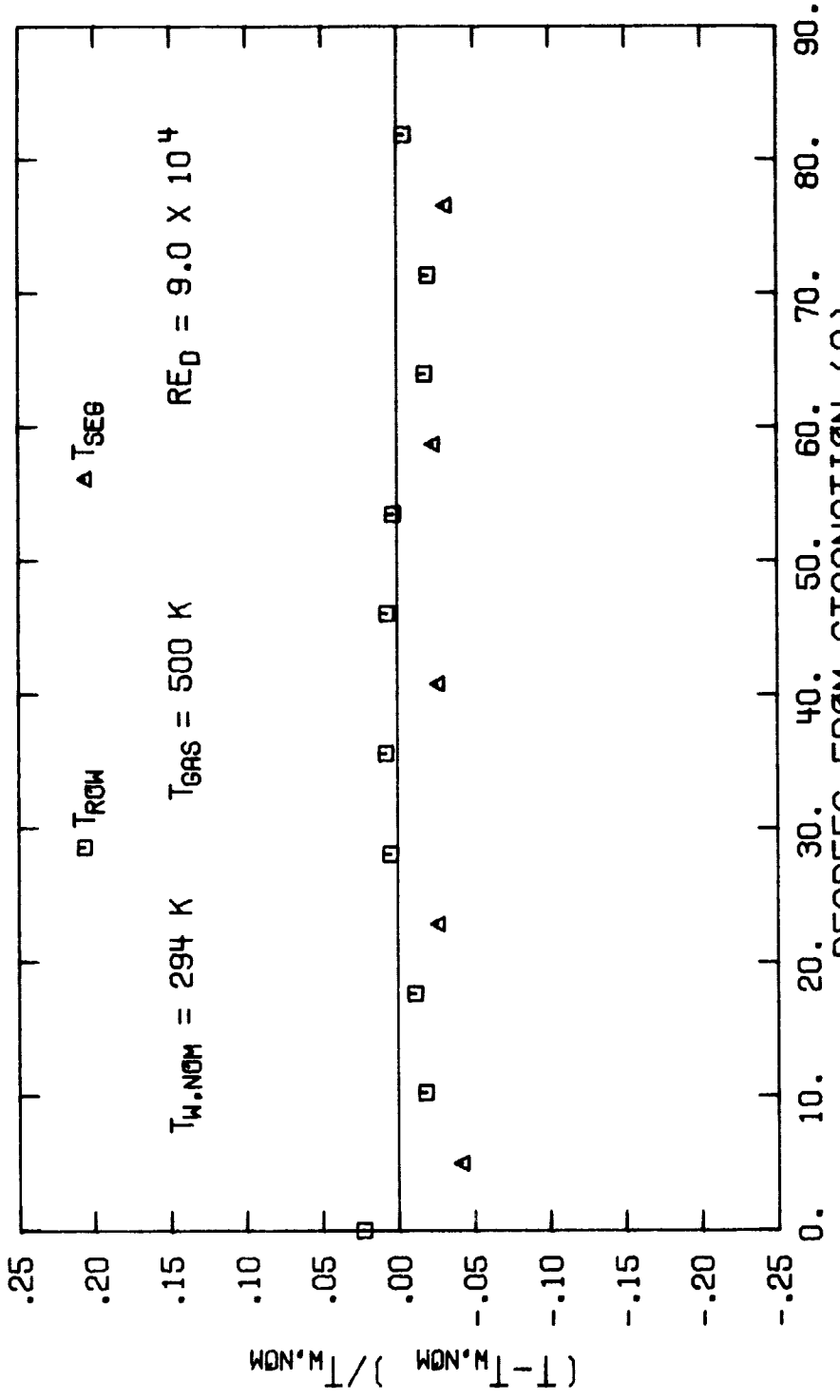

Figure 13. Distribution of Test Cylinder Surface Temperature

III.E. Spanwise Distribution of Coolant Blowing Ratio and Dimensionless Coolant Temperature

Coolant blowing ratio (M) and dimensionless coolant temperature (θ_c) were based on average values for the five primary coolant holes. The spanwise (hole-to-hole) variations of blowing ratio and dimensionless temperature were monitored through the course of the subject study.

The spanwise distribution of blowing ratio typically was uniform within ± 3.4% of the average value. The smallest variation seen was ± 0.9%, the largest was ± 8%. The distribution of dimensionless temperature typically was uniform within ± 2.8% of the mean. The smallest variation seen was ± 1.0%, and the largest was ± 6.9%. In general, the largest spanwise variations in M and θ_c were seen with low values of blowing ratio.

III.F. Heat Transfer Without Film Cooling

In both the previous study [1] and the present study, cylinder surface heat transfer was measured without film cooling (referred to as "dry wall" heat transfer). The measurements of the present study served to verify the integrity of the heat flux gages and to establish the repeatability of dry wall heat transfer data in [1].

The parameter used to describe dry wall surface heat transfer is $Nu/\sqrt{Re_D^*}$, where Nu is the local Nusselt number ($Nu = hD/k_f$) and Re_D^* is a freestream Reynolds number ($Re_D^* = \rho_{\infty,o} V_{\infty,o} D/\mu_f$). As conventionally used in literature on cylinder heat transfer, the properties viscosity and thermal conductivity in Nu and Re_D^* are based on the mean film temperature, T_f, and the density in Re_D^* is based on freestream temperature $T_{\infty,o}$.[1]

The value of $Nu/\sqrt{Re_D^*}$ for each heat flux gage was monitored throughout the present study. An average value of $Nu/\sqrt{Re_D^*}$ was calculated for each gage for a given angular location from stagnation. This average value was considered the property of a particular heat flux gage and angular location and was used as a basis of examining gage output repeatability.

---

[1] Film cooling experiments were performed with a value of Re_D, based on film temperature, $Re_D = 9.0 \times 10^4$. The corresponding value based on freestream density is $Re_D^* = 7.1 \times 10^4$.

The results of the present study for the average value of $Nu/\sqrt{Re_D^*}$ for each gage (and common angular location) were compared to the results of the previous study [1]. For the majority of the heat flux gages, the value of average $Nu/\sqrt{Re_D^*}$ was within +20%, -0% of the value reported in [1] for the corresponding gage. Heat flux gages which indicated a value of average $Nu/\sqrt{Re_D^*}$ greater than +20% of the corresponding value in [1] were considered inoperational in the present study.

The comparison with the dry wall heat transfer results of [1] showed a group of heat flux gages which reproduced the results of [1]. These heat flux gages are listed in Table 1 showing the streamwise and spanwise locations of the operational heat flux gages. Reference to Figure 10 shows that the operational gages covered the cylinder surface from x/d_o = 1.50 to x/d_o = 11.50 downstream from Row 1.

The results of the present study for the average value of $Nu/\sqrt{Re_D^*}$ for each gage were used to quantify the repeatability of heat transfer measurements made during the course of the present study. For each gage, the average value of $Nu/\sqrt{Re_D^*}$ for a given angular location was used to calculate normalized values, $(Nu/\sqrt{Re_D^*})/(Nu/\sqrt{Re_D^*})_{avg.}$ The range of repeatability for all operational heat flux gages and all dry wall heat transfer data over the course of the subject study is shown in Figure 14 in terms of the normalized value for $Nu/\sqrt{Re_D^*}$. The vertical bands encompass the range from maximum to minimum values of normalized $Nu/\sqrt{Re_D^*}$ observed for a gage throughout the subject study. The results show that two-thirds of the heat flux gages indicated values of $Nu/\sqrt{Re_D^*}$ within ± 15% of the average for that gage. Ninety five percent of the gages indicated values of $Nu/\sqrt{Re_D^*}$ within ± 20% of the average for that gage.

III.G. Film Cooling with θ_c = 1.0

Film cooling experiments in the first part of this investigation [1] were conducted using a coolant dimensionless temperature of θ_c = 1.0. As part of the process to qualify the performance of the test apparatus for the subject study, experiments were conducted with a coolant temperature θ_c = 1.0.

For these preliminary experiments, the test apparatus coolant supply system was restored to the configuration used in [1]. With reference to

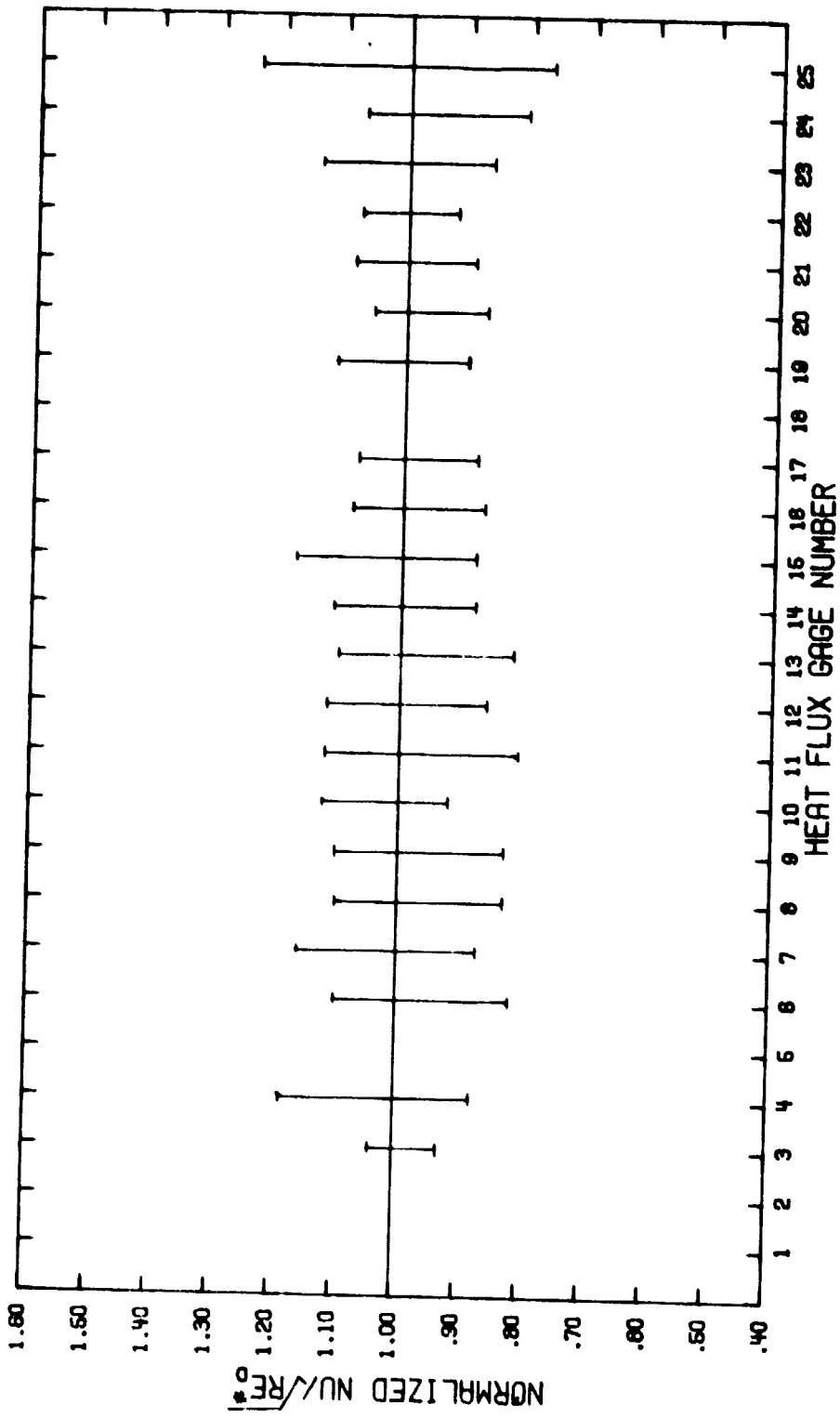

Figure 14. Band of Normalized Drywall Heat Transfer

Figure 8, the nitrogen heat exchanger was removed from the flow path and the eleven coolant supply lines were routed to a common plenum in the methanol heat exchanger. However, the coolant supply lines (rubber vacuum tubing) in the present study were used instead of replacing with the vinyl tubing used in the previous study [1]. Experiments were conducted with a single row of film coolant holes located at $\theta_i = 22.9°$ from the cylinder stagnation line with the blowing ratio varied over the range $0.25 \leq M \leq 3.00$. Results are presented in the form of Stanton Number Reduction, SNR, as a function of blowing ratio, M, for selected heat flux gages. The value of blowing ratio was taken as the blowing ratio of the film coolant hole directly upstream of the particular heat flux gage which was necessary due to the variation of blowing ratio that resulted from the differences inflow resistance in each of the installed rubber coolant supply lines.

Results for SNR vs. M are presented in Figure 15 for heat flux gages 8 and 10. These gages were selected because of similar locations on the cylinder surface: $x/d_0 = 1.50$, $z/S = 0.33$ (see Table 1 and Figure 10). The results obtained in the present study show good agreement when comparing the results for gage 8 to that for gage 10. Also, good agreement is obtained when comparing results for the present study to those of the previous study [1]. Best agreement is seen for $M \gtrsim 1.0$.

Similar conclusions are reached when examining the results for gages 12 and 14 ($x/d_0 = 3.50$, $z/S = 0.33$) as shown in Figure 16. Agreement between gages 12 and 14 is good. Agreement with the results of [1] is good, with best agreement for $M \gtrsim 1.0$. The discrepancy at $M = 2.4$ may be due to the possible unstable nature of the flow situation producing values of $SNR < 0.0$ [1].

It was concluded that the experimental aparatus of the present study reproduced results obtained in the previous study [1]. The results of [1], for $\theta_c \simeq 1.0$, were used in comparison with the results of the present study, $\theta_c > 1.0$, to determine the influence of coolant dimensionless temperature (θ_c) on film cooling performance.

Additional comparison of the heat flux gage reproducibility from the previous study [1] and the present are presented in Appendix F.

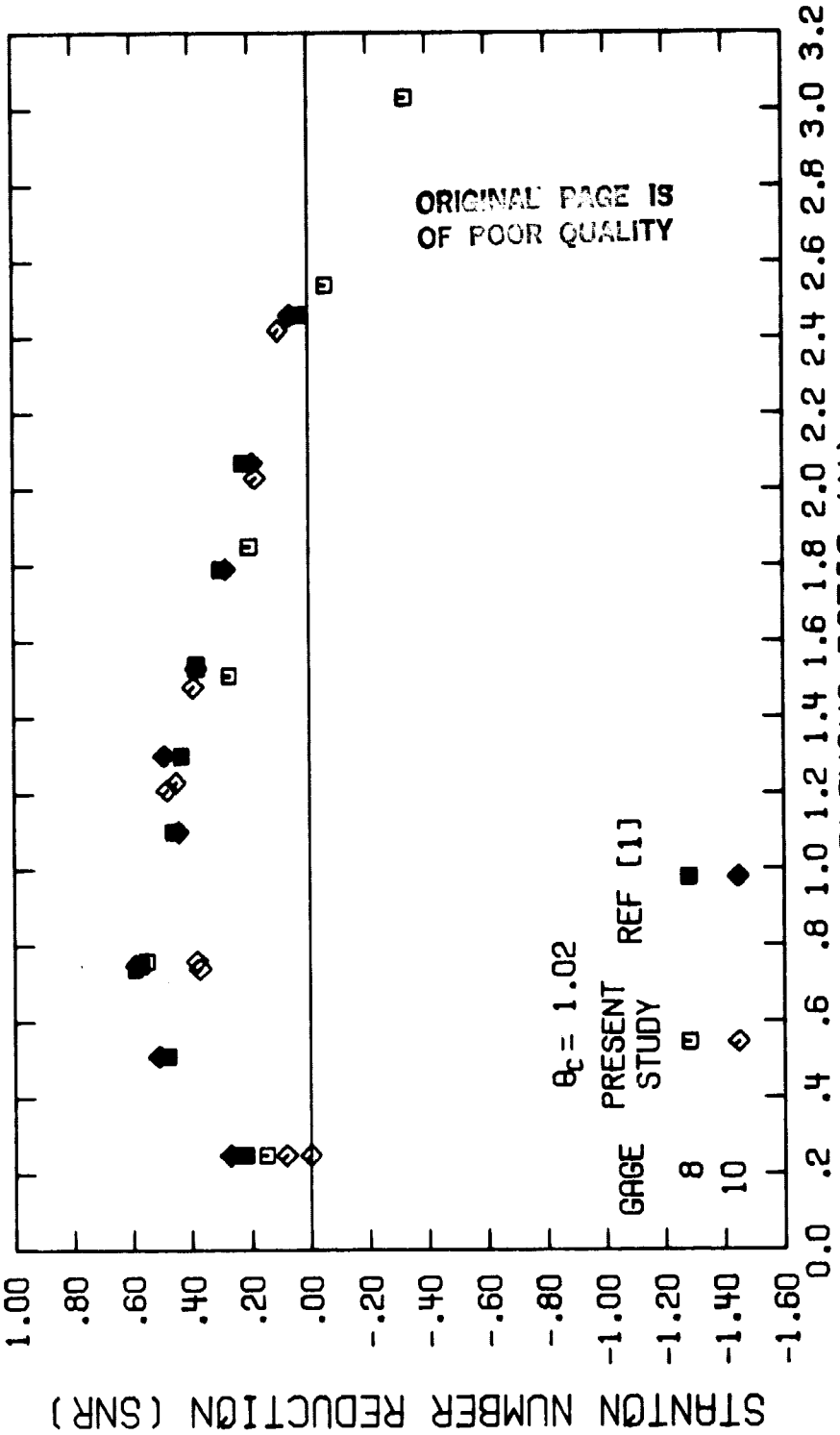

Figure 15. Comparison of Stanton Number Reduction with Blowing Ratio (Gages 8 and 10)

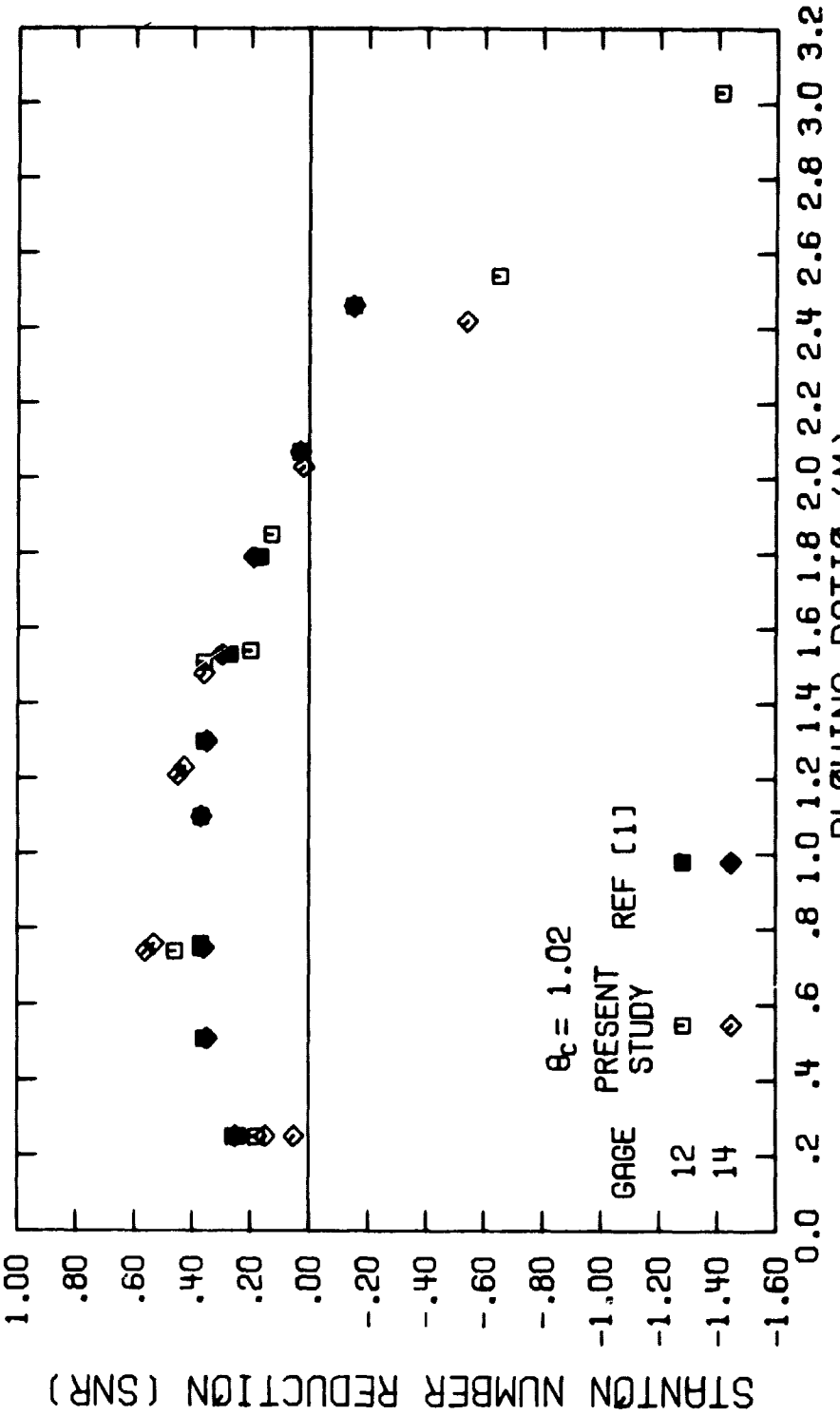

Figure 16. Comparison of Stanton Number Reduction with Blowing Ratio (Gages 12 and 14)

IV. RESULTS

IV.A. Introduction

Film cooling experiments were conducted to examine the effects of dimensionless coolant temperature (θ_c) on film cooling performance. The results discussed in this chapter show that changing θ_c results in a change in the level of local surface heat flux and also a shift in the distribution of local surface heat flux.

Experiments were conducted with blowing from a single row of coolant holes, with the row located at three angular locations relative to stagnation, θ_i = 5.0°, 22.9°, 40.8°. These angular locations were selected to match those used in the previous study [1], where single and multiple row film cooling experiments were performed with $\theta_c \simeq 1.0$. The range of blowing ratio simulated in the present study ($0.25 \leq M \leq 10.23$) reproduced the range reported in [1]. The present study extends the range of θ_c to $1.18 \leq \theta_c \leq 1.56$.

The film cooling results are presented in terms of the Stanton Number Reduction, defined as

$$\text{Stanton Number Reduction, SNR} \equiv 1 - \frac{St_{FC}}{St_o} .$$

Positive values of SNR represent the fractional reduction in heat flux due to film cooling while negative values correspond to an increase in heat flux due to film cooling. The condition SNR = 1 corresponds to an adiabatic (locally) film cooled surface and SNR > 1 implies heat transfer <u>from</u> the film cooled surface.

The value of θ_c quoted for each experimental test condition was calculated from the freestream temperature ($T_{\infty,o}$), the nominal wall temperature ($T_{w,nom}$), and the average of the coolant temperatures for the five primary coolant holes (T_c) in the instrumented region of the test cylinder. Thus,

$$\theta_c = \frac{T_c - T_{\infty,o}}{T_{w,nom} - T_{\infty,o}} .$$

The blowing ratio for each experimental test condition was calculated as the average value of the blowing ratio for each of the five primary coolant holes.

The data from [1] for single row film cooling with $\theta_c \simeq 1.0$ were used for direct comparison with the data of the present study for $\theta_c > 1$. Data for $\theta_c \simeq 1.0$ at values of M not reported in [1] were obtained by linear interpolation from the tabular data in Appendix III, reference [1].

The results are presented to show the influence of θ_c on the local level of SNR and on the calculated spanwise averaged Stanton Number Reduction, SNR_{AVG}. The data are interpreted to illustrate the influence of θ_c on the apparent coolant jet location. Finally, the results are viewed in terms of the linear superposition model to quantify the influence of θ_c on SNR.

IV.B. Effect of Dimensionless Coolant Temperature on Stanton Number Reduction

IV.B.1. Distribution of Stanton Number Reduction

Selected results for the local distribution of SNR are presented in this section to illustrate the major trends shown by the data.[1] The results for four combinations of injection location (θ_i) and blowing ratio (M) are discussed for the conditions shown below.

θ_i	5.0°	22.9°	22.9°	40.8°
M	2.01	1.23[2]	2.07	1.14
θ_c	1.03	1.02	1.02	1.04
	1.29	1.30	1.29	1.40
		1.56	1.36	

[1] Appendix E contains a complete listing of all data in graphical and tabular form.

[2] For the present study, M was held constant within ± 0.01 as θ_c was varied. The nominal value of M quoted is the average value. (See tabular data in Appendix E).

The data for $\theta_c \simeq 1.0$ were taken from the previous study, Appendix III, [1], with linear interpolation with respect to M when necessary.

Figures 17, 18 and 19 show the spanwise distribution of Stanton Number Reduction for the location $\theta_i = 5.0°$ at a blowing ratio of M = 2.01. Each plot shows SNR (along the ordinate) as a function of spanwise location z/S (along the abscissa[1]). Symbols defined in the legend represent the data for the values of x/d_o and θ_c. The range of the abscissa, the spanwise distance from z/S = 0.0 to z/S = 1.0, represents the spacing between the centers of two adjacent coolant holes ($S/d_o = 5$). The hash marks along the abscissa illustrate the break-out length of the coolant holes, extending to $z/S = \pm 0.24$.

The symbols representing data taken in the present study (for $\theta_c > 1.0$) are connected with solid or dashed lines to <u>suggest</u> the profile shape and to facilitate reading of the plots. For the locations $x/d_o = 6.50$ and $x/d_o = 8.50$ (e.g., Figure 18) dotted lines extend from the measured data points to z/S = 0.0 and z/S = 1.0. The value of SNR at z/S = 0.0 (reflected to z/S = 1.0) for $x/d_o = 6.50$ and $x/d_o = 8.50$ was calculated by linear interpolation of the data of Appendix E at z/S = 0.0 between $x/d_o = 3.50$ and $x/d_o = 11.50$.

Figures 17, 18 and 19 show the spanwise distribution of SNR at the location $\theta_i = 5.0°$, for $1.50 \leq x/d_o \leq 11.50$, at a value of blowing ratio of M = 2.01. Figure 17 shows an increase in SNR at $x/d_o = 1.50$ when θ_c is increased from $\theta_c = 1.03$ to $\theta_c = 1.29$. It is seen that behind the coolant hole, at $x/d_o = 1.50$, z/S = 0.0, with $\theta_c = 1.03$, the value of SNR was SNR = 0.0 (no effect of the coolant), while increasing θ_c to $\theta_c = 1.29$ provided a heat flux reduction of SNR = 0.45. At z/S = 0.33, $x/d_o = 1.50$ (Figure 17), the value of SNR was increased from SNR = 0.23 with $\theta_c = 1.03$ to SNR = 0.39 with $\theta_c = 1.29$.

The general pattern of increased SNR with increased θ_c is seen at all streamwise locations (Figures 17, 18 and 19, $1.50 \leq x/d_o \leq 11.50$) though the SNR levels diminish with downstream distance.

---

[1] The value of SNR at z/S = 1.00 was taken to be the same as the value of SNR at z/S = 0.0.

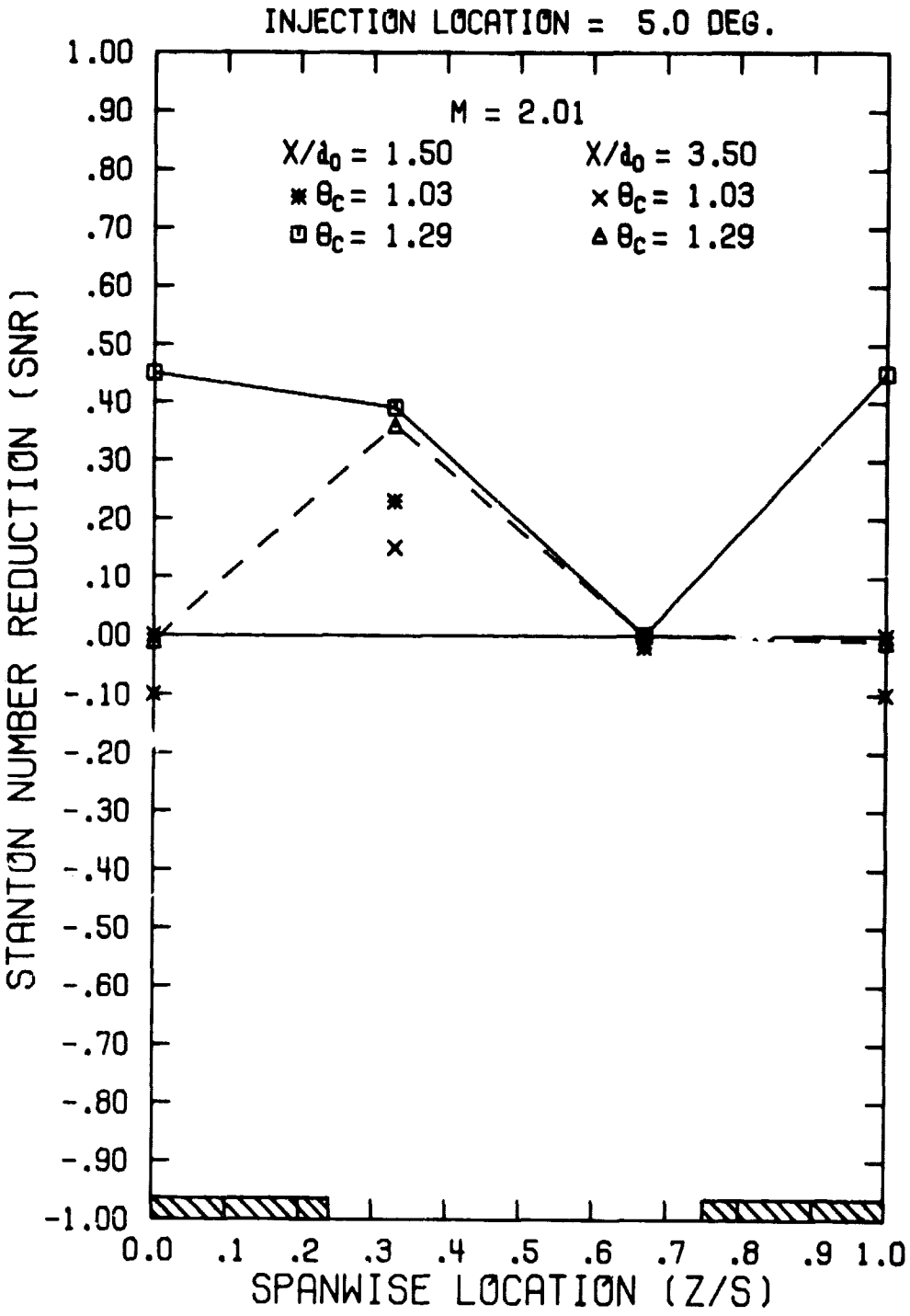

Figure 17. Spanwise Variation in Stanton Number Reduction (θ_i=5.0°, M=2.01, x/d_0=1.50 and 3.50)

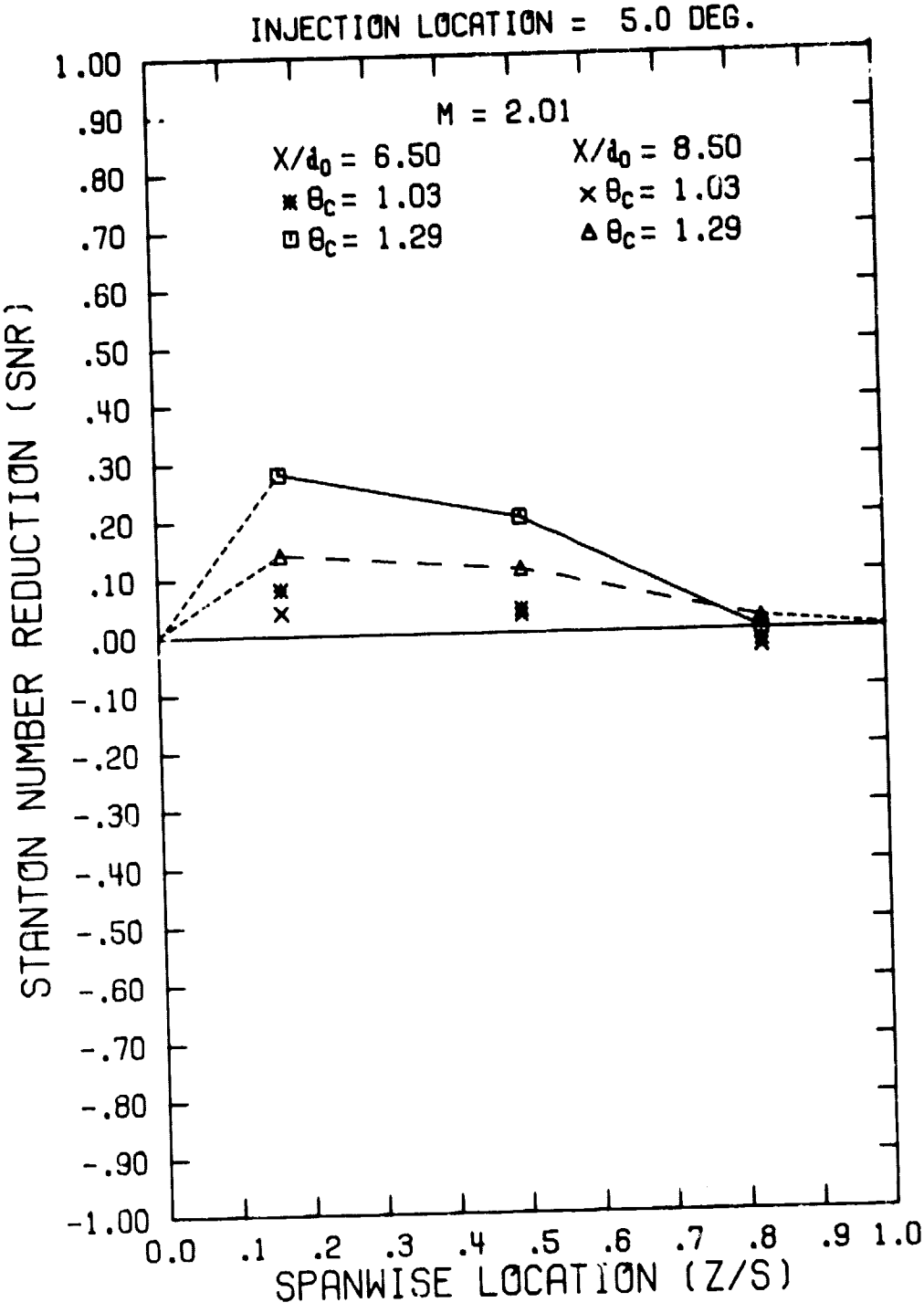

Figure 18. Spanwise Variation in Stanton Number Reduction (θ_i=5.0°, M=2.01, x/d_0=6.50 and 8.50)

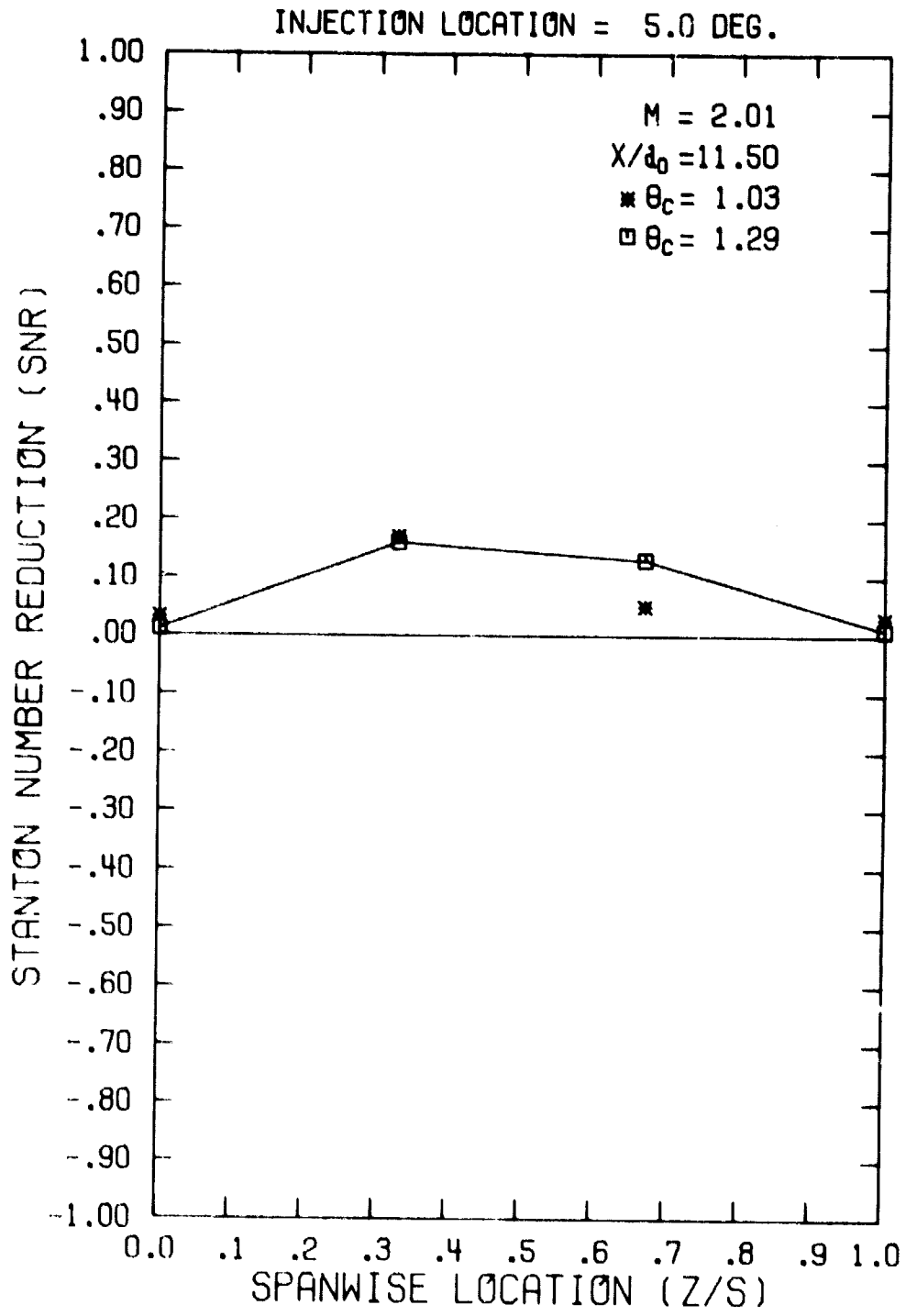

Figure 19. Spanwise Variation in Stanton Number Reduction (θ_i=5.0°, M=2.01, x/d_0=11.50)

The value of SNR was unaffected by a change in θ_c at locations $z/S = 0.67$ for $x/d_0 = 1.50$ and $x/d_0 = 3.50$ (Figure 17) and at $z/S = 0.83$, for $x/d_0 = 6.50$ and $x/d_0 = 8.50$ (Figure 18). It is inferred that the localized coolant jet did not influence those spanwise locations. Further discussion of the effects of θ_c on the distribution of SNR is found in Section IV.C.

At $\theta_i = 22.9°$, the plots of Figures 20 through 24 present the spanwise distribution of SNR, for a value of blowing ratio $M = 1.23$.[1] As seen in the legend for each plot, results are presented for three values of θ_c: $\theta_c = 1.02$, 1.30 and 1.56.

The effect of increasing the value of θ_c at $\theta_i = 22.9°$, $M = 1.23$ is to increase the levels of SNR. At all x/d_0 locations, the maximum values of SNR with $\theta_c = 1.30$ or $\theta_c = 1.56$ are greater than the maximum values of SNR with $\theta_c = 1.02$. Directly behind the coolant hole ($x/d_0 = 1.50$, $z/S = 0.0$, Figure 20), the value of SNR with $\theta_c = 1.30$ is a large positive number, where it is seen that the value of SNR with $\theta_c = 1.02$ was a negative number.

At the value of blowing ratio $M = 1.23$, film cooling with $\theta_c = 1.56$ provides large increases in SNR levels, with the maximum value of SNR for $\theta_c = 1.56$ at the downstream location $x/d_0 = 11.50$ (Figure 24) nearly equal to the maximum value of SNR with $\theta_c = 1.02$ at the location $x/d_0 = 1.50$.

The results for a larger value of blowing ratio at $\theta_c = 22.9°$, $M = 2.07$, are shown in Figures 25 through 29, where the distribution of SNR is shown at three values of θ_c, 1.02, 1.29 and 1.36. Figures 25 through 29 show that the result of film cooling with $\theta_c = 1.02$ at a blowing ratio of $M = 2.07$ was generally detrimental to the cooling of the surface, with significant negative values of SNR and low positive values of SNR found in the range $1.50 \leq x/d_0 \leq 11.50$. Results with a value of θ_c of 1.29 show that the cooling level was improved, largely at $x/d_0 = 1.50$ (Figure 25) but also at locations in the range $1.50 \leq x/d_0 \leq 11.50$. However, significant negative values of SNR were still observed with $\theta_c = 1.29$ at locations $x/d_0 \geq 3.50$.

[1] The value of SNR was unavailable at some locations (e.g. $x/d_0 = 1.50$, $z/S = 0.33$ and 0.67, $\theta_c = 1.56$) due to heat flux gage malfunction. See Appendix D.

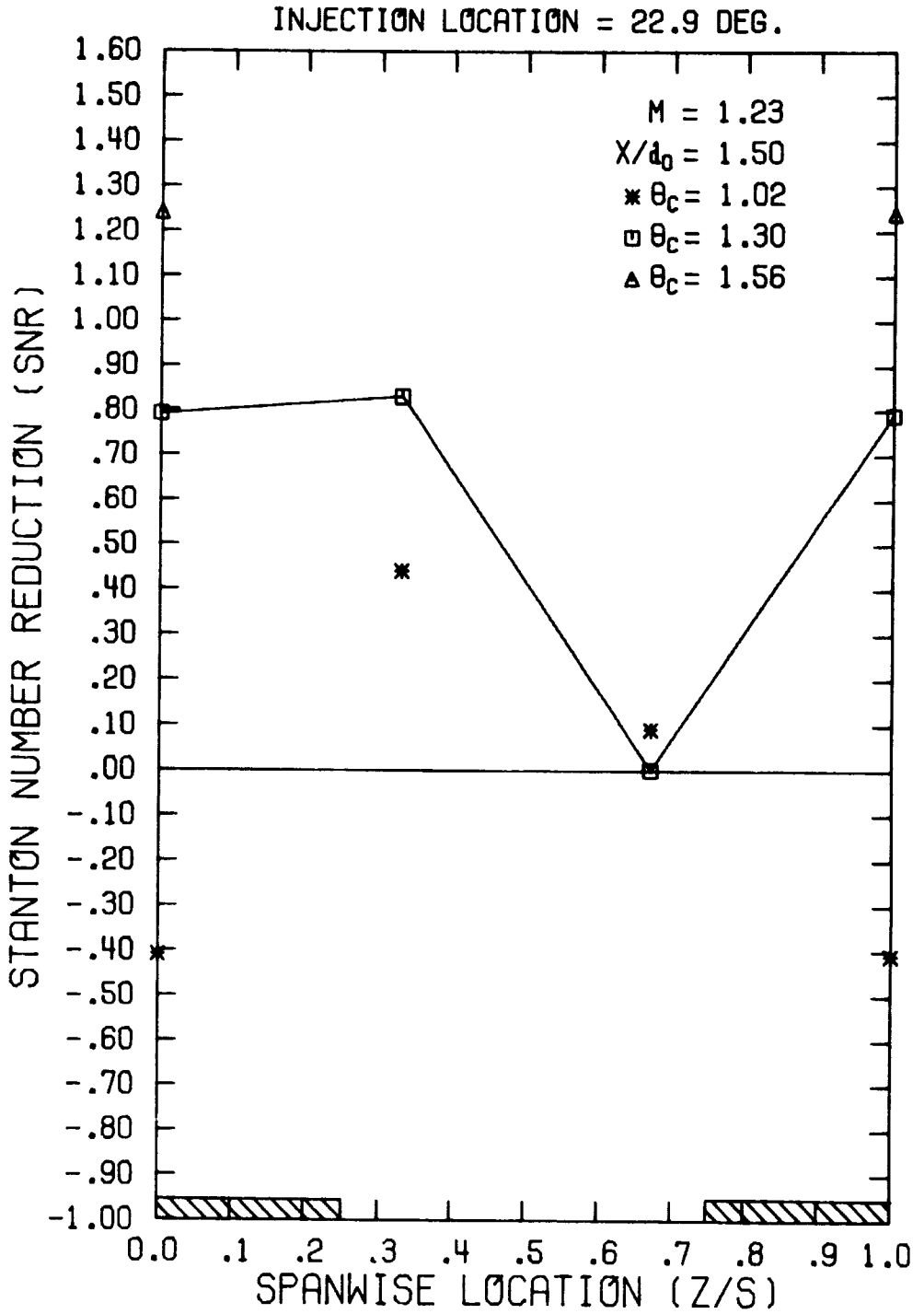

Figure 20. Spanwise Variation in Stanton Number Reduction (θ_i=22.9°, M=1.23, x/d_0=1.50)

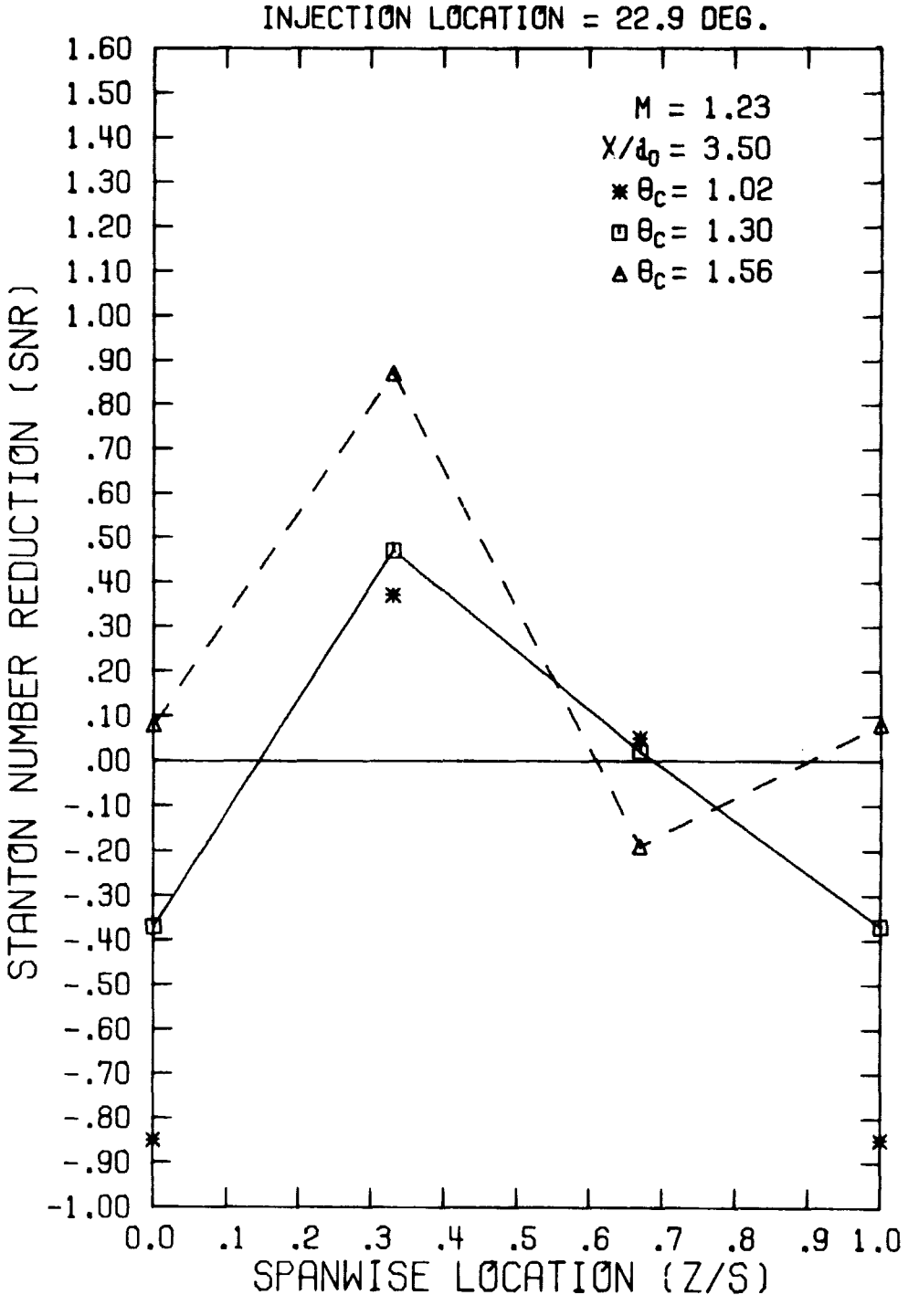

Figure 21. Spanwise Variation in Stanton Number Reduction (θ_i=22.9°, M=1.23, x/d_o=3.50)

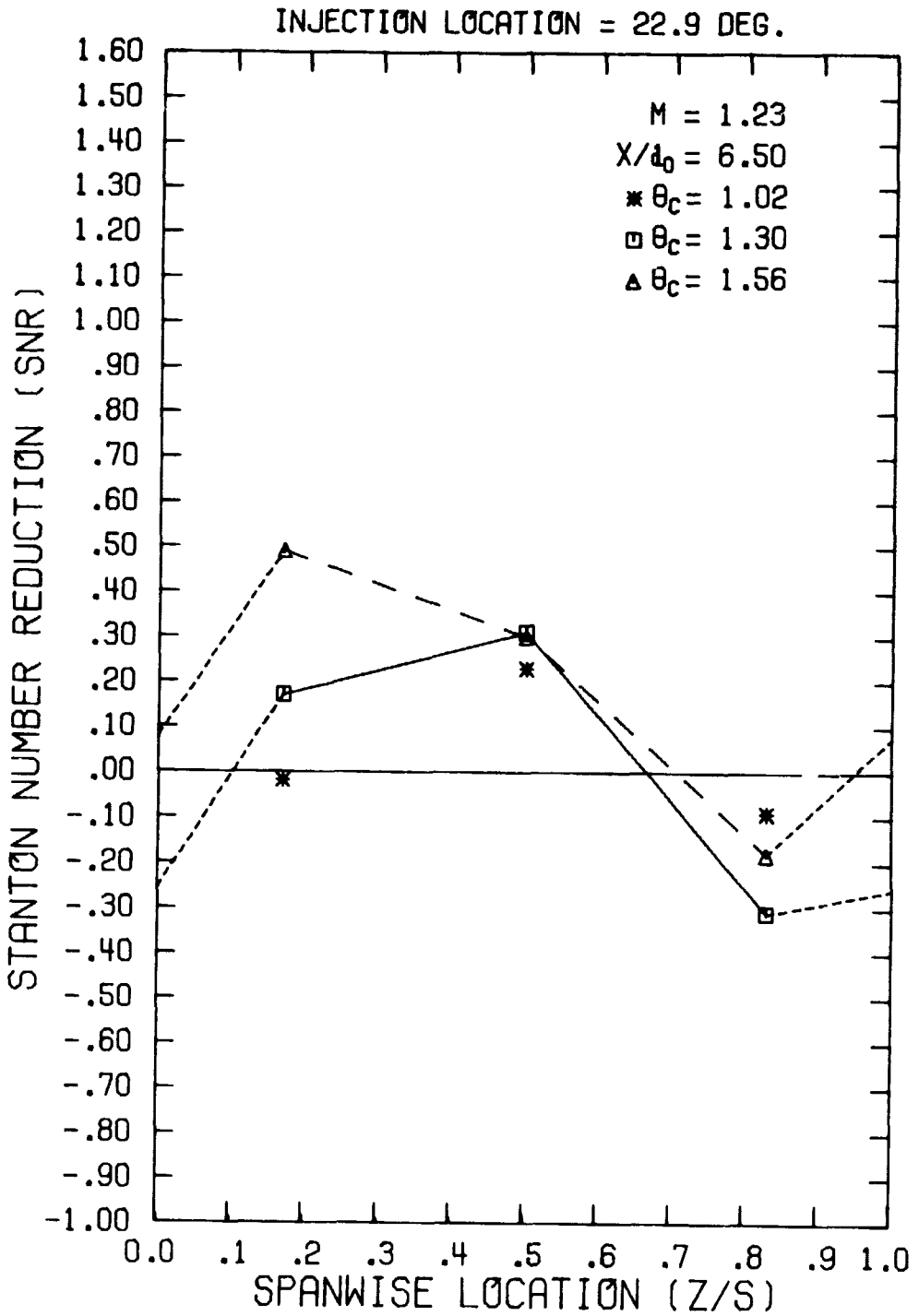

Figure 22. Spanwise Variation in Stanton Number Reduction (θ_i=22.9°, m=1.23, x/d_0=6.50)

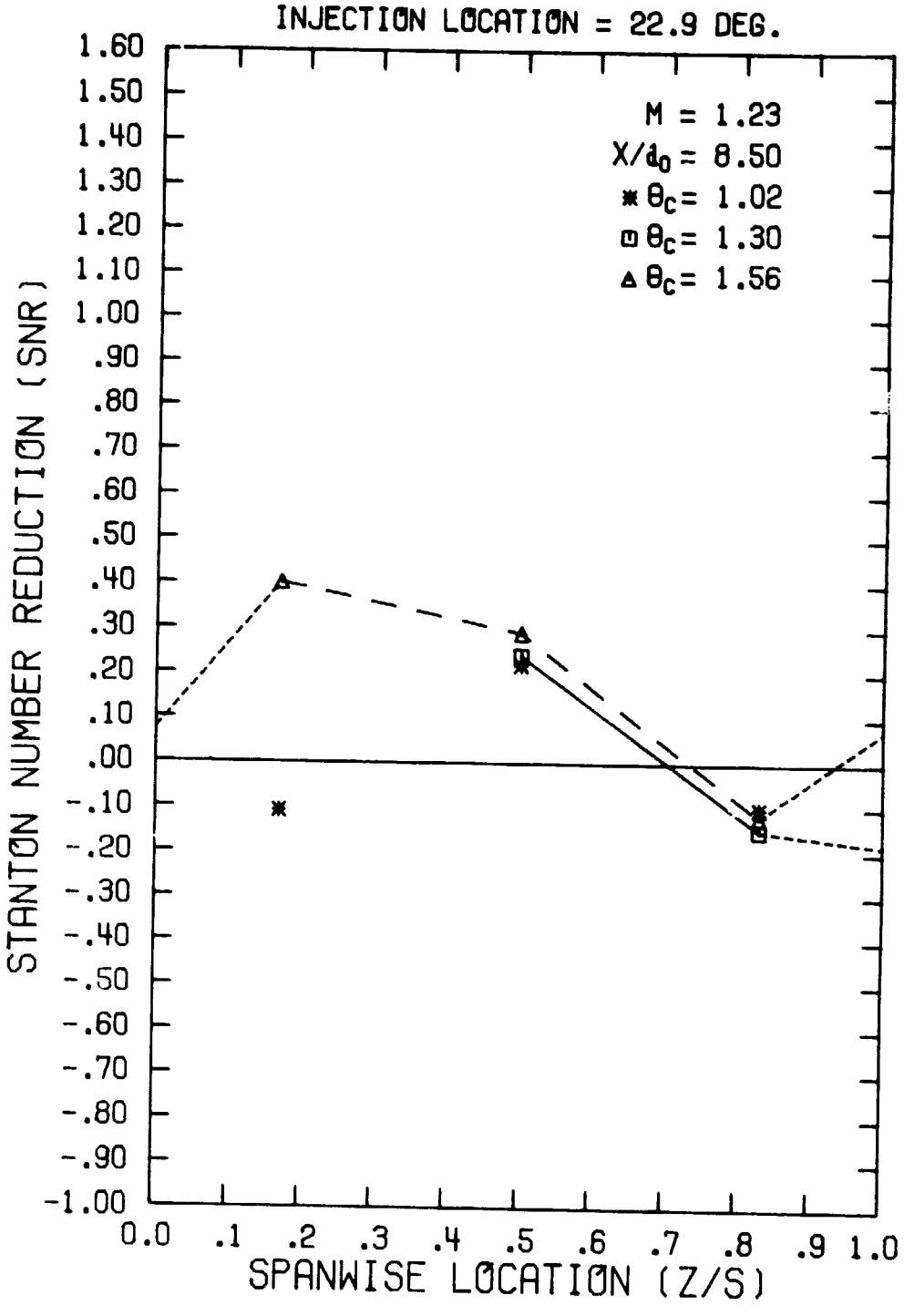

Figure 23. Spanwise Variation in Stanton Number Reduction (θ_i=22.9°, M=1.23, x/d_o=8.50)

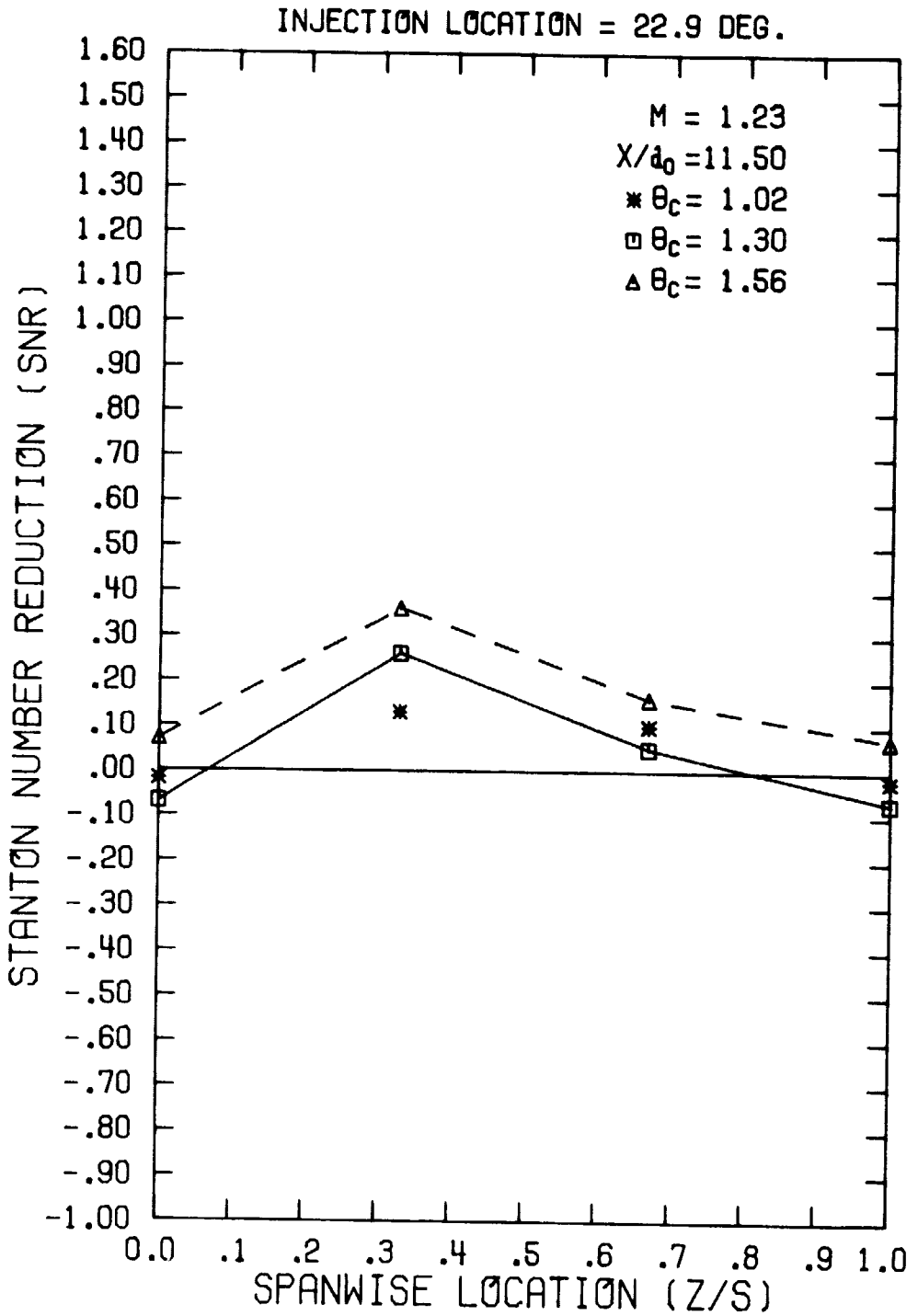

Figure 24. Spanwise Variation in Stanton Number Reduction (θ_i=22.9°, M=1.23, x/d_0=11.50)

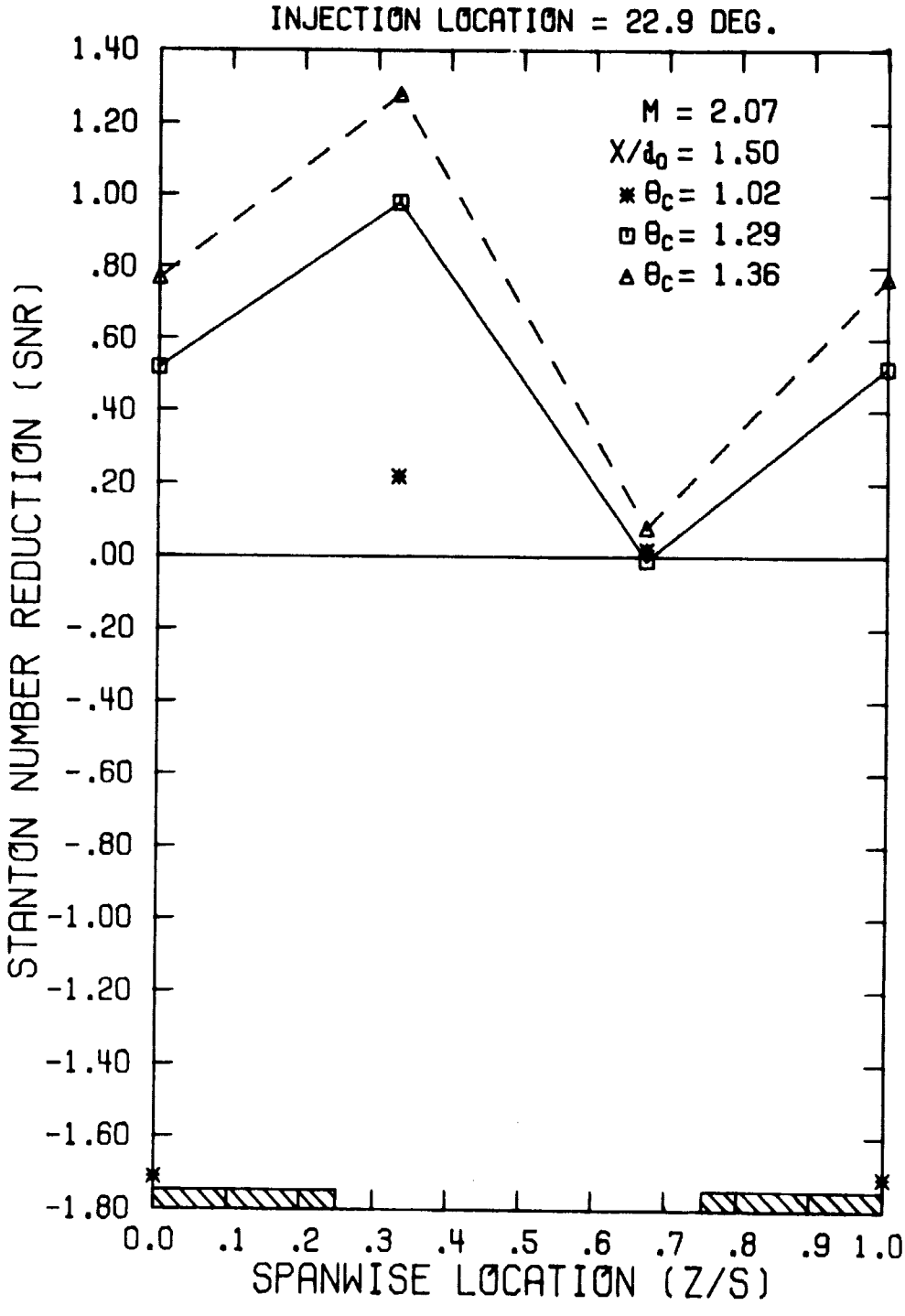

Figure 25. Spanwise Variation in Stanton Number Reduction (θ_i=22.9°, M=2.07, x/d_0=1.50)

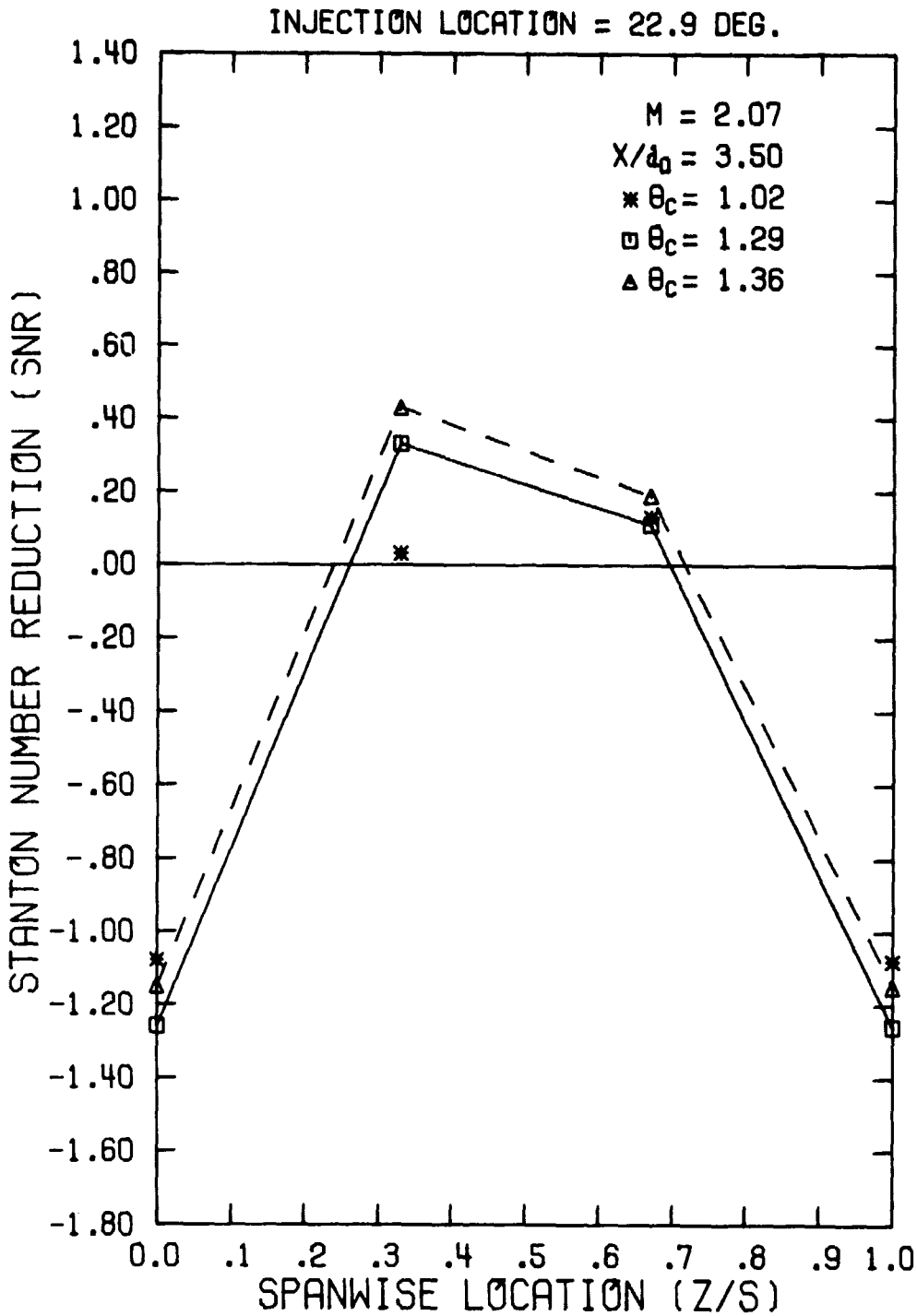

Figure 26. Spanwise Variation in Stanton Number Reduction (θ_i=22.9°, M=2.07, x/d_0=3.50)

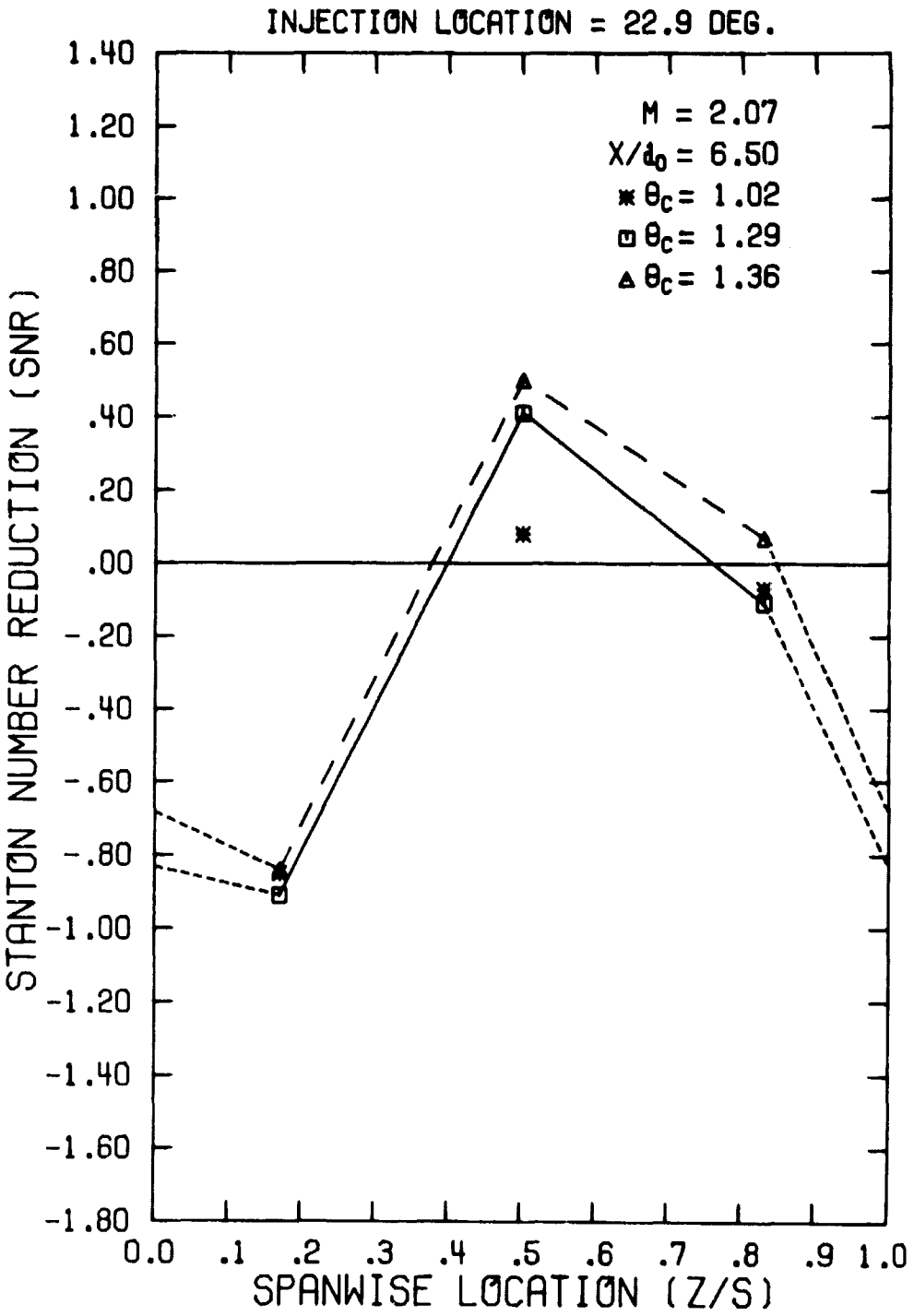

Figure 27. Spanwise Variation in Stanton Number Reduction (θ_i=22.9°, M=2.07, x/d_o=6.50)

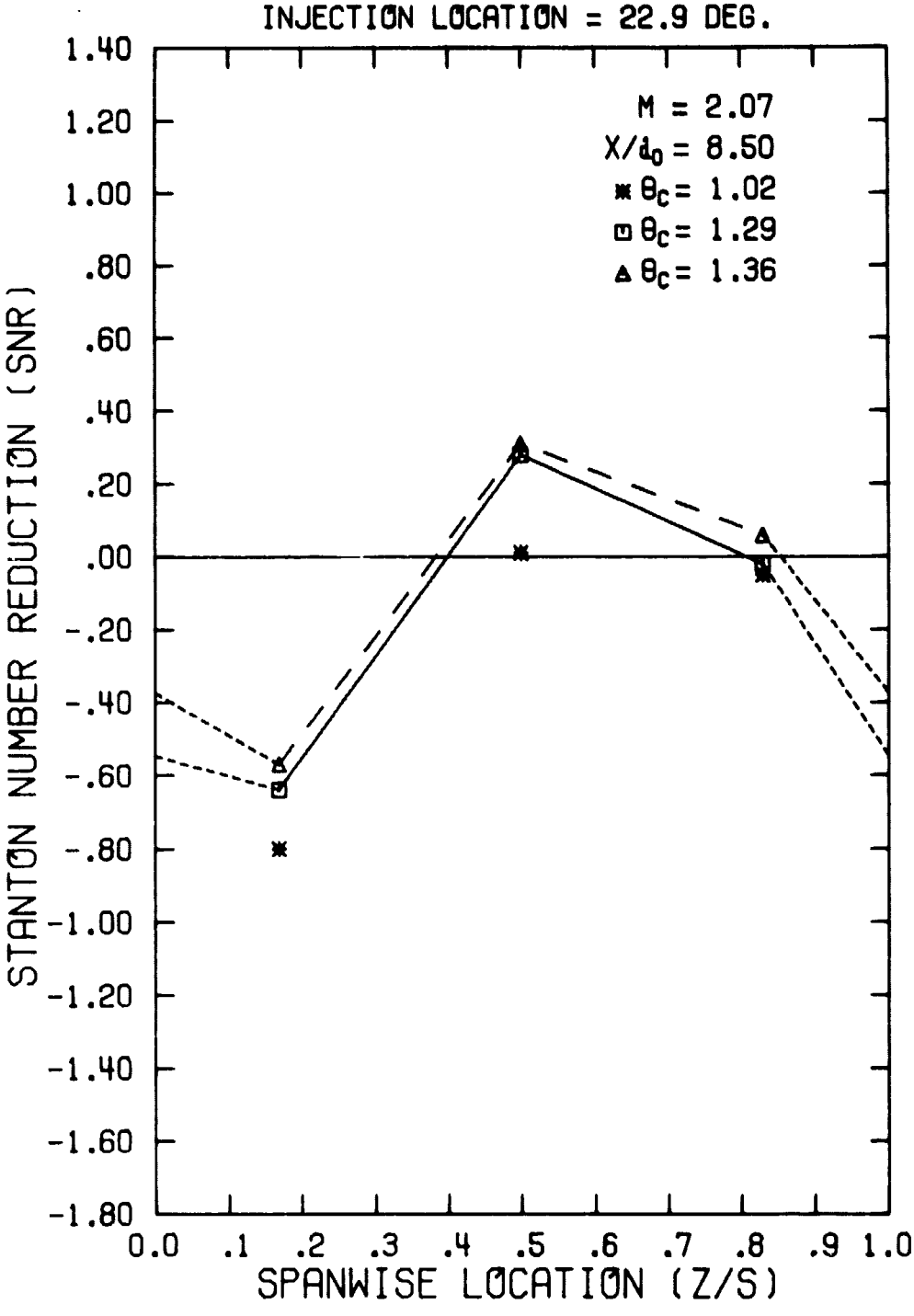

Figure 28. Spanwise Variation in Stanton Number Reduction (θ_i=22.9°, M=2.07, x/d_o=8.50)

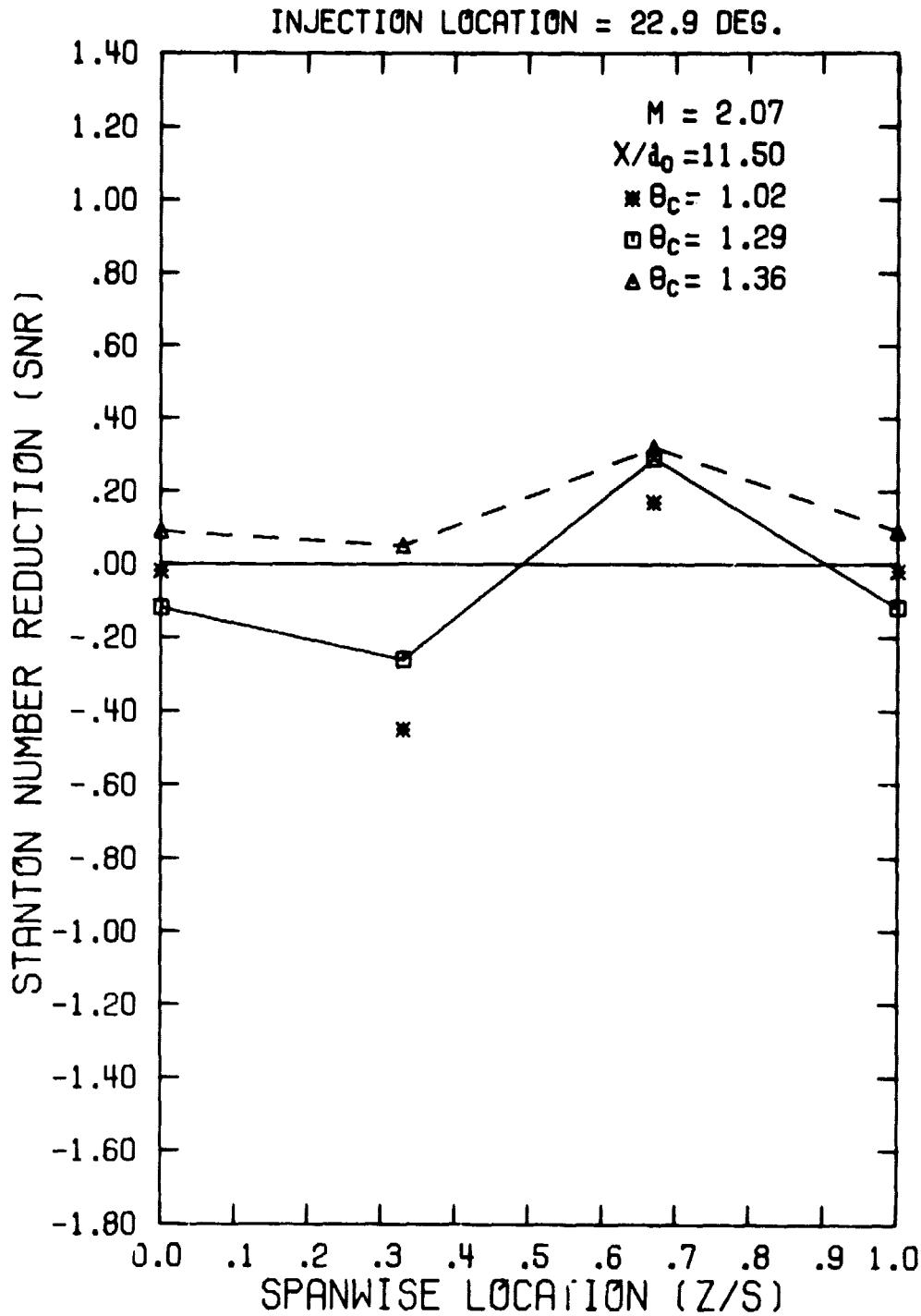

Figure 29. Spanwise Variation in Stanton Number Reduction (θ_i=22.9°, M=2.07, x/d_o=11.50)

With an increase in θ_c from 1.29 to θ_c = 1.36, a value of SNR greater than 1.0 was observed at x/d_0 = 1.50, z/S = 0.33 (Figure 25). There was an overall increase in SNR over the case with θ_c = 1.29, but large negative values of SNR remained in the range $3.50 \leq x/d_0 \leq 8.50$.

Results for θ_j = 40.8°, M = 1.14 are shown in Figures 30, 31 and 32. The plots for SNR vs. z/S and x/d_0 present the data taken with θ_c = 1.04 and θ_c = 1.40. As was the case with θ_j = 5.0° and θ_j = 22.9°, increasing θ_c caused an increase in SNR in regions where the coolant apparently was localized. The value of SNR was greater than 1.0 at x/d_0 = 1.50, z/S = 0.33, and the maximum level of SNR was increased downstream through x/d_0 = 11.50.

To summarize, the local film cooling performance at all values of blowing ratio, dimensionless coolant temperature, and injection location exhibits increased values of SNR with an increase in θ_c as would be expected from the linear superposition model. As will be discussed in IV.C, the trends for the distribution of SNR with z/S or x/d_0 suggest that the localized behavior of the coolant, i.e. the flow field, is also dependent on the dimensionless coolant temperature.

IV.B.2. Results for Spanwise-averaged Stanton Number Reduction

In the application of film cooling data to turbine vane cooling designs, it is convenient to have film cooling performance averaged in the spanwise direction (i.e. average hole-to-hole). The results from the present study (Appendix E) were used to determine the spanwise-averaged Stanton Number Reduction, SNR_{AVG}. The value of SNR_{AVG} for a particular x/d_0 location was computed as follows:

(a) a series of straight line segments were fit through the data points of SNR vs z/S for the range $0 \leq z/S \leq 1$,

(b) the value for SNR at z/S = 0 (when a heat flux gage was not located at that point) was obtained by linear interpolation (at z/S = 0) from values for SNR at x/d_0 = 3.50 and x/d_0 = 11.50,

(c) the value of SNR at z/S = 1 was assumed equal to the value at z/S = 0, and

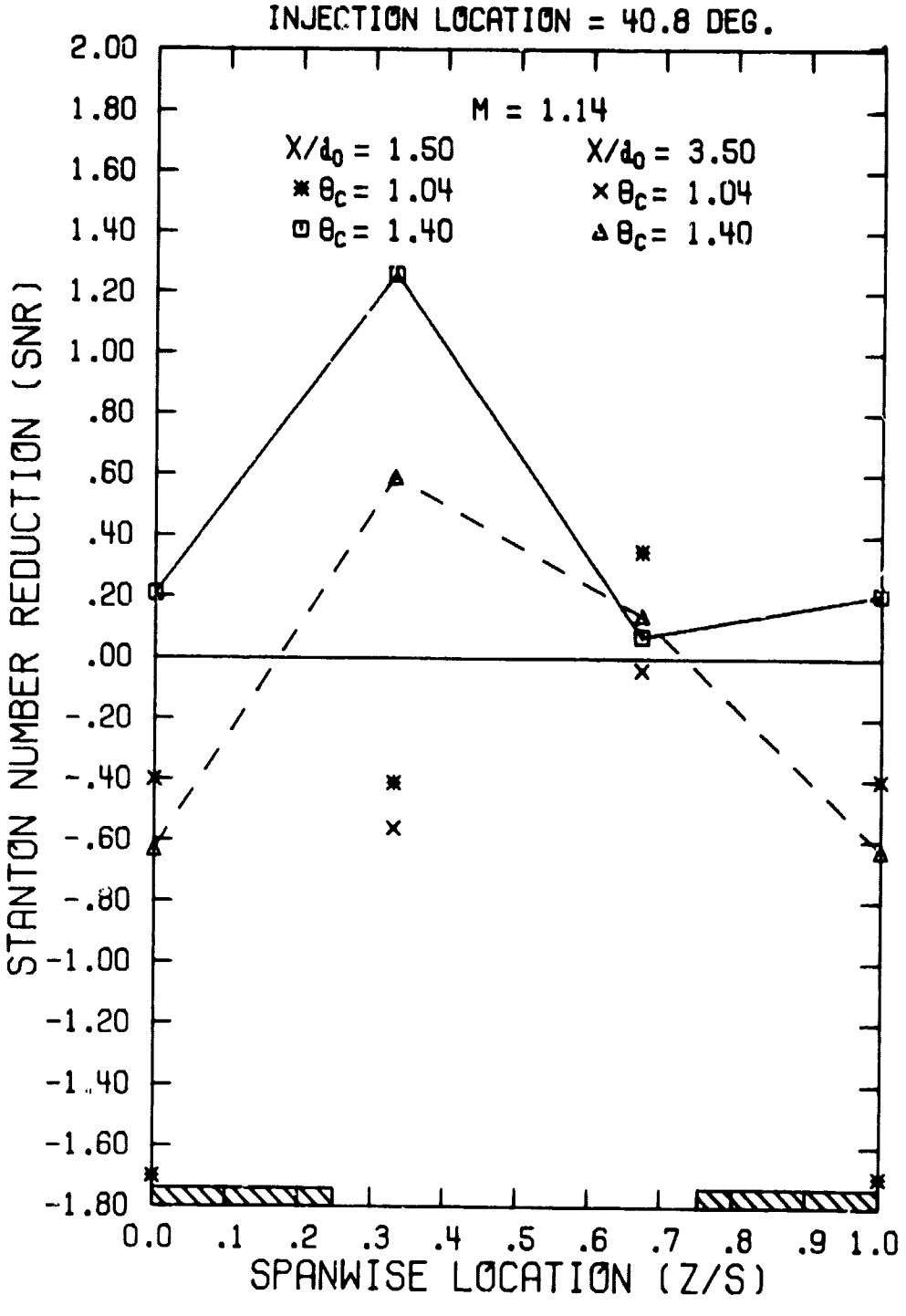

Figure 30. Spanwise Variation in Stanton Number Reduction (θ_i=40.8°, M=1.14, x/d_o=1.50 and 3.50)

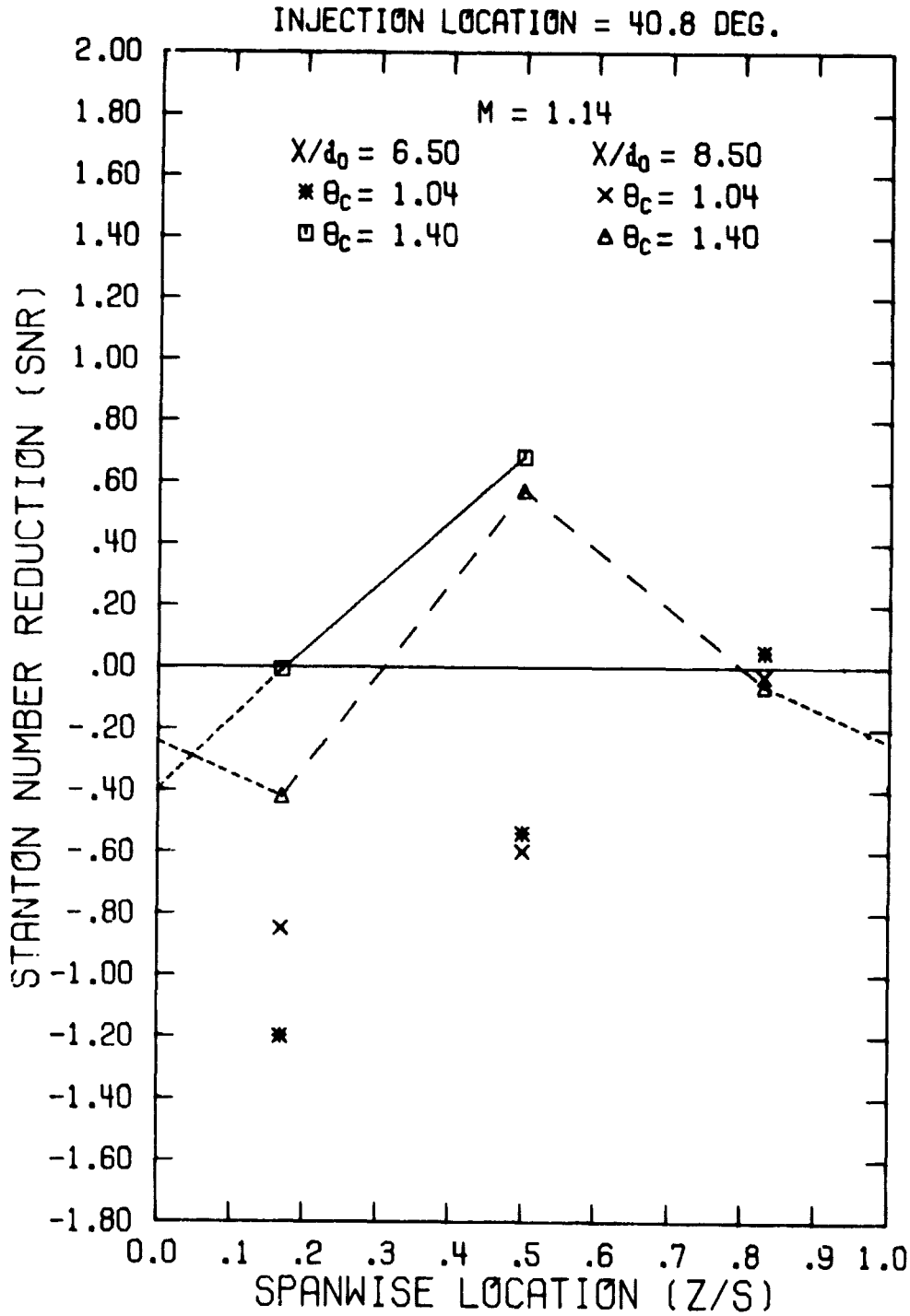

Figure 31. Spanwise Variation in Stanton Number Reduction (θ_i=40.8°, M=1.14, x/d_0=6.50 and 8.50)

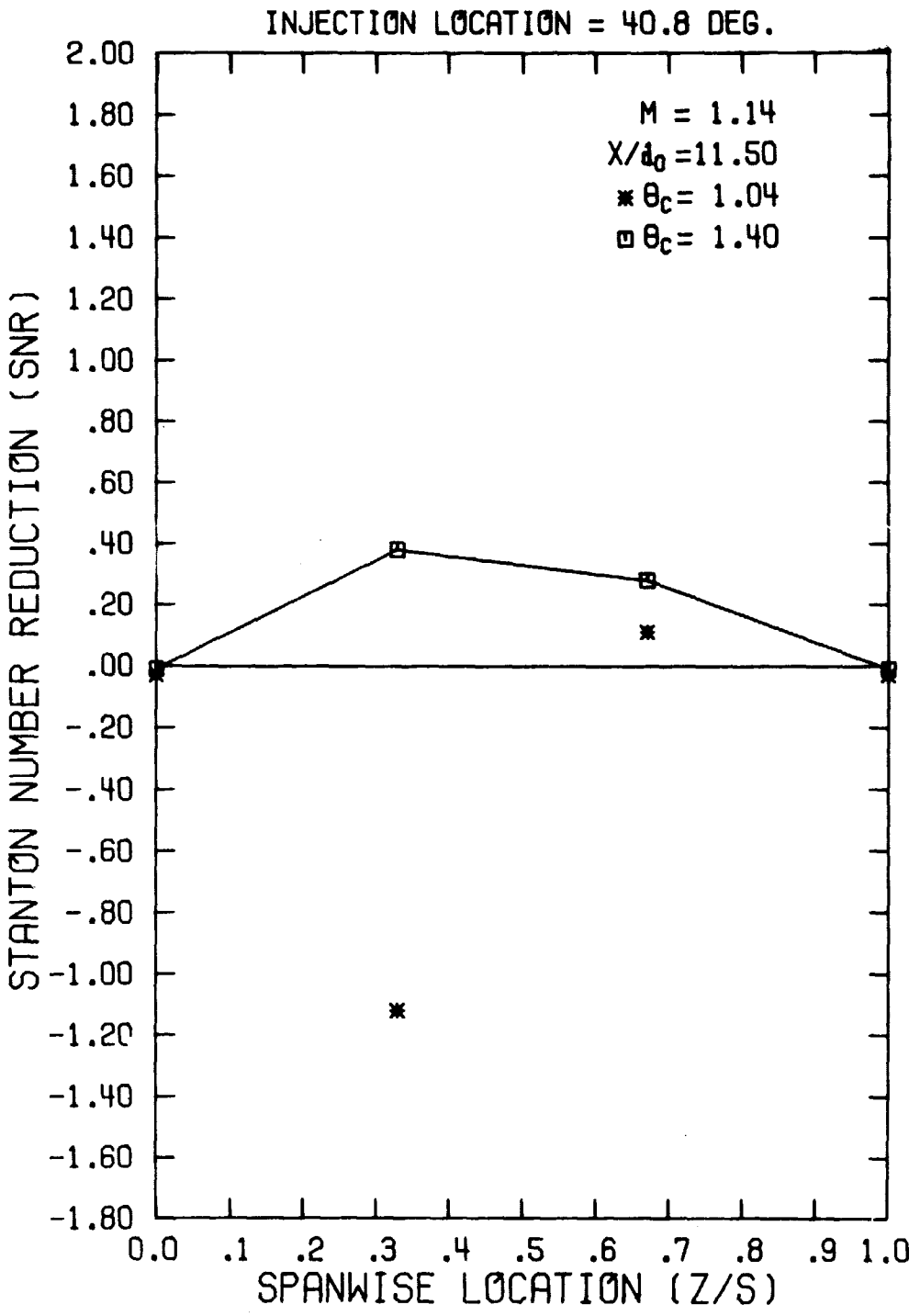

Figure 32. Spanwise Variation in Stanton Number Reduction (θ_i=40.8°, M=1.14, x/d_0=11.50)

(d) the value of SNR_{AVG} was obtained by integration under the straight line segment curve:

$$SNR_{AVG} = \int_0^1 SNR\ d(z/S)$$

A complete tabulation of the computed values of SNR_{AVG} is given in Appendix E.

The user of spanwise averaged data should note that averaging tends to smear out localized effects. A low value of SNR_{AVG} could result from a profile with a large negative value of SNR compensated by a large positive value of SNR. Or the value of SNR could be more uniform across the span with SNR_{AVG} a good representation of the spanwise distribution of SNR.

Figures 33 and 34 show the values of spanwise-averaged Stanton Number Reduction, SNR_{AVG}, as a function of downstream distance for the four values of blowing ratio investigated with $\theta_i = 5.0°$. The legend defines the corresponding values of θ_c. Both Figures 36 and 37 show that the level of SNR_{AVG} increased with an increase in θ_c.

The effect on SNR_{AVG} of increasing θ_c was largest at the location $x/d_o = 1.50$. The effect of θ_c diminished along the surface, with SNR_{AVG} tending toward 0.0 as x/d_o approached $x/d_o = 11.50$.

Figures 35 through 39 show results for SNR_{AVG} for the five blowing conditions tested with an injection location $\theta_i = 22.9°$. The legend of each plot defines the symbols representing values of θ_c for the test conditions.

At a blowing ratio of M = 0.25, Figure 35 shows that there was a slight effect on the levels of SNR_{AVG} when θ_c was increased from 1.03 to 1.18. At the downstream location $x/d_o = 11.50$, the level of SNR_{AVG} approached zero.

Figure 36 presents the data for SNR_{AVG} at a blowing ratio of M = 0.74. It is seen that increasing the value of θ_c to 1.45 resulted in an increase in SNR_{AVG} for downstream locations $x/d_o \leq 8.50$. Similar results for M = 1.23 are shown in Figure 37.

Figures 36 through 39 indicate that increasing the blowing ratio, for θ_c = constant, generally caused SNR_{AVG} to decrease and to become

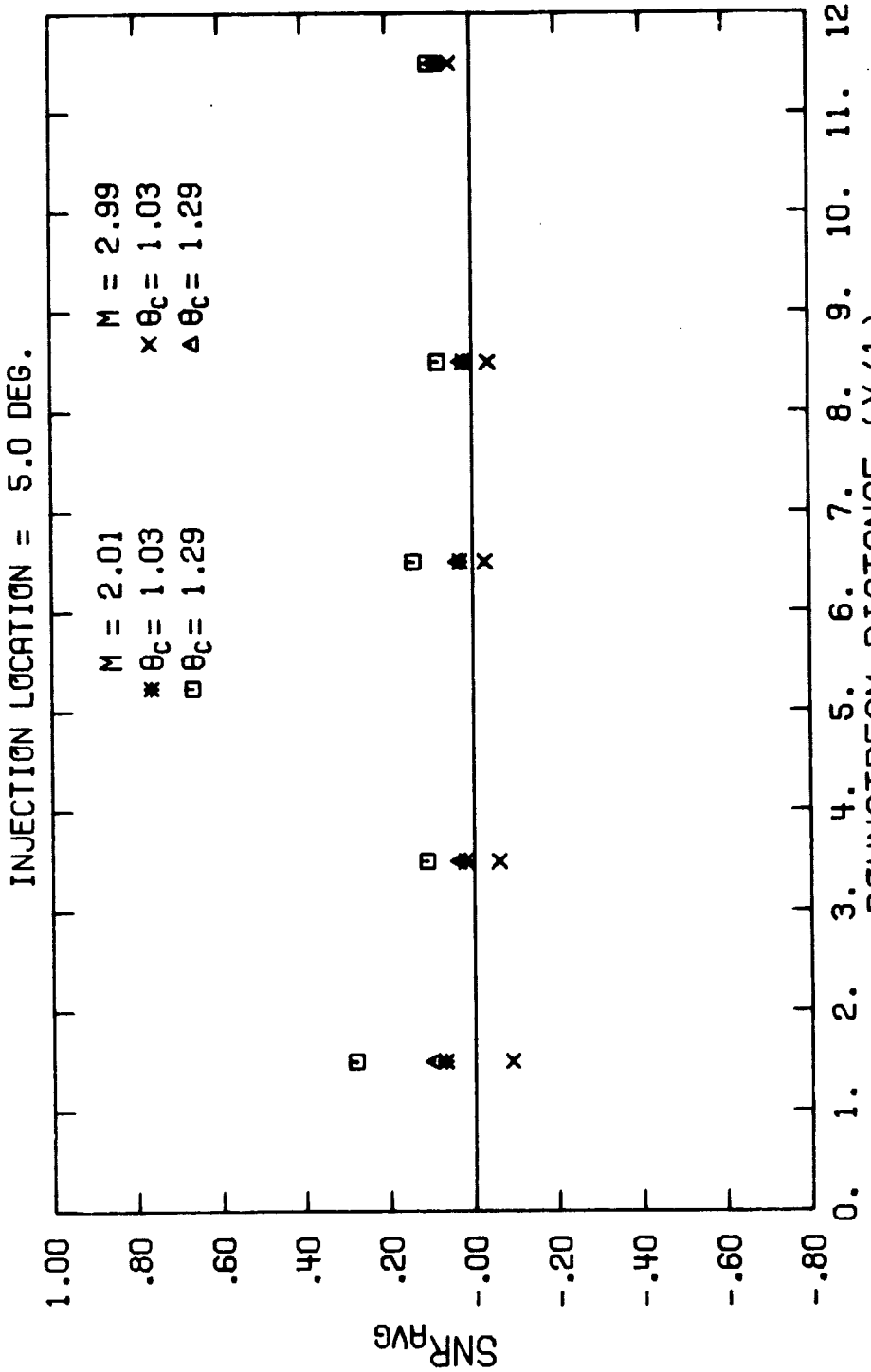

Figure 33. Variation in Spanwise-averaged Stanton Number Reduction with Downstream Distance (θ_i=5.0°, M=2.01 and 2.99)

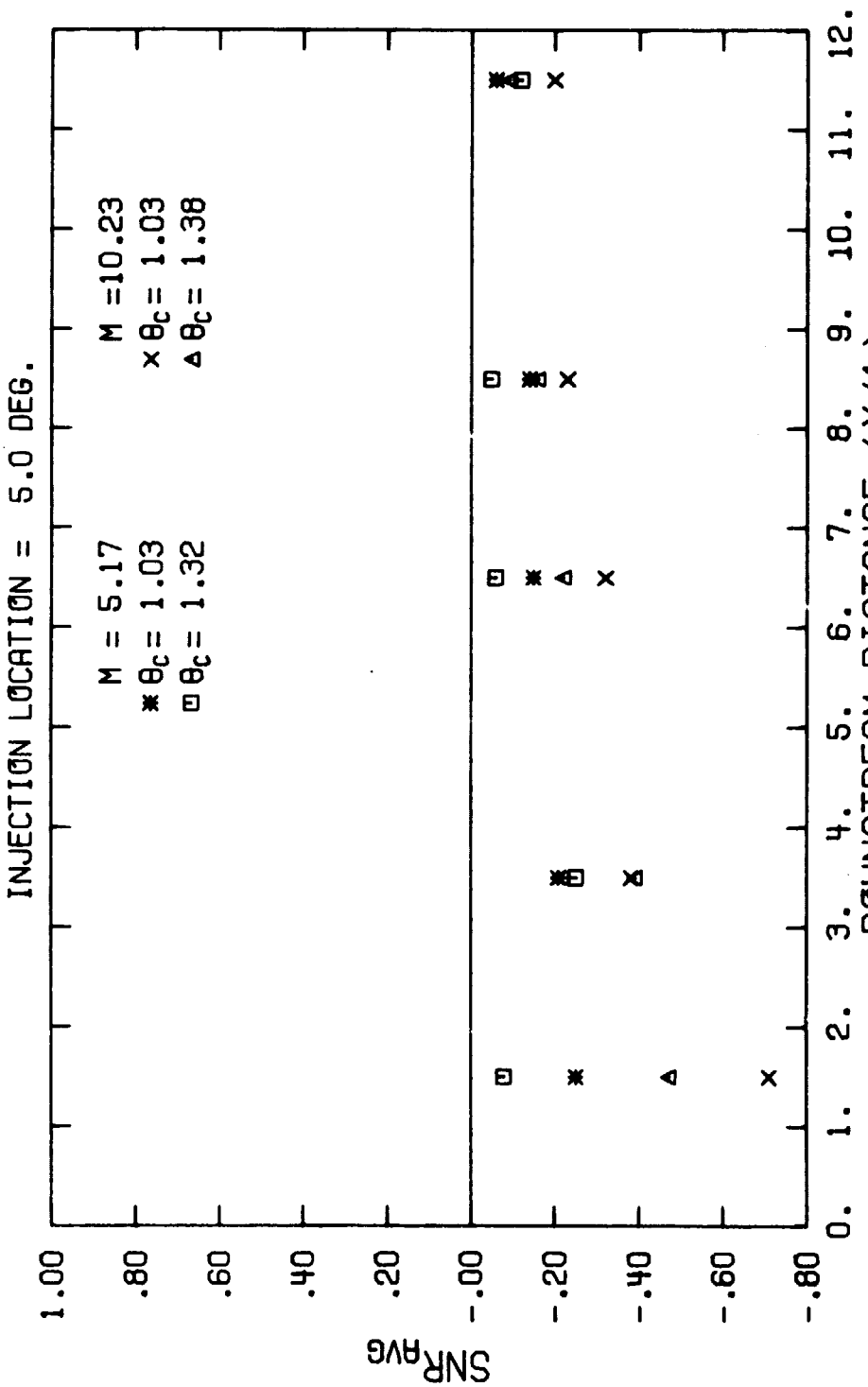

Figure 34. Variation in Spanwise-averaged Stanton Number Reduction with Downstream Distance (θ_i=5.0°, M=5.17 and 10.23)

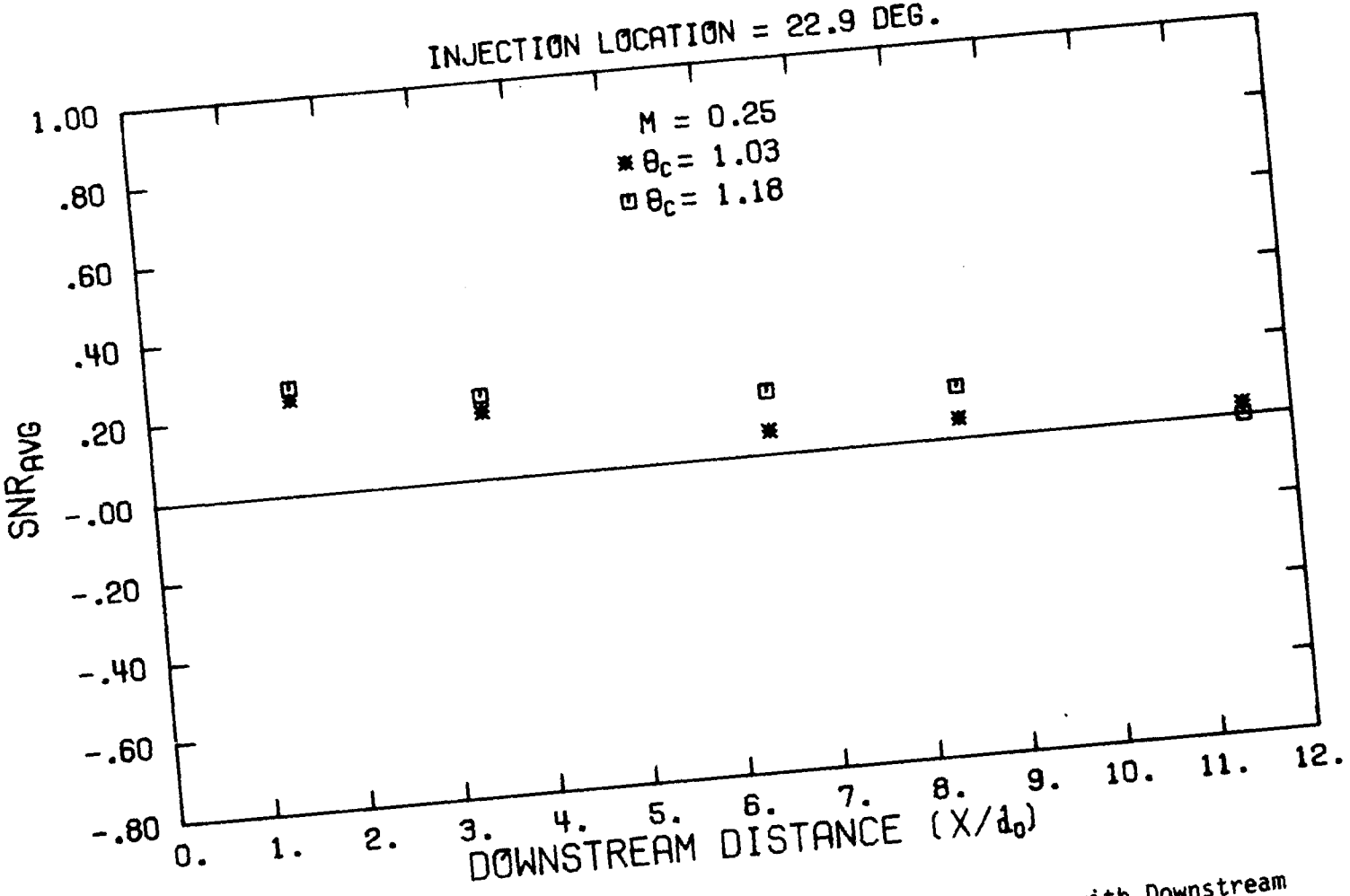

Figure 35. Variation in Spanwise-averaged Stanton Number Reduction with Downstream Distance (θ_i=22.9°, M=0.25)

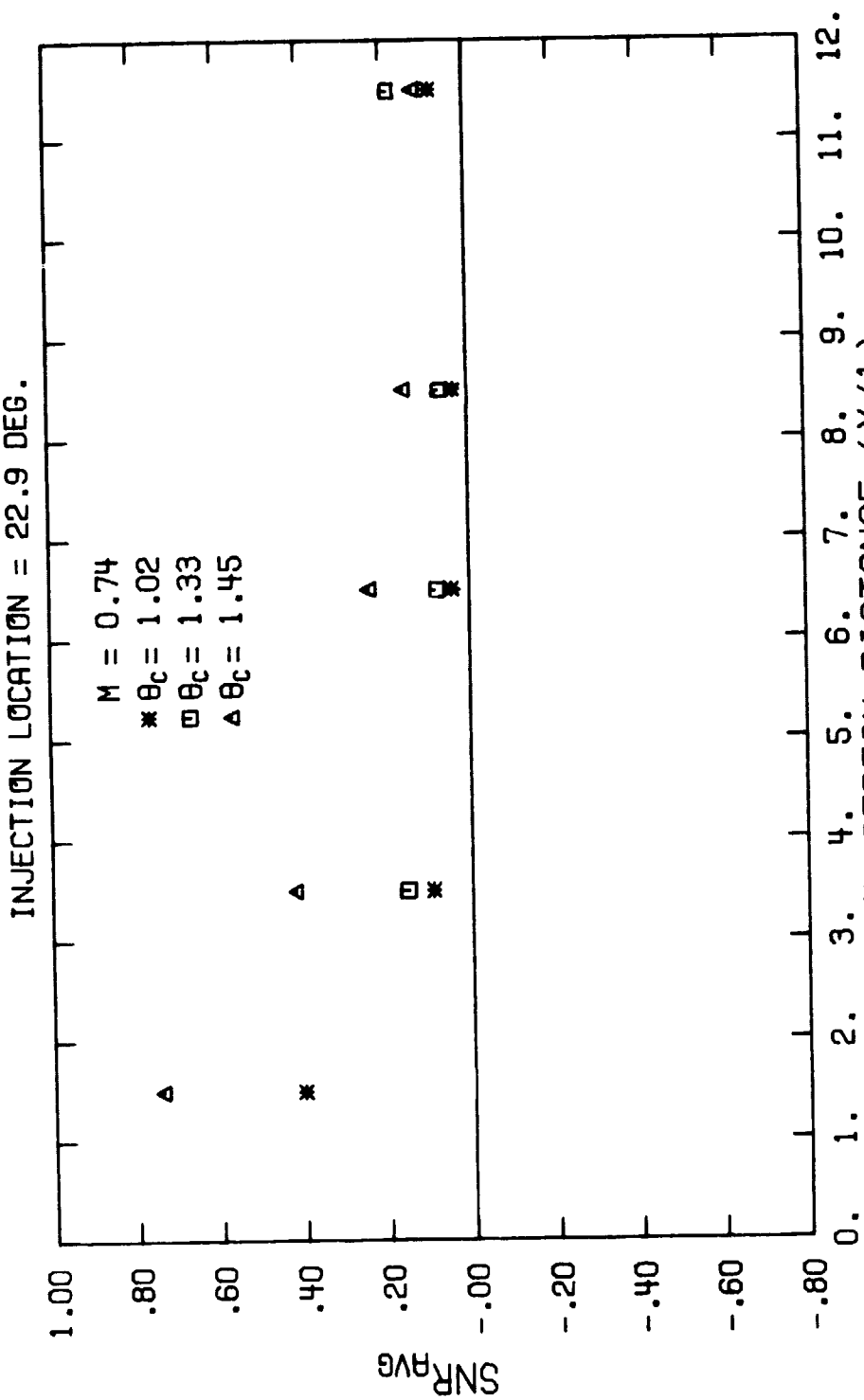

Figure 36. Variation in Spanwise-averaged Stanton Number Reduction with Downstream Distance (θ_i=22.9°, M=0.74)

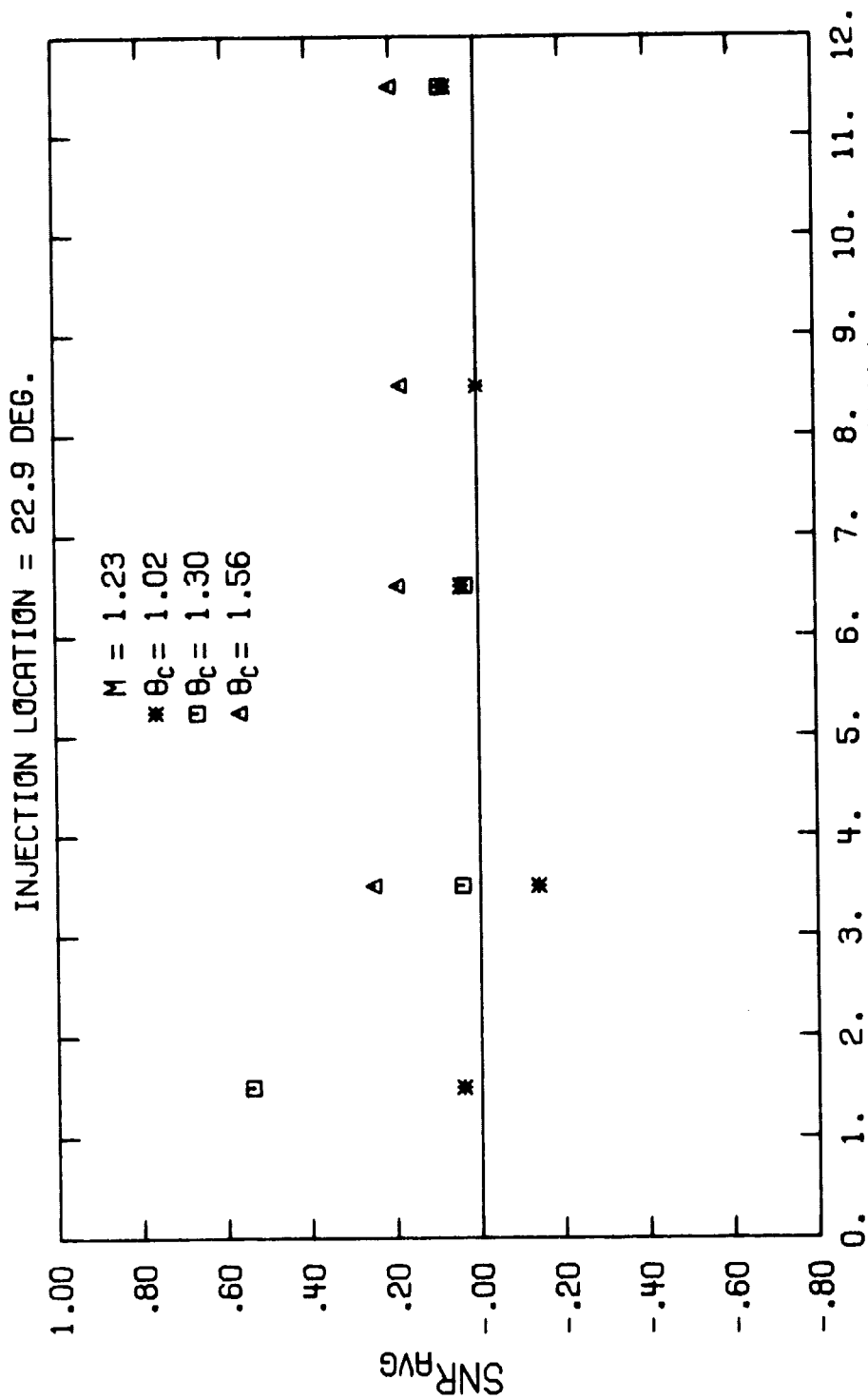

Figure 37. Variation in Spanwise-averaged Stanton Number Reduction with Downstream Distance (θ_i=22.9°, M=1.23)

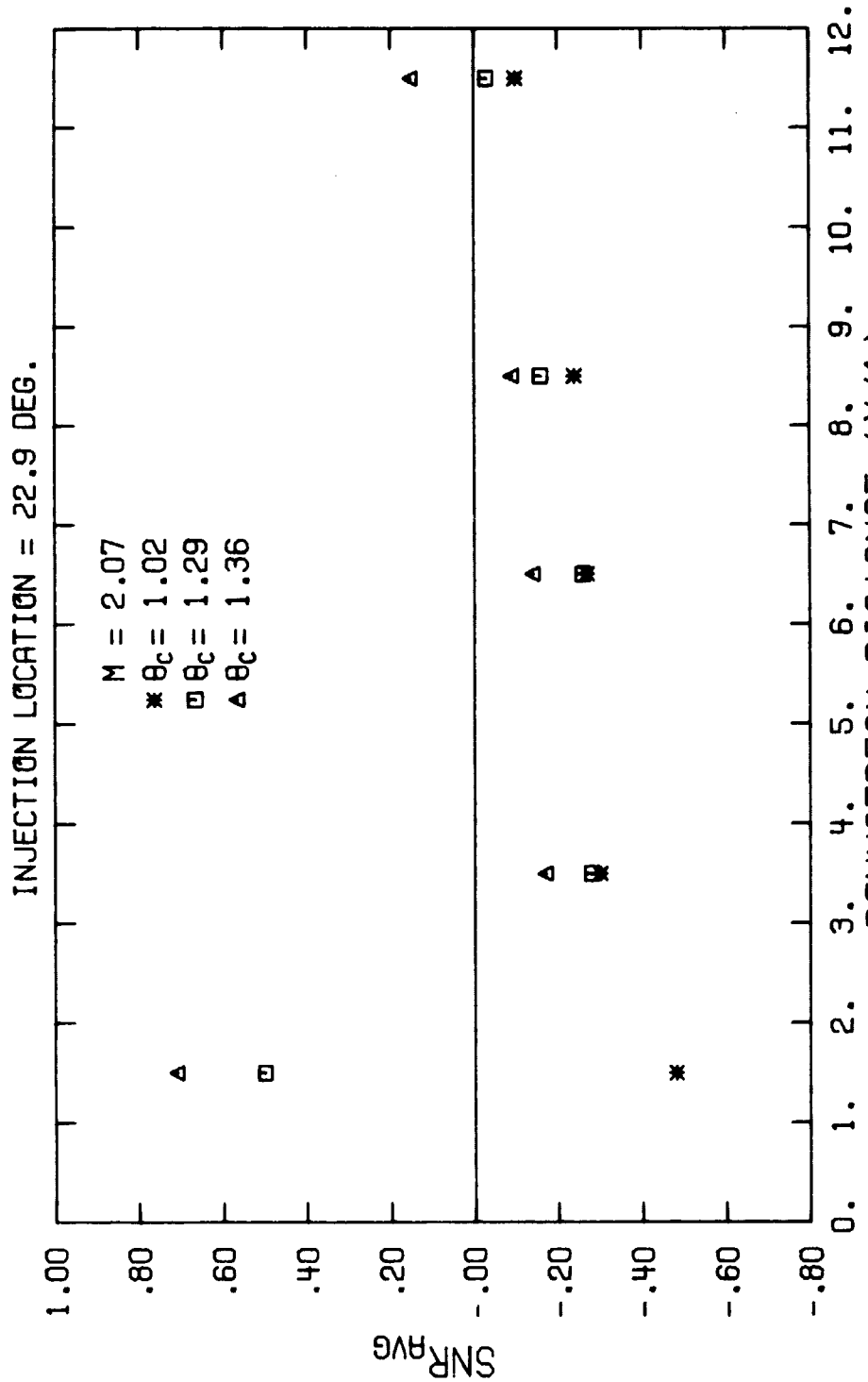

Figure 38. Variation in Spanwise-averaged Stanton Number Reduction with Downstream Distance (θ_1=22.9°, M=2.07)

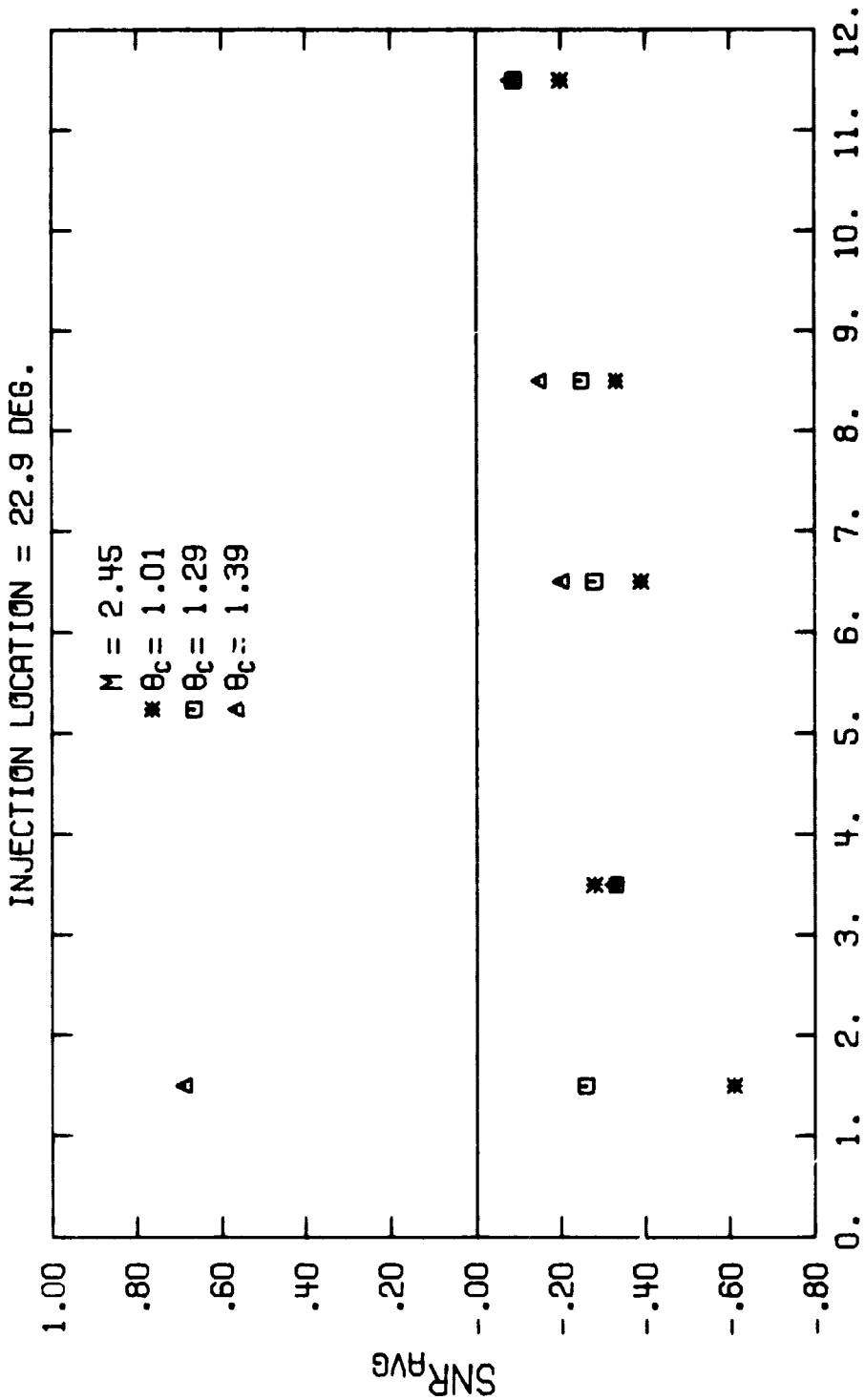

Figure 39. Variation in Spanwise-averaged Stanton Number Reduction with Downstream Distance (θ_i=22.9°, M=2.45)

increasingly negative. However, for any value of blowing ratio, the effect of increasing θ_c was to increase the level of SNR_{AVG}.

Figures 40, 41 and 42 show the results for SNR_{AVG} at the five values of blowing ratio tested for injection at θ_i = 40.8°. The legend of each figure defines the values of M and θ_c.

Figure 40, the results for M = 0.51, shows that increased values of θ_c bring about a general increase in the value of SNR_{AVG}. The largest increases are seen at x/d_o = 1.50 and x/d_o = 3.50. Though values of SNR_{AVG} decrease with distance downstream, the effect of increased θ_c remains as an increase in SNR_{AVG}.

Similar trends were found with values of blowing ratio M = 0.74, 0.95 and 1.14 (Figures 41 and 42). Film cooling with $\theta_c \simeq 1.0$ at each of the blowing ratios resulted in negative values of SNR_{AVG}, while the data for $\theta_c > 1.0$ showed significant increases in SNR_{AVG}.

In summary, the results for injection at θ_i = 40.8° follow the patterns extablished at θ_i = 5.0° and 22.9°. Film cooling with increased values of θ_c resulted in a general increase in the level of SNR_{AVG} over the levels seen with $\theta_c \simeq 1.0$. The largest increase in SNR_{AVG} with θ_c was observed at x/d_o = 1.50.

A comparison of the results for SNR_{AVG} for different injection locations (θ_i), shows that as the injection location is moved further from the cylinder stagnation line, the change in SNR_{AVG} with a change in θ_c also increased.

IV.C. Effect of Dimensionless Coolant Temperature on the Distribution of Stanton Number Reduction

The previous discussion described the effect of θ_c on the level of SNR. The data of Figures 17 through 32, showing local values of SNR, and Figures 33 through 42, showing SNR_{AVG}, demonstrate that an increase in θ_c resulted in an increase in the level of SNR.

Equations (4) and (5), Chapter I, also show that a variation of θ_c, while M and T_∞/T_w are held constant, results in a variation of the coolant-to-freestream velocity and momentum flux ratios, V_c/V_∞ and I. Consequently, it can be expected that θ_c (through V_c/V_∞ and I) may have an influence on the fluid dynamic behavior of the coolant. For model

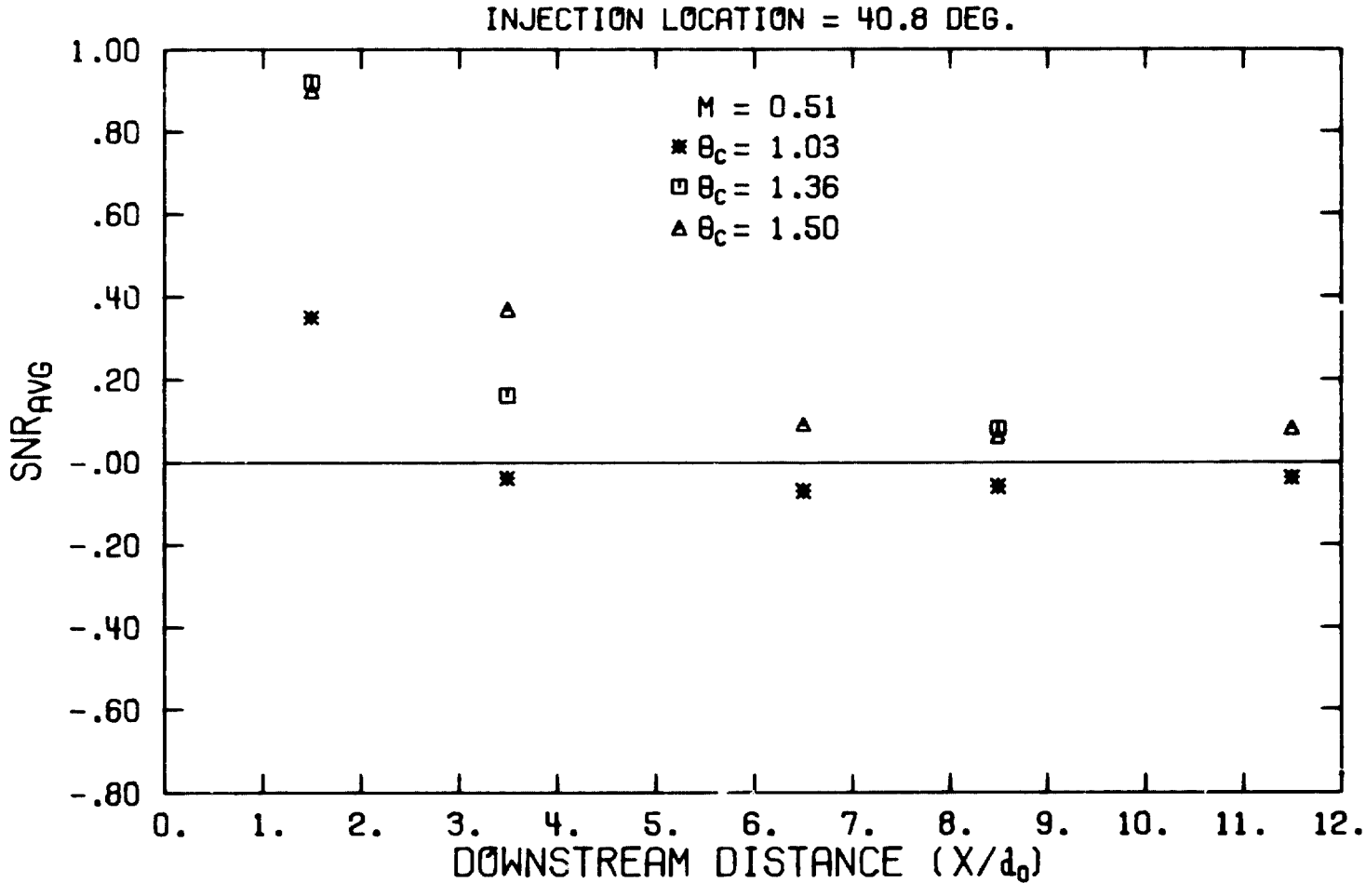

Figure 40. Variation in Spanwise-averaged Stanton Number Reduction with Downstream Distance (θ_i=40.8°, M=0.51)

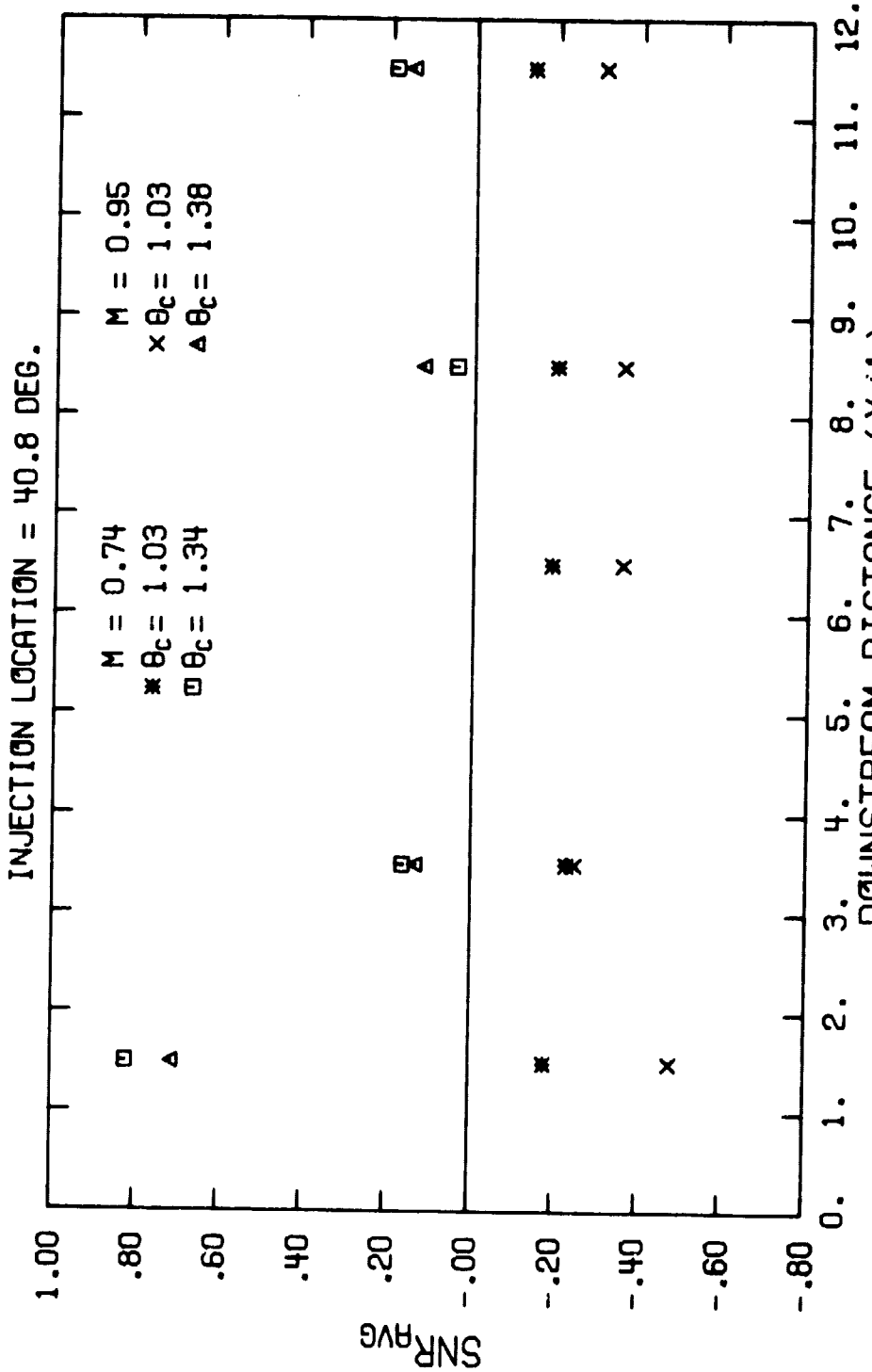

Figure 41. Variation in Spanwise-averaged Stanton Number Reduction with Downstream Distance (θ_i=40.8°, M=0.74 and 0.95)

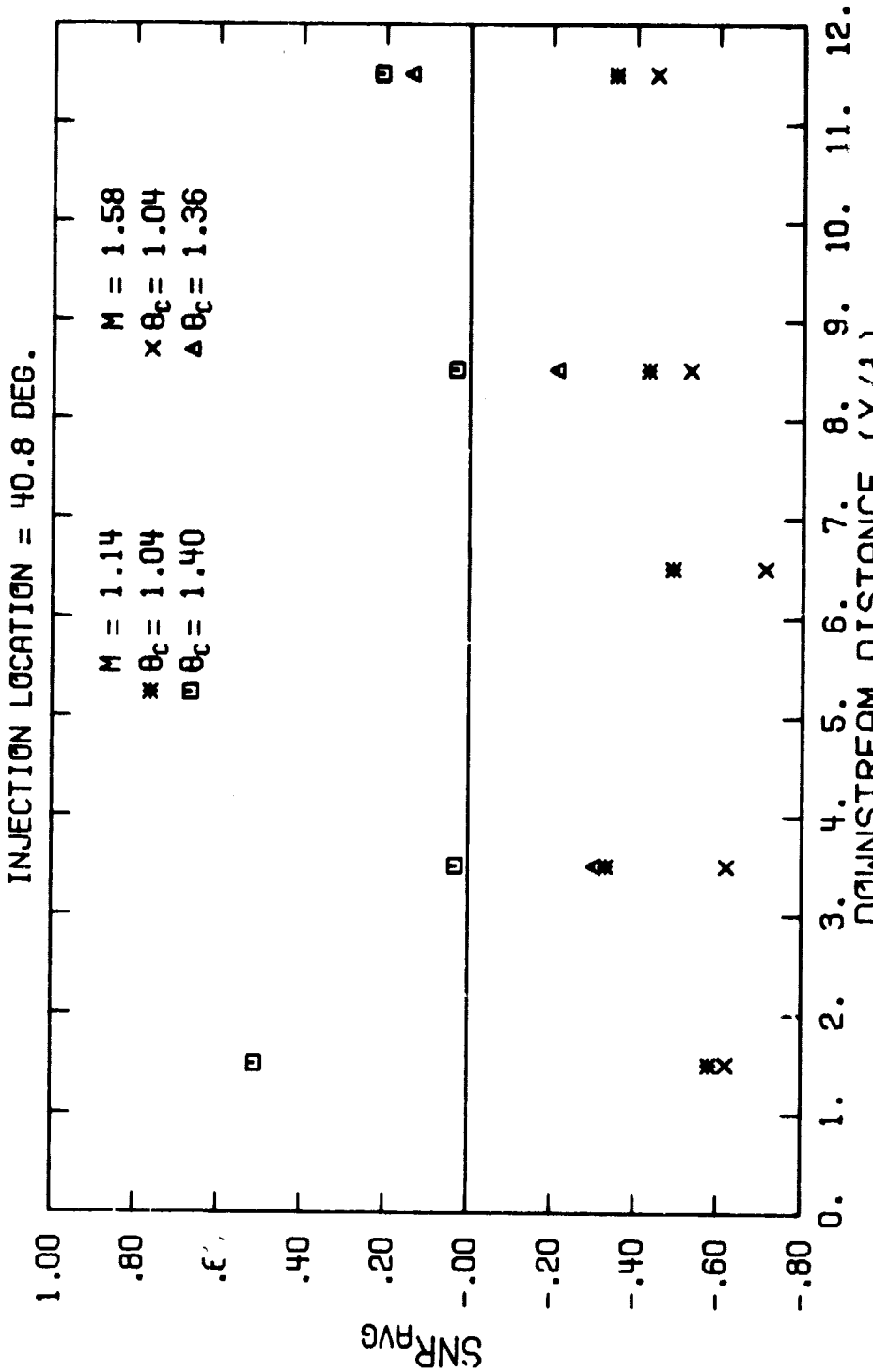

Figure 42. Variation in Spanwise-averaged Stanton Number Reduction with Downstream Distance (θ_j=40.8°, M=1.14 and 1.58)

experiments wherein $0.93 \leq T_\infty/T_w \leq 1.07$ [5], large changes in θ_c (e.g. 1.0 to 1.4) correspond to less than a ten percent change in V_c/V_∞ and I, and consequently, the effect on the flow field is probably insignificant. However, in the present study, where $T_\infty/T_w \sim 1.7$, an increase in θ_c from 1.0 to 1.3 corresponds to a 21% reduction in V_c/V_∞ and I. In this section, the results presented in Figures 17 through 32 (and those in Appendix E) are interpreted to demonstrate that changes in θ_c can result in a change in the fluid dynamic behavior of the coolant.

A parameter SNR_{MAX} is introduced to aid in the description of the surface heat transfer distribution. SNR_{MAX} is defined as the maximum value of SNR measured at a given streamwise location, x/d_o. The spanwise (z/S) location of the occurance of SNR_{MAX} is used to define the approximate location on the surface of the coolant jet. By reference to the local distributions of SNR vs z/S and x/d_o it is possible to determine the coordinates (z/S vs x/d_o) of SNR_{MAX} and thereby define the approximate trajectory of the coolant along the test surface. This technique was used to examine the influence of dimensionless coolant temperature (θ_c) on the trajectory of the coolant.

Of the selected cases presented in sections IV.B.1, the data for $\gamma_i = 40.8°$, M = 1.14 (Figures 30 through 32) most clearly demonstrates the influence of θ_c on the SNR distribution and the implied affect on coolant trajectory. Figure 30 shows that at $x/d_o = 1.50$, for $\theta_c = 1.04$, the maximum value of SNR, SNR_{MAX}, occurred at z/S = 0.67. With $\theta_c = 1.40$, the location of SNR_{MAX} is shifted to z/S = 0.33. At $x/d_o = 3.50$, a similar shift from z/S = 0.67 to 0.33 is indicated when θ_c was increased from 1.04 to 1.40. Figures 31 and 32 show a similar trend for the coolant trajectory (i.e. SNR_{MAX} coordinate) to shift toward z/S = 0 as θ_c was increased.[1]

To illustrate the influence of θ_c on the localized behavior of the coolant, the foregoing technique was used to construct plots of the coordinates (z/S vs x/d_o) of SNR_{MAX}.

---

[1] In instances where two adjacent measurement points indicated equal values for the maximum SNR (within the SNR data band, ± 0.05 units), the z/S location of SNR_{MAX} was taken as the midpoint between the two measurement points.

The results for θ_i = 5.0° are presented in Figure 43 showing, to scale, the coolant hole orientation, the z/S and x/d_o coordinates, and the directions of coolant and freestream flow. The curves represent the coolant jet trajectory (inferred from SNR_{MAX} coordinates) for each of the run conditions tested.

The results for M = 2.01 shown in Figure 43 indicate a small effect on coolant trajectory as θ_c was increased from 1.03 to 1.29. For M = constant, the colder coolant (θ_c = 1.29) was ejected with a lower velocity resulting in less movement in the spanwise direction when compared to the trajectory for θ_c = 1.03.

For increased values of the blowing ratio, the data of Appendix E for θ_i = 5.0° and M $\geq$ 2.99 show no apparent shift in the location of SNR_{MAX} as shown in Figure 43. The trajectory of the coolant for M $\geq$ 2.99 was unaffected by a change in θ_c, for the range of values of θ_c tested.

Figures 44a and 44b show the approximate coolant trajectories for θ_i = 22.9°.[1] From Figure 44a, it is seen that the coolant trajectory for M = 0.25, θ_c = 1.18, as inferred from the locations of SNR_{MAX}, remained nearer the z/S = 0.0 location than did the coolant trajectory for M = 0.25, θ_c = 1.03. There was little spanwise movement of the colder coolant jet.

The results for θ_i = 22.9°, M = 0.74, shown in Figure 44a, indicate that the coolant trajectory was relatively unaffected by increasing θ_c from θ_c = 1.02 to θ_c = 1.33, but there was an effect with θ_c = 1.45, with the colder coolant exhibiting less spanwise movement. Similar plots of coolant trajectory for M = 1.23, 2.07 and 2.45 are shown in Figures 44a and 44b. There is a small reduction in spanwise movement of the coolant when θ_c is increased from $\simeq$ 1.0 to $\simeq$ 1.30 and a much more pronounced reduction for $\theta_c \simeq$ 1.45 - 1.56.

The results for injection at θ_i = 40.8° shown in Figure 45 exhibit similar trends. For the five values of blowing ratio shown, it is seen that increasing θ_c at constant M causes the coolant trajectory to shift toward z/S = 0.0.

---

[1] Figure 44b shows trajectories for M = 1.23 and M = 2.45. For clarity, two plots were used to present the trajectories for film cooling at θ_i = 22.9°.

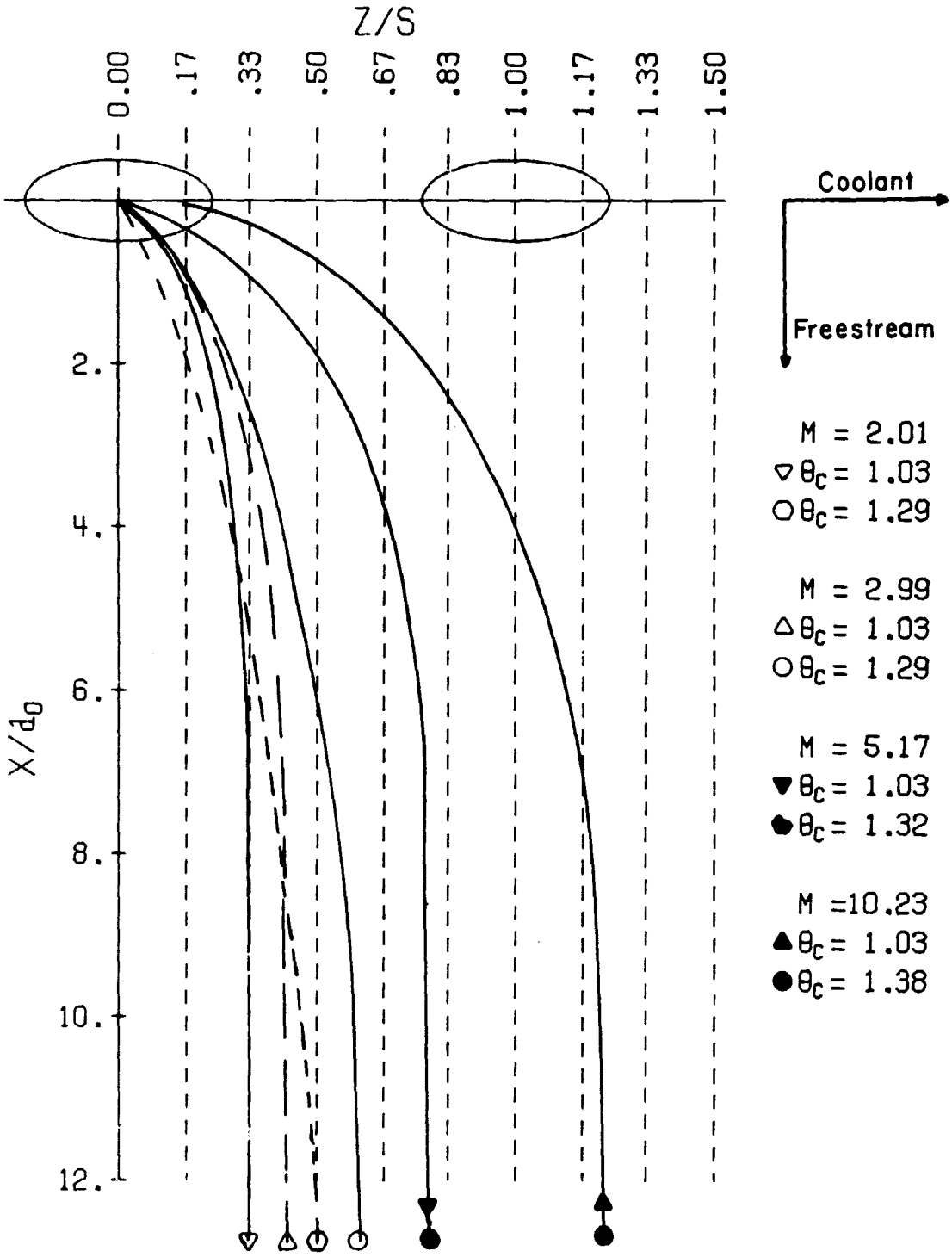

Figure 43. Coolant Jet Trajectory (α_j=5.0°)

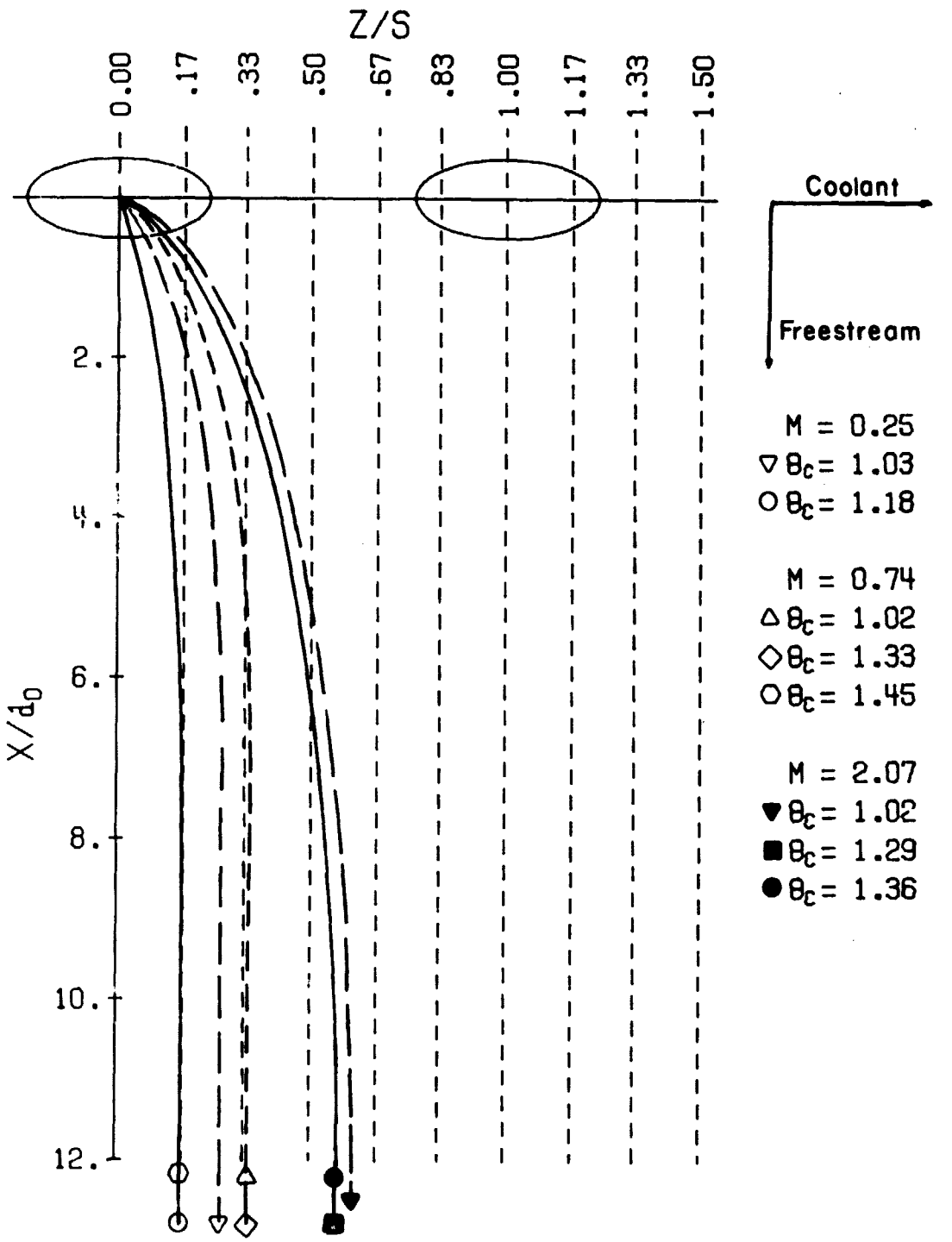

Figure 44a. Coolant Jet Trajectory (θ_j=22.9°, M=0.25, 0.74 and 2.07)

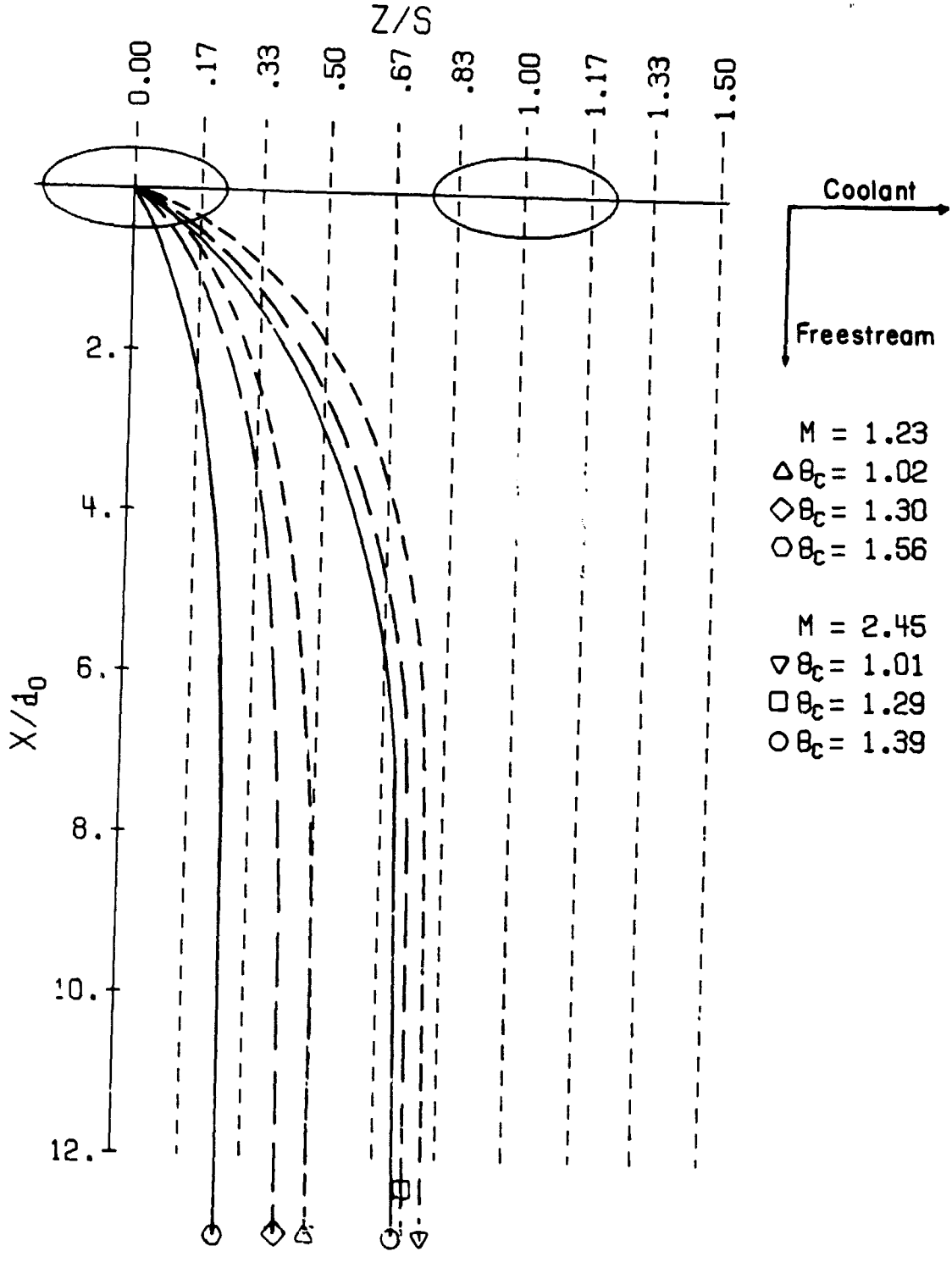

Figure 44b. Coolant Jet Trajectory (θ_j=22.9°, M=1.23 and 2.45)

It is concluded from these interpretations that a change in θ_c can produce a change in the fluid dynamic behavior of the coolant jet in addition to the influence of θ_c on the surface heat flux level.

IV.D. Effect of Dimensionless Coolant Temperature on Heat Transfer

The experiments of the present study were conducted to examine the effects of dimensionless coolant temperature, θ_c, on film cooling performance. The experiments were performed with film cooling from a single row of coolant holes, with the row located at three injection locations, θ_i = 5.0°, 22.9° and 40.8°, relative to stagnation.

The results presented in the previous sections have shown that increasing the value of θ_c with a constant blowing ratio can have two effects: (a) an increase in the Stanton Number Reduction (SNR), and (b) an alteration of the local SNR distribution (i.e. coolant trajectory). In some instances, the change in Stanton Number Reduction was relatively small (see Figures 17 through 19 for θ_i = 5.0°, M = 2.01) and the affect on coolant trajectory was insignificant (Figure 43). There were some cases where an increase in θ_c resulted in large differences in SNR and coolant position (see Figures 30 through 32, and Figure 45 for θ_i = 40.8°, M = 1.14). Because of this twofold influence of θ_c, it is difficult to quantify the effect of dimensionless coolant temperature on film cooling performance. The linear superposition model of Choe, Kays and Moffat [5] does suggest one approach to characterize the influence of θ_c on the heat transfer to the film cooled surface.

The linear superposition model for an isothermal surface, constant property flow [5] shows that the film cooled surface heat flux (St_{FC}) for an arbitrary coolant temperature (θ_c) is given by the linear relationship

$$St_{FC} = St_{FC1} + \frac{St_{FC2} - St_{FC1}}{\theta_{c2} - \theta_{c1}} (\theta_c - \theta_{c1}) \qquad (7)$$

where St_{FC1} and St_{FC2} correspond to the values of Stanton number with film cooling when using coolant dimensionless temperatures θ_{c1} and θ_{c2}, respectively. The Stanton number (St_{FC}) can be normalized with respect

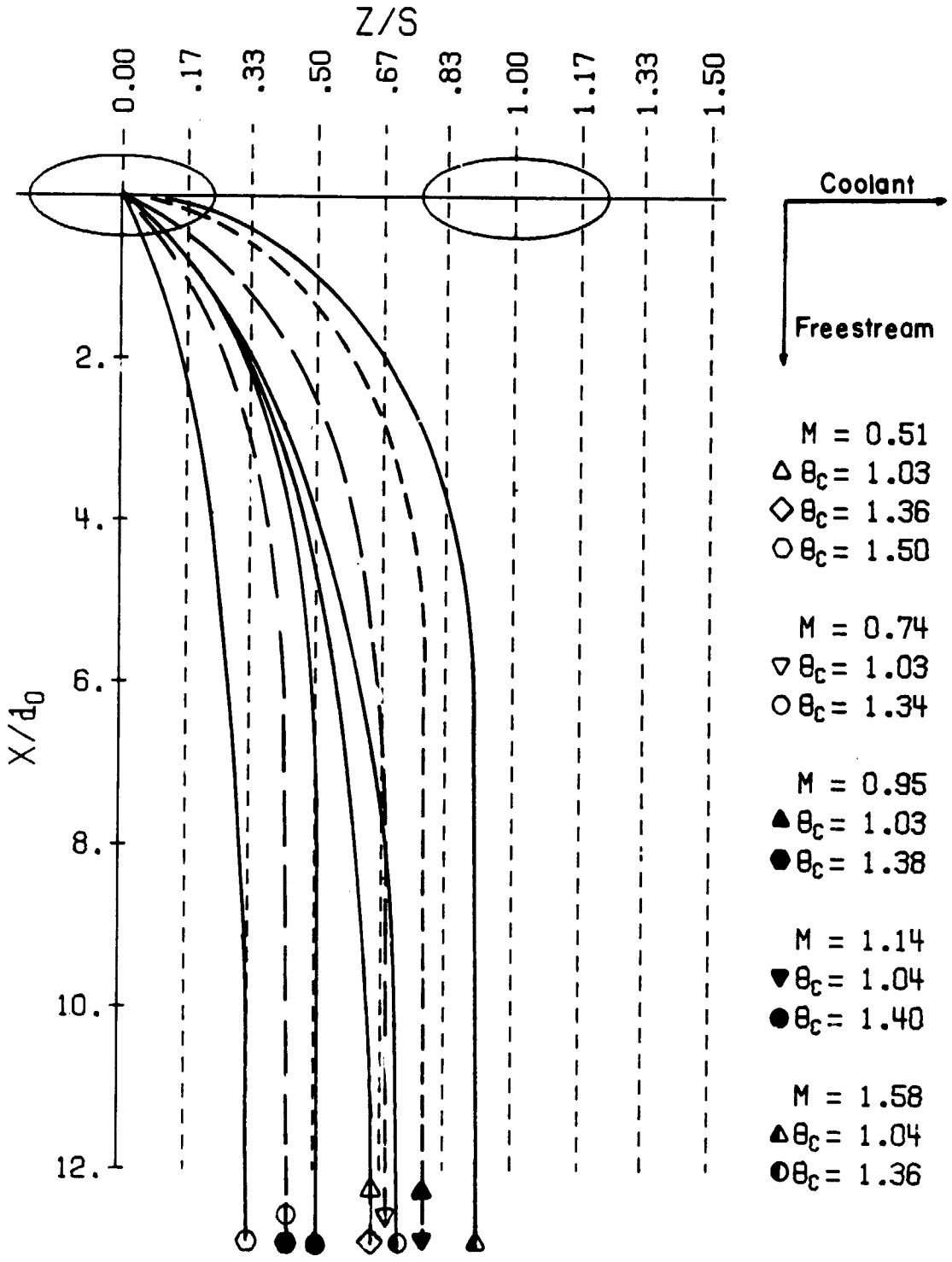

Figure 45. Coolant Jet Trajectory (θ_i=40.8°)

to the local Stanton number without film cooling (St_o) giving

$$\frac{St_{FC}}{St_o} = \frac{St_{FC1}}{St_o} + \left[\frac{St_{FC2}}{St_o} - \frac{St_{FC1}}{St_o}\right] \frac{\theta_c - \theta_{c1}}{\theta_{c2} - \theta_{c1}} \tag{8}$$

The Stanton number Ratio (St_{FC}/St_o) given by equation (8) is directly related to the Stanton Number Reduction (SNR) used to present the film cooling data of the present study. Noting that

$$\text{Stanton Number Reduction, SNR} \equiv 1 - \frac{St_{FC}}{St_o}$$

we can rewrite equation (8) as

$$STR = STR_1 + m\,(\theta_c - \theta_{c1}) \tag{9}$$

where

$$STR \equiv \frac{St_{FC}}{St_o} = 1 - SNR$$

$$m \equiv \frac{STR_2 - STR_1}{\theta_{c2} - \theta_{c1}} = \frac{SNR_1 - SNR_2}{\theta_{c2} - \theta_{c1}}$$

The experimental data from the present study (values of SNR for selected values of θ_c) were used to calculate the value of the slope, m. The empirical values for m, when used in conjunction with equation (9), provide a means for determining the influence of θ_c on film cooled surface heat transfer.

To determine the slope, m, from the experimental data of the present study, it was necessary to note that the coolant jet trajectory can be changed by an increase in θ_c. It was seen from the data that the region of the surface affected by the coolant jet was dependent on the value of θ_c (see Figures 43 through 45). For this reason, two different approaches were adopted to correlate the effect of θ_c on the surface heat transfer. First, since engineering application of film cooling data frequently

deals with spanwise-averaged analysis, the effect of θ_c on the surface heat transfer was based on the spanwise averaged data, SNR_{AVG}. Values of the slope based on SNR_{AVG} for a given M were calculated as

$$m_{AVG} = \frac{SNR_{AVG,1} - SNR_{AVG,2}}{\theta_{c2} - \theta_{c1}}$$

Second, because of the localized influence of the coolant, the effect of θ_c on the surface heat flux was based on the spanwise maximum data, SNR_{MAX}. Values of the slope based on SNR_{MAX} for a given M were calculated as

$$m_{MAX} = \frac{SNR_{MAX,1} - SNR_{MAX,2}}{\theta_{c2} - \theta_{c1}}$$

The value for m_{MAX} was determined using the spanwise maximum values $SNR_{MAX,1}$ at θ_{c1} and $SNR_{MAX,2}$ at θ_{c2}. It should be noted that the spanwise location (z/S) for $SNR_{MAX,1}$ and $SNR_{MAX,2}$ may be different due to the effect of θ_c on the coolant jet trajectory.

Results of the calculations for m_{AVG} using SNR_{AVG} at $\theta_i = 5.0°$ are shown in Figure 46 as a function of the downstream distance (x/d_o). The ordinate scale was chosen to permit comparison with results for other injection locations. Symbols defined in the legend denote values of the blowing ratio studied and the lines represent the data band defining the range of most of the data points.

From the data of Figure 46, it is seen that the values of m_{AVG} were generally negative due to the increase in SNR_{AVG} with an increase in θ_c. The data show that the absolute value of m_{AVG} decreased with downstream distance. Most of the data fell within the band, $-0.8 \leq m_{AVG} \leq -0.1$, independent of the blowing ratio.

The band of data shown in Figure 46 is approximately ± 0.2. This is not unreasonable when viewed in relation to an uncertainty in the change in STR_{AVG} ($\Delta STR_{AVG} = \pm 0.05$) ratioed to the change of θ_c ($\Delta\theta_c = 0.25$). A small data band is believed to be due to the similarity of the spanwise profiles for SNR data at $\theta_c \simeq 1.0$ and $\theta_c > 1.0$. The alteration in profile shape with an increase in θ_c at $\theta_i = 5.0°$ was small, and most

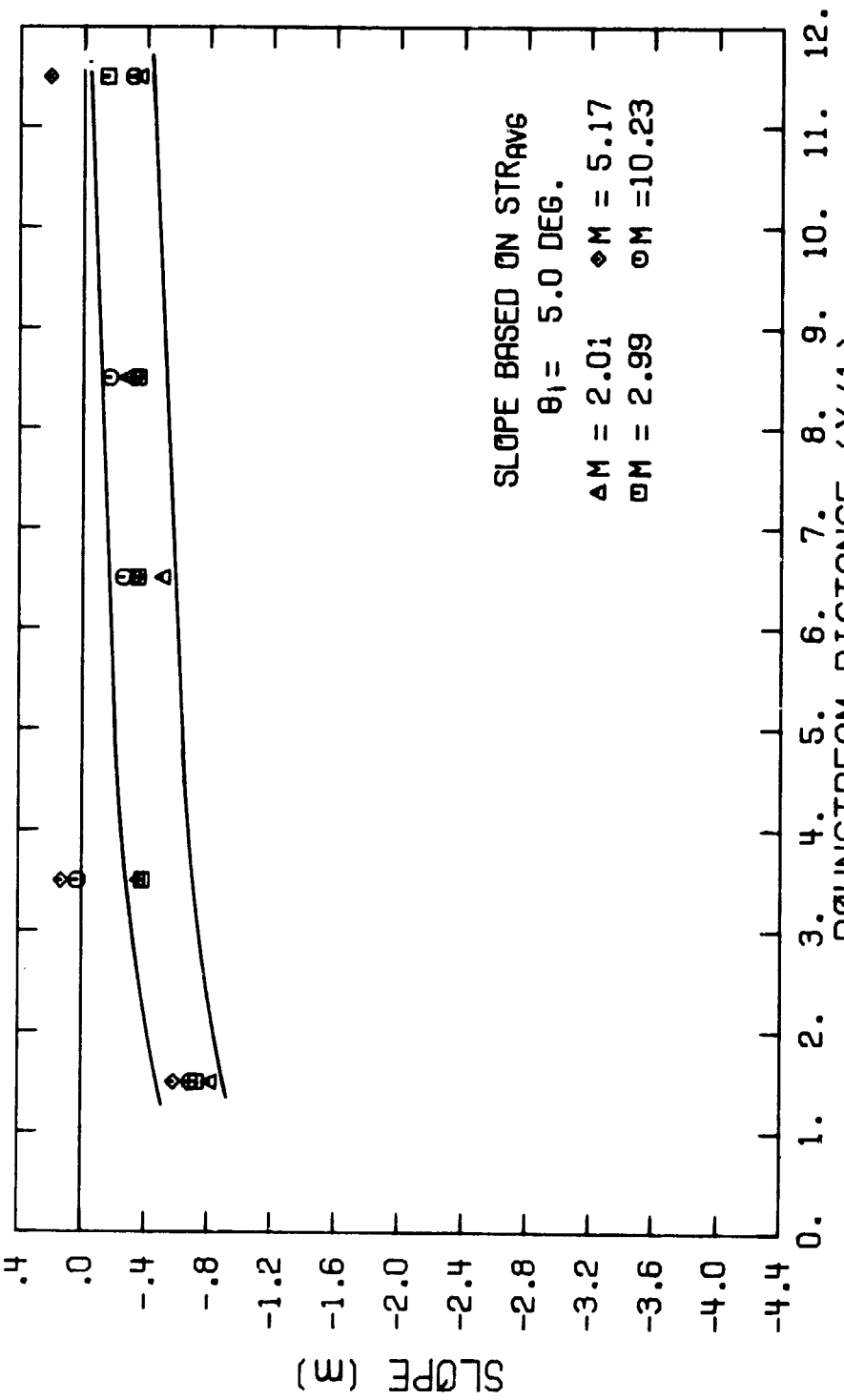

Figure 46. Variation in Slope (Based on STR_{AVG}) with Downstream Distance (θ_i=5.0°)

measuring points seemed to experience a change in coolant temperature with little or no change in coolant jet trajectory.

It should be remembered that use of the parameter m_{AVG}, based on SNR_{AVG}, involves averaging the values of SNR across the span from hole to hole, and tends to smear out localized effects. To examine the influence of θ_c on local film cooling performance, the value of m_{MAX}, based on SNR_{MAX}, was calculated.

Figure 47 shows the values calculated for m_{MAX} using the results for $\theta_i = 5.0°$. The solid lines drawn represent the data band for m_{AVG} (Figure 46). Figure 47 shows that the effect of θ_c was largest at $x/d_o = 1.50$, and decreased with x/d_o. The values of m_{MAX} were of the same magnitude as the values of m_{AVG} (represented by the band), but the data for m_{MAX} show more scatter. There was no significant trend with respect to blowing ratio.

A more detailed examination of the effect of θ_c was obtained from the data taken at the injection location $\theta_i = 22.9°$. For $M \geq 0.74$ data were available for two values of $\theta_c > 1.0$ in addition to the data for $\theta_c \simeq 1.0$ from [1] (see Appendix E, Table A9). This enabled the calculation of two values of m_{AVG}, m_{MAX} (designated as Regions 1 and 2) for each value of M. For example, with M = 0.74, data were available for $\theta_c = 1.02$, 1.33, and 1.45. Region 1 defines the values of m_{AVG}, m_{MAX} obtained for θ_c increasing from 1.02 to 1.33. Region 2 defines the values of m_{AVG}, m_{MAX} for θ_c increasing from 1.33 to 1.45.

The results for m_{AVG} from the data for injection at $\theta_i = 22.9°$ are shown in Figure 48. The open and filled symbols show the results for Regions 1 and 2, respectively. The solid lines were drawn to represent the bands of the data in Region 1 and Region 2, as labeled. The data in both regions show that the absolute value of m_{AVG} was largest at $x/d_o = 1.50$, and generally decreased with increasing x/d_o. Downstream from $x/d_o = 1.50$, Region 1 shows m_{AVG} in the range $-0.6 \leq m_{AVG} \leq 0.0$, similar to that for injection at $\theta_i = 5.0°$, while Region 2, shows the range of m_{AVG} $-1.6 \leq m_{AVG} \leq -0.6$. In both regions the results show no significant trend with respect to blowing ratio.

Figure 49 shows the results for m_{MAX} for injection at $\theta_i = 22.9°$. The data bands for Region 1 and Region 2 from Figure 48 are reproduced

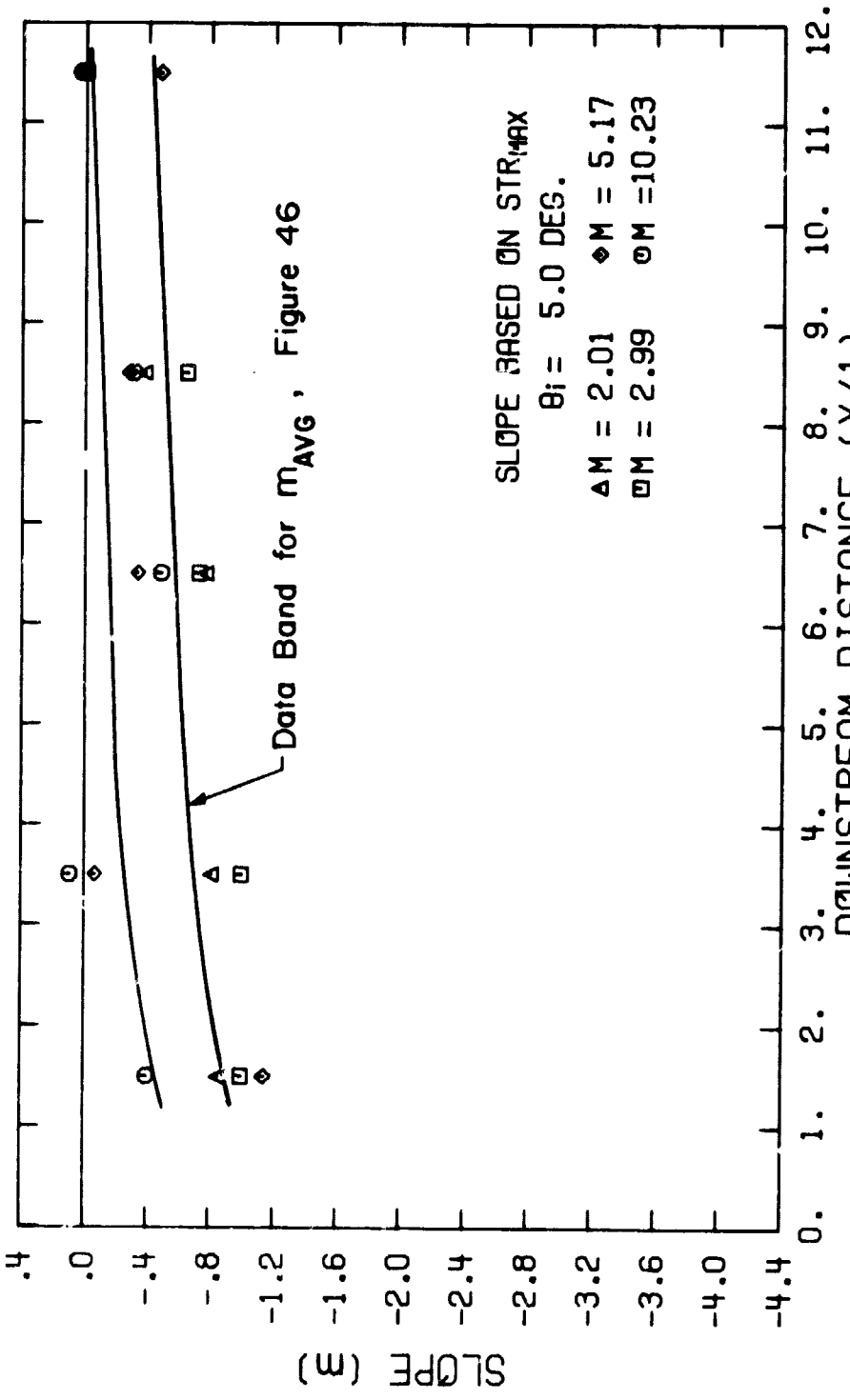

Figure 47. Variation in Slope (Based on STR_{MAX}) with Downstream Distance (θ_i=5.0°)

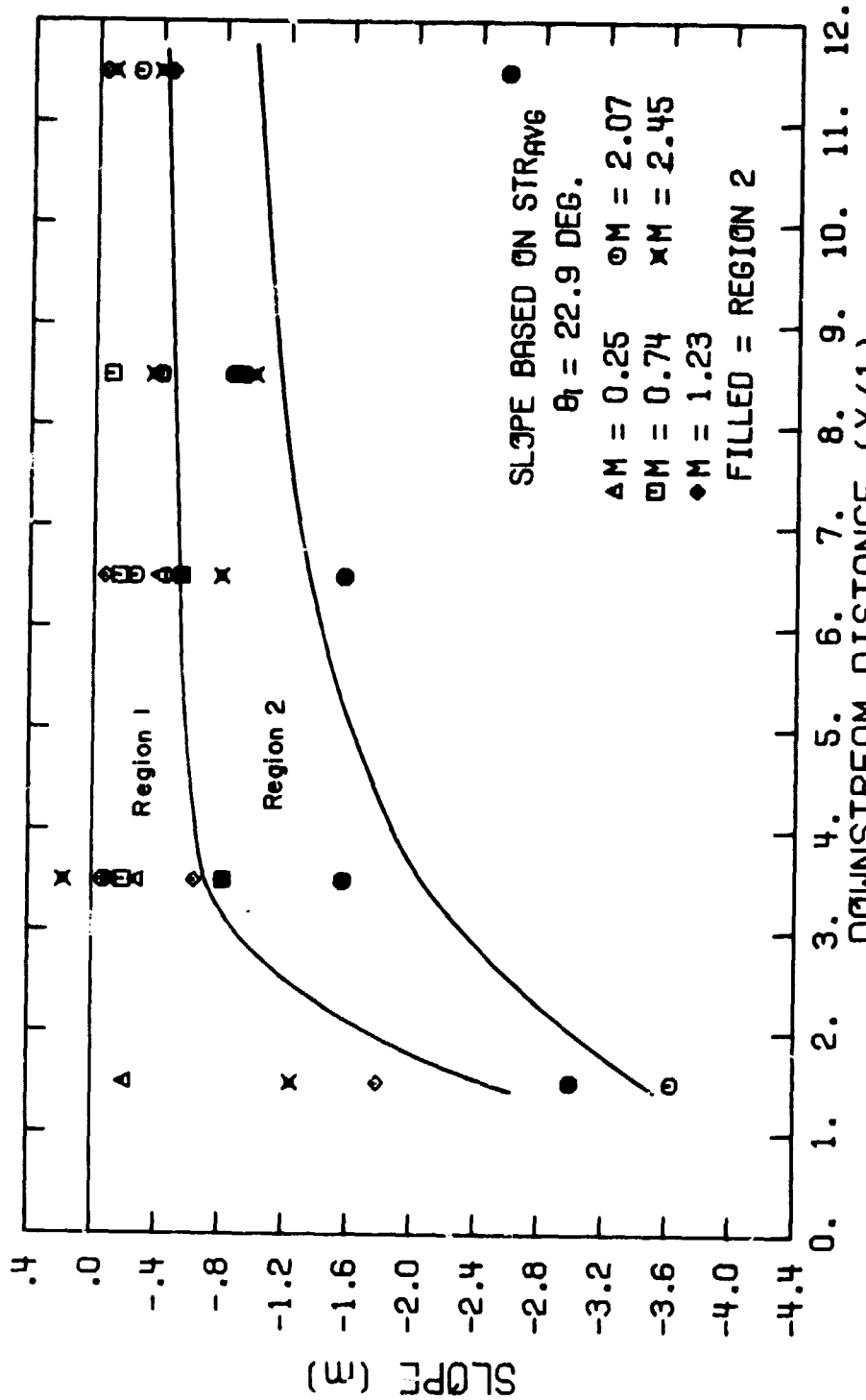

Figure 48. Variation in Slope (Based on STR_{AVG}) with Downstream Distance (θ_i=22.9°)

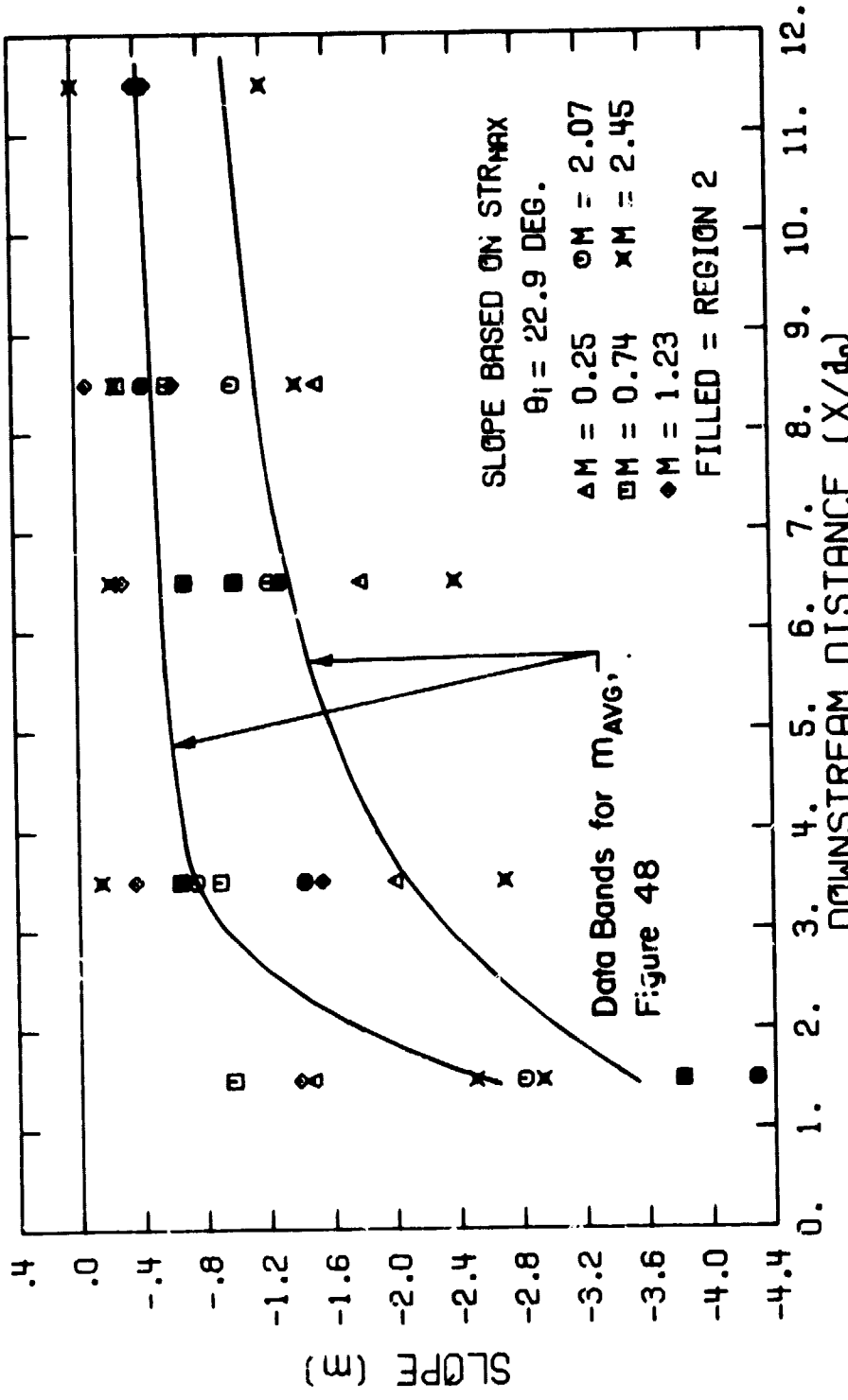

Figure 49. Variation in Slope (Based on STR_{MAX}) with Downstream Distance (θ_j=22.9°)

on Figure 49. The magnitudes of the slope based on SNR_{AVG} and SNR_{MAX} are comparable, but there is more scatter and less separation of the regions when SNR_{MAX} is used.

The data for m_{AVG} with injection at $\theta_i = 40.8°$ are shown in Figure 50. The solid lines represent the band of the data. In the range $1.50 \leq x/d_o \leq 8.50$, the values of m_{AVG} were comparable to those found in Region 2, for $\theta_i = 22.9°$. The large (unrealistic) values of m_{AVG} at $x/d_o = 11.50$ are attributed to the existence of negative values of SNR_{AVG} for the data with $\theta_c \simeq 1.0$.

The values for m_{MAX} for injection at $\theta_i = 40.8°$ are shown in Figure 51, along with the data band from Figure 50. As before, the data for m_{MAX} are more scattered than for m_{AVG}. A comparison of the values of m_{AVG} for the three injection locations shows that the influence of θ_c was greatest for $\theta_i = 40.8°$.

In summary, the effect of dimensionless coolant temperature (θ_c) on the surface heat transfer is illustrated by the results obtained for m_{AVG} and m_{MAX}. As expected, an increase in θ_c generally gives rise to a decrease in STR ($m<0$). The magnitude of the decrease in STR is dependent on the downstream location (x/d_o) and the injection location (θ_i). The absolute value of m_{AVG} increased as θ_i increased and x/d_o decreased. The results for injection at $\theta_i = 22.9°$ (Region 1 vs Region 2) indicate that the influence of θ_c is not linear; that is, the value of m depends on the range of θ_c. While the values of m_{AVG} and m_{MAX} did vary some with respect to M, it was concluded that the blowing ratio had little influence on the slope when considering the data bands that resulted.

C-2

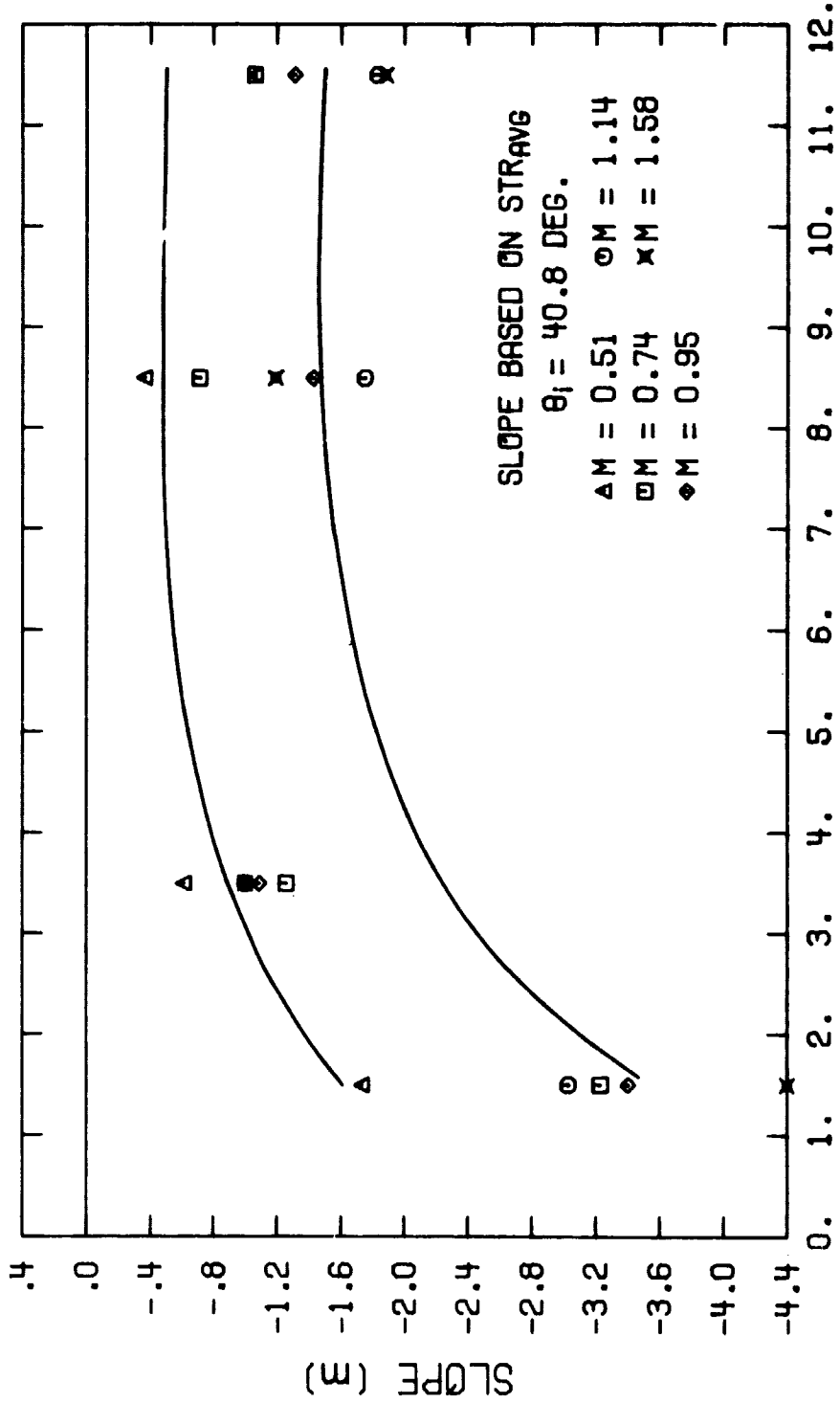

Figure 50. Variation in Slope (Based on STR_{AVG}) with Downstream Distance (θ_i=40.8°)

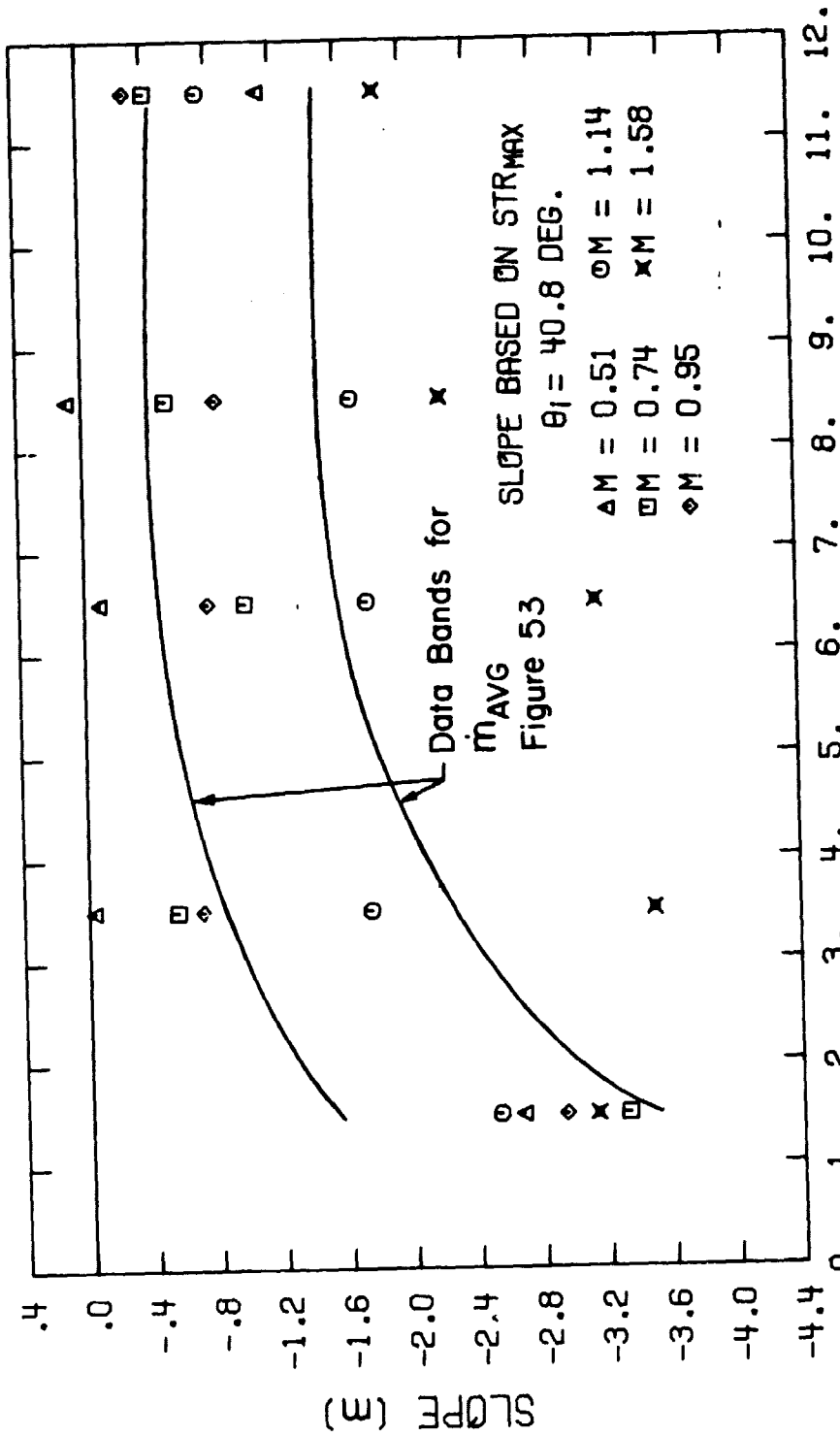

Figure 51. Variation in Slope (Based on STR_{MAX}) with Downstream Distance (θ_i=40.8°)

V. CONCLUSIONS

This investigation was conducted using the stagnation region of a cylinder in cross-flow to investigate the film cooling performance typical of a turbine vane leading edge. Experiments were conducted with film coolant injection from a single row of coolant holes angled in the spanwise direction with $\beta = 25°$. A freestream-to-wall temperature ratio of $T_\infty/T_w = 1.7$ and a Reynolds number of $Re_D = 9 \times 10^4$ were maintained throughout the investigation to simulate the gas turbine environment.

The test cylinder was instrumented with miniature heat flux gages and thermocouples to determine the Stanton Number Reduction with film cooling, $SNR = 1 - (St_{FC}/St_o)$. The data are presented in terms of SNR as a function of the distance downstream from injection (x/d_o) and the location between adjacent coolant holes (z/S). The local values of SNR were integrated to determine the spanwise-averaged Stanton Number Reduction, SNR_{AVG}, as well.

The objective of the present study was to examine the influence of dimensionless coolant temperature, θ_c, on film cooling performance for single row injection. Data were taken with the row of coolant holes located at three injection locations, $\theta_i = 5.0°$, 22.9° and 40.8°, using a hole-to-hole spacing of $S/d_o = 5$. The results for $1.18 \leq \theta_c \leq 1.56$ were compared with those from the previous study [1] where similar experiments were conducted with $\theta_c \simeq 1.0$. From analysis of the data, the following observations and conclusions were drawn concerning the effects of dimensionless coolant temperature on film cooling in the stagnation region.

1) The data revealed that the effect of increasing the dimensionless coolant temperature, θ_c, was to increase the value of SNR in the spanwise region of the surface affected by the coolant. Typically, an increase in the local value of SNR of 0.25 to 0.50 units was observed near the row of holes as θ_c was increased from ~1.0 to ~1.3.

2) The spanwise averaged data demonstrated a similar increase in SNR_{AVG} as θ_c increased, with a rapid decay of the effect with downstream distance (x/d_o).

3) An analysis of the heat transfer distribution (SNR vs z/S) was utilized to identify the apparent trajectory of the coolant jet along the surface. The results showed that an increase in θ_c could yield significant changes in coolant jet trajectory depending on the injection location, the magnitude of θ_c and the blowing ratio.

4) The data for SNR_{AVG} and SNR_{MAX} were used in conjunction with the linear superposition model [5] to determine the change in surface heat transfer with respect to a change in θ_c. The calculated results for the slope, m_{AVG} (m_{MAX}), showed that the influence of θ_c on the heat transfer increased as the injection location (θ_i) was varied from 5° to 40.8°.

BIBLIOGRAPHY

1. Luckey, D.W., and L'Ecuyer, M.R., "Stagnation Region Gas Film Cooling - Spanwise Angled Injection from Multiple Rows of Holes," NASA CR-165333, April 1981.

2. Goldstein, R.J., "Film Cooling," Advances in Heat Transfer, New York, Academic Press, 1971, Vol. 7, pp. 321-379.

3. Luckey, D.W., and L'Ecuyer, M.R., "Stagnation Region Gas Film Cooling - Spanwise Angled Coolant Injection," Thermal Sicences and Propulsion Center, Purdue University, Technical Report No. TSPC-TR-76-2, December 1976.

4. Winstanley, D.K., and L'Ecuyer, M.R., "Stagnation Region Gas Film Cooling - Experiments on the Effects of Density Ratio with Injection through Laterally Inclined Holes and on the Effects of Geometry with Injection through Streamwise Inclined Holes," Thermal Sciences and Propulsion Center, Purdue University, Technical Report No. TSPC-TR-80-02, May 1980.

5. Choe, H., Kays, W.M., and Moffat, R.J., "Turbulent Boundary Layer on a Full-Coverage Film Cooled Surface - An Experimental Heat Transfer Study with Normal Injection," NASA CR-2642, January 1976.

6. Ito, S., "Film Cooling and Aerodynamic Loss in a Gas Turbine Cascade," Ph.D. thesis, University of Minnesota, 1976.

7. Poferl, D., Svehla, R., and Lewandowski, K., "Thermodynamic and Transport Properties of Air and the Combustion Products of Natural Gas and of ASTM-A-1 Fuel with Air," NASA TN D-5452, October 1969.

8. Bonnice, M.A., "Stagnation Region Gas Film Cooling-Effects of Dimensionless Coolant Temperature," MSME Thesis, Purdue University, May 1982.

9. Holman, J.P., Heat Transfer, Fourth Edition, New York, McGraw-Hill Book Company, 1976.

10. Kline, S.J., and McClintock, F.A., "Describing Uncertainties in Single-Sample Experiments," Mechanical Engineering, Vol. 75, 1953, pp. 3-8.

11. Achenbach, E., "The Effect of Surface Roughness on the Heat Transfer from a Circular Cylinder to the Cross Flow of Air," International Journal of Heat and Mass Transfer, Vol. 20, 1977, pp. 359-369.

Appendix A

COOLANT MASS FLOW DISTRIBUTION

Film coolant air was supplied to the five primary coolant holes in the instrumented region of the test cylinder, via the primary plenum, the nitrogen heat exchanger, and the five coolant delivery-supply lines (Figure 8). The distribution of coolant flowrate among the five lines was calculated from a model derived from the momentum equation, using measured values of the primary plenum pressure, temperature, and flowrate, and the measured temperature of the coolant ($T_{c,in}$) as it entered each tube in the drop-in segment (see Figures 11, 12, and A1).

Variations in coolant flowrate from line-to-line are coupled with variations in temperature change from line-to-line. Examination of the momentum equation for a given coolant delivery-supply line (i) shows the effect of temperature change on flowrate.

The momentum equation for flow through line (i) is

$$-F_{si} + (A_p P_p - A_c P_c) = \dot{m}_i (V_{c,i} - V_{p,i}) \qquad \text{(A1)}$$

where

F_s = friction surface force on walls of tubing
A = cross-sectional area
P = static pressure
$\dot{m}$ = mass flowrate
V = velocity
$( )_p$ = primary plenum condition at entrance to line
$( )_c$ = coolant condition at exit of coolant hole.

Assuming

$$V = \frac{\dot{m}}{\rho A}$$

then equation (A1) becomes

$$-F_{si} + (A_{pi}\,P_{pi} - A_{ci}\,P_{pi}) = \dot{m}_i^2 \left(\frac{1}{\rho_{ci}\,A_{ci}} - \frac{1}{\rho_{pi}\,A_{pi}}\right)$$

Rearranging gives an expression for mass flowrate:

$$\dot{m}_i = \left\{\frac{(A_{pi}\,P_{pi} - A_{ci}\,P_{ci}) - F_{si}}{\left[\left(\frac{A_{pi}}{A_{ci}}\,\rho_{pi} - \rho_{ci}\right)/\rho_{pi}\,\rho_{ci}\,A_{pi}\right]}\right\}^{1/2} \qquad \text{(A2)}$$

The ratio of the flowrate in a second line (j) to that in line (i) is

$$\frac{\dot{m}_j}{\dot{m}_i} = \left\{\frac{\left[(A_{pj}P_{pj} - A_{cj}P_{cj}) - F_{sj}\right]\left(\frac{A_{pi}}{A_{ci}}\,\rho_{pi}-\rho_{ci}\right)(\rho_{pj}\rho_{cj}A_{pj})}{\left[(A_{pi}P_{pi} - A_{ci}P_{ci}) - F_{si}\right]\left(\frac{A_{pj}}{A_{cj}}\,\rho_{pj}-\rho_{cj}\right)(\rho_{pi}\rho_{ci}A_{pi})}\right\}^{1/2} \qquad \text{(A3)}$$

The above equation shows that the coolant density (or temperature) achieved at the coolant hole exit, ρ_{ci}, has an effect on the mass flow rate, $\dot{m}_i$. Temperature differences between line (i) and line (j) are then coupled with flow rate differences between line (i) and line (j).

The above equation can be reduced further by noting that:

(1) all coolant lines have the same geometry, $A_{pi} = A_{pj}$ and $A_{ci} = A_{cj}$,

(2) all coolant lines have the same inlet condition, $P_{pi} = P_{pj}$, $\rho_{pi} = \rho_{pj} = \rho_p$,

(3) all coolant holes exhaust to a common injection location on the cylinder, $P_{ci} = P_{cj}$,

(4) an order of magnitude calculation for the friction contribution, based on $F_s = 1/2\ \rho V^2 A C_f$, shows that the value of F_s is at least an order of magnitude lower than the value of $(A_pP_p - A_cP_c)$, and can be neglected.

Thus, equation (A3) reduces to

$$\frac{\dot{m}_j}{\dot{m}_i} = \left[\frac{\left(\frac{A_p}{A_c} \rho_p - \rho_{ci} \right) \rho_{cj}}{\left(\frac{A_p}{A_c} \rho_p - \rho_{cj} \right) \rho_{ci}} \right]^{1/2} \tag{A4}$$

Assuming ideal gas behavior, the density is given as

$$\rho_c = \frac{P_c}{RT_c}$$

By defining the parameter α as

$$\frac{A_p}{A_c} \rho_p = \frac{A_p}{A_c} \frac{P_p}{T_p} \frac{1}{R} \equiv \frac{\alpha}{R} \tag{A5}$$

then equation (A4) for the ratio of mass flow rates becomes

$$\frac{\dot{m}_j}{\dot{m}_i} = \left[\frac{\left(\alpha - \frac{P_c}{T_{ci}} \right)}{\left(\alpha - \frac{P_c}{T_{cj}} \right)} \frac{P_c}{T_{cj}} \frac{T_{ci}}{P_c} \right]^{1/2}$$

which is simplified to

$$\frac{\dot{m}_j}{\dot{m}_i} = \left[\frac{(\alpha T_{ci} - P_c)}{(\alpha T_{cj} - P_c)} \right]^{1/2} \tag{A6}$$

The ratio of the total flowrate supplied to the primary plenum to the flowrate in tube (i) is

$$\frac{\dot{m}_{TOTAL}}{\dot{m}_i} = \sum_{j=1}^{5} \frac{\dot{m}_j}{\dot{m}_i}$$

Therefore, the fraction of the total flowrate delivered through line (i) is given by

$$\frac{\dot{m}_i}{\dot{m}_{TOTAL}} = \frac{1}{\sum_{j=1}^{5} \frac{\dot{m}_j}{\dot{m}_i}} \qquad \text{(A7)}$$

The model developed above was used to calculate the distribution of the mass flow rate for the five primary coolant delivery-supply lines using the following procedure.

1. Measured values of primary plenum pressure and temperature were used to calculate α.
2. Measured values of the coolant temperature entering the tubes in the drop-in segment ($T_{c,in}$) (see Figures 11, 12 and A1) were used to calculate T_{ci} using the calibration of Appendix B for the coolant temperature rise in the hole.
3. An iterative calculation was required. An initial guess for $\dot{m}_i$ was used to calculate T_{ci} from the calibration of Appendix B. The value of m_i was then calculated from the momentum equation model herein. By iterating until convergence of $\dot{m}_i$ and T_{ci}, the distribution of coolant flowrate and temperature was obtained.

Appendix B

TEMPERATURE RISE IN FILM COOLANT HOLE

The present study was conducted to determine the effects of dimensionless coolant temperature (θ_c) on film cooling performance. The dimensionless coolant temperature at the exit of the coolant hole was calculated from the measured values of coolant flow rate, coolant hole wall temperature, and coolant temperature at the inlet of each tube in the drop-in segment. This Appendix details the development of the correlation between these measured parameters and the coolant temperature at the exit from the hole.

B.1. Model for Coolant Temperature Rise

An illustration of a typical film coolant hole is shown in Figure A1. The hole was drilled into a drop-in segment at an angle of $\beta = 25°$. A copper tube was inserted into the inlet of the hole (a) to provide for the connection of the film coolant supply line, and (b) to support a thermocouple to measure the entering coolant temperature (T_{bi}) (see Figures 7, 11 and 12). The screen at the tube inlet was used to promote a uniform velocity profile. Two thermocouples (not shown, see Figures 7 and 12) were installed to measure the coolant hole wall temperature.

An energy balance for the differential control volume shown in Figure A1 yields

$$\dot{m}\, c_p \frac{\partial T_b}{\partial x} = h_x P(T_w - T_b) \qquad (A8)$$

where

$\dot{m}$ = coolant mass flow rate

c_p = specific heat at constant pressure

T_b = coolant bulk temperature

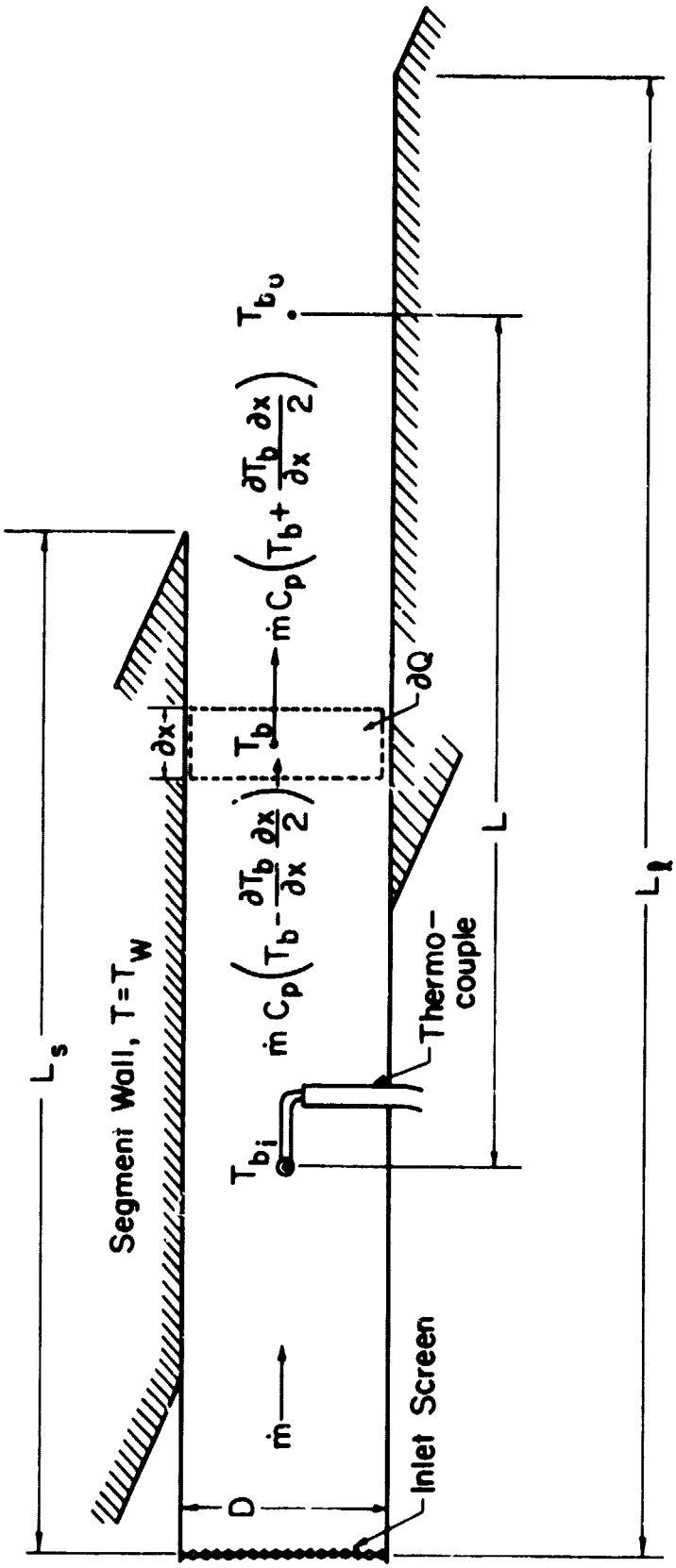

Figure A1. Schematic of Film Coolant Hole

$h_x = q''/(T_w - T_b)$

P = perimeter of hole, πD[1]

Assuming a constant coolant hole wall temperature, equation (A8) can be rearranged to

$$\frac{d(T_b - T_w)}{(T_b - T_w)} = -\frac{h_x \pi D}{\dot{m} c_p} dx \qquad \text{(A9)}$$

Equation (A9) can be integrated with the limits

$x = o \quad T_b = T_{bi}$ (inlet temperature measured)

$x = L \quad T_b = T_{bo}$ (coolant temperature at hole exit)

Assuming D and c_p are constant gives

$$\ln\left[\frac{(T_{bo} - T_w)}{(T_{bi} - T_w)}\right] = -\frac{\pi D}{\dot{m} c_p} \int_o^L h_x \, dx \qquad \text{(A10)}$$

Equation (A10) is put in conventional form by defining an average heat transfer coefficient for the hole

$$h_m = \frac{1}{L} \int_o^L h_x \, dx$$

then

$$\ln\left[\frac{(T_{bo} - T_w)}{(T_{bi} - T_w)}\right] = -\frac{\pi D L h_m}{\dot{m} c_p} \qquad \text{(A11)}$$

Equation (A11) is transformed to dimensionless form by defining

$$\theta_m = \frac{(T_{bo} - T_w)}{(T_{bi} - T_w)}$$

$$Re = \frac{4\dot{m}}{\pi \mu D} \qquad Pr = \frac{\mu c_p}{k} \qquad Nu_m = \frac{h_m D}{k}$$

---

[1] $D = d_o$ = coolant hole diamter

Then

$$\ln \theta_m = -\frac{\pi D h_m L}{\dot{m} c_p} = -\frac{4 Nu_m L}{RePrD}$$

and

$$\theta_m = e^{-4 Nu_m x^+} \tag{A12}$$

where $x^+ = \frac{L/D}{RePr}$

Equation (A12) can be rewritten to enable the calculation of the coolant temperature rise in the coolant hole ($T_{bo} - T_{bi}$) using an empirical correlation for Nu_m. Thus,

$$\frac{(T_{bo} - T_{bi})}{(T_w - T_{bi})} = 1 - e^{-4 Nu_m x^+} \tag{A13}$$

Two correlations for flow in the entrance region of a tube are recommended by Holman [9]. For laminar flow in the entrance region, the correlation by Hausen [9] is

$$Nu_m = 3.66 + \frac{0.0668}{x^+ + 0.04 (x^+)^{1/3}} \tag{A14}$$

For turbulent flow in the entrance region, the correlation by Nusselt [9] is

$$Nu_m = 0.036\ Re^{0.8}\ Pr^{1/3}\ (D/L)^{0.055} \qquad \text{for } 10 < \frac{L}{D} < 400$$

or

$$Nu_m = \frac{0.036}{(x^+)^{0.8}}\ Pr^{-0.47}\ \left(\frac{L}{D}\right)^{0.745} \tag{A15}$$

Table A1 shows a comparison of the values for Nu_m computed from equations (A14) and (A15) and the corresponding coolant temperature rise from equation (A13). For the present study, Pr = 0.7 and L/D = 9.23.

Table A1. Estimation of Nu_m and $(T_{bo} - T_{bi})$ in the Coolant Hole

	Laminar (Hausen [9])		Turbulent (Nusselt [9])	
x^+	Nu_m	$\frac{(T_{bo} - T_{bi})}{(T_w - T_{bi})}$	Nu_m[1]	$\frac{(T_{bo} - T_{bi})}{(T_w - T_{bi})}$
0.002	13.15	0.100	32.2	0.227
0.005	9.30	0.170	15.5	0.267
0.02	5.82	0.372	5.10	0.335
0.04	4.90	0.543	2.93	0.374

[1] Pr = 0.7, L/D = 9.23

Because of the uncertainty of the correlation for Nu_m to be used in equation (A13), experiments were conducted to determine a correlation for Nu_m vs x^+ for the coolant hole geometry used in the present study.

B.2. Experimental Apparatus

One of the drop-in segments was removed from the test cylinder and arranged in a configuration where velocity and temperature profiles could be measured at the coolant hole exit. The experimental apparatus is illustrated in Figure A2. The drop-in segment was supported by a mounting jig. Electrical heater plates were clamped to either side of the segment to maintain the wall temperature approximately constant. High conductivity thermal paste was applied between the heater strips and the segment. The copper tube fixture was inserted into the film coolant hole to support a vinyl coolant supply line and an inlet thermocouple. Two thermocouples were embedded to measure the segment wall temperature. Air flow was supplied to the film coolant hole and the air flow rate was measured with a hot-film mass flow meter. The film coolant flowed through a circular tube of length, L/D = 9.23, from the inlet thermocouple to the center of the coolant hole exit plane. The length from the screen to the center of the exit plane was L/D = 12.32.

A copper wedge, drilled with a coolant hole identical to the segment, was mounted over the coolant hole, and was sealed to the segment with RTV compound. The drilled wedge was installed to permit the velocity and temperature profile measurements in the coolant hole exit plane without influence from the free jet expansion of the coolant into room air.

Temperature and velocity traverses in the coolant hole exit plane were obtained using two separate probes. The temperature probe was constructed from a length of rigid 1.59mm o.d. tube. A copper-constantan thermocouple ran through the length of the tube. A bare length (5.1mm, ~20 wire dia.) of thermocouple lead extended from the tube to the sensing bead.[1]

---

[1] An analysis of the temperature measurement error was performed [8] (Appendix B) using a one-dimensional model with the following values: d_{wire}=0.25mm, d_{bead}=0.43mm, l_{wire}=5.1mm, k_{wire}=398W/mK, Re_{bead}=47-430, h_{bead}=29-74 W/m^{2}K, T_w=367K. The worst error, $(T_{bead}-T_{bi})/T_{bi}$, was less than 0.5% at the lowest coolant flow rate.

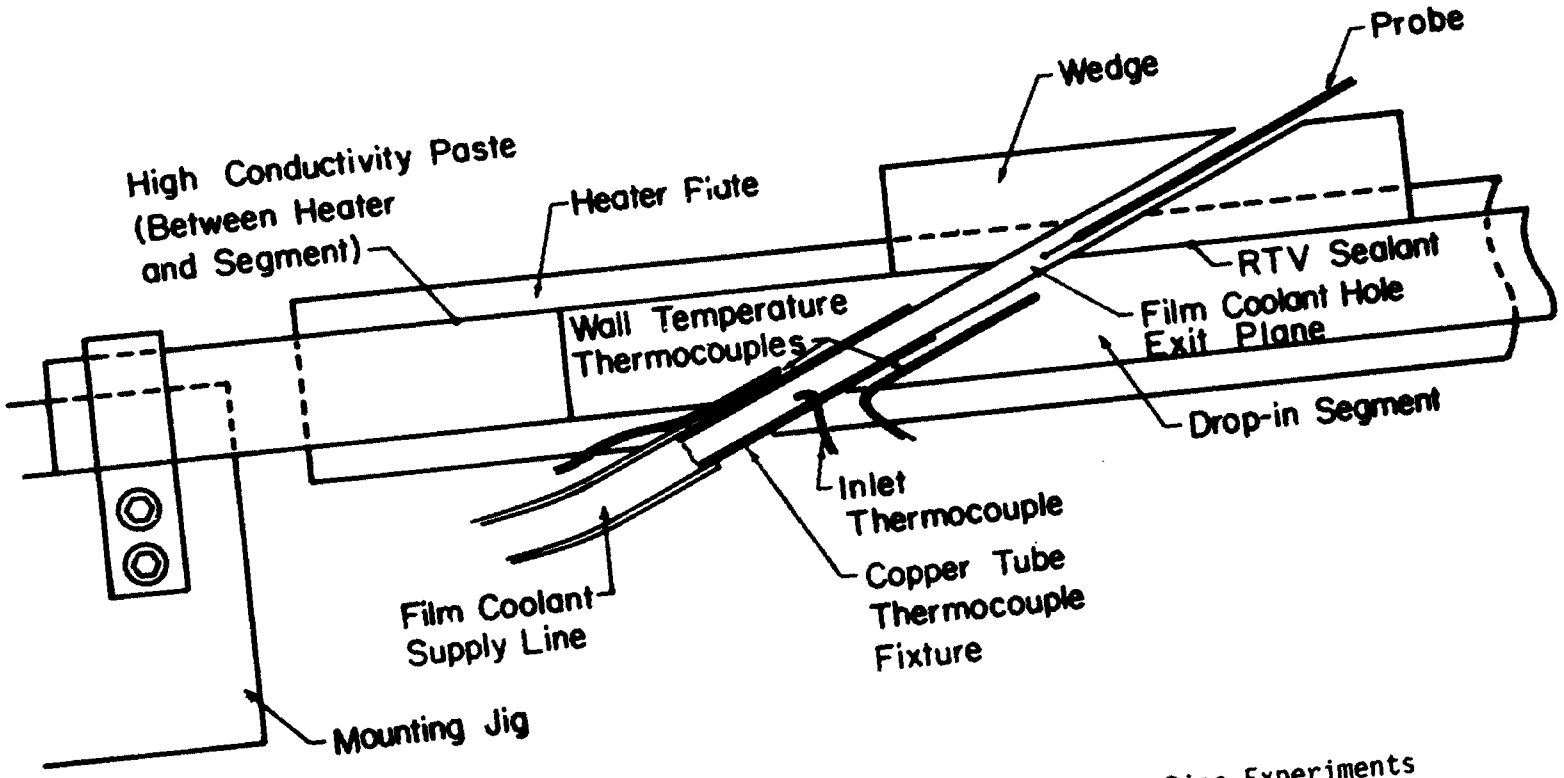

Figure A2. Experimental Apparatus for Coolant Temperature Rise Experiments

The velocity probe was constructed from hypodermic tubing (0.51mm i.d., 0.94mm o.d.). The velocity probe was used to measure the total pressure profile in the coolant hole exit plane using an inclined manometer with vernier scale (resolution = 0.025mm deflection).

The location of either probe in the coolant hole exit plane was measured with the use of dial indicators attached to the probe traversing mechanism (resolution = 0.013mm).

The static pressure was measured by a wall tap (0.46mm dia.) drilled in the wedge at a location 1.59mm downstream from the coolant hole exit plane.

B.3. Description of Experiment

The flow conditions used in the coolant hole calibration were chosen to simulate conditions encountered during the film cooling experiments. For the film cooling experiments, the coolant mass flow rate through one hole, for film cooling, was in the range $0.137 \leq \dot{m} \leq 1.37$ Kg/hr. The segment wall temperature had a nominal value of 294K and the coolant inlet temperature fell in the range $155 \lesssim T_{bi} \lesssim 300$K. This combination of temperature and flowrate extremes results in a range for x^+ [1] of $1.7 \times 10^{-3} < x^+ < 2.3 \times 10^{-2}$. The range of inlet temperature difference $(T_w - T_{bi})$ was $-6 < \Delta T < 140$K°.

For the coolant hole calibration, an inlet temperature difference was created by heating the segment to a wall temperature of about 360K. The resulting inlet temperature difference was in the range $40<(T_w-T_{bi})<55$K°. By varying the coolant flow rate, the range of x^+ investigated in the calibration was $2.4 \times 10^{-3} < x^+ < 2.3 \times 10^{-2}$.

For a given calibration experiment, the coolant mass flow rate and electrical power to the heater plates were adjusted to give the desired values of x^+ and inlet temperature difference. The temperature and velocity profiles in the coolant hole exit plane were measured to evaluate T_{bo}.

---

[1] The properties in x^+ were based on an inlet film temperature, $T_{fi} = (T_{bi} + T_w)/2$.

Figure A3 illustrates the typical grid used for measuring the coolant temperature and velocity in the coolant hole exit plane. Prior to probe insertion, the alignment of the probe traversing mechanism was checked with a dial indicator to ensure traversing in the x-z plane. The temperature probe was inserted to locate the probe tip at the center of the coolant hole exit plane. The probe was traversed along lines of constant x, in increments of approximately 1.02mm. Probe movement in the z-direction was halted when the probe body contacted the wedge, as determined by electrical continuity between the probe body and the wedge.

When the temperature traverse was completed, the flow conditions were maintained constant and the total pressure probe was inserted and located at the center of the coolant hole exit plane. The total pressure was measured at selected grid points as shown in Figure A3.

After completing the total pressure traverse, the total pressure probe was placed at the center of the coolant hole and the wall static pressure at the exit of the coolant hole was measured.

B.4. Bulk Temperature Evaluation

The bulk temperature is defined to represent the energy convected through a given area.

$$\dot{m}c_pT_b = \int_A \rho c_p T\,(\bar{V} \cdot \overline{dA})$$

Assuming the variation of specific heat is negligible, the expression for bulk temperature at the coolant hole exit plane can be written as

$$T_{bo} = \frac{1}{\dot{m}} \int_A \rho T(V\sin\beta dA) \qquad (A16)$$

where $\bar{V} \cdot \overline{dA} = VdA\cos(\pi/2-\beta) = VdA\sin\beta$

dA = element of area in the coolant hole exit plane

β = angle between hole centerline and segment surface

The integration is performed over the coolant hole exit plane area where temperature, velocity and density are functions of x and z.

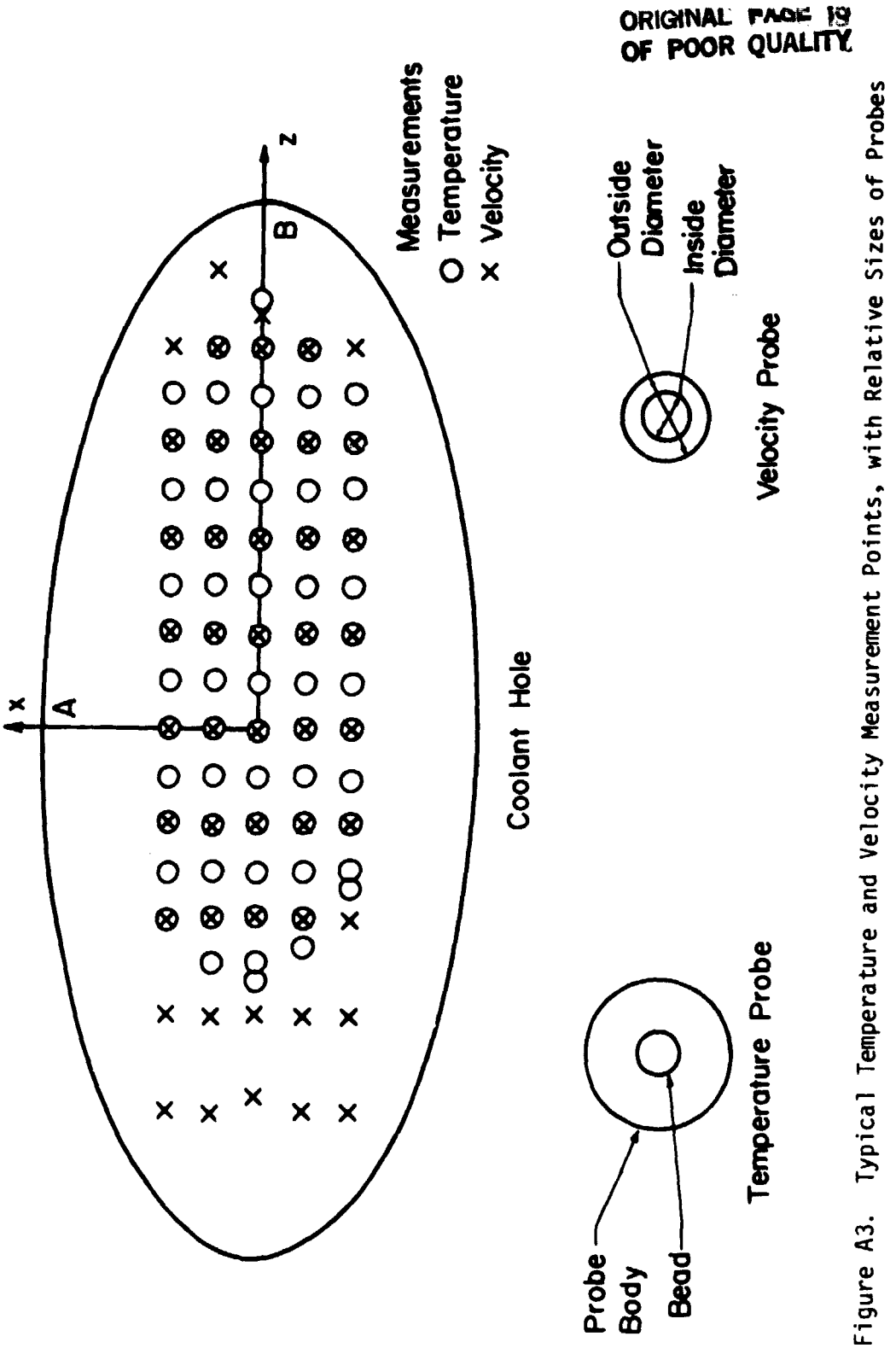

Figure A3. Typical Temperature and Velocity Measurement Points, with Relative Sizes of Probes

Equation (A16) can be put in dimensionless form by defining

$$\theta = \frac{T_w - T}{T_w - T_{bi}}$$

then

$$T_{bo} = \frac{1}{\dot{m}} \int_A \rho V[T_w - \theta(T_w - T_{bi})]\sin\beta dA$$

Rearranging the above gives

$$\dot{m}(T_w - T_{bo}) = \int_A \rho V\theta(T_w - T_{bi})\sin\beta dA$$

Then noting

$$\theta_m = \frac{T_w - T_{bo}}{T_w - T_{bi}} \quad ; \quad \dot{m} = \int_A \rho V \sin\beta dA$$

we obtain

$$\theta_m = \frac{\int_A \rho V\theta dA}{\int_A \rho V dA} \tag{A17}$$

Assuming ideal gas behavior for the air and a uniform static pressure in the coolant hole exit plane, equation (A17) becomes

$$\theta_m = \frac{\int_A \theta \frac{V}{T} dA}{\int_A \frac{V}{T} dA} \tag{A18}$$

The measurements of temperature and velocity in the coolant hole exit plane were used in conjunction with equation (A18) to determine θ_m by numerical integration.

B.5. Data Reduction

For each calibration experiment, the following data were recorded.

(1) coolant mass flow rate, $\dot{m}$, (uncertainty ± 5%),

(2) coolant inlet temperature, T_{bi}, and coolant hole wall temperature, T_w (average of two wall thermocouples),

(3) coolant temperature distribution, T(x,z), (see Figure A3),

(4) coolant total pressure distribution, $P_T(x,z) - P_{atm}$, (see Figure A3),

(5) coolant static pressure, $P_s - P_{atm}$, (total pressure probe centered) and atmospheric pressure.

At each location of temperature measurement, the value of dimensionless temperature (θ) was calculated as

$$\theta(x,z) = \frac{[T(x,z) - T_w]}{(T_{bi} - T_w)}$$

At the wall, the value of $\theta(x,z)$ was set equal to zero.

The velocity was calculated, assuming incompressible flow, as

$$V(x,z) = \sqrt{2[P_T(x,z) - P_s]/\rho(x,z)}.$$

where

$$\rho(x,z) = \frac{P_s}{RT(x,z)}$$

To account for small variations of T_{bi} and T_w during the course of an experiment, the temperature, T(x,z), was determined using the value of $\theta(x,z)$ from the temperature profile measurements and the values of T_{bi} and T_w observed during the total pressure survey. At velocity measurement locations which did not coincide with temperature locations (see Figure A3), θ was determined by interpolation using a second order polynomial.

The dimensionless bulk temperature at the coolant hole exit plane was determined from equation (A18).

$$\theta_m = \frac{\int_x \int_z \theta(x,z) \frac{V(x,z)}{T(x,z)} \, dx \, dz}{\int_x \int_z \frac{V(x,z)}{T(x,z)} \, dx \, dz} \tag{A18}$$

The integrals were evaluated numerically using a second order polynomial fit to the data.

The average Nusselt number was calculated from equation (A12)

$$Nu_m = \frac{-\ln \theta_m}{4 x^+} \tag{A19}$$

where x^+ was based on the measured coolant mass flow rate with fluid properties based on the inlet film temperature, $T_{fi} = (T_{bi} + T_w)/2$.

The velocity profile also was used to calculate the coolant mass flow rate according to

$$\dot{m}_{calc} = \sin\beta \frac{P_s}{R} \int \frac{V}{T} \, dx \, dz \tag{A20}$$

The integration was performed numerically using a second order polynomial fit of the data.

B.6. Results

The calibration for temperature rise in the coolant hole was performed for four flow conditions: $x^+ = 2.40 \times 10^{-3}$, 3.30×10^{-3}, 6.28×10^{-3} and 2.27×10^{-2}. This section presents the temperature and velocity profiles for each flow condition and the resulting data for Nusselt number vs. x^+.

Figures A4 through A11 present plots of the dimensionless temperature and velocity for the four flow conditions. The abscissa for each is the nondimensional z coordinate, z/B, normalized with respect to half the

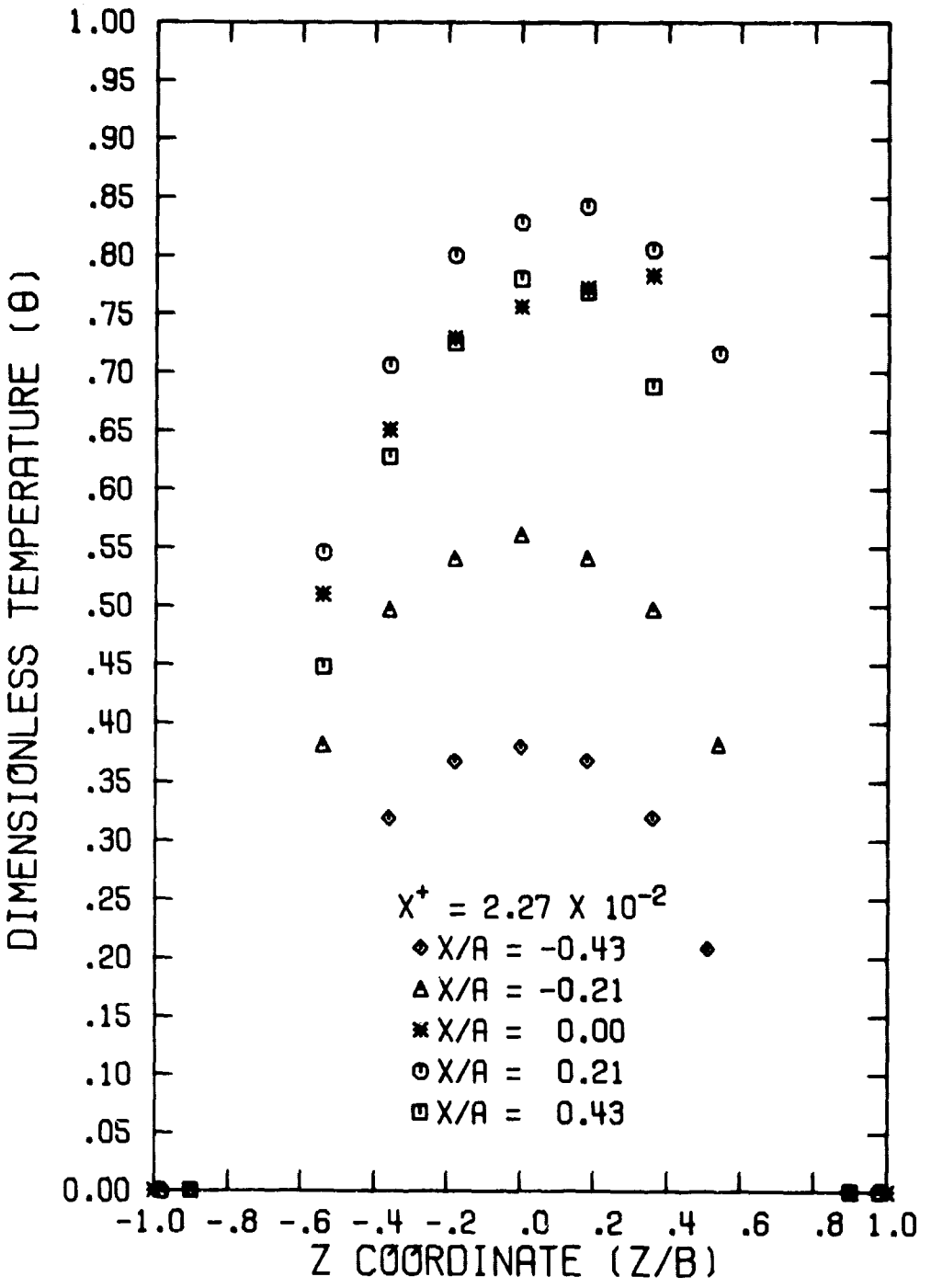

Figure A4. Profile of Coolant Hole Exit Dimensionless Temperature ($x^+=2.27x10^{-2}$)

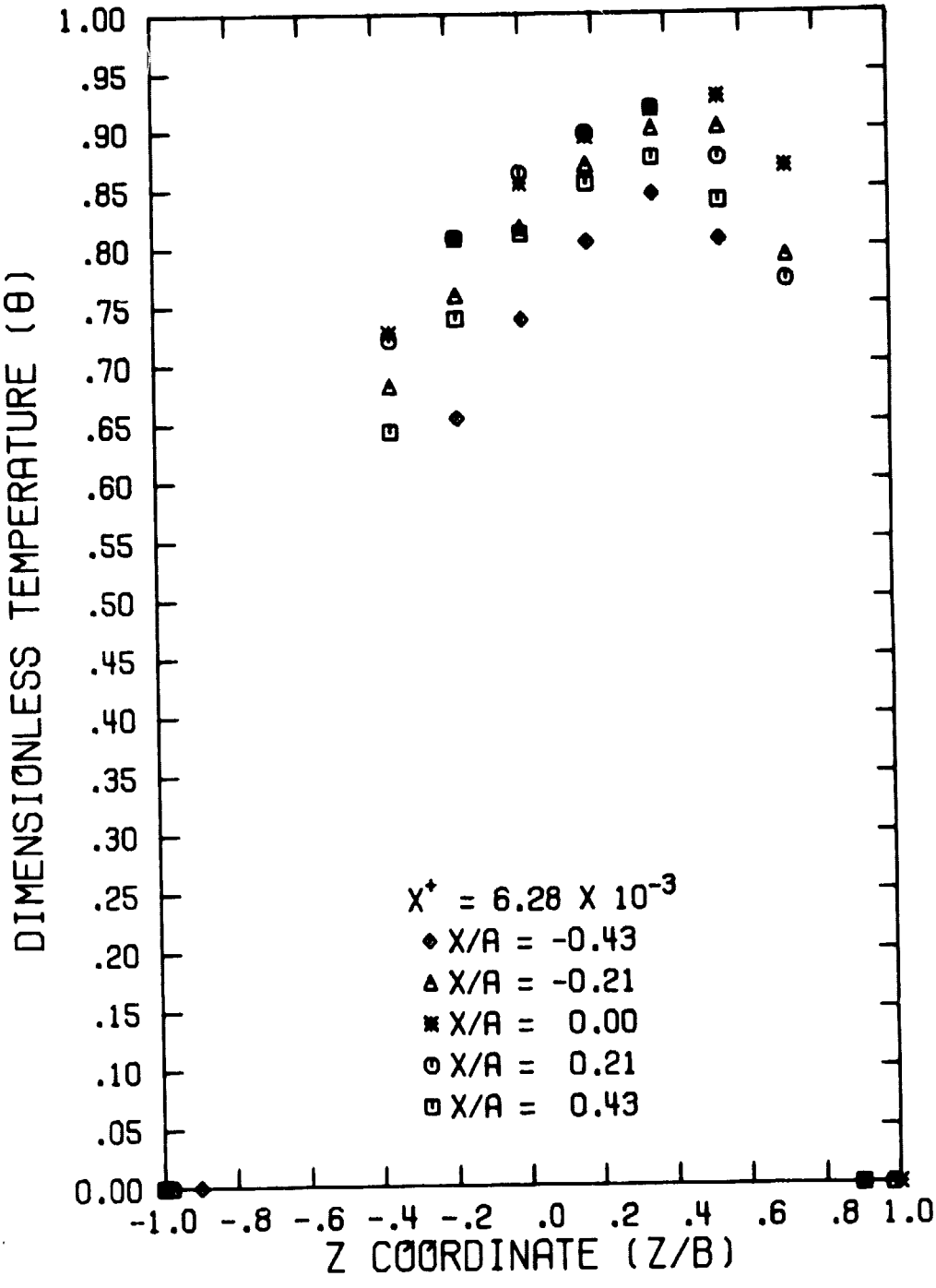

Figure A5. Profile of Coolant Hole Exit Dimensionless Temperature ($x^+=6.28\times10^{-3}$)

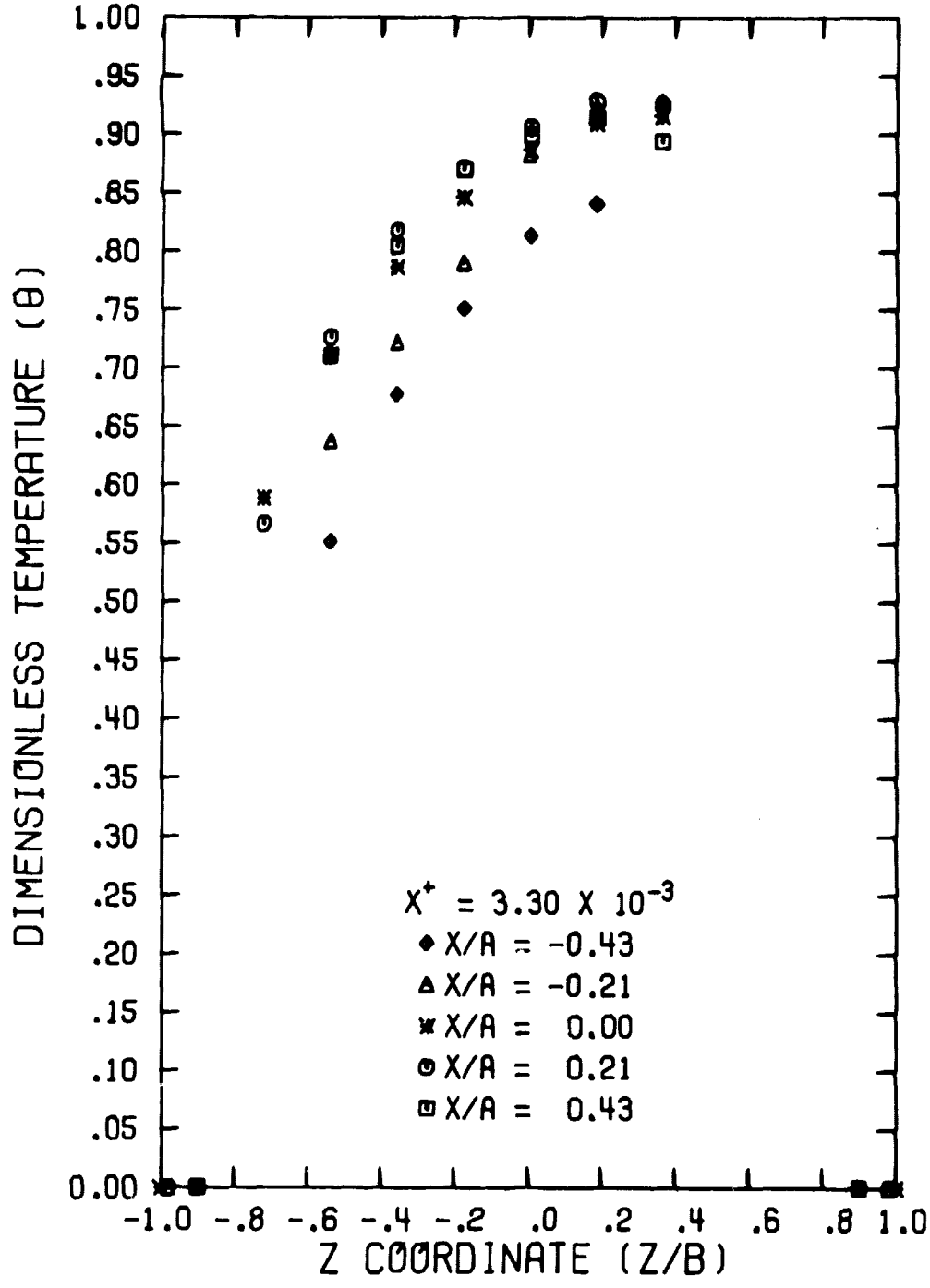

Figure A6. Profile of Coolant Hole Exit Dimensionless Temperature ($x^+=3.30x10^{-3}$)

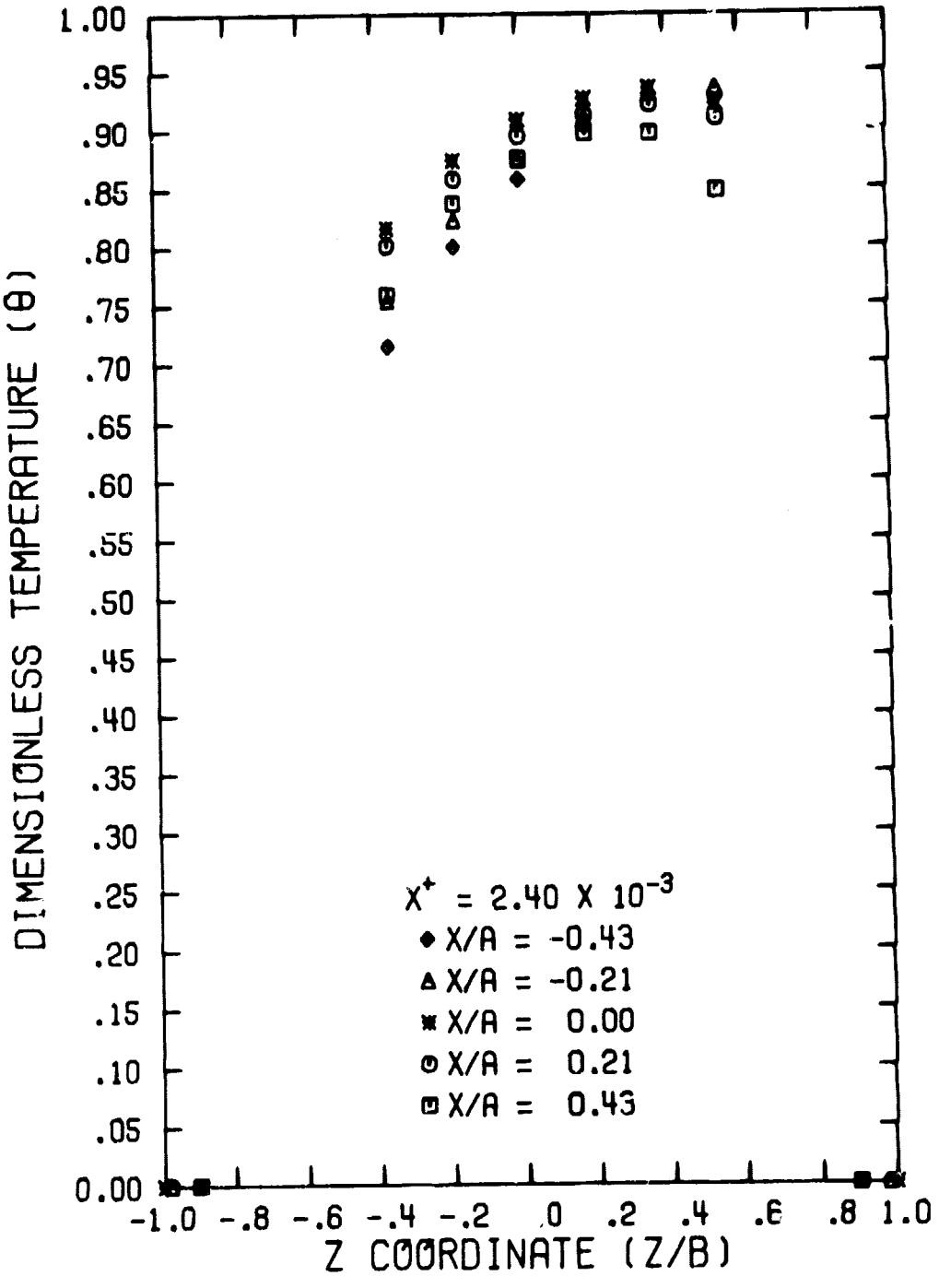

Figure A7. Profile of Coolant Hole Exit Dimensionless Temperature ($x^+=2.40\times10^{-3}$)

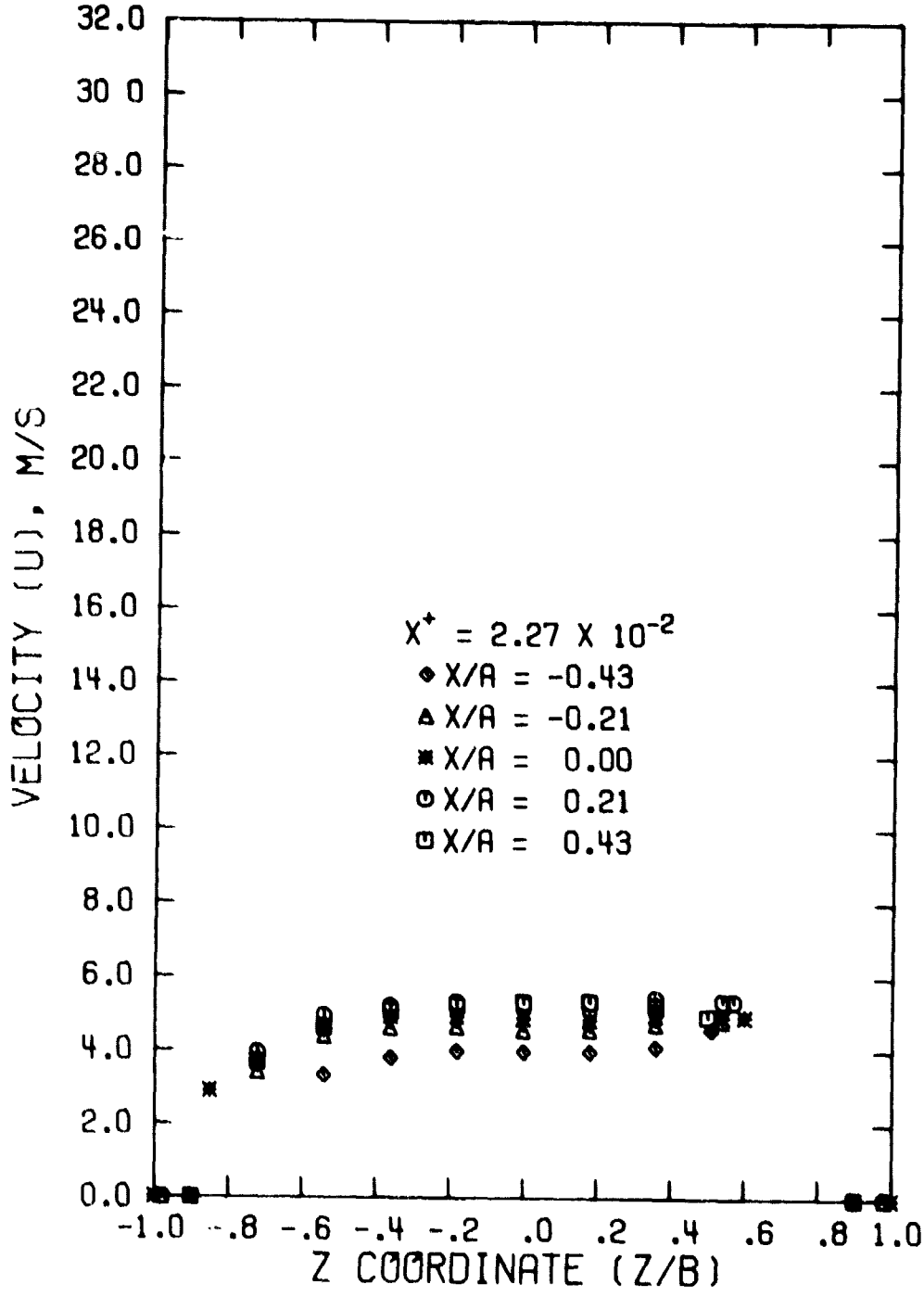

Figure A8. Profile of Coolant Hole Exit Velocity ($x^+=2.27x10^{-2}$)

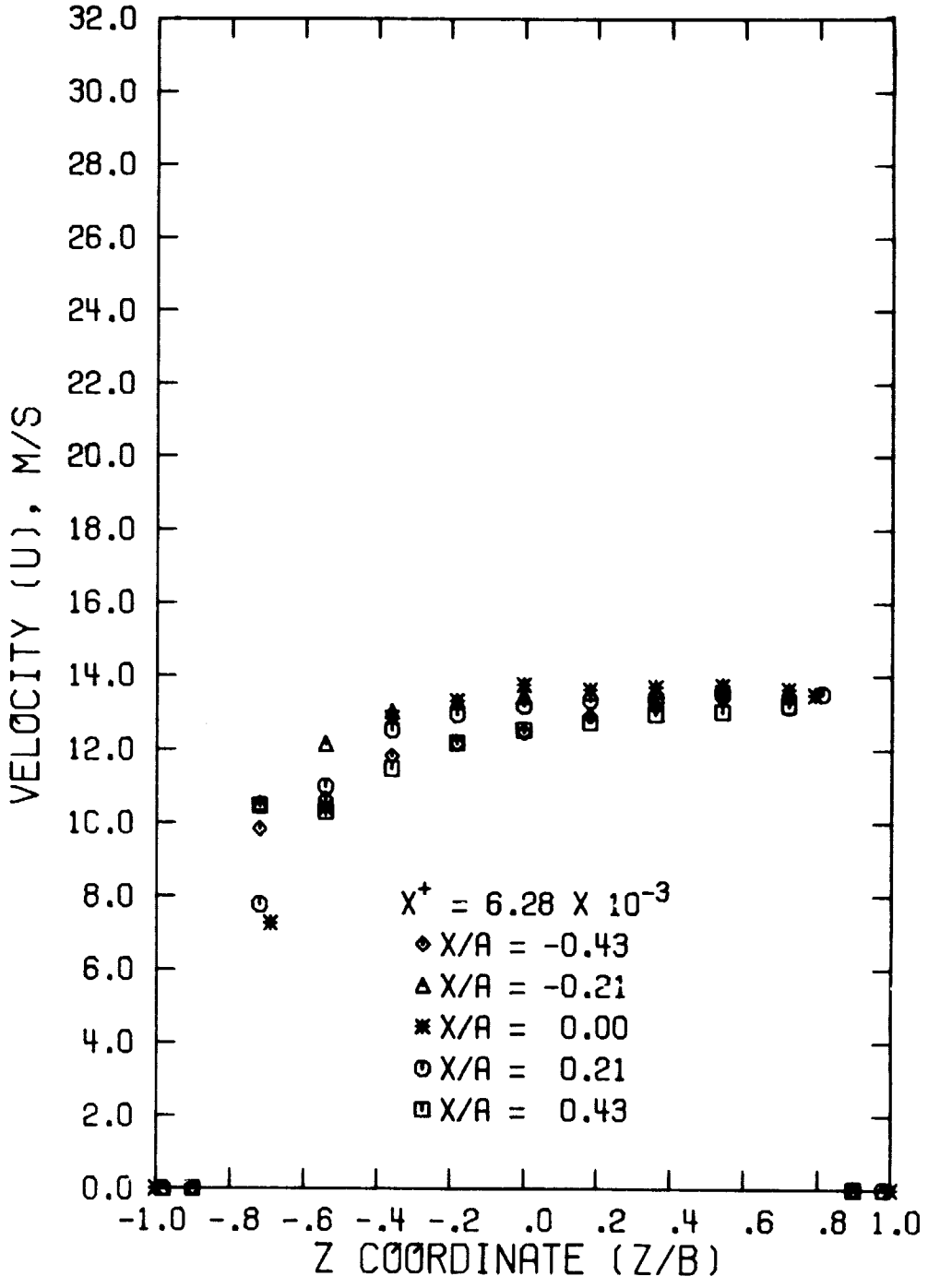

Figure A9. Profile of Coolant Hole Exit Velocity ($x^+=6.28x10^{-3}$)

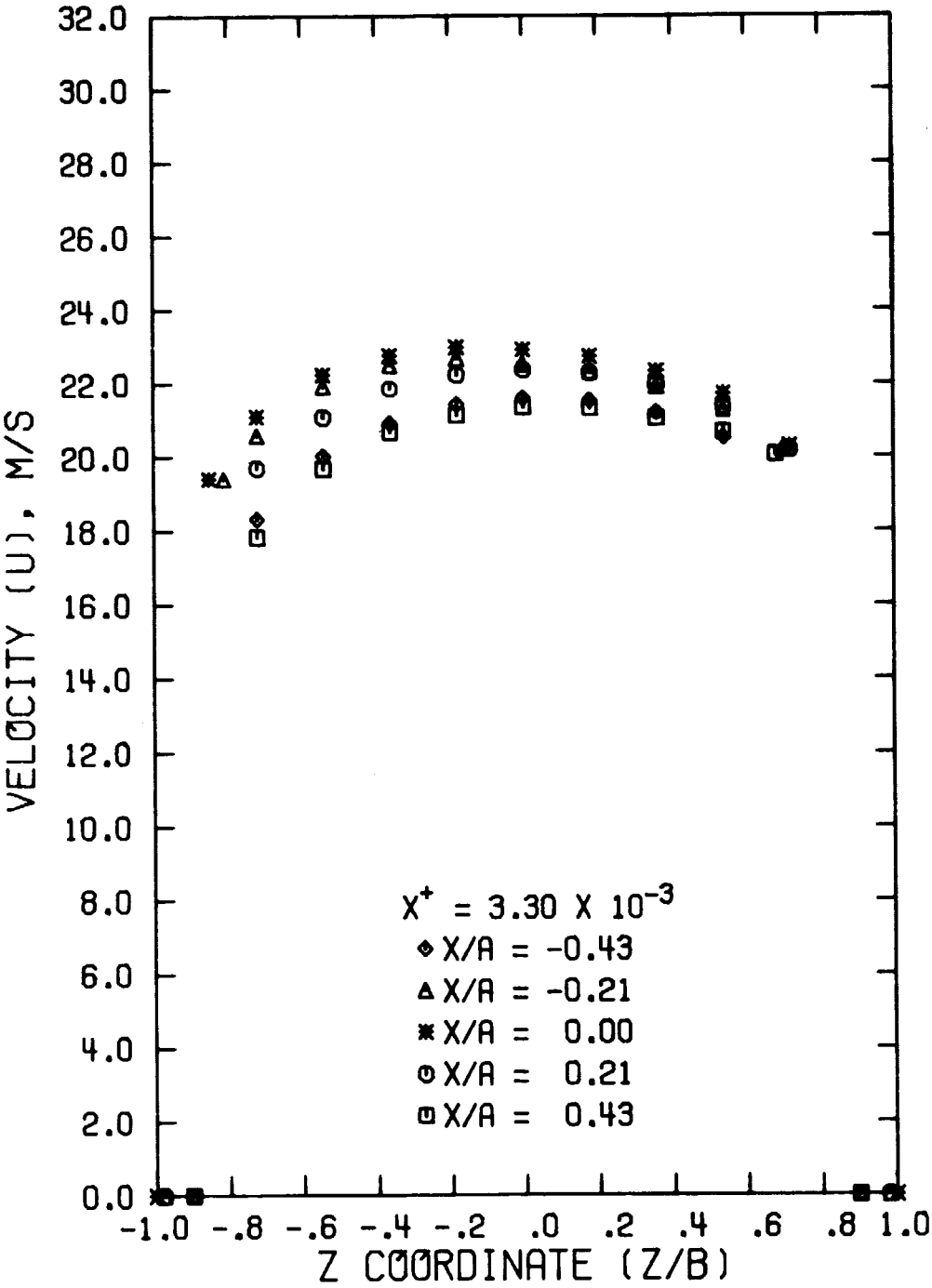

Figure A10. Profile of Coolant Hole Exit Velocity ($x^+=3.30x10^{-3}$)

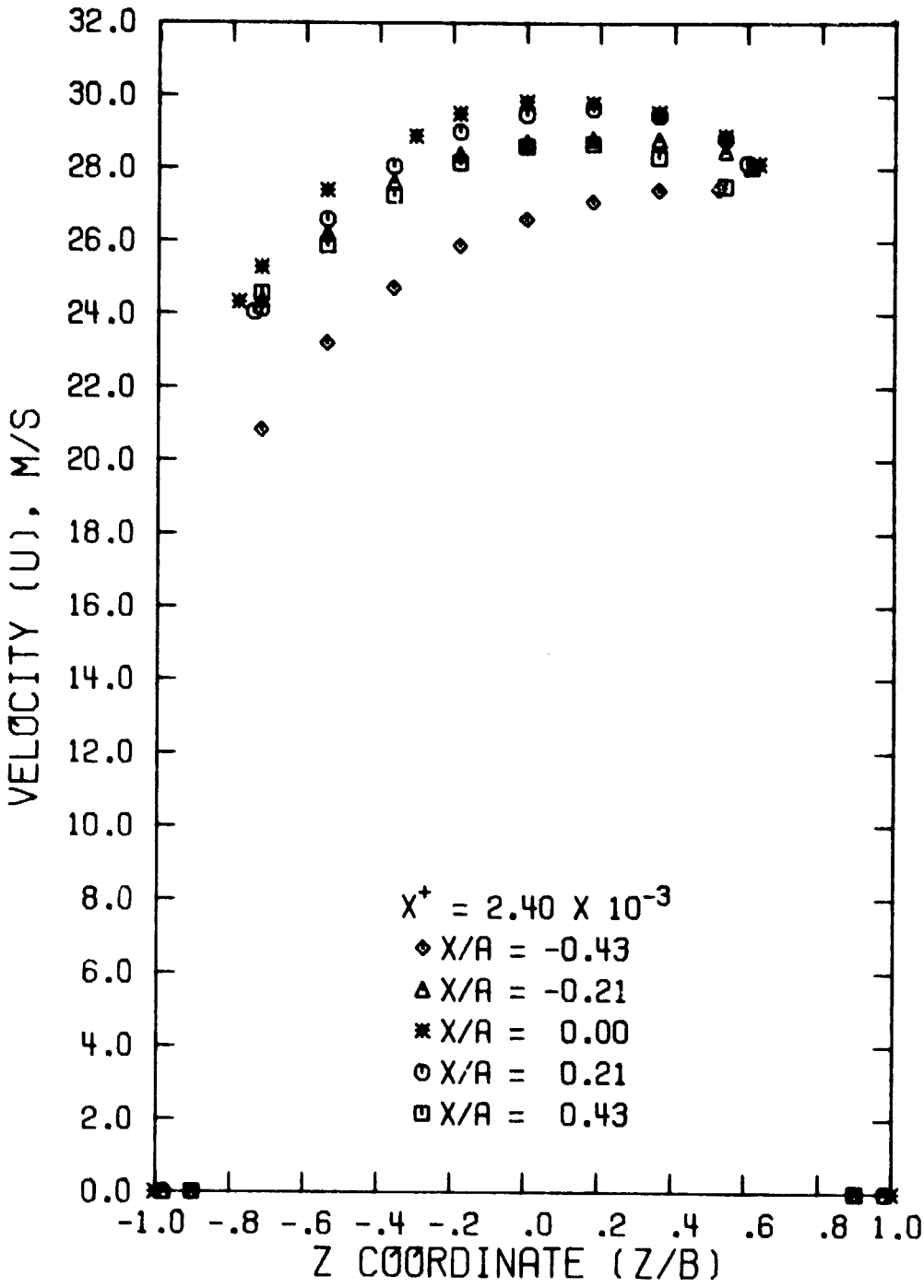

Figure A11. Profile of Coolant Hole Exit Velocity (x^+=2.40x10^{-3})

length of the major axis (see Figure A3). Symbols, defined in the legend represent the nondimensional x coordinate, x/A, (A = half the length of minor axis, Figure A3) for a traverse at constant x.

The plots for dimensionless temperature (Figures A4 through A7) show that the value of θ increases as x^+ decreases, indicating that the temperature at the hole exit tends toward the inlet temperature (T_{bi}) as mass flow rate increases. The profiles generally are skewed with the point of maximum θ (minimum coolant temperature) usually found when $z > 0$.

Figures A8 through A11 show similar results for the velocity measurements. The profiles are relatively flat for the two larger values of x^+ (smaller coolant flow rate). The velocity profiles are somewhat skewed toward $z > 0$.

The skewing of the temperature and velocity profiles may be attributed to the shallow angle of the coolant hole. Reference to Figure A1, for a coolant hole at $\beta = 25°$, indicates a centerline length of L/D=12.32 from the screen, L/D = 9.23 from the inlet thermocouple. The surface length along the bottom of the hole, x/A = 0, z/B = +1, is L/D = 13.37 from the screen, while the surface length along the top of the hole, x/A = 0, z/B = -1, is L/D = 11.27 from the screen. An additional influence on the profiles may be the presence of the inlet temperature thermocouple which protrudes from the lower surface, halfway into the flow stream.

The velocity profile data were integrated (equation (A20)) for each flow condition, to determine $\dot{m}_{calc}$ for comparison with the mass flow rate indicated by the flowmeter. Figure A12 shows the percent error in the calculated mass flow rate, $(\dot{m}_{true} - \dot{m}_{calc})/\dot{m}_{true}$, using the flowmeter reading as the true flow rate. It is seen that the integrated results agreed within ± 20% of the flowmeter flow rate. An analysis to determine the effect of velocity profile on the integrated value of the bulk dimensionless temperature [8] Appendix B, showed that an error in the shape of the velocity profile would cause a maximum uncertainty in θ_m of about ±6% for $2.4 \times 10^{-3} \leq x^+ \leq 6.3 \times 10^{-3}$ and an uncertainty of about ±16% in θ_m for x^+ near 2.3×10^{-2} (low flow rate).

The final results of the calibration experiments are shown in Figure A13. The Nusselt number was calculated from equation (A19) after integrating

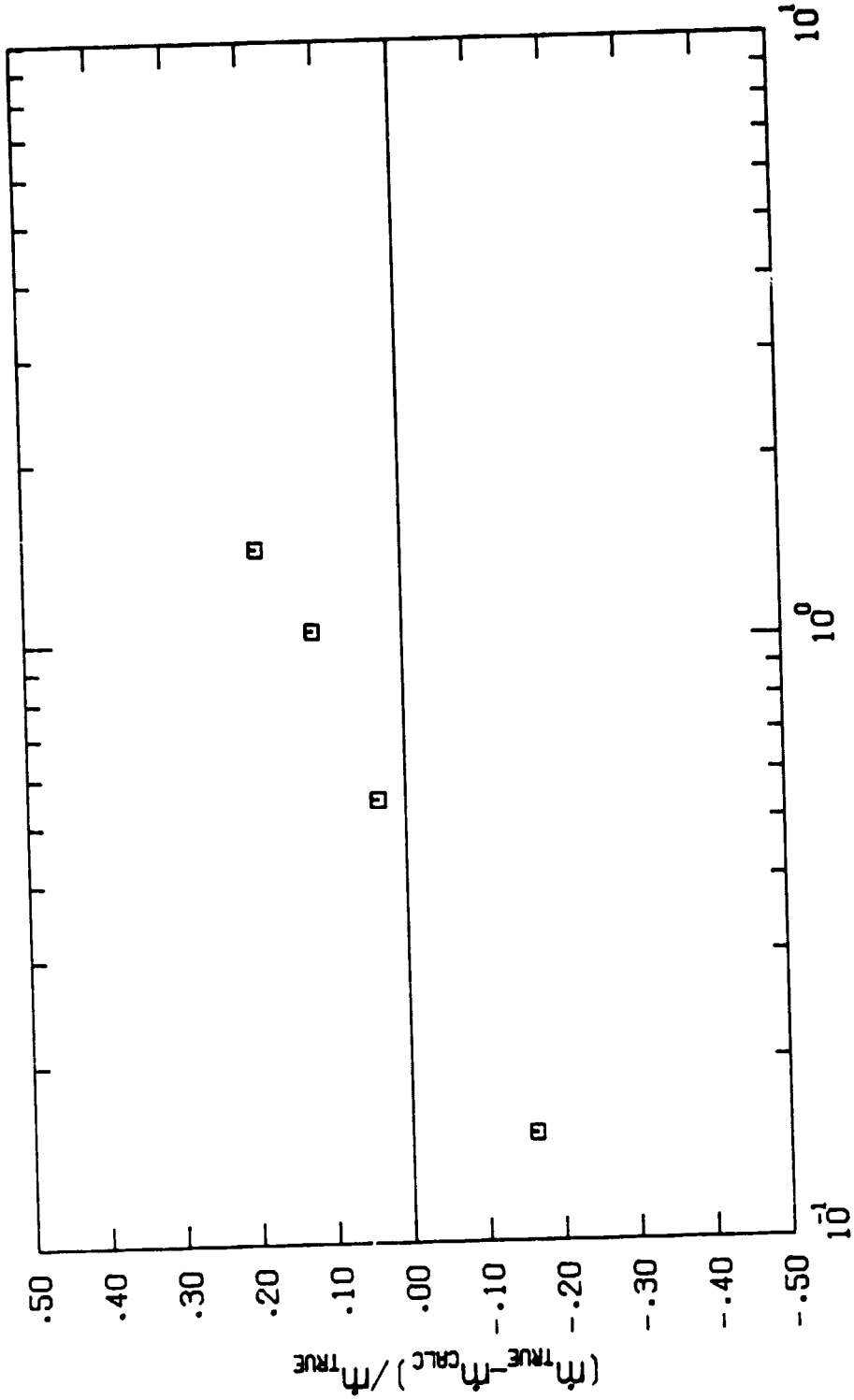

Figure A12. Error in Integrated Mass Flow Rate

the profile data for θ_m. Also shown on Figure A13 are two curves representing the correlations of Nusselt and Hausen. There is good agreement between the data of the present study and the curve for turbulent flow in the range $x^+ \leq 0.007$ ($Re \geq 1900$). The data are higher than the correlation for laminar flow which may be due to the presence of the screen at the inlet to the coolant hole.

Figure A13 indicates the estimated uncertainty in the value of mean Nusselt number. Using the method of Kline and McClintock [10], the uncertainty in x^+ was determined to be ± 6%, due mostly to the uncertainty in the flowmeter calibration. Using this estimate for uncertainty in x^+, and the previously mentioned uncertainty in θ_m due to profile errors, the estimated uncertainty in Nu_m is about ± 10% for $x^+ \leq 6.3 \times 10^{-3}$ and about ±17% for $x^+ \geq 6.3 \times 10^{-3}$.

A second order least squares curve fit to the data for mean Nusselt number versus bulk dimensionless temperature yielded the following equation

$$Nu_m = 14.85\, x^{+\,(0.686 + 0.302 \log x^+)} \qquad \text{(A21)}$$

For the film cooling experiments, the coolant exit temperature (T_c) was determined by equation (A13) ($T_c = T_{bo}$) using equation (A21) for Nu_m, the measured values of T_{bi} and T_w, and the coolant hole mass flow rate determined as described in Appendix A.

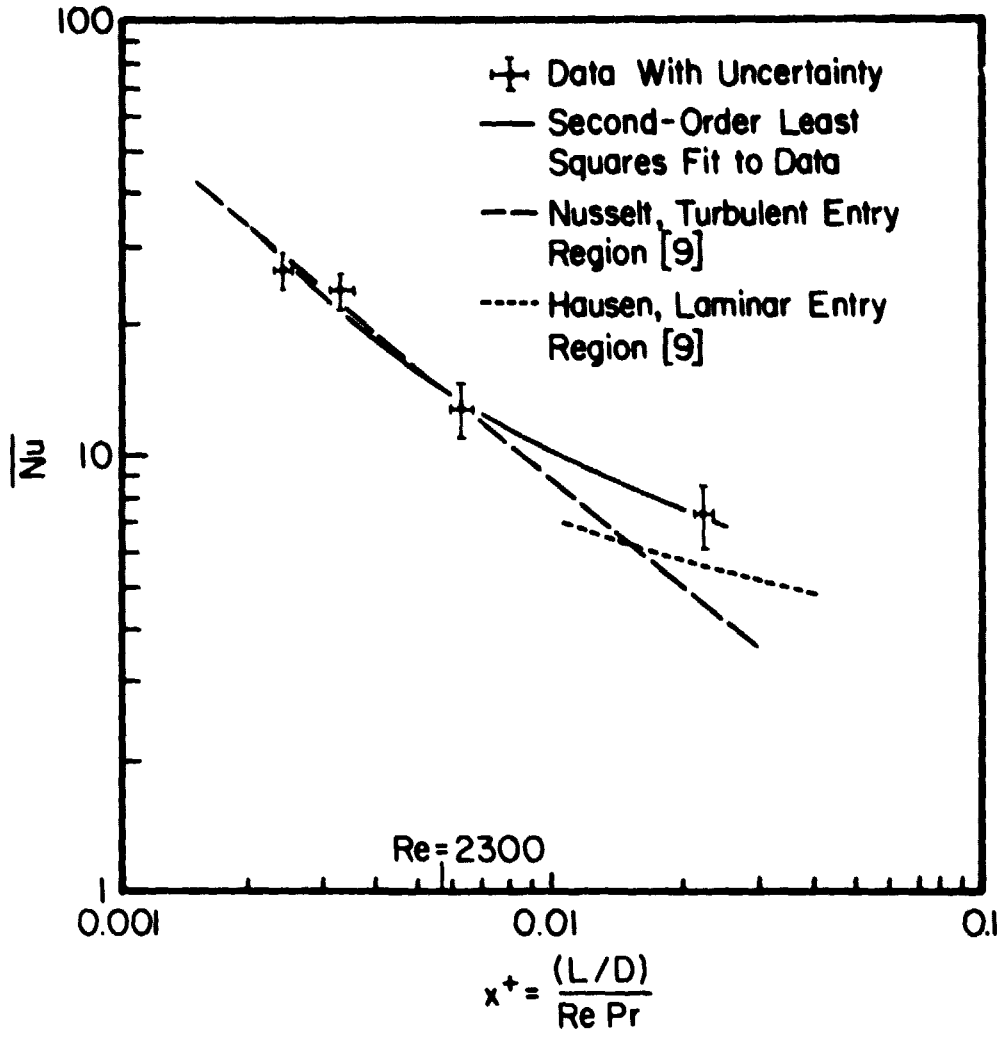

Figure A13. Correlation of Heat Transfer in Film Coolant Hole

Appendix C

SURFACE ROUGHNESS

The instrumented test cylinder was equipped with drop-in segments. Measurements were made of the surface roughness created by the segments, and the effect of roughness was evaluated in terms of findings in the literature on the effects of roughness on cylinder surface heat transfer (see [1] for more details).

The roughness at the seam between the cylinder surface and the segment was measured by rotating the cylinder past a dial indicator (6μm resolution). The roughness was measured along all seams with the resulting step-changes in surface height shown on Figure A14.

Figure A14 shows, to scale, a schematic of the five drop-in segments (S1-S5), with ticmarks along both seams of each segment representing the locations along the segment at which the step-change in height was measured. The measuring point locations are shown relative to the side walls of the flow channel and relative to the heat flux gage locations. Numerical values for roughness are given in microns, with a positive sign denoting a step increase in height between the cylinder surface and the segment, and a minus sign denoting a step decrease in height between the cylinder surface and the segment.

The measurements show that the largest roughness measured was $K = -228\mu m$, or, nondimensionalized, $K/D = 15.0 \times 10^{-4}$ (D = cylinder diameter). This was located at the end of Segment 2, far from the instrumented region of the cylinder. Considering the instrumented region, the largest roughness measured was $K = 126\mu m$, $K/D = 8.3 \times 10^{-4}$ (along the second and third segments).

The effect of roughness on cylinder heat transfer was studied by Achenbach [11], where roughness was created by attaching emery paper to a test cylinder surface. When tested with a Reynolds number of $Re_D^* = 8.3 \times 10^4$, and a sand-grain roughness of $K_s/D = 7.5 \times 10^{-4}$, the heat transfer around the cylinder, compared to that of a smooth cylinder,

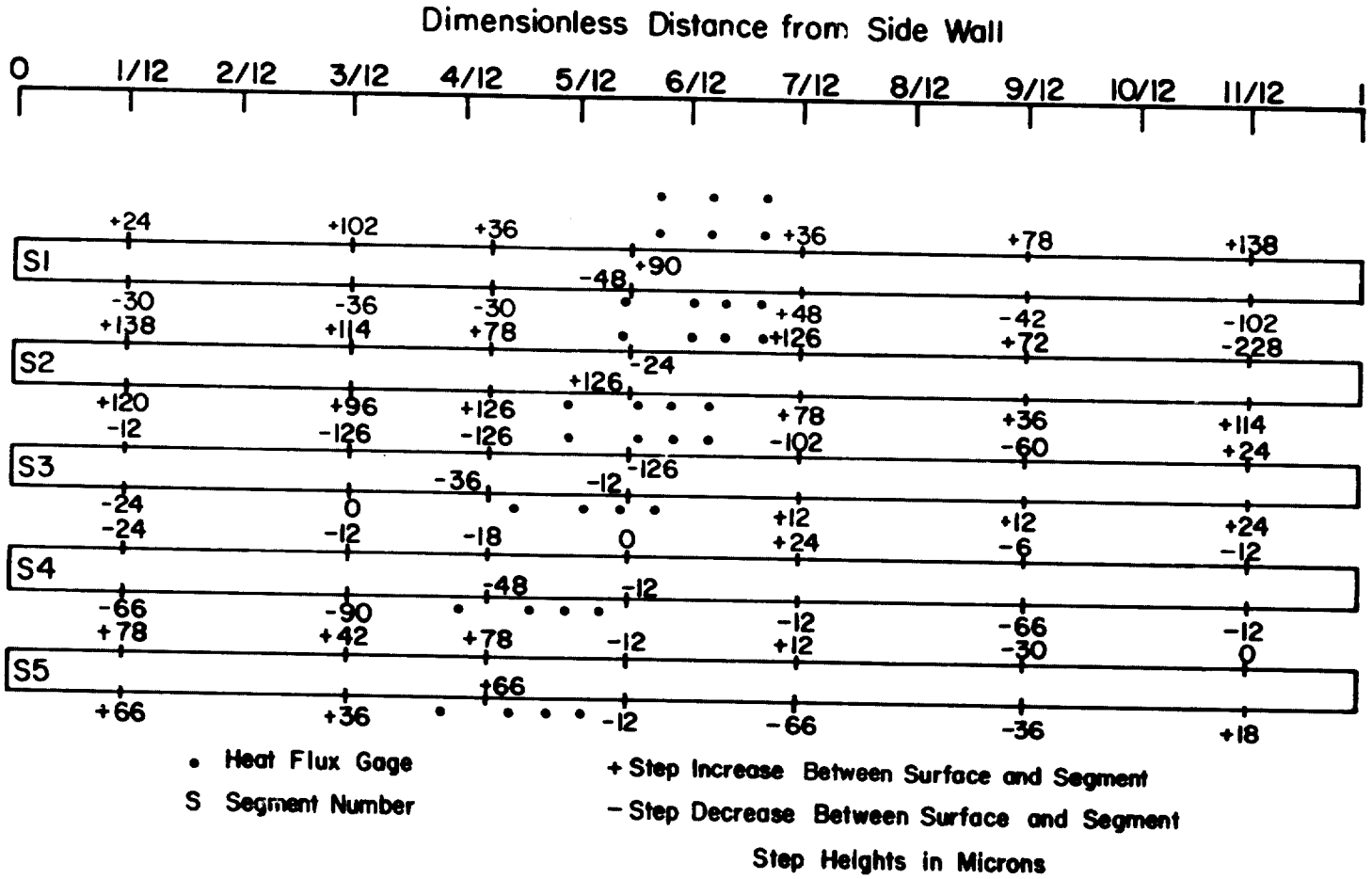

Figure A14. Measurements of Test Cylinder Surface Roughness

was unaffected by the roughness. The heat transfer around the cylinder was unaffected by a four-fold increase in roughness, $K_s/D = 30 \times 10^{-4}$, at the Reynolds number $Re_D^* = 6.3 \times 10^4$.

It was concluded from Achenbach's results that the heat flux data of the present study, conducted under conditions of $Re_D^* = 7.1 \times 10^4$ $K/D \leq 8.3 \times 10^{-4}$, were unaffected by surface roughness.

Appendix D

ADDITIONAL COMMENTS ON HEAT FLUX GAGE BEHAVIOR

Throughout the present study, the reproducibility of the heat flux gage output was carefully monitered because of the increase in indicated dry wall heat flux by some gages between the previous study [1] and the present.

It has been mentioned previously (Section III.F.) that some heat flux gages were disqualified on the basis of an increase in $Nu/\sqrt{Re_D^*}$ of greater than 20% over the results of [1]. These gages were disqualified throughout the present study. The data from other gages, however, were occasionally disregarded when their output was seen to be erratic.

In cases where heat flux gage output was disregarded, it was due to large variations in the four readings obtained at a given condition (see Section II.E.). When inspected after finding a given gage had produced an erratic reading, the physical reason for gage malfunction could be seen. For an erratic gage, it was found that a residue had deposited over the heat flux gage surface. The residue was believed to be caused by the oxidation of the beryllium-copper surface.

The fact that the residue appeared during runs in this study and not in the previous study [1] is likely caused by a difference in run technique. Between blowing ratio conditions in this study, the hot freestream gas flow was shut off while the liquid nitrogen heat exchanger reached a new steady heat transfer condition. In the meantime, condensate developed on the test surface. It is believed that the combination of the condensate and possible oxidation caused a residue to develop on the gage after the combustor was restarted and the condensate evaporated. In the previous study [1], experiments were run from start to finish in the presence of the hot freestream gas flow without the opportunity for condensate to form.

In the present study, when a gage was observed to indicate erratically, the output from that gage was consistently erratic throughout the

remainder of that test, and thus was discarded. After the test, when the cylinder surface was routinely cleaned, the residue was removed and the gage was returned to normal operation.

A list of gages and the conditions under which their output was discarded is contained in Table A2.

Table A2. List of Conditions Under Which Specified Gage Was Erratic

Condition			Gage	Location	
θ_i	M	θ_c		x/d_o	z/S
22.9°	0.25	1.18	25	11.50	0.67
	0.75	1.33	9	1.50	0.67
		1.44	13	3.50	0.67
			19	8.50	0.50
		1.45	8	1.50	0.33
			9	1.50	0.67
	1.23	1.30	20	8.50	0.83
		1.56	8	1.50	0.33
			9	1.50	0.67
40.8°	0.51	1.36	25	11.50	0.67
	$0.51 \leq M \leq 1.58$	$1.3 \leq \theta_c \leq 1.4$	16	6.50	0.83
			20	8.50	0.83
	1.58	1.36	7	1.50	0.00

Appendix E

TABULATION AND PLOTS OF EXPERIMENTAL DATA

Tables A3 through A5 summarize the data of the present investigation for film cooling with $\theta_c > 1.0$. Tabular entries give the value of SNR at the streamwise (x/d_o) and spanwise (z/S) coordinate for each heat flux gage. The value of blowing ratio M, was calculated as the average value of the blowing ratios for the five primary coolant holes. The value of θ_c, was calculated as the average of the values of θ_c for the five primary coolant holes.

Table A6 lists the spanwise-averaged Stanton Number Reduction, SNR_{AVG}, and the corresponding streamwise location of the row of gages.

A dash (-) in the table means no data was available at that condition (see Appendix D).

Figures A15 through A50 are plots of the data in Tables A3, A4 and A5. Plots that are presented in Chapter IV (Figures 17 through 32) are not repeated here. The plots illustrate the spanwise distribution of SNR. The plots and the data were used to calculate values of SNR_{AVG} and the coolant trajectories as discussed in Chapter IV. All plots of SNR_{AVG} are presented in Chapter IV (Figures 33 through 42).

Table A3. Stanton Number Reduction for $\theta_i = 5.0^o$

	M	2.01	2.99	5.17	10.23
	θ_c	1.29	1.29	1.32	1.38
x/d_o	z/S				
1.50	.00	.45	-.23	-.72	-.61
1.50	.33	.39	.55	.56	-1.03
1.50	.67	.00	-.02	-.08	.23
1.50	1.33	.42	.48	.67	-.25
3.50	.00	-.01	-.27	-.28	-.13
3.50	.33	.36	.42	-.55	-.71
3.50	.67	.00	-.03	.09	-.32
3.50	1.33	.50	.45	-.26	-.57
6.50	.50	.20	.25	.10	-.39
6.50	.83	.00	-.04	.09	-.32
6.50	1.17	.28	-.03	-.36	.02
8.50	.50	.11	.18	.02	-.29
8.50	.83	.02	.00	.08	-.31
8.50	1.17	.14	-.04	-.21	.10
8.50	1.83	.03	.01	.10	-.20
11.50	.00	.01	-.02	-.02	-.05
11.50	.33	.16	.13	-.49	-.02
11.50	.67	.13	.15	.14	-.19

Table A4. Stanton Number Reduction for $\theta_i = 22.9^o$

	M	.25	.74	.74	.75	1.24	1.22	2.06	2.08	2.46	2.44
	θ_c	1.18	1.33	1.45	1.44	1.30	1.56	1.29	1.36	1.29	1.39
x/d_o	z/S										
1.50	.00	.71	.64	1.49	1.29	.79	1.24	.52	.77	-1.79	.73
1.50	.33	.06	.87	-	.75	.83	-	.98	1.28	.90	1.15
1.50	.67	.05	-	-	.09	.00	-	-.01	.08	.12	.18
1.50	1.33	-.03	.78	.24	-	.76	1.08	1.17	1.05	.55	1.24
3.50	.00	.56	-.30	.67	.72	-.37	.08	-1.26	-1.15	-.88	-1.02
3.50	.33	.08	.65	.39	.33	.47	.87	.33	.43	-.29	-.40
3.50	.67	.00	.11	.20	-	.02	-.19	.11	.19	.18	.45
3.50	1.33	.02	.74	.62	.39	.68	.59	.29	.66	-.12	.11
6.50	.50	.03	.35	.15	.02	.31	.30	.41	.50	.05	.29
6.50	.83	-.09	-.31	-.05	-.04	-.31	-.18	-.11	.07	.00	.03
6.50	1.17	.43	.23	.48	.46	.17	.49	-.91	-.84	-.80	-.81
8.50	.50	.02	.29	.14	-	.24	.29	.28	.31	-.18	.01
8.50	.83	-.04	-.15	.02	.00	-.15	-.12	-.02	.06	.07	.21
8.50	1.17	.34	.04	.33	.32	-	.40	-.64	-.57	-.58	-.60
8.50	1.83	-.02	.01	-.03	.05	-.11	-.02	.05	-.01	.06	.06
11.50	.00	.13	.00	.15	.16	-.07	.07	-.12	.09	-.05	.03
11.50	.33	.08	.34	.37	.24	.26	.36	-.26	.05	-.34	-.51
11.50	.67	-	.16	-.11	-.04	.05	.16	.29	.32	.13	.25

Table A5. Stanton Number Reduction for $\theta_i = 40.8^o$

	M	.51	.51	.74	.95	1.14	1.58
	θ_c	1.36	1.50	1.34	1.38	1.40	1.36
x/d_o	z/S						
1.50	.00	1.46	1.63	1.25	.97	.21	1.14
1.50	.33	1.24	.99	1.17	1.24	1.26	1.11
1.50	.67	.07	.08	.04	-.07	.07	.13
1.50	1.33	.47	.18	.88	1.11	1.20	1.05
3.50	.00	.13	.34	.04	-.11	-.63	-1.86
3.50	.33	.49	.60	.50	.51	.59	.62
3.50	.67	-.12	.15	-.06	-.01	.14	.34
3.50	1.33	.72	.63	.67	.81	.73	.66
6.50	.50	.35	.25	.41	.49	.68	.42
6.50	.83	-	-.38	-	-	-	-
6.50	1.17	-.03	.24	-.01	.12	-.01	-1.22
8.50	.50	.24	.12	.24	.38	.57	.29
8.50	.83	-	-.17	-	-	-	-
8.50	1.17	-.11	.15	-.13	-.17	-.42	-1.15
8.50	1.83	.06	-.33	-.06	.20	-.06	.40
11.50	.00	.07	.07	.07	-.04	-.01	.01
11.50	.33	.30	.27	.45	.33	.38	-.06
11.50	.67	-	-.11	.05	.17	.28	.47

Table A6. Spanwise Averaged Stanton Number Reduction

a) $\theta_i = 5.0^0$

M	2.01	2.99	5.17	10.23
θ_c	1.29	1.29	1.32	1.38
x/d_0				
1.50	.28	.10	-.08	-.47
3.50	.11	.04	-.25	-.39
6.50	.16	.06	-.05	-.23
8.50	.09	.05	-.04	-.17
11.50	.10	.09	-.12	-.09

c) $\theta_i = 40.8^0$

M	.51	.51	.74	.95	1.14	1.58
θ_c	1.36	1.50	1.34	.138	1.40	1.36
x/d_0						
1.50	.92	.90	.82	.71	.51	.79
3.50	.16	.37	.16	.13	.03	-.03
6.50	-	.04	-	-	-	-
8.50	.06	.03	.02	.14	.03	-.16
11.50	-	.08	.19	.15	.21	.14

b) $\theta_i = 22.9^0$

M	.25	.74	.74	.75	.124	1.22	2.06	2.08	.246	2.44
θ_c	1.18	1.33	1.45	1.44	1.30	1.56	1.29	1.36	1.29	1.39
x/d_0										
1.50	.27	-	-	.71	.54	-	.50	.71	-.26	.69
3.50	.21	.15	.42	-	.04	.25	-.28	-.17	-.33	-.32
6.50	.12	.06	.19	.15	.06	.20	-.20	-.09	-.25	-.17
8.50	.11	.05	.17	-	-	.19	-.13	-.07	-.23	-.13
11.50	-	.17	.14	.12	.08	.20	-.03	.15	-.09	-.08

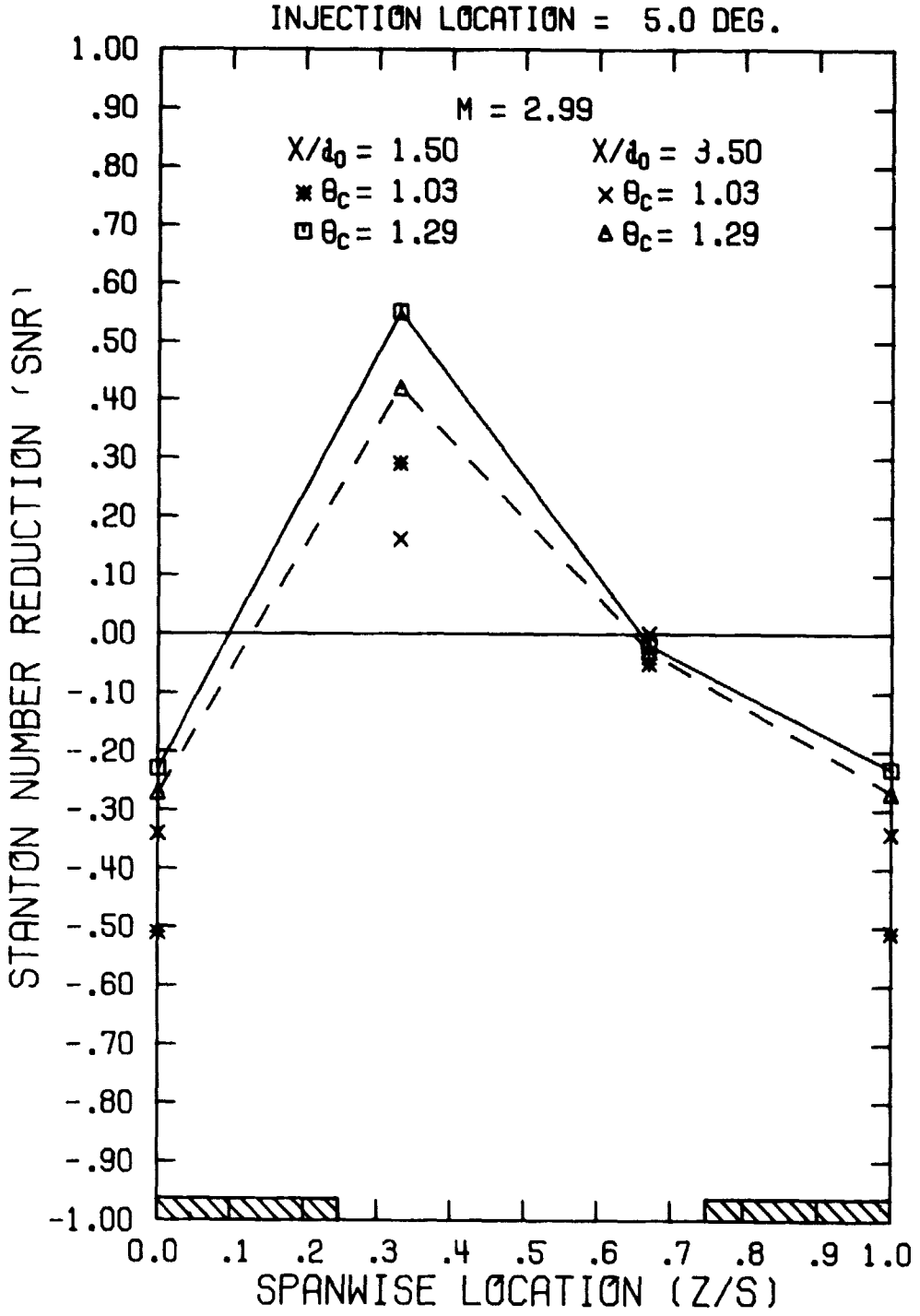

Figure A15. Spanwise Variation in Stanton Number Reduction (θ_i=5.0°, M=2.99, x/d_o=1.50 and 3.50)

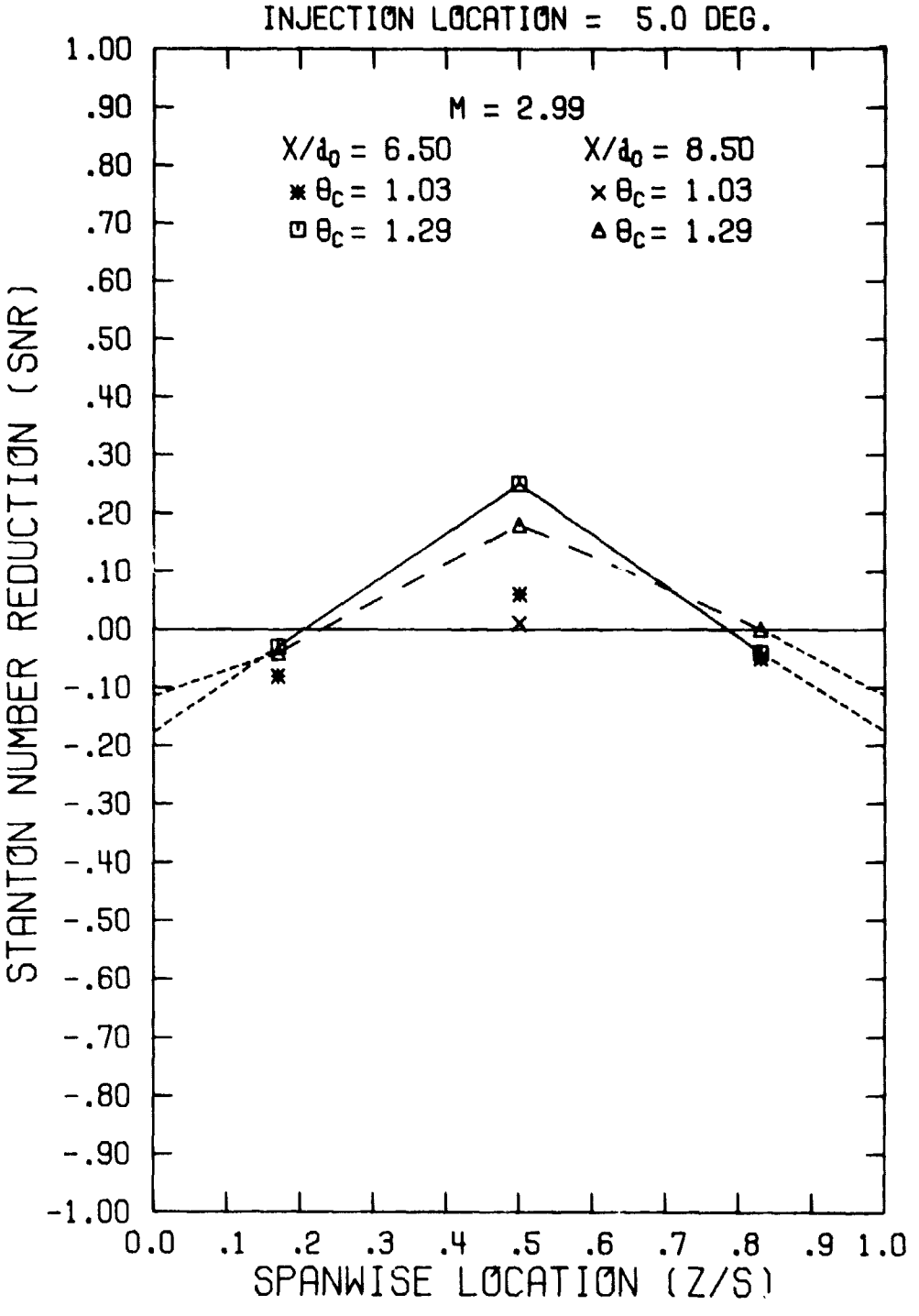

Figure A16. Spanwise Variation in Stanton Number Reduction (θ_i=5.0°, M=2.99, x/d_o=6.50 and 8.50)

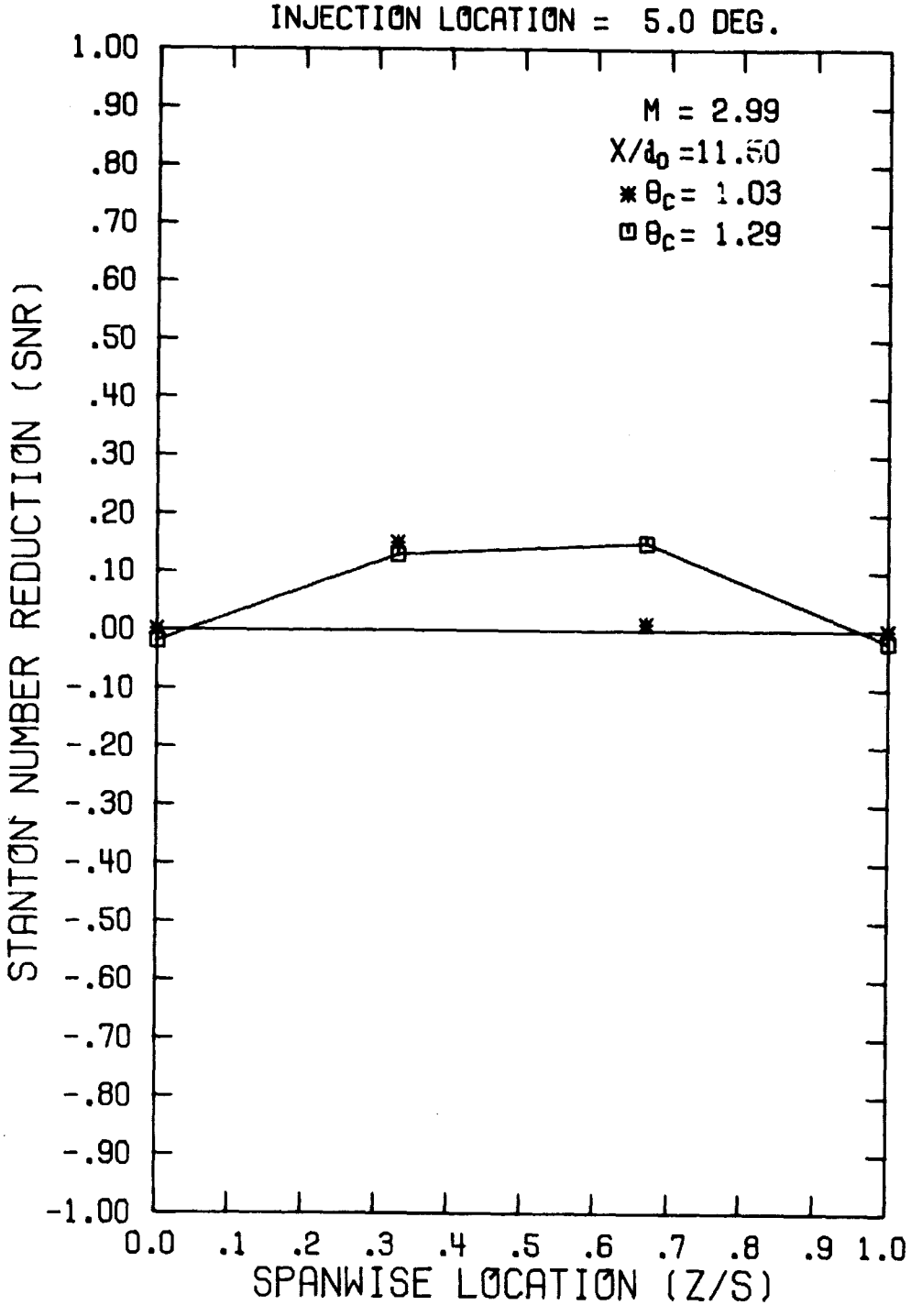

Figure A17. Spanwise Variation in Stanton Number Reduction (θ_i=5.0°, M=2.99, x/d_o=11.50)

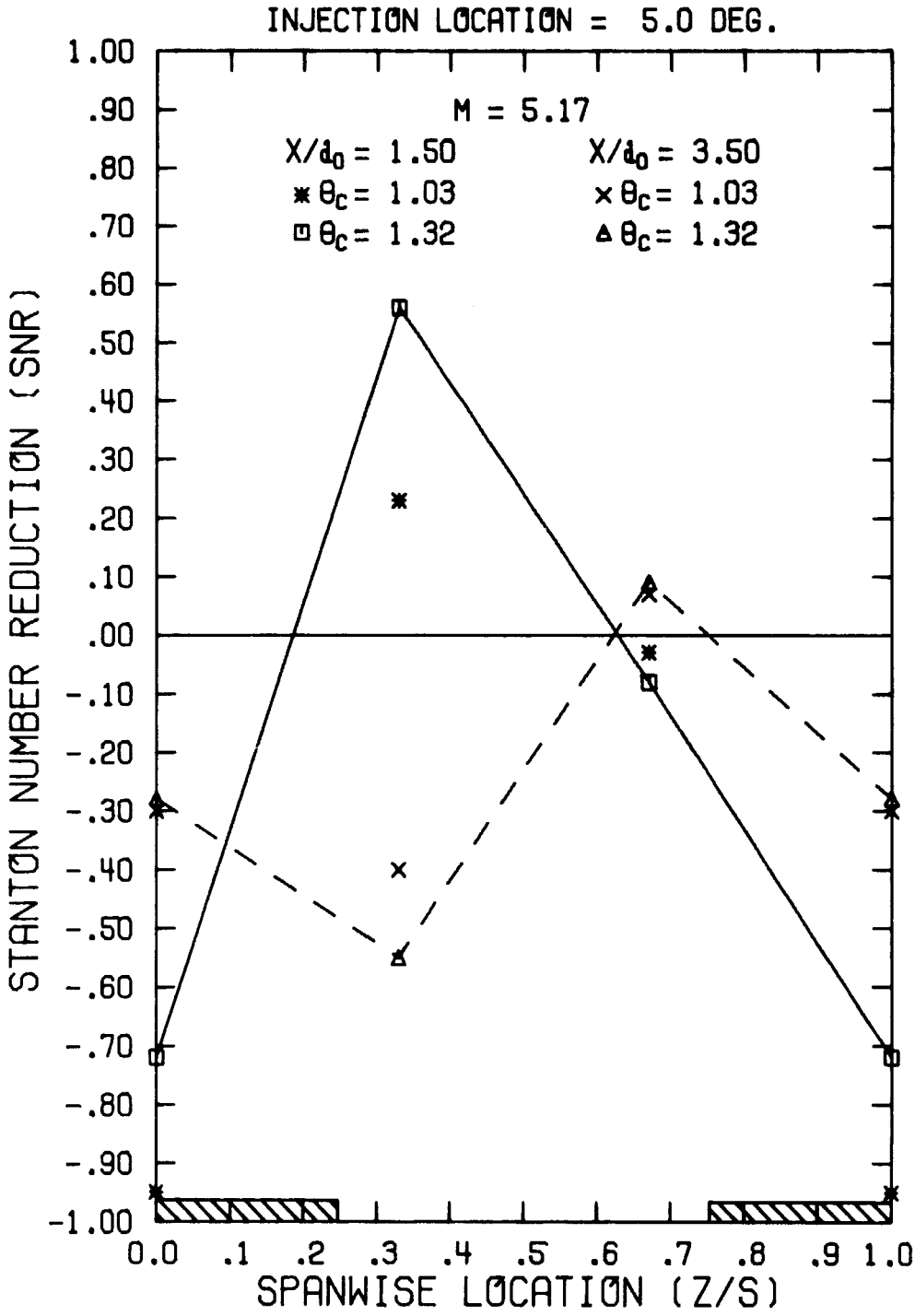

Figure A18. Spanwise Variation in Stanton Number Reduction (θ_i=5.0°, M=5.17, x/d_o=1.50 and 3.50)

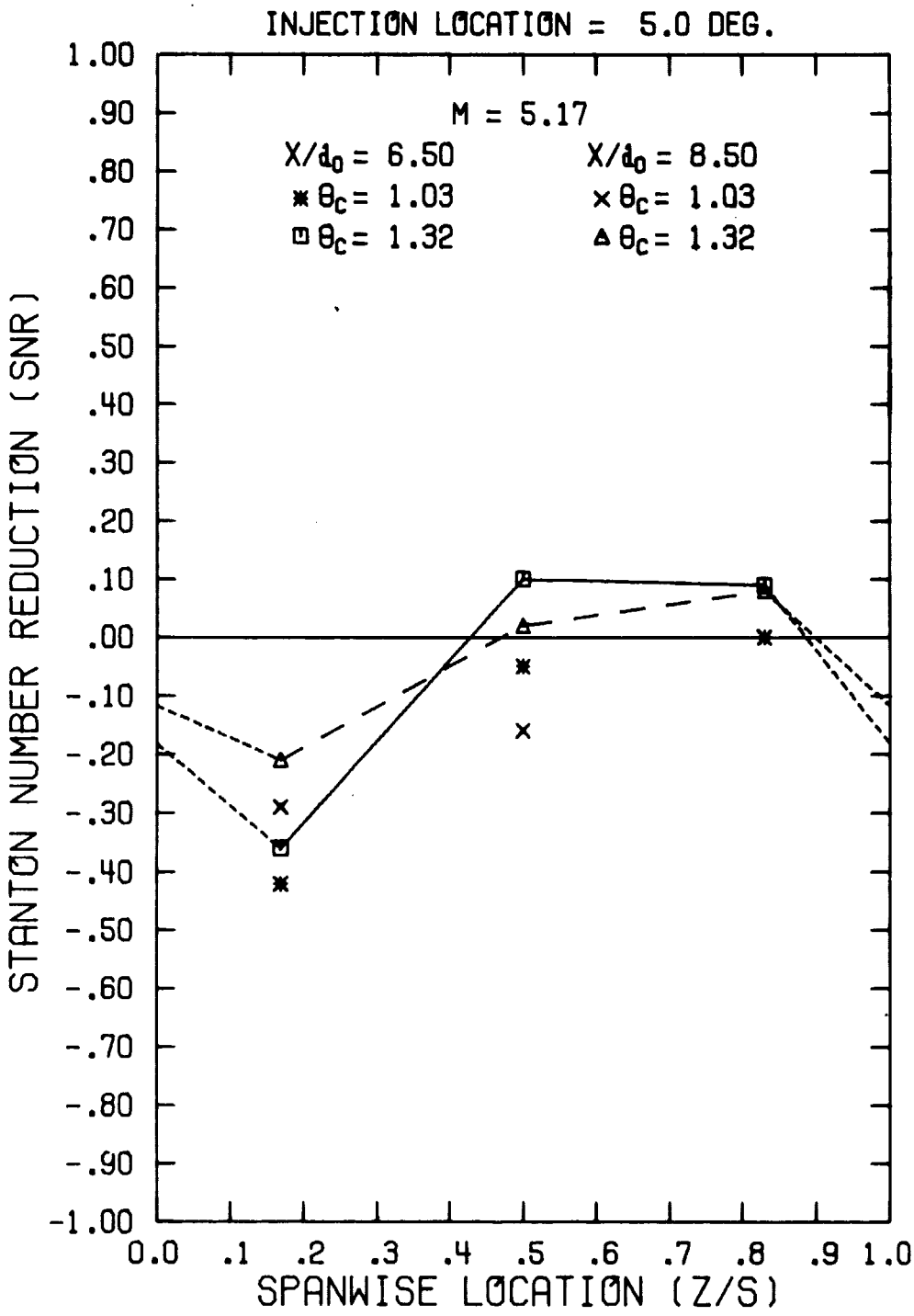

Figure A19. Spanwise Variation in Stanton Number Reduction (θ_i=5.0°, M=5.17, x/d_0=6.50 and 8.50)

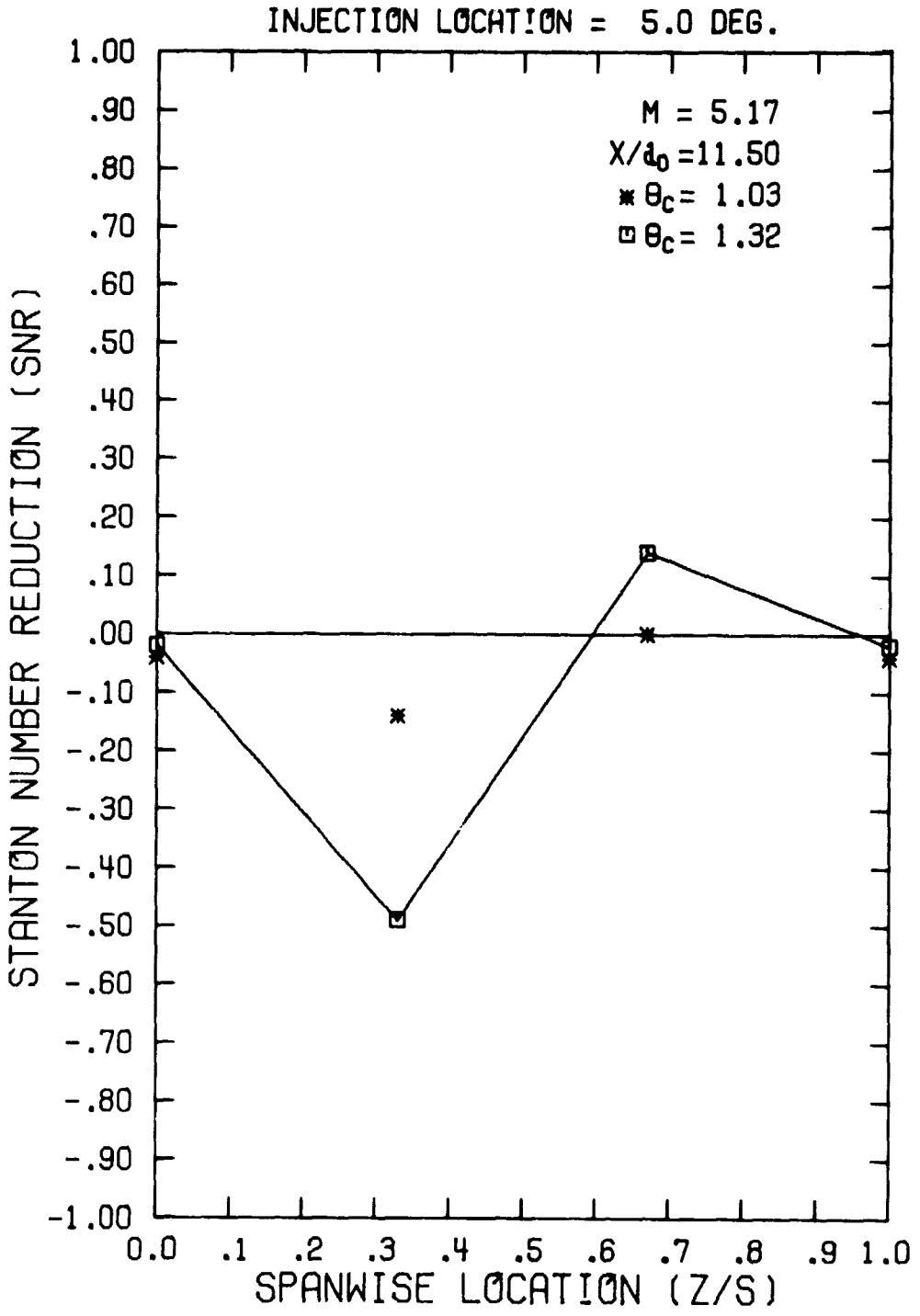

Figure A20. Spanwise Variation in Stanton Number Reduction (θ_j=5.0°, M=5.17, x/d_0=11.50)

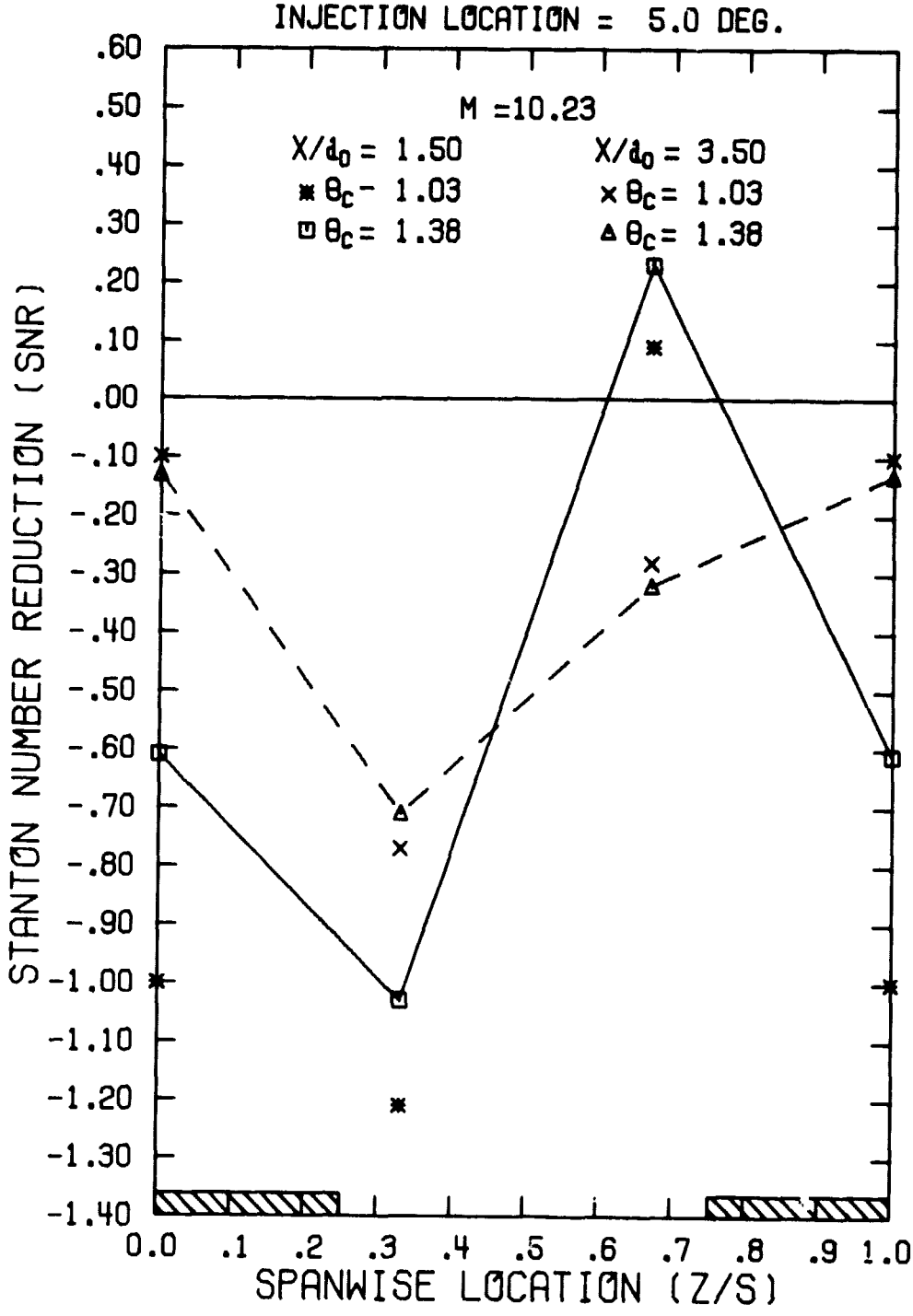

Figure A21. Spanwise Variation in Stanton Number Reduction (θ_i=5.0°, M=10.23, x/d_o=1.50 and 3.50)

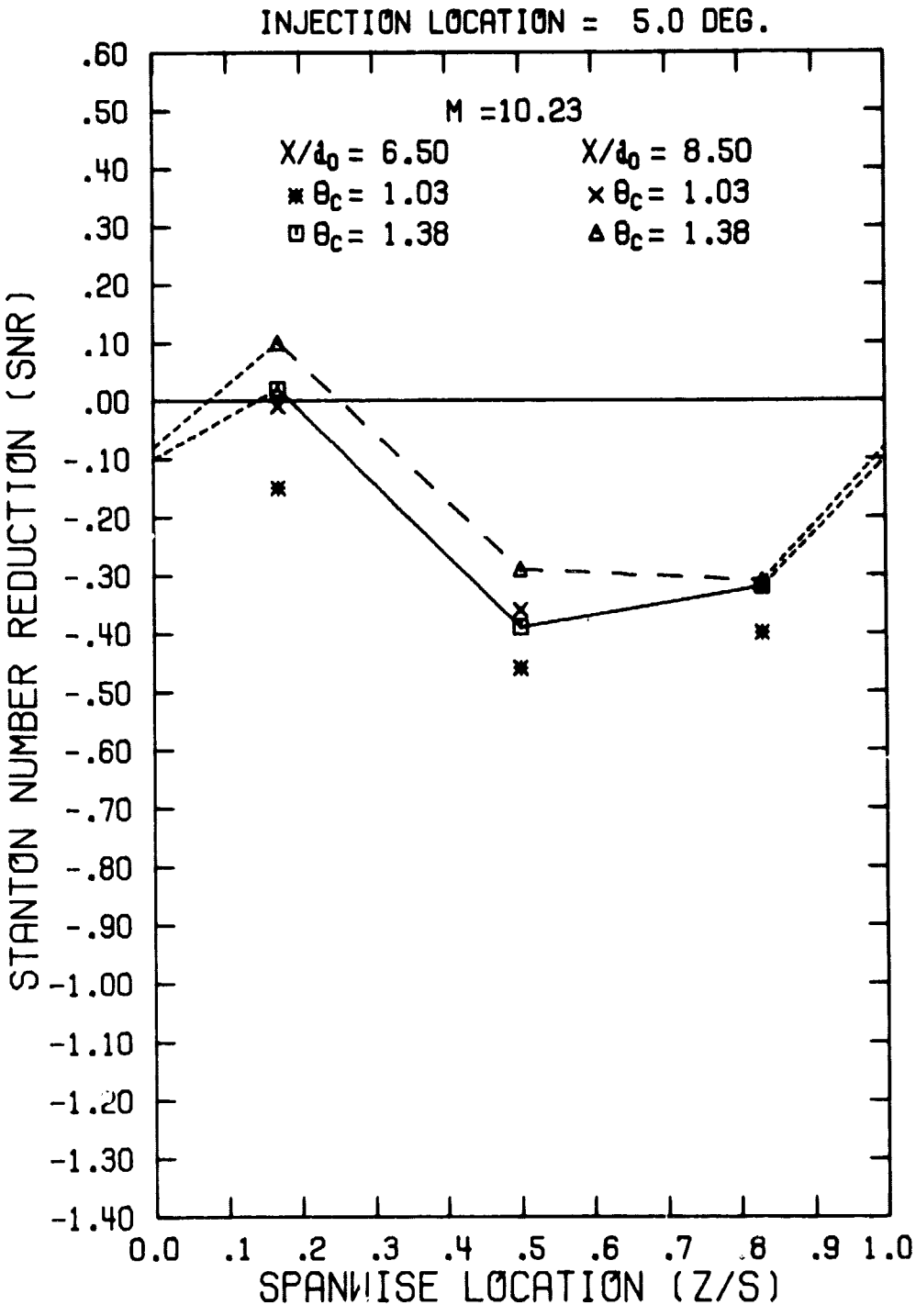

Figure A22. Spanwise Variation in Stanton Number Reduction (θ_i=5.0°, M=10.23, x/d_o=6.50 and 8.50)

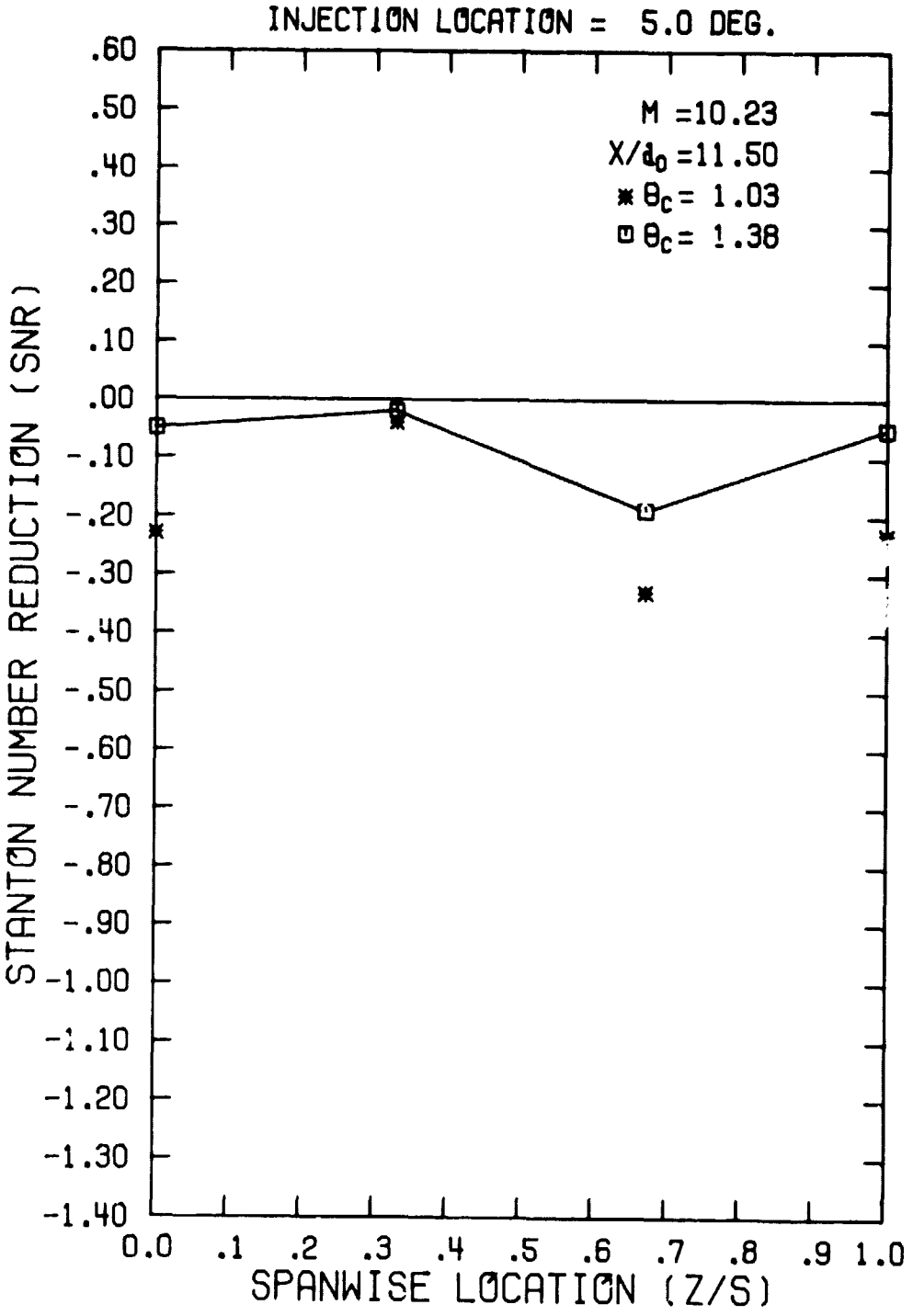

Figure A23. Spanwise Variation in Stanton Number Reduction (θ_i=5.0°, M=10.23, x/d_o=11.50)

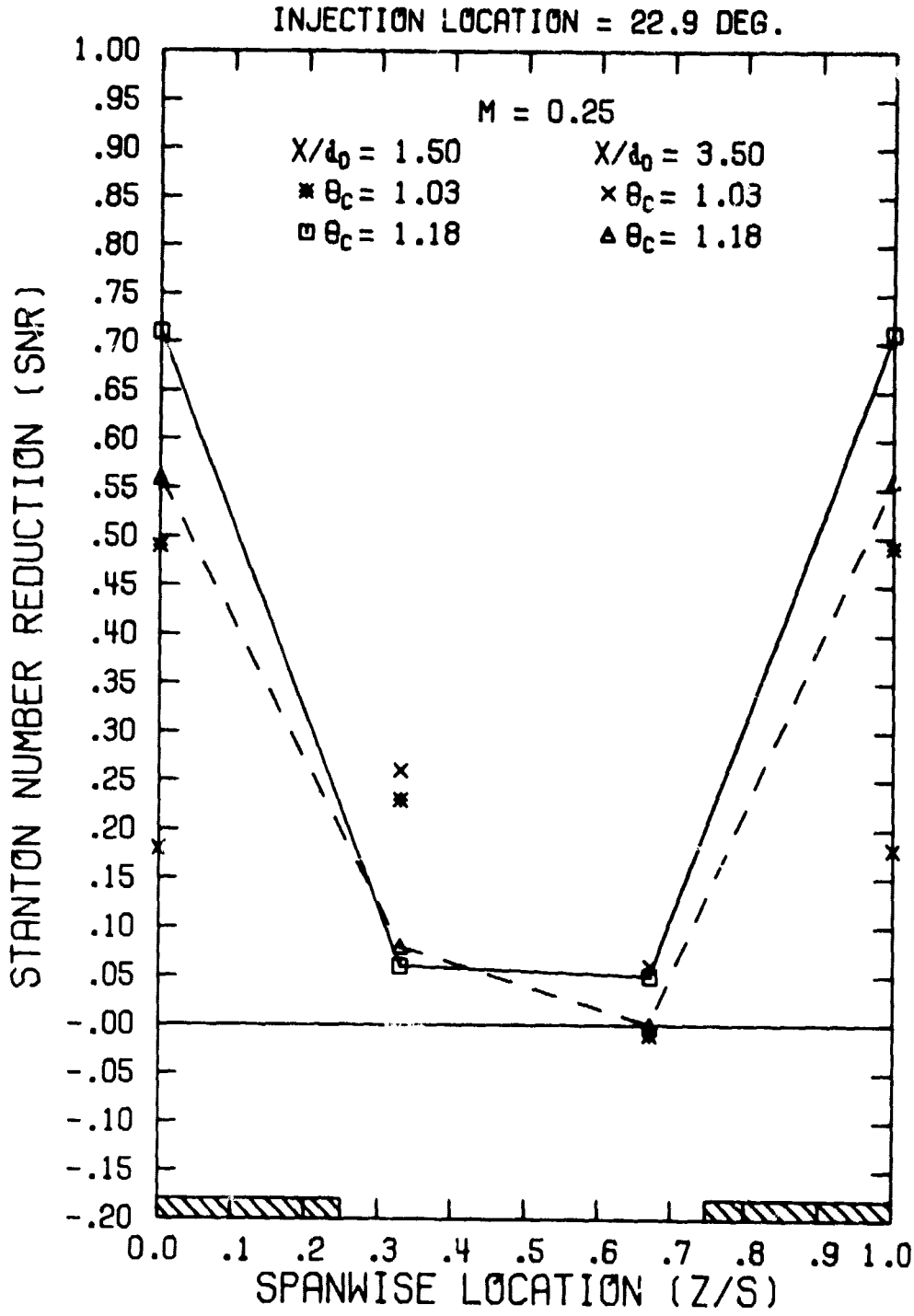

Figure A24. Spanwise Variation in Stanton Number Reduction (θ_i=22.9°, M=0.25, x/d_o=1.50 and 3.50)

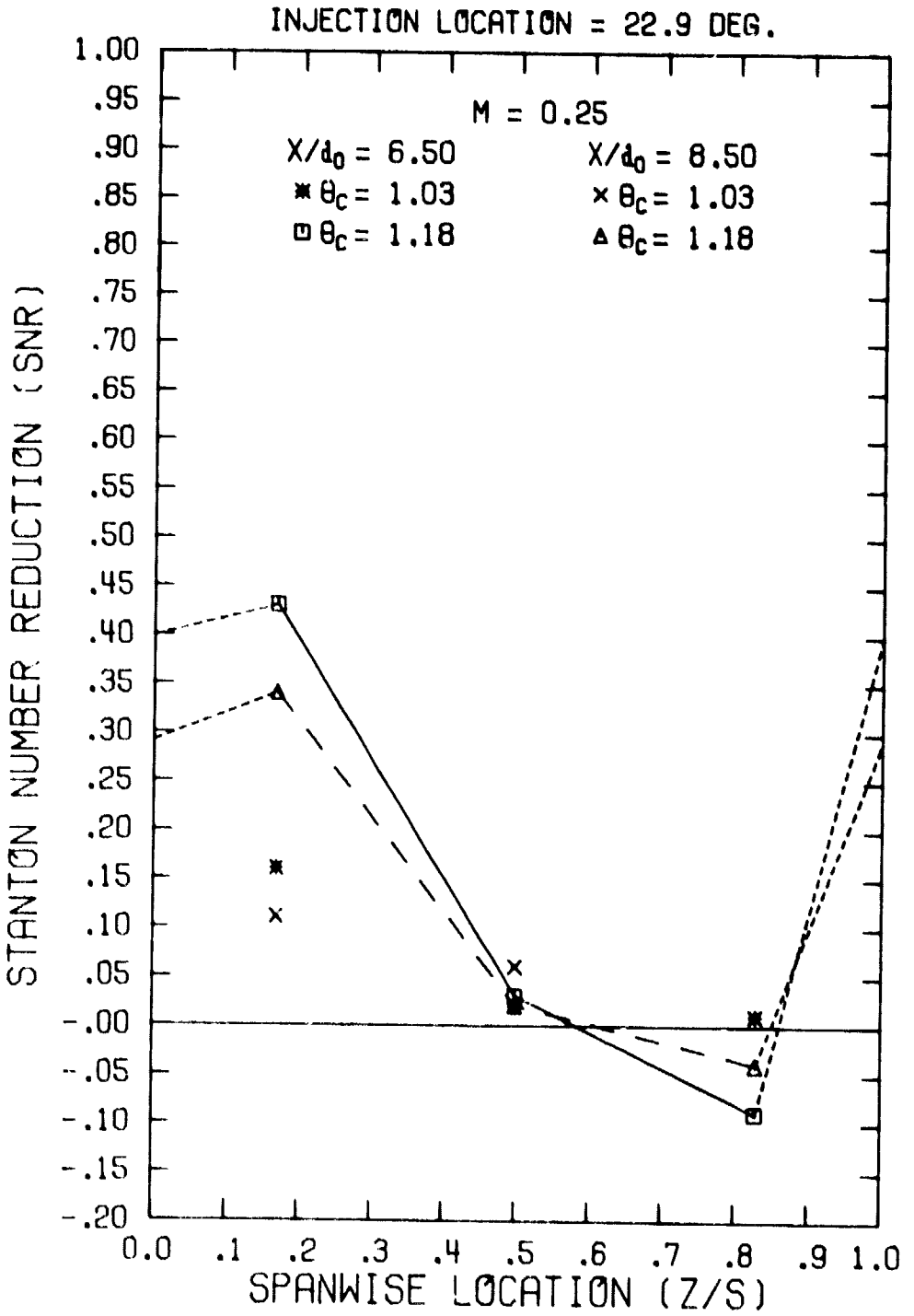

Figure A25. Spanwise Variation in Stanton Number Reduction (α_i=22.9°, M=0.25, x/d_0=6.50 and 8.50)

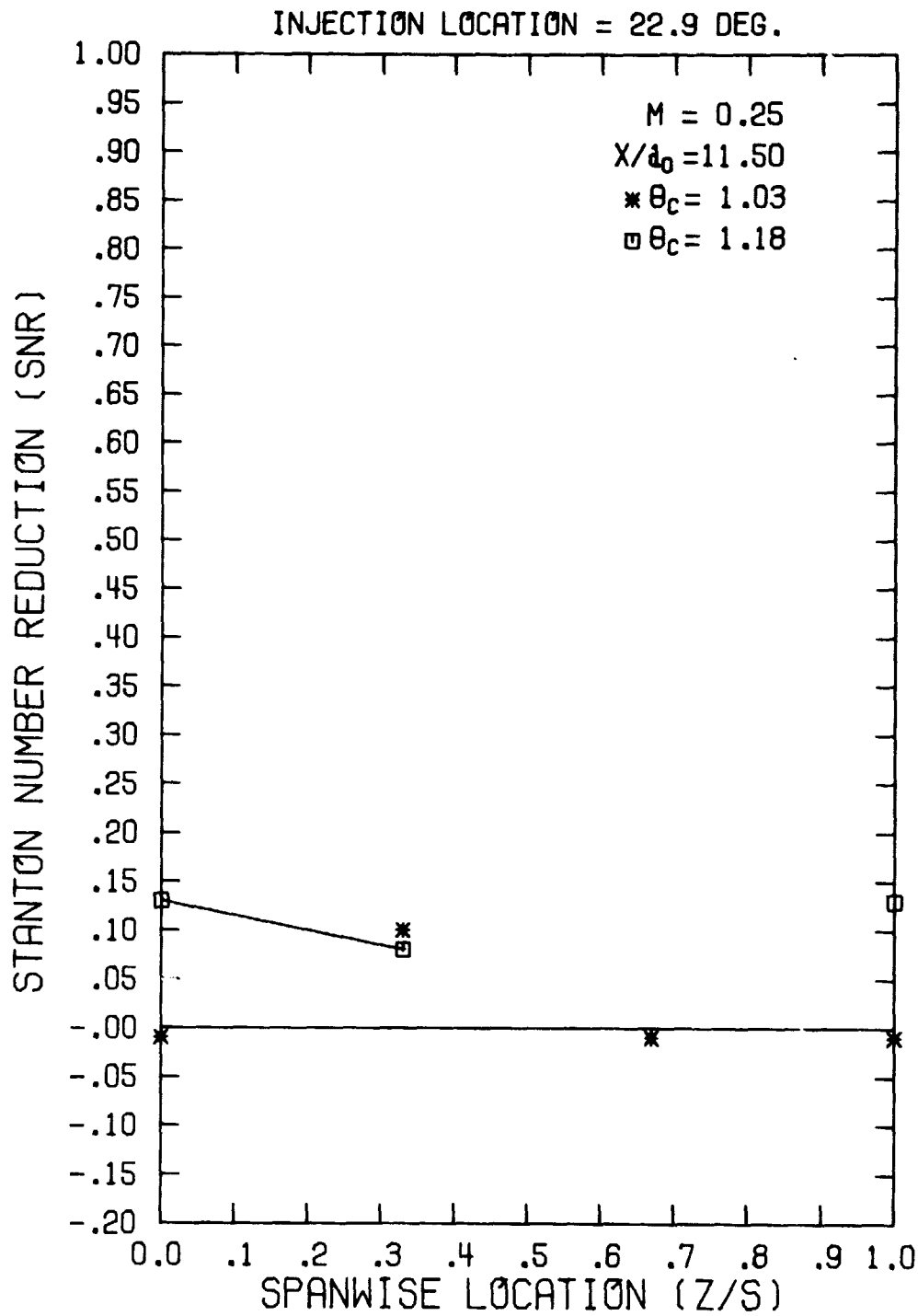

Figure A26. Spanwise Variation in Stanton Number Reduction (θ_i=22.9°, M=0.25, x/d_0=11.50)

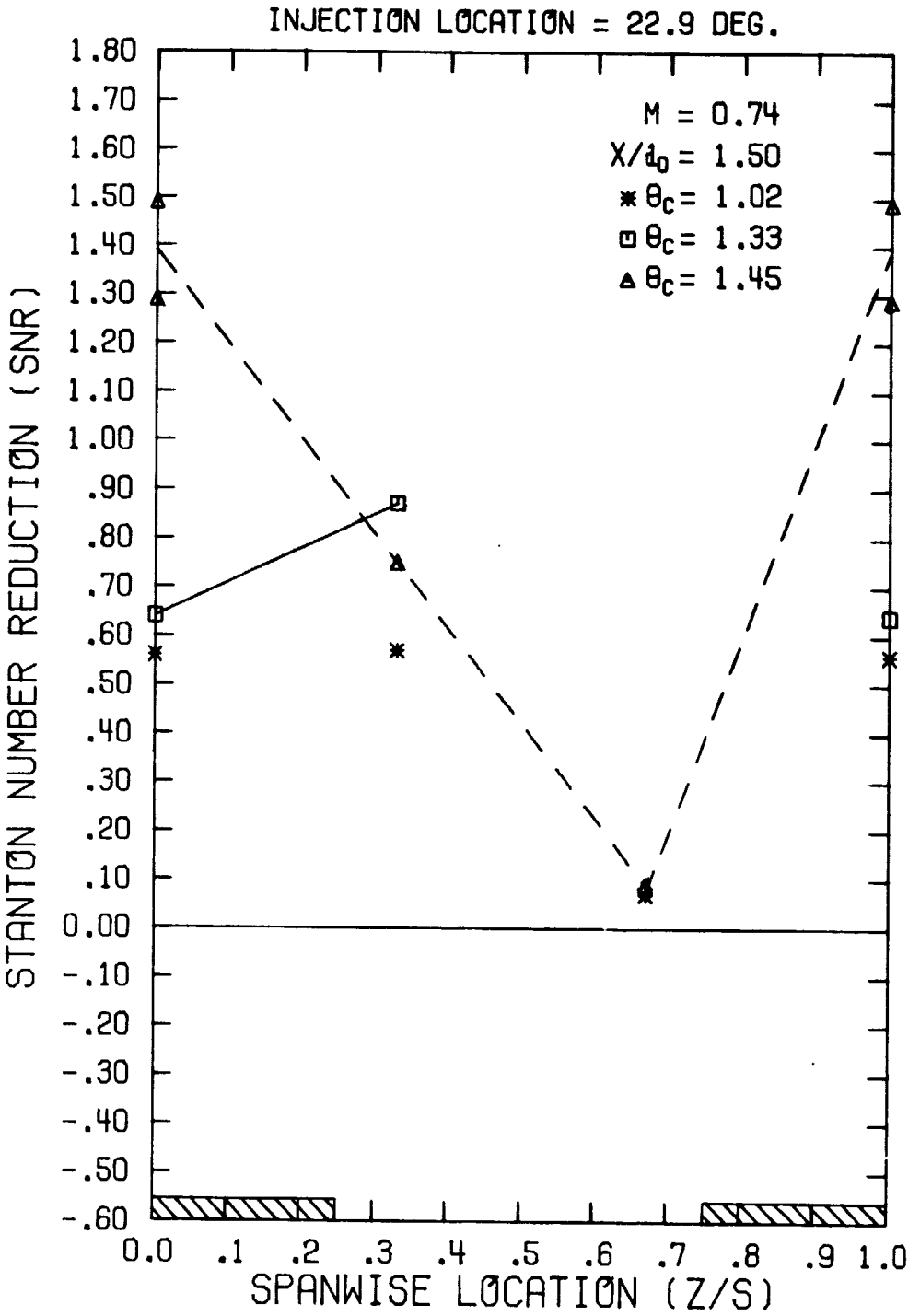

Figure A27. Spanwise Variation in Stanton Number Reduction (θ_i=22.9°, M=0.74, x/d_o=1.50)

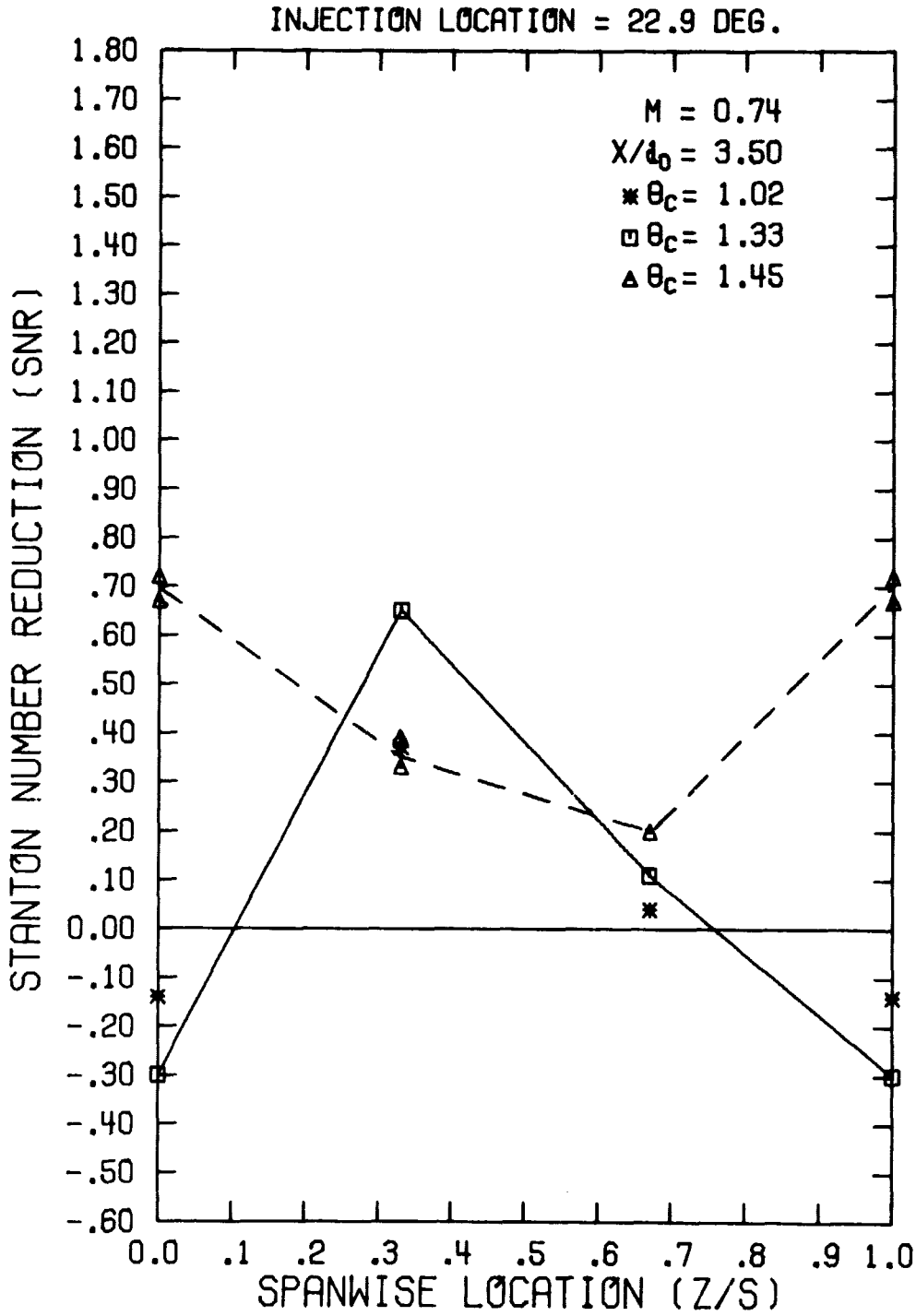

Figure A28. Spanwise Variation in Stanton Number Reduction (θ_i=22.9°, M=0.74, x/d_0=3.50)

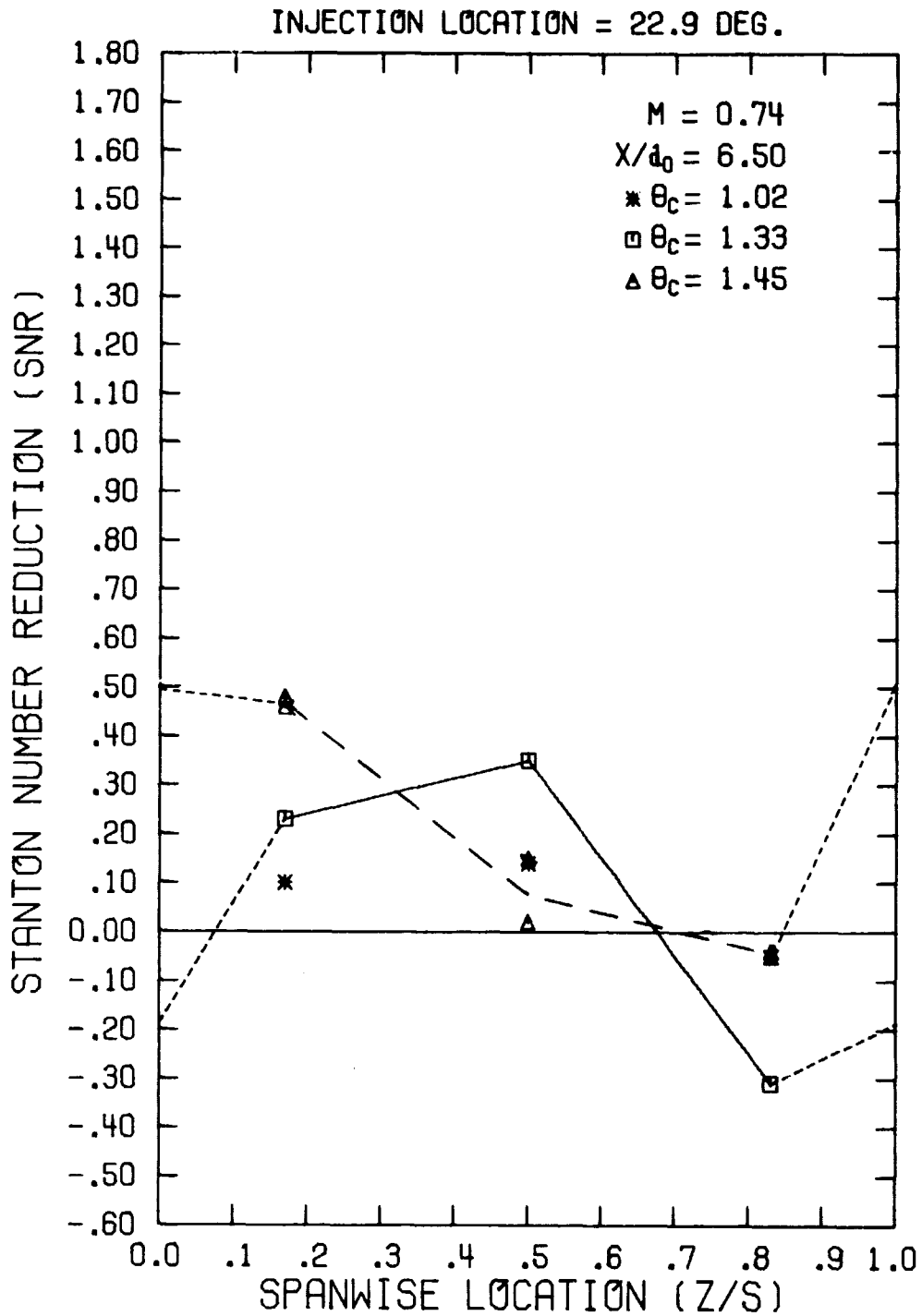

Figure A29. Spanwise Variation in Stanton Number Reduction (θ_i=22.9°, M=0.74, x/d_o=6.50)

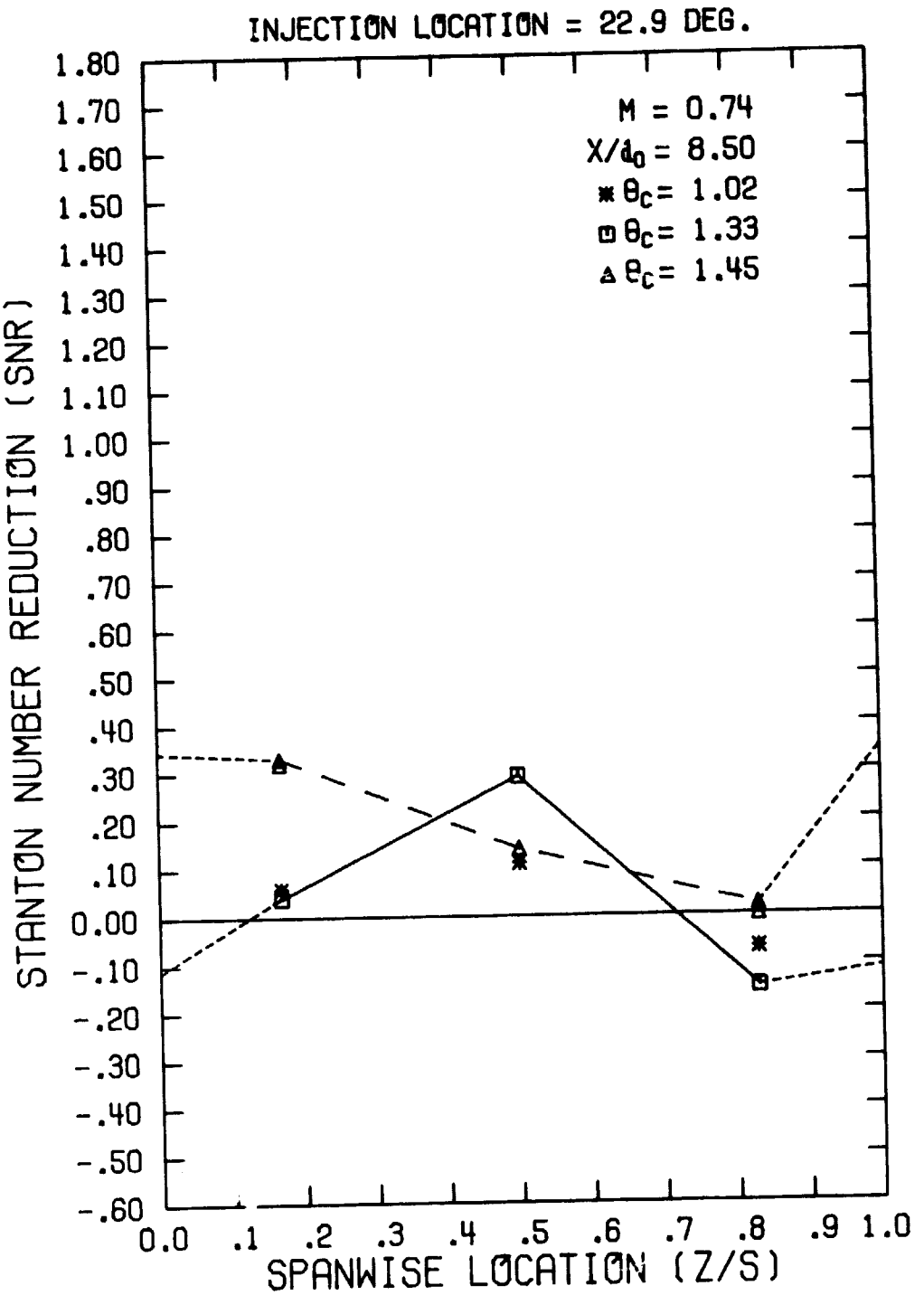

Figure A30. Spanwise Variation in Stanton Number Reduction (θ_i=22.9°, M=0.74, x/d_0=8.50)

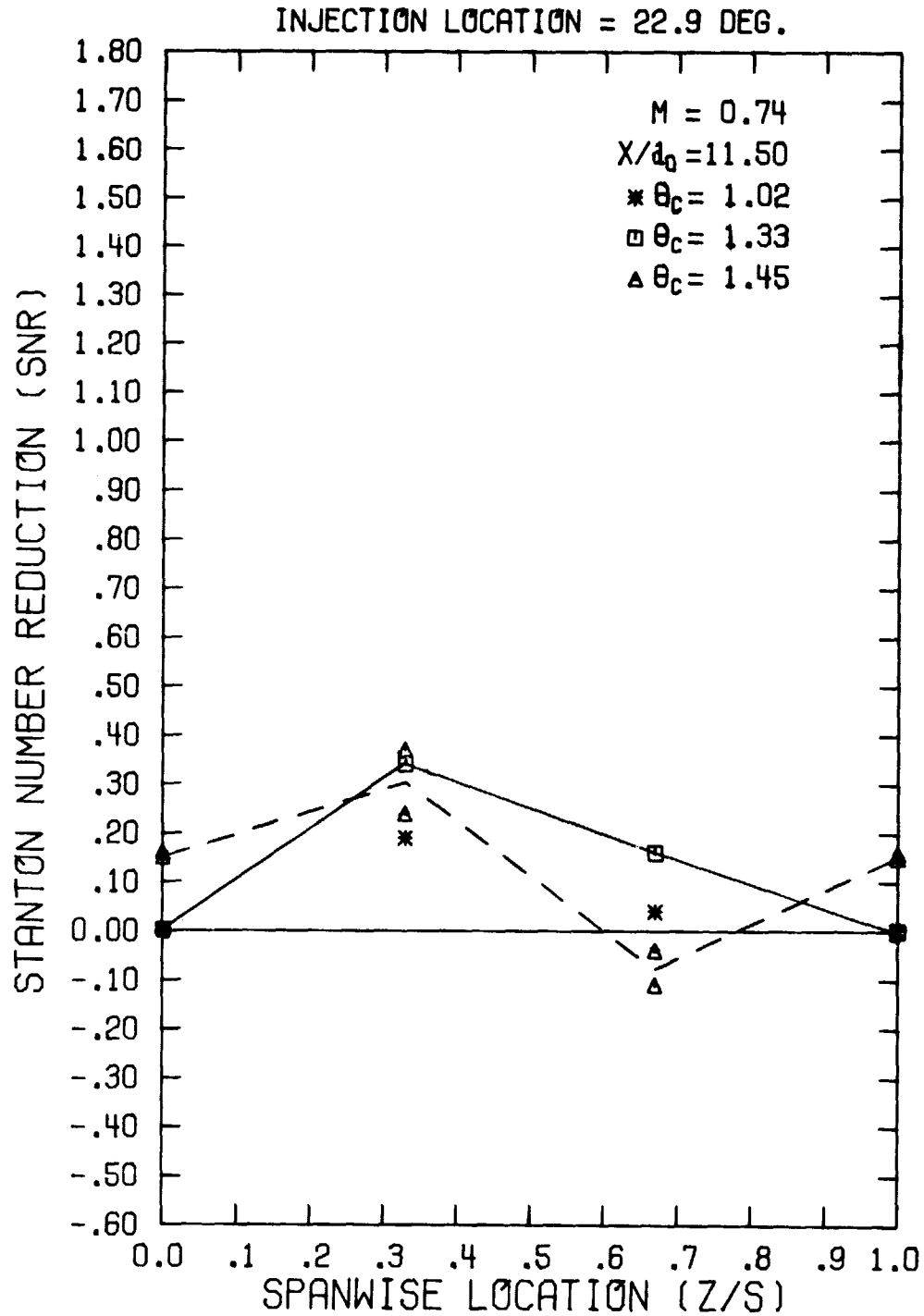

Figure A31. Spanwise Variation in Stanton Number Reduction (θ_i=22.9°, M=0.74, x/d_o=11.50)

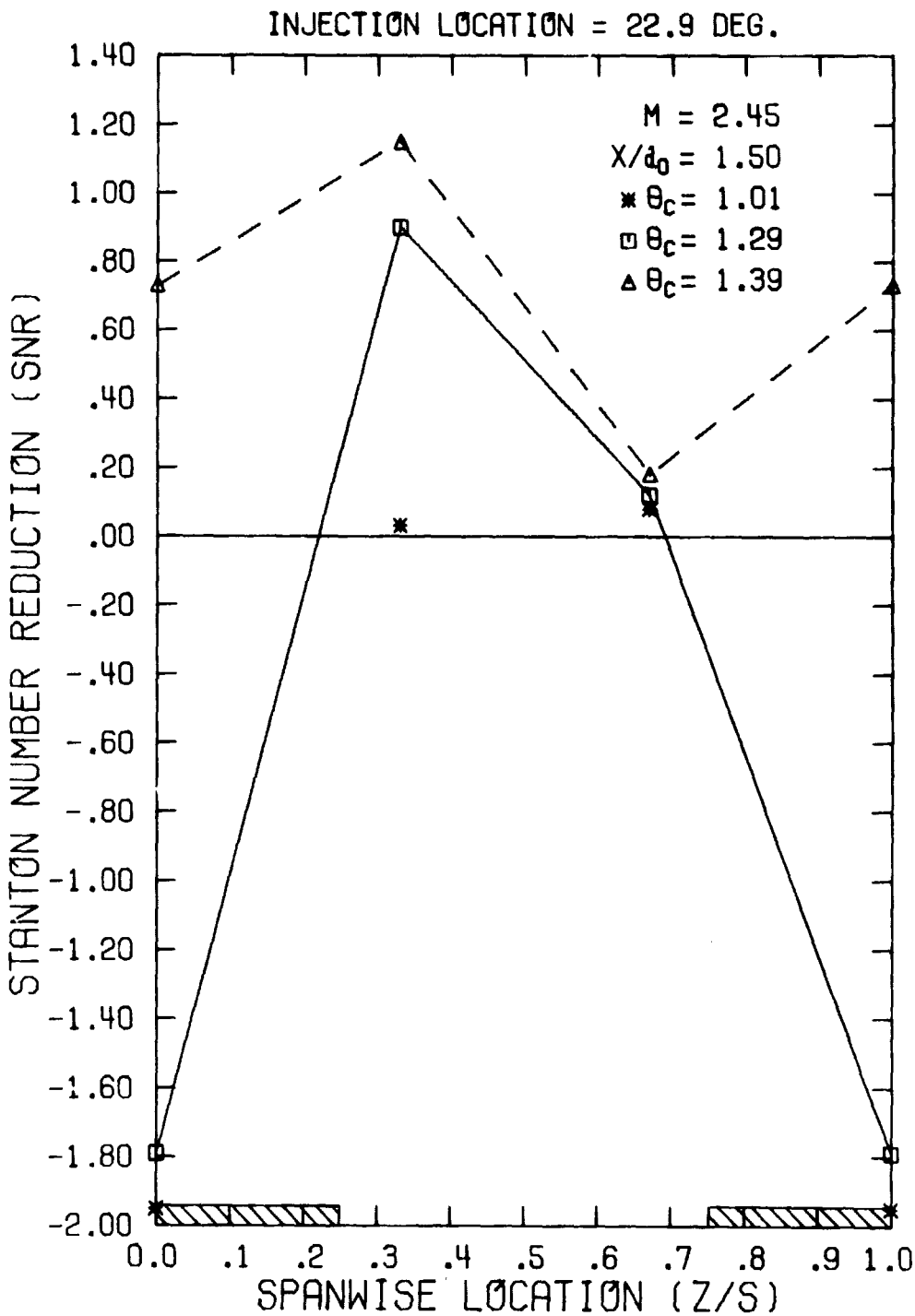

Figure A32. Spanwise Variation in Stanton Number Reduction (θ_i=22.9°, M=2.45, x/d_0=1.50)

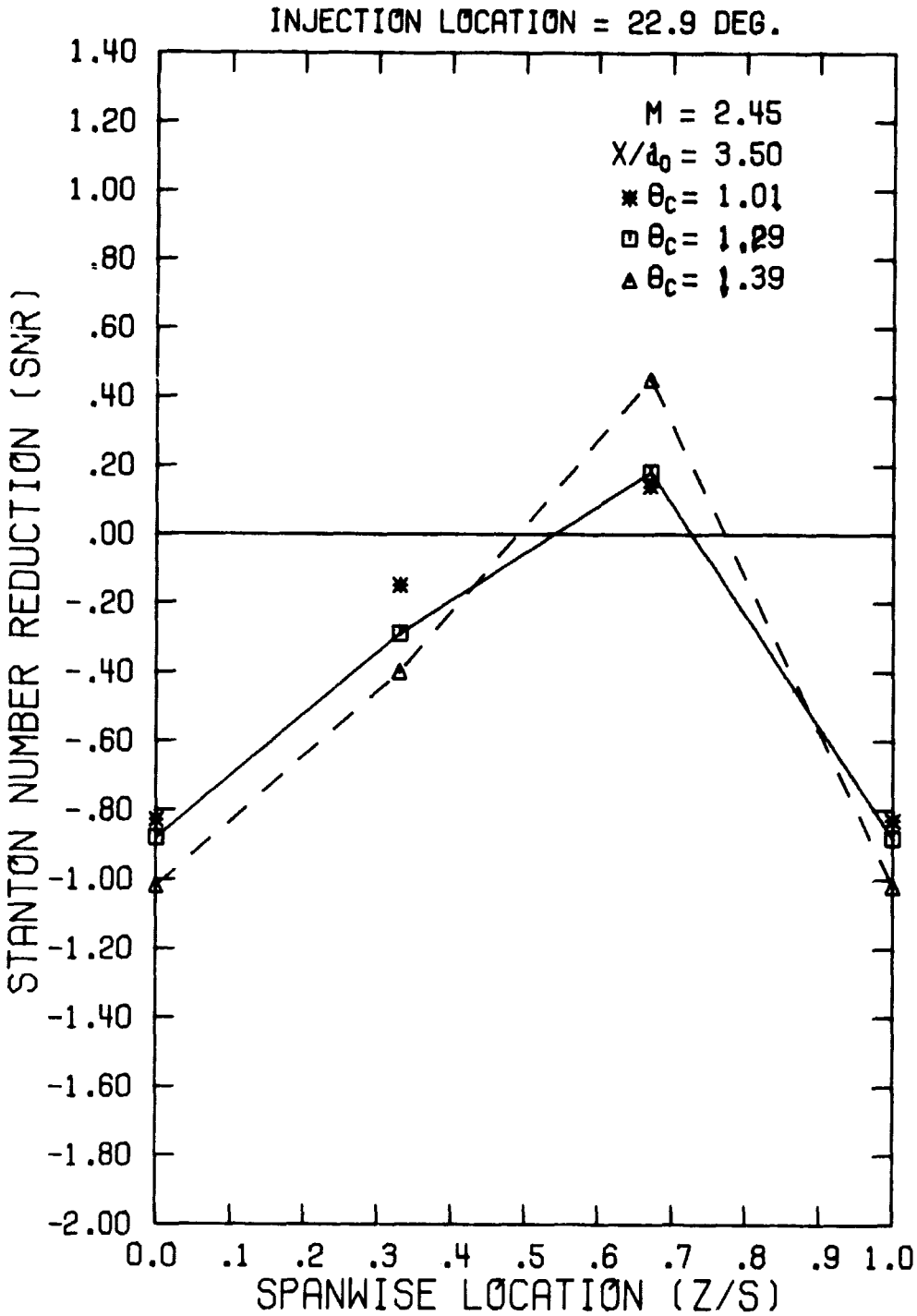

Figure A33. Spanwise Variation in Stanton Number Reduction (θ_i=22.9°, M=2.45, x/d_0=3.50)

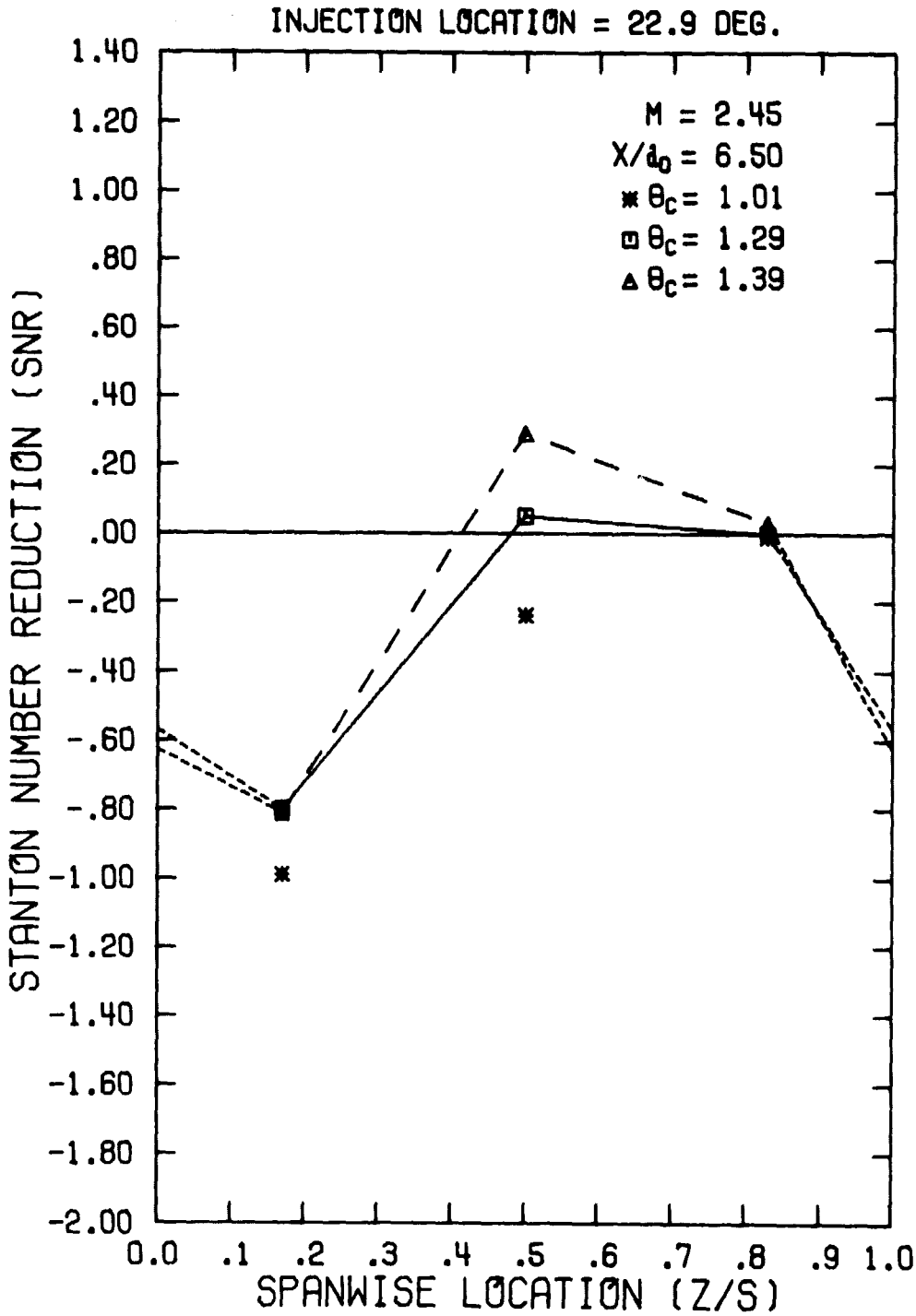

Figure A34. Spanwise Variation in Stanton Number Reduction (θ_i=22.9°, M=2.45, x/d_o=6.50)

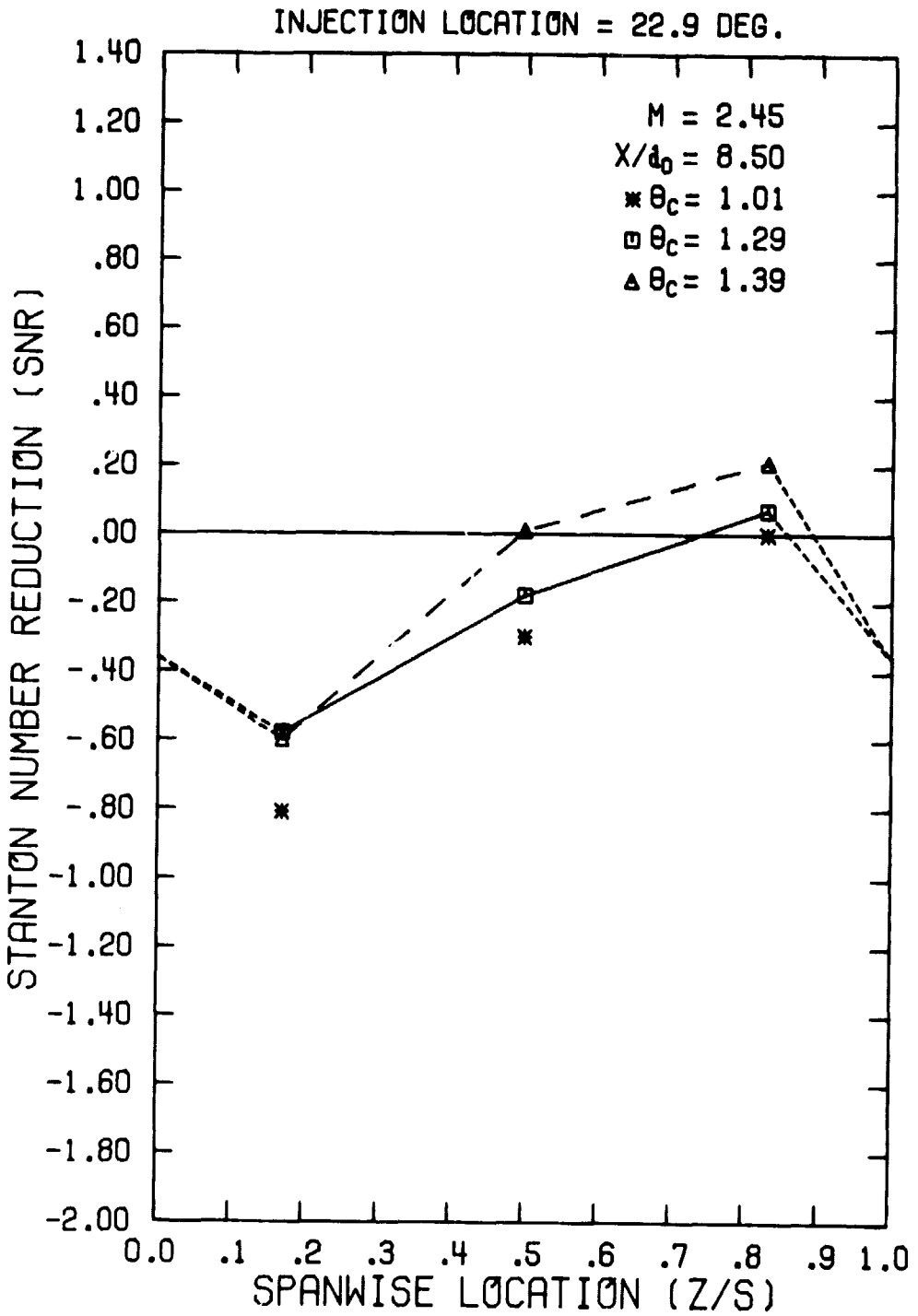

Figure A35. Spanwise Variation in Stanton Number Reduction (θ_i=22.9°, M=2.45, x/d_0=8.50)

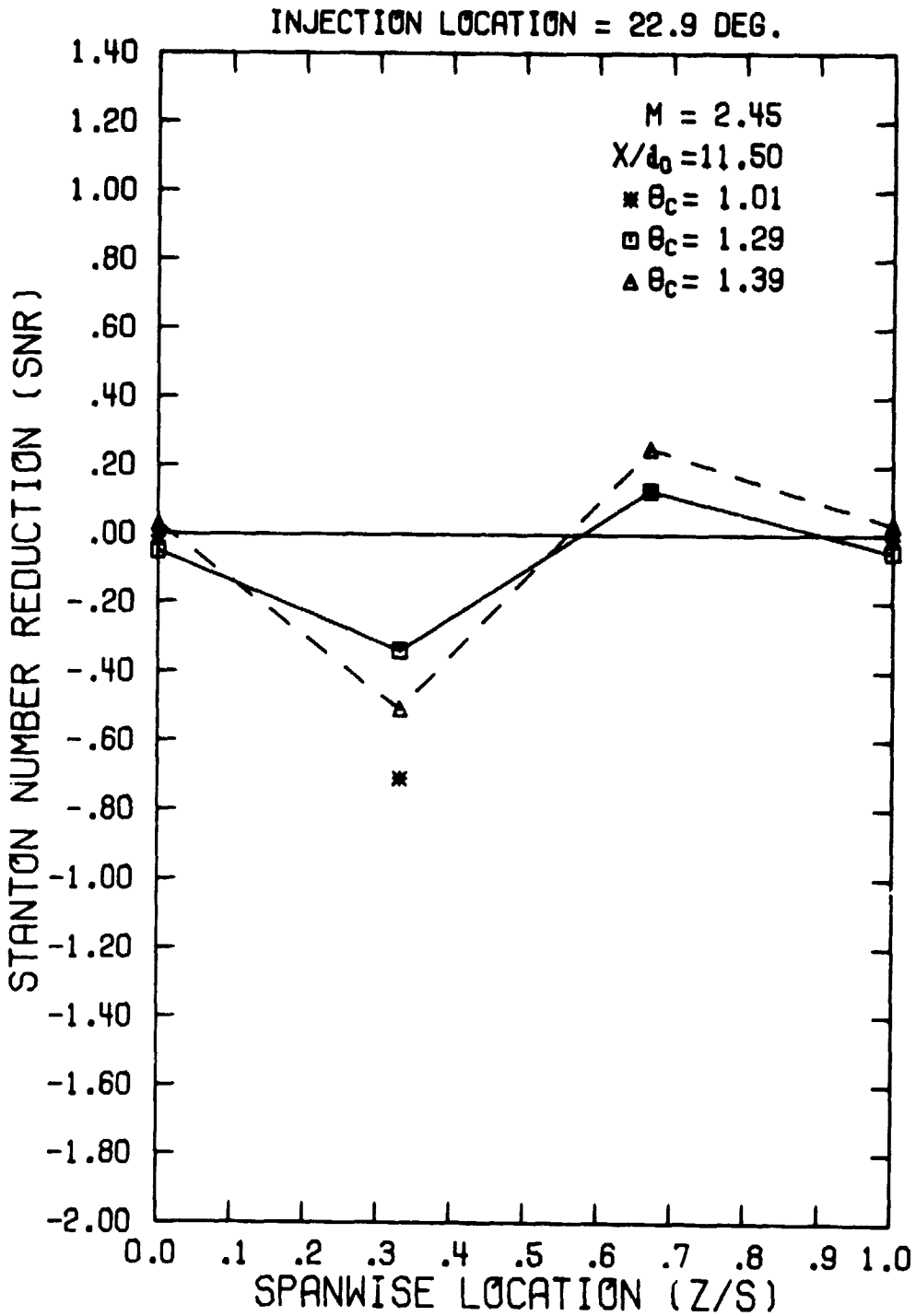

Figure A36. Spanwise Variation in Stanton Number Reduction (θ_j=22.9°, M=2.45, x/d_0=11.50)

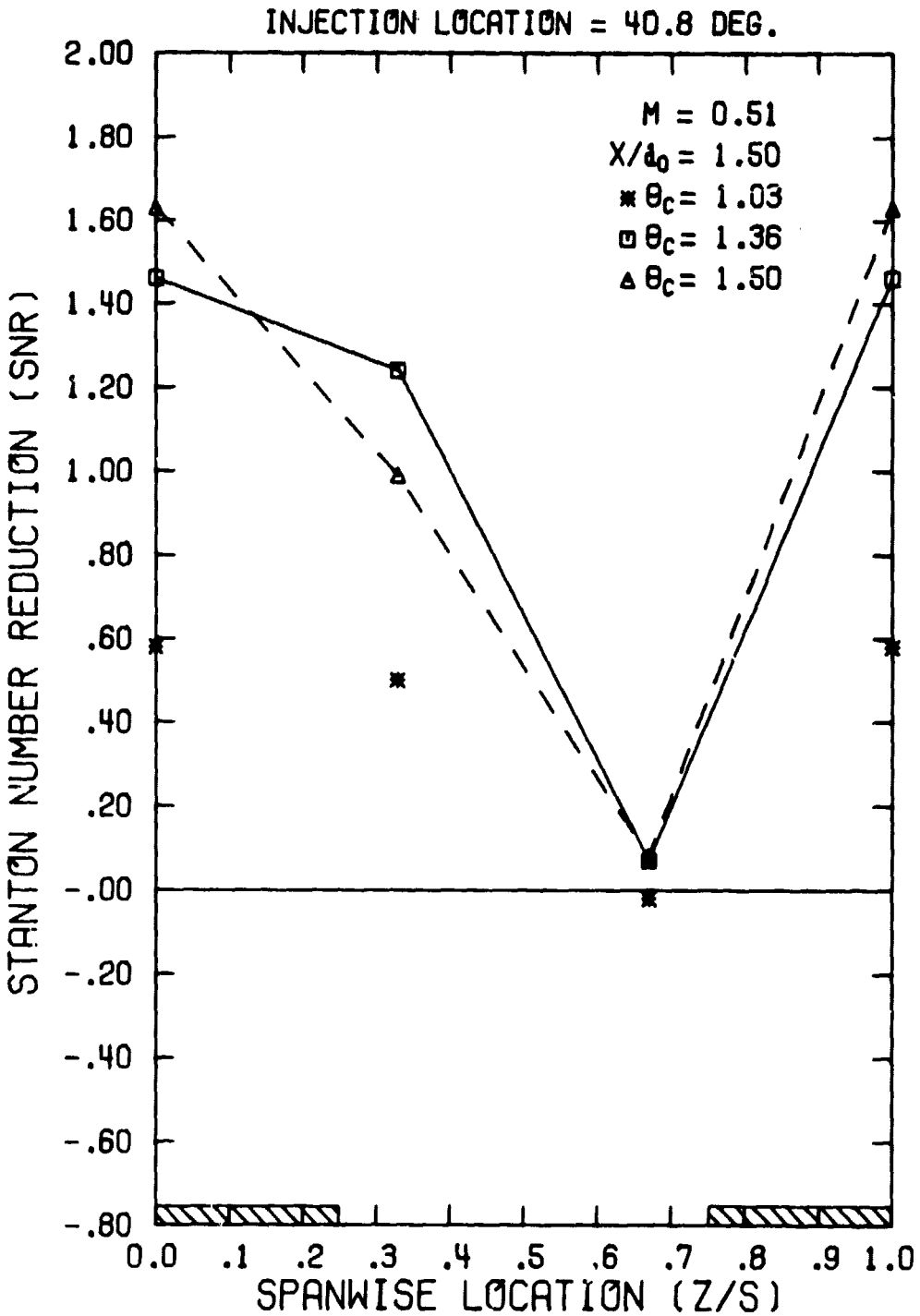

Figure A37. Spanwise Variation in Stanton Number Reduction (θ_i=40.8°, M=0.51, x/d_0=1.50)

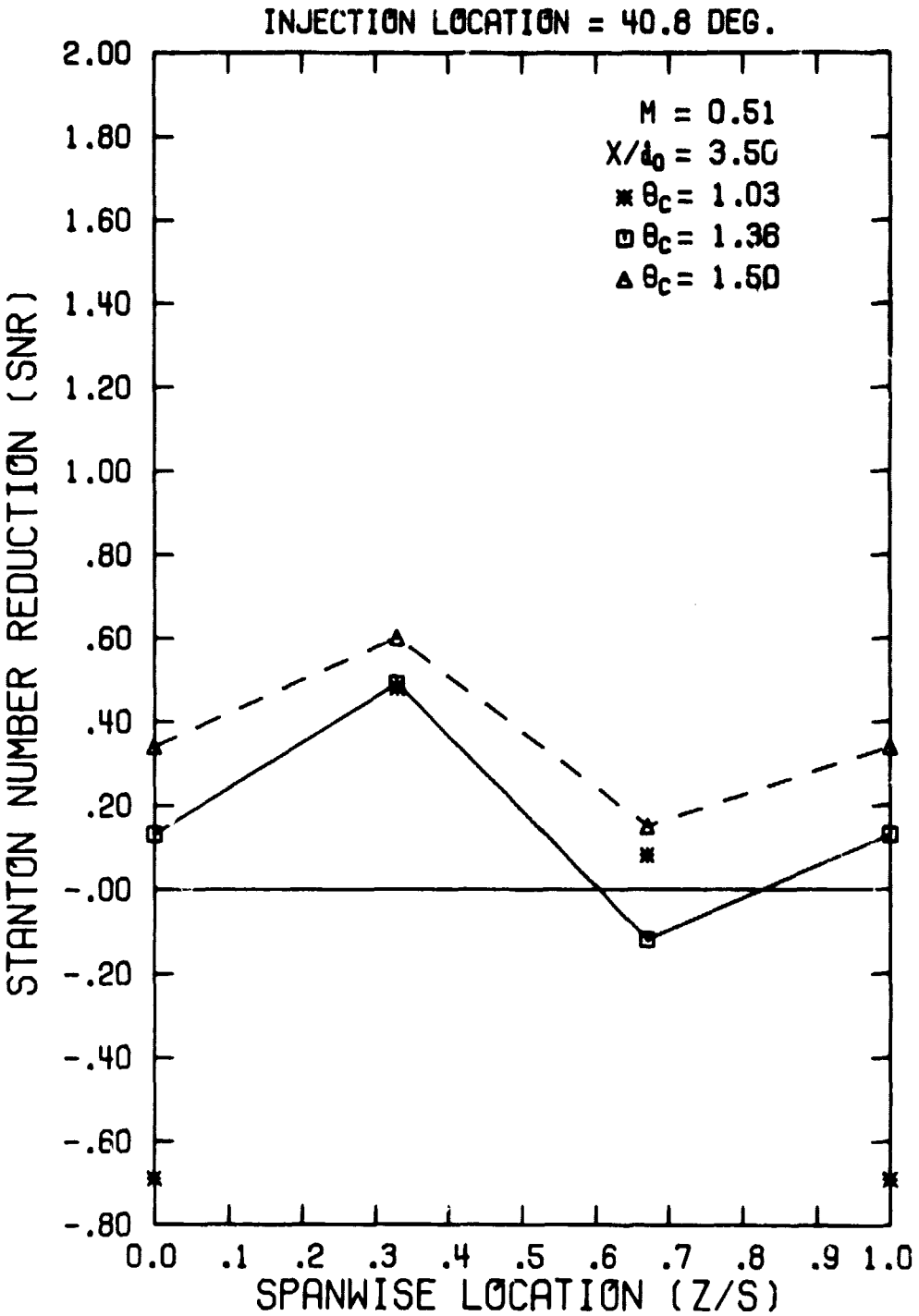

Figure A38. Spanwise Variation in Stanton Number Reduction (θ_i=40.8°, M=0.51, x/d_0=3.50)

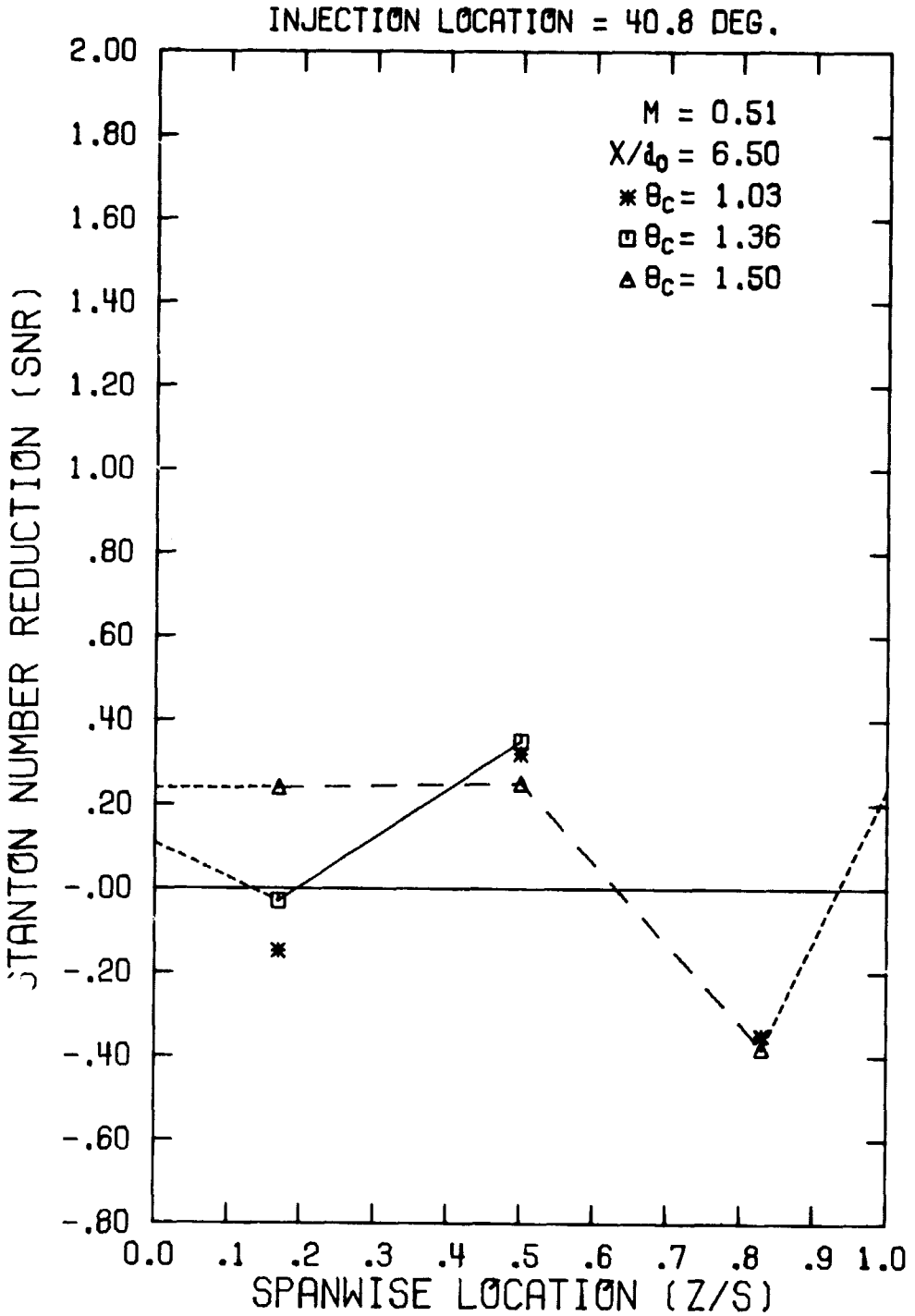

Figure A39. Spanwise Variation in Stanton Number Reduction (θ_i=40.8°, M=0.51, x/d_o=6.50)

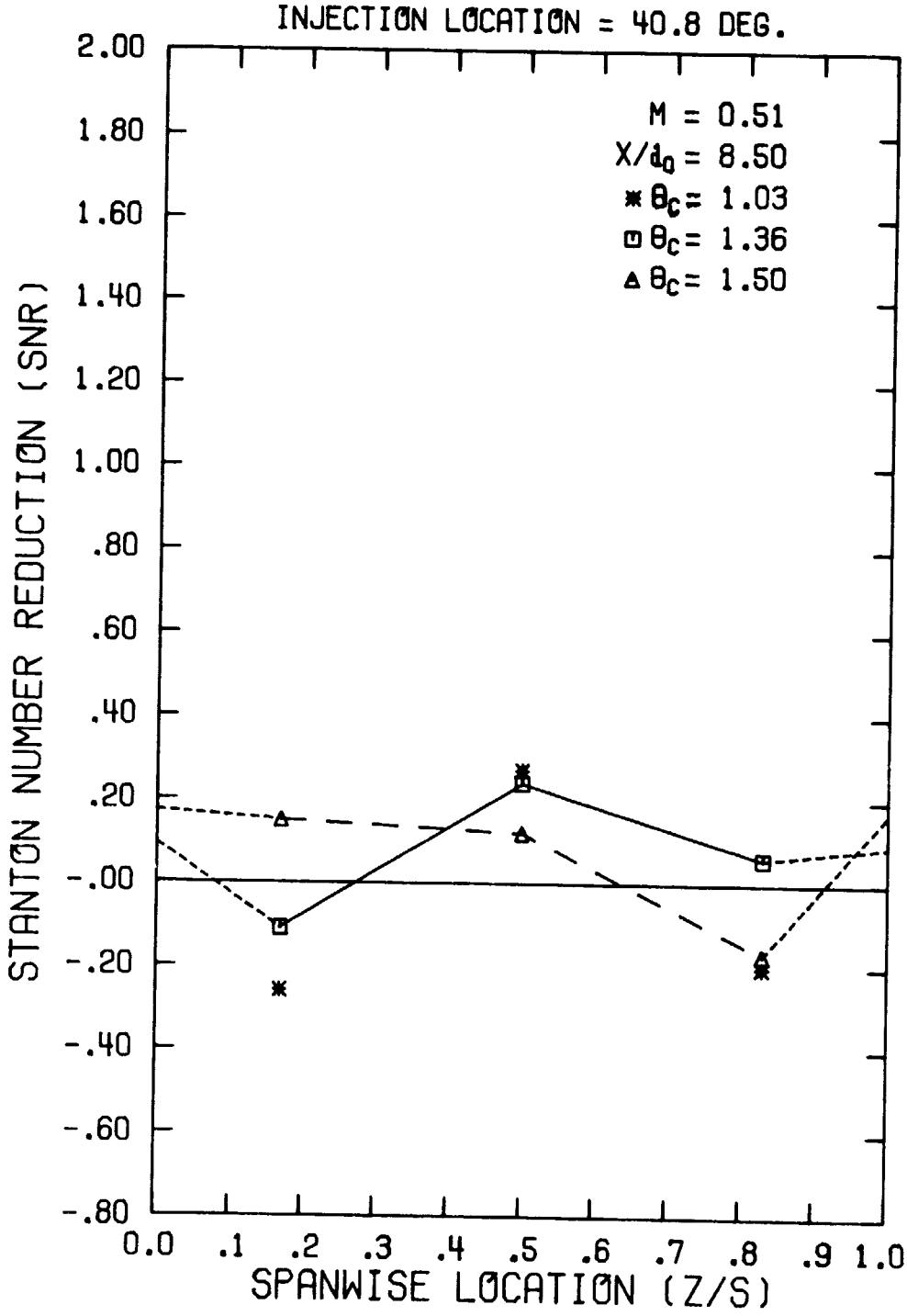

Figure A40. Spanwise Variation in Stanton Number Reduction (θ_i=40.8°, M=0.51, x/d_o=8.50)

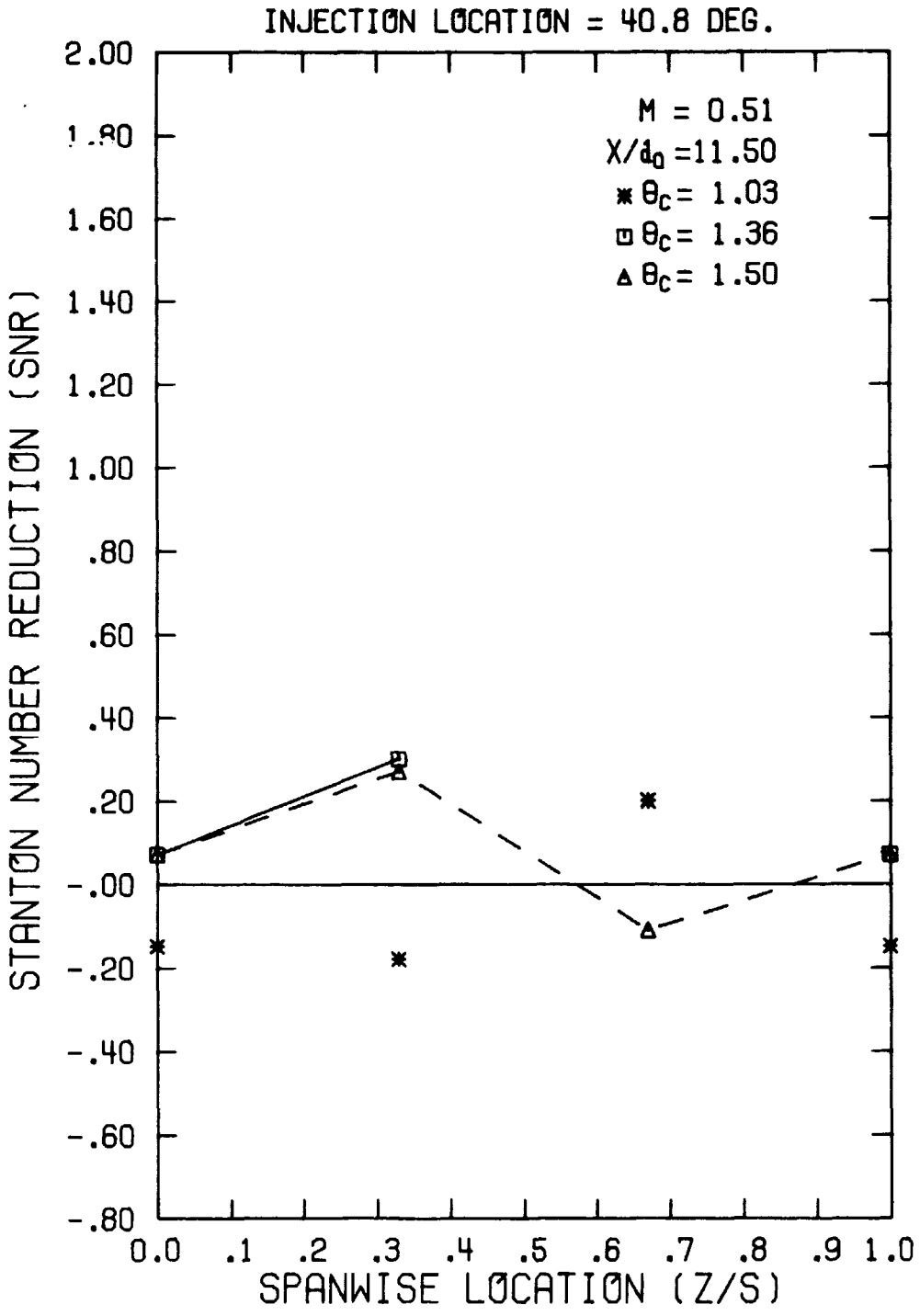

Figure A41. Spanwise Variation in Stanton Number Reduction (θ_i=40.8°, M=0.51, x/d_o=11.50)

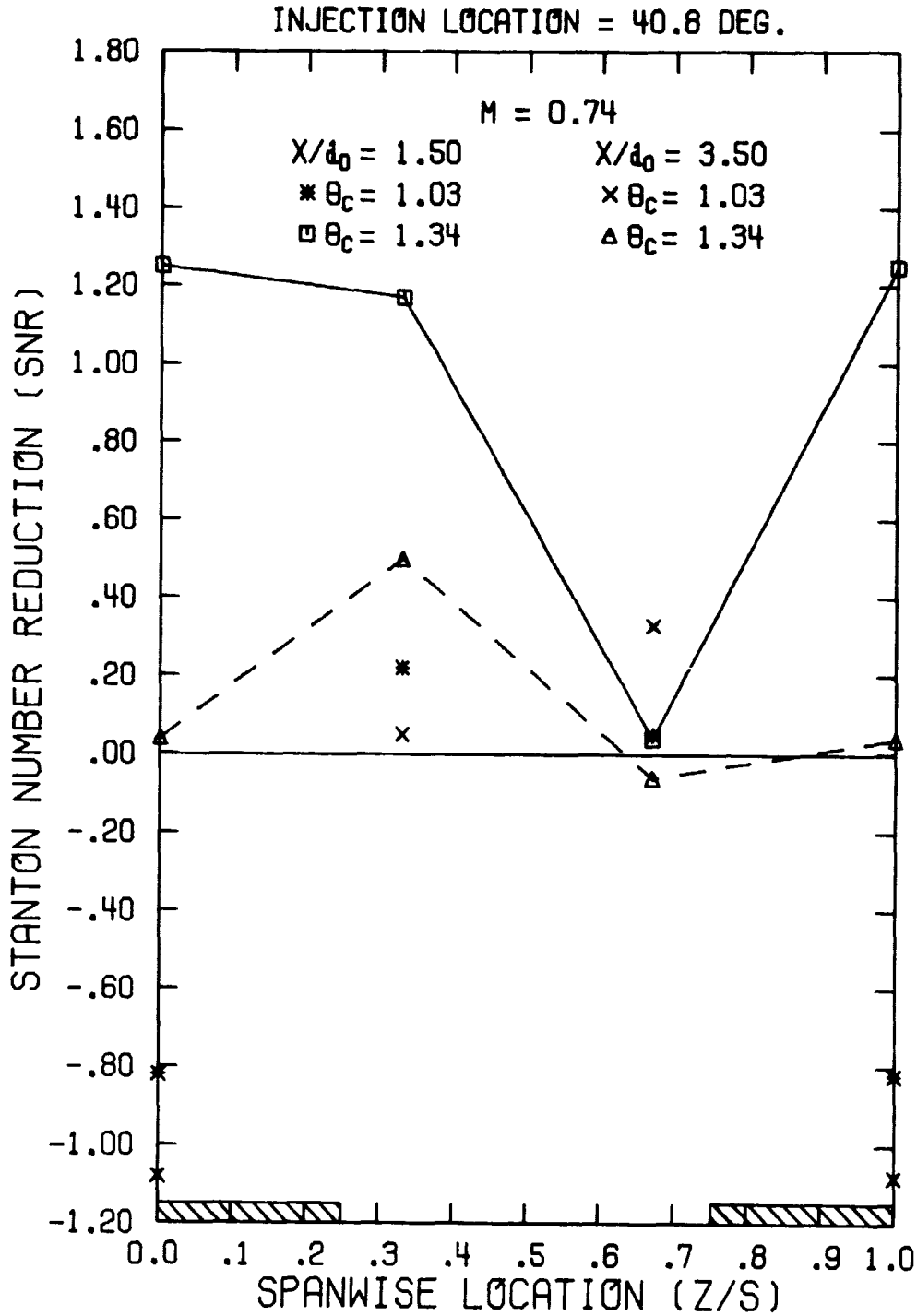

Figure A42. Spanwise Variation in Stanton Number Reduction (θ_i=40.8°, M=0.74, x/d_0=1.50 and 3.50)

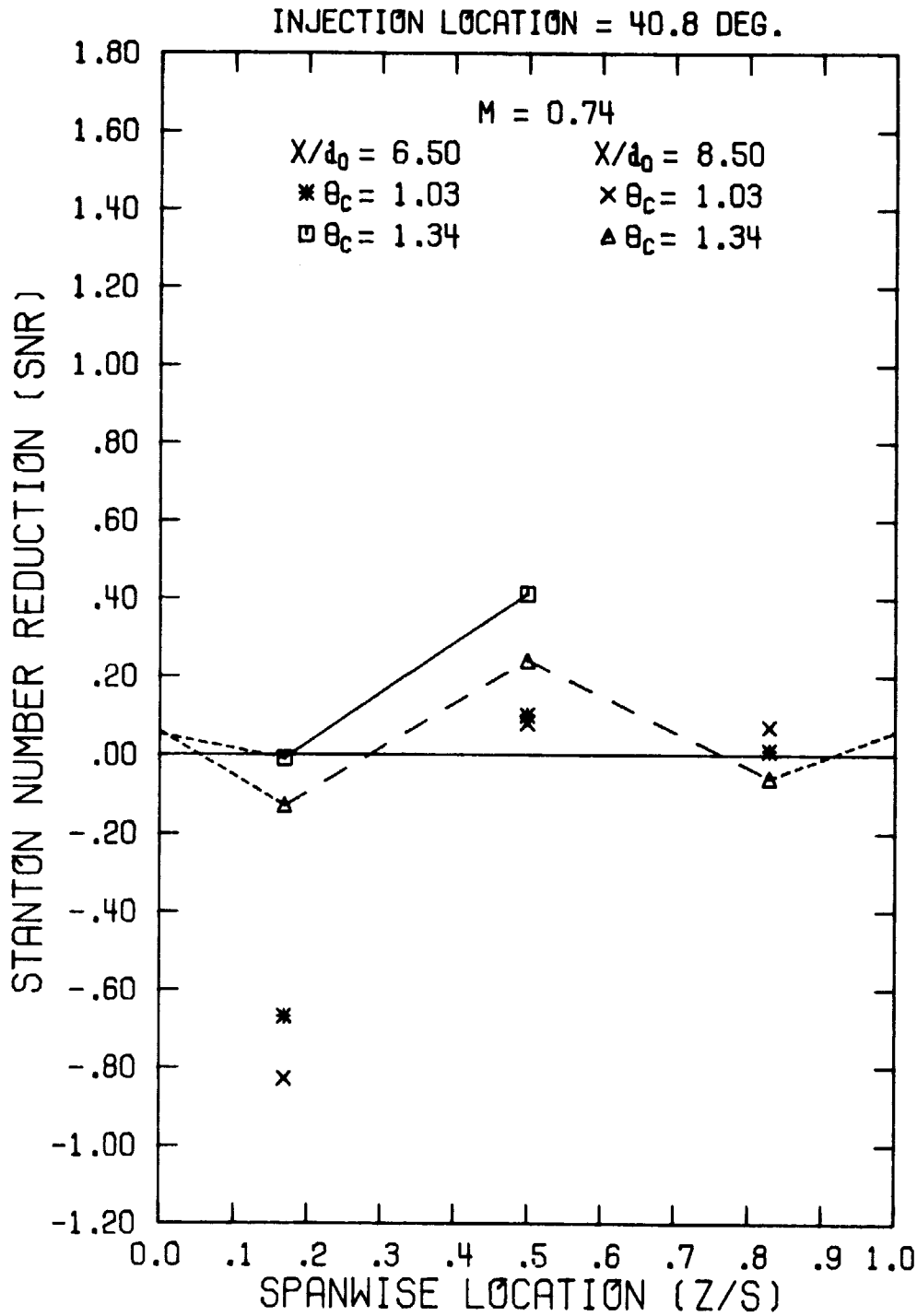

Figure A43. Spanwise Variation in Stanton Number Reduction (θ_i=40.8°, M=0.74, x/d_0=6.50 and 8.50)

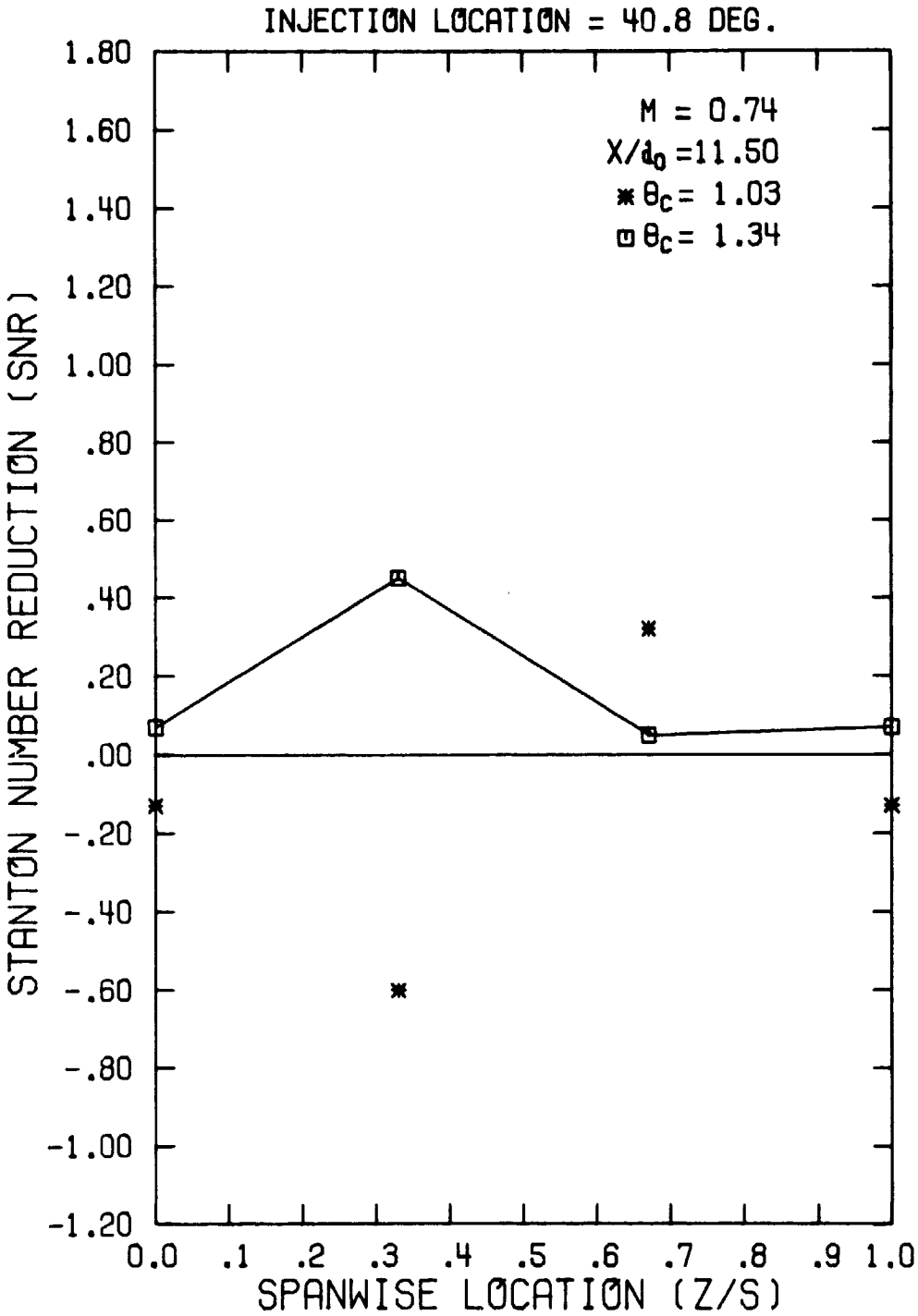

Figure A44. Spanwise Variation in Stanton Number Reduction (θ_i=40.8°, M=0.74, x/d_o=11.50)

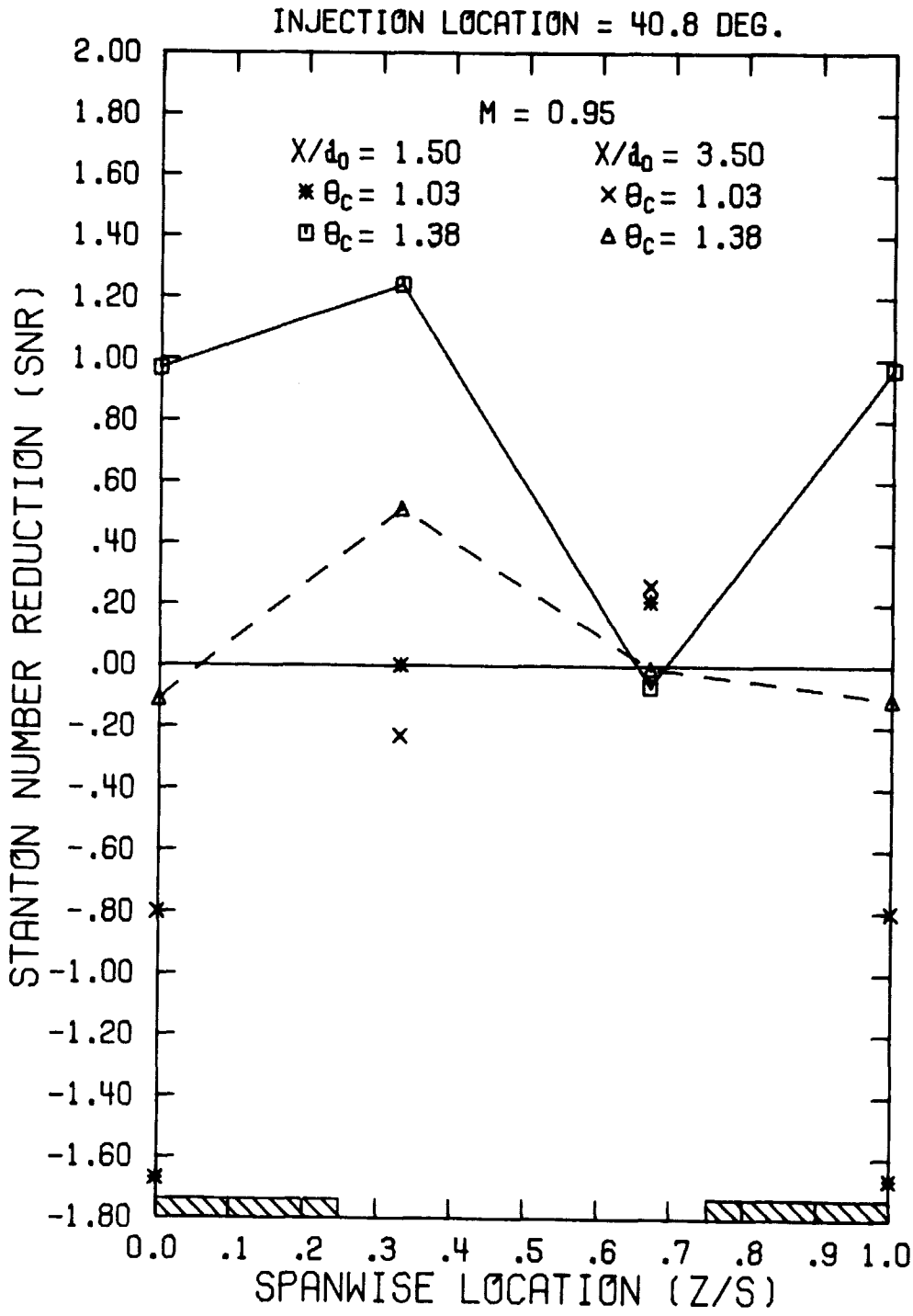

Figure A45. Spanwise Variation in Stanton Number Reduction (θ_i=40.8°, M=0.95, x/d_0=1.50 and 3.50)

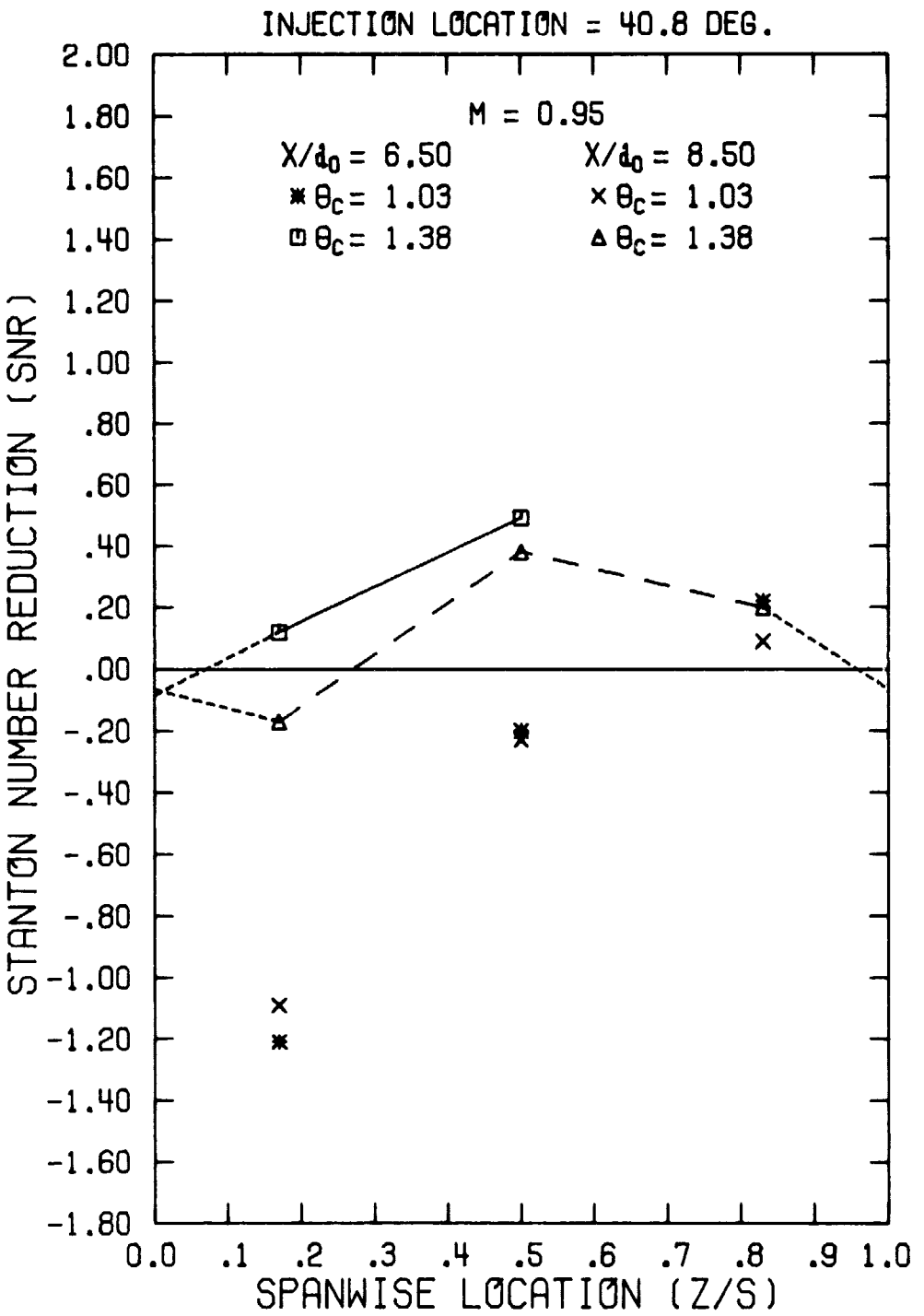

Figure A46. Spanwise Variation in Stanton Number Reduction (θ_i=40.8°, M=0.95, x/d_0=6.50 and 8.50)

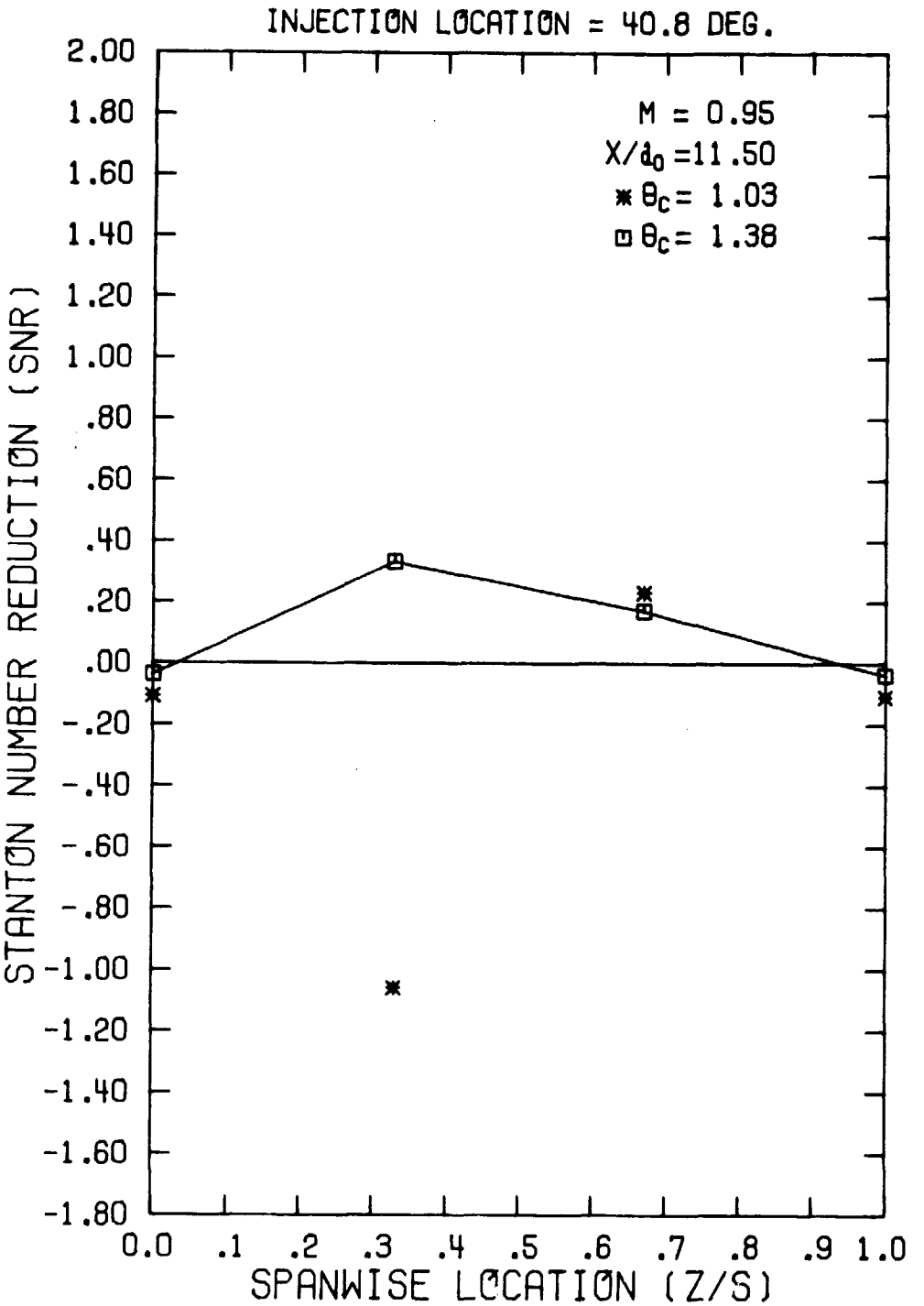

Figure A47. Spanwise Variation in Stanton Number Reduction (θ_i=40.8°, M=0.95, x/d_o=11.50)

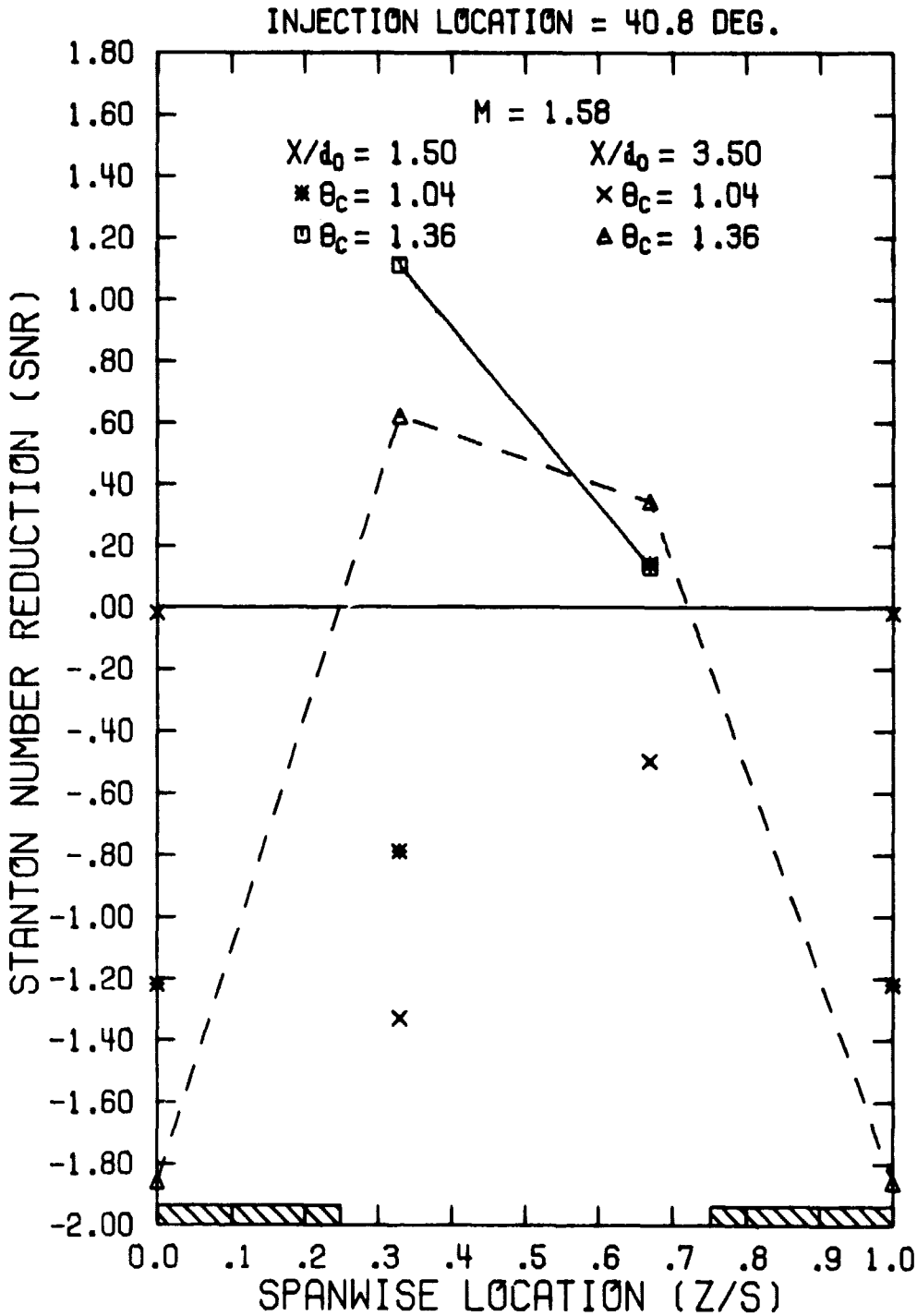

Figure A48. Spanwise Variation in Stanton Number Reduction (θ_i=40.8°, M=1.58, x/d_0=1.50 and 3.50)

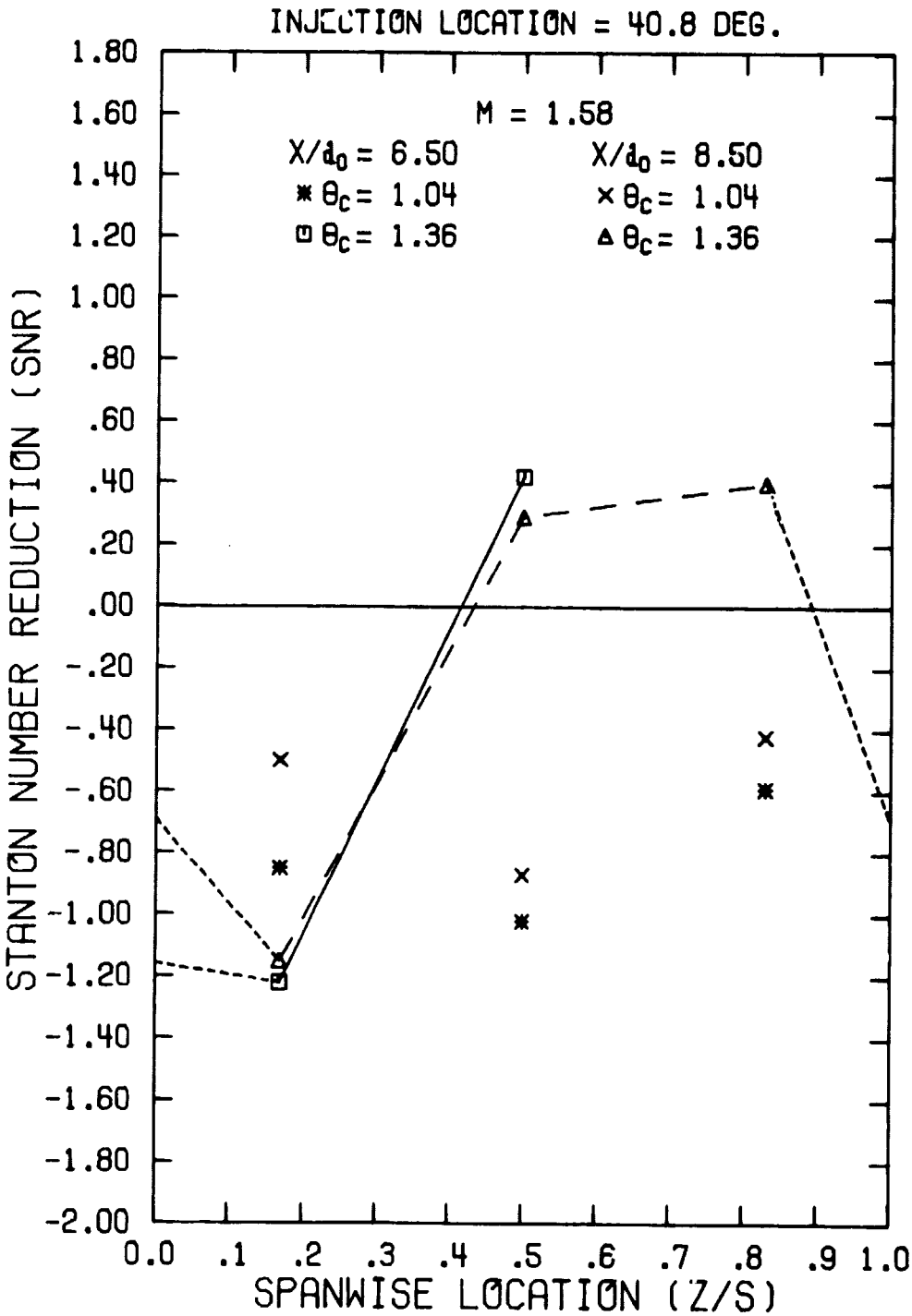

Figure 449. Spanwise Variation in Stanton Number Reduction (θ_i=40.8°, M=1.58, x/d_0=6.50 and 8.50)

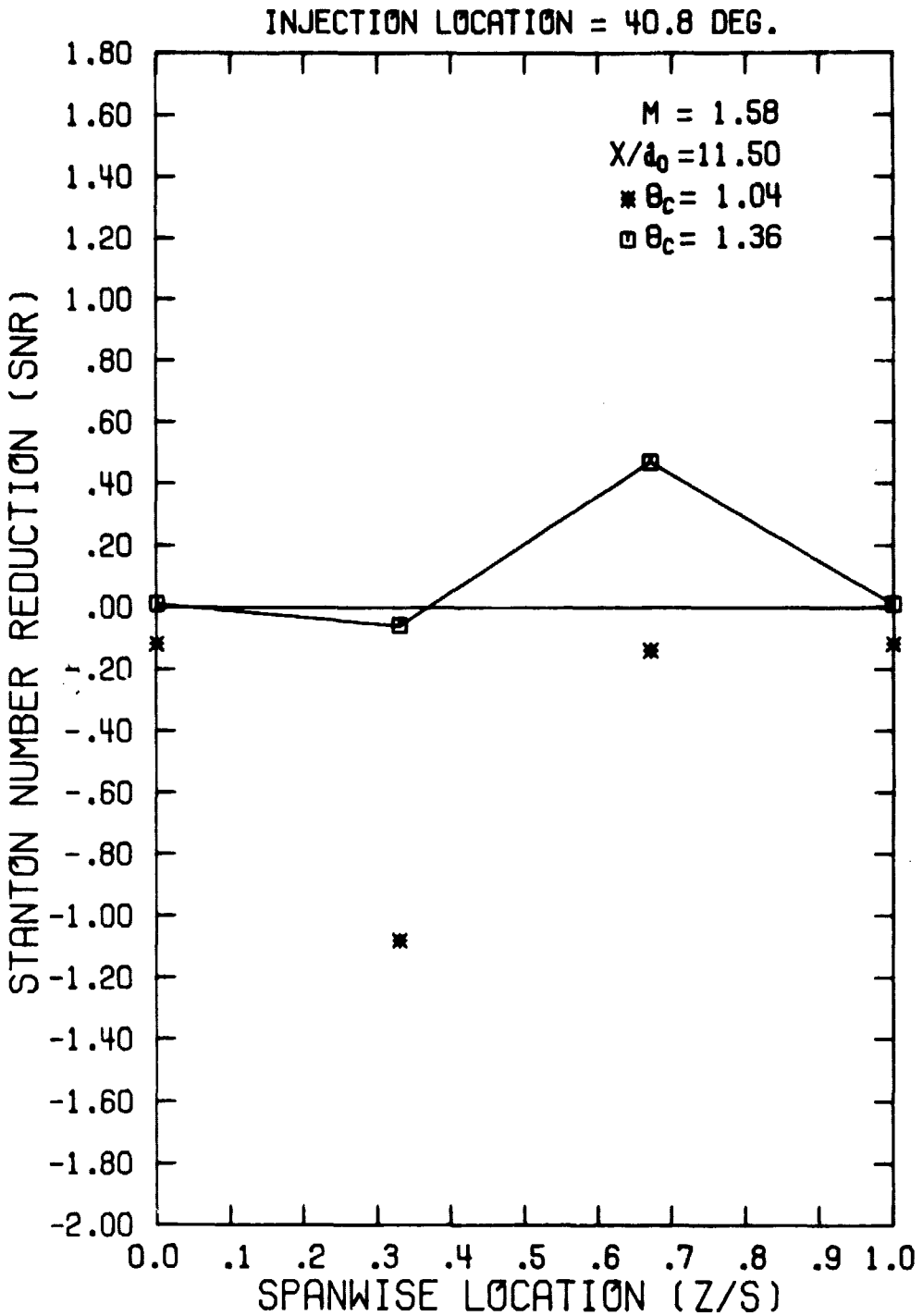

Figure A50. Spanwise Variation in Stanton Number Reduction (θ_i=40.8°, M=1.58, x/d_0=11.50)

Appendix F

HEAT FLUX REPRODUCIBILITY ($\theta_c \simeq 1.0$)

Preliminary film cooling experiments were conducted in the present study with $\theta_c \simeq 1.0$ to verify the reproducibility of data obtained in Reference [1]. See Section III.G. for discussion. Figures A51 through A58 show the data for additional heat flux gages ($\theta_i = 22.9°$) from the present and previous studies. The value of the blowing ratio was taken as the blowing ratio of the film coolant hole directly upstream of the particular heat flux gage. This was necessary due to the variation of blowing ratio that resulted from the differences in flow resistance in each of the installed rubber coolant supply lines. In general, the agreement of the data from the two studies was good.

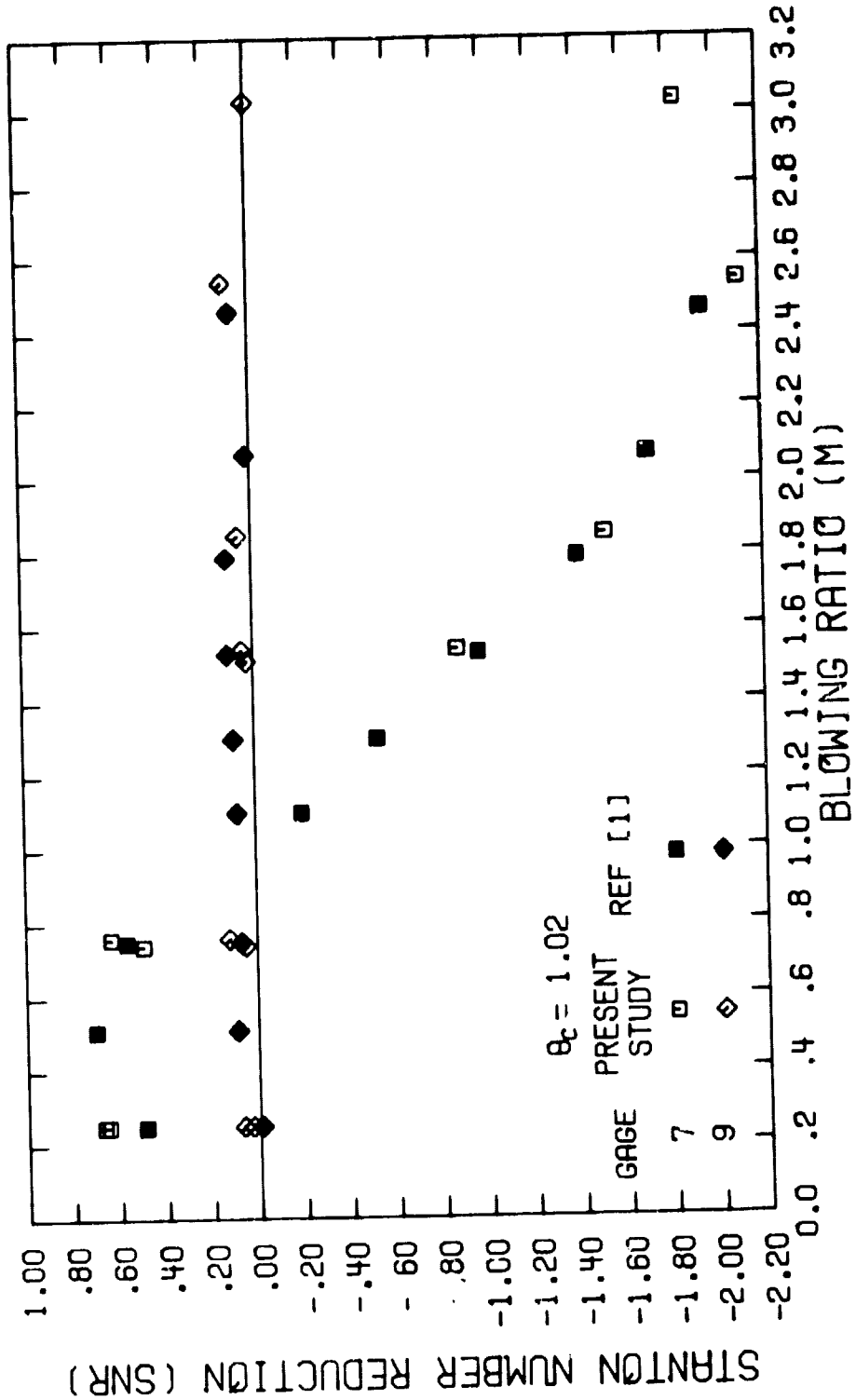

Figure A51. Comparison of Variation in Stanton Number Reduction with Blowing Ratio (Gages 7 and 9)

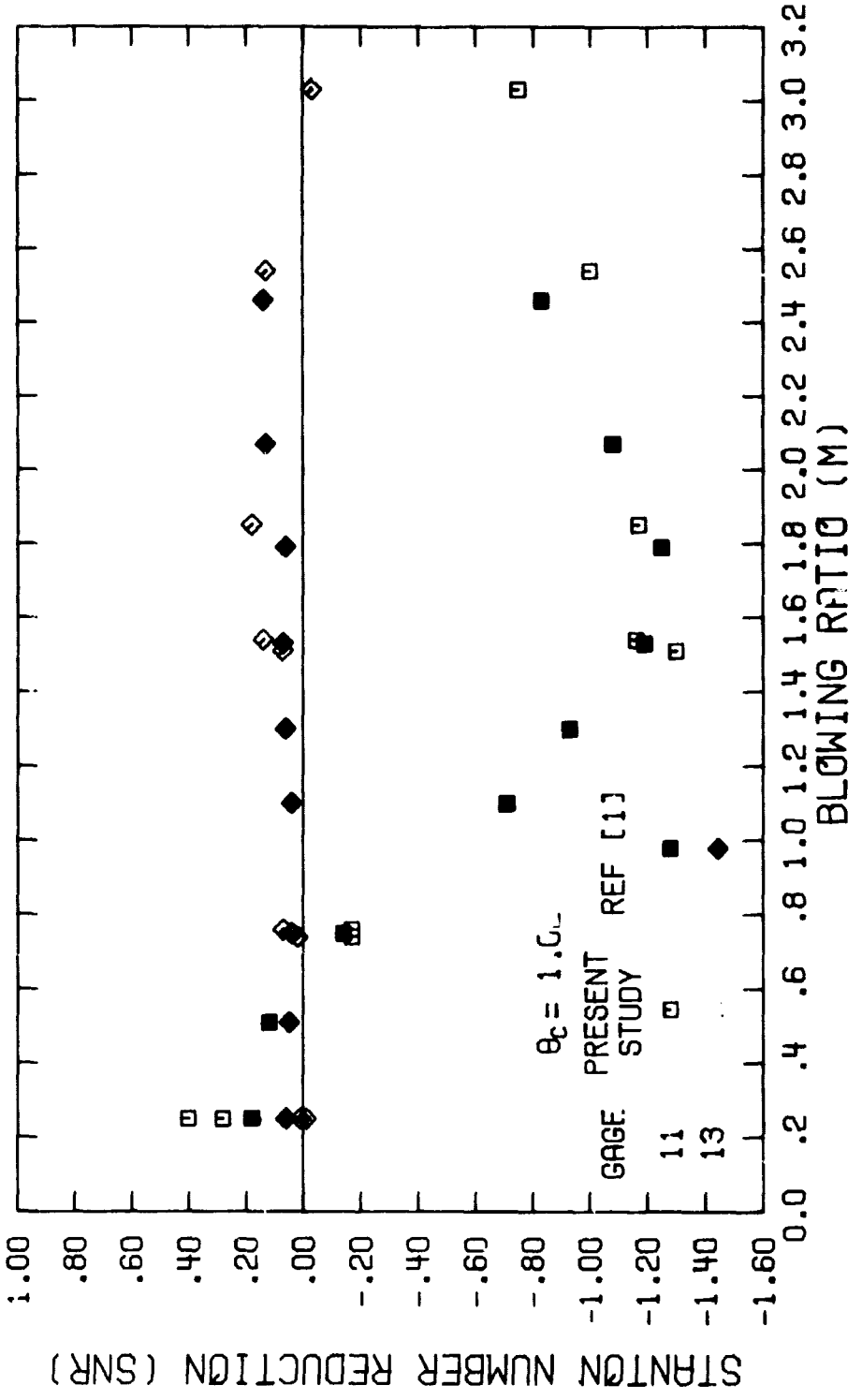

Figure A52. Comparison of Variation in Stanton Number Reduction with Blowing Ratio (Gages 11 and 13)

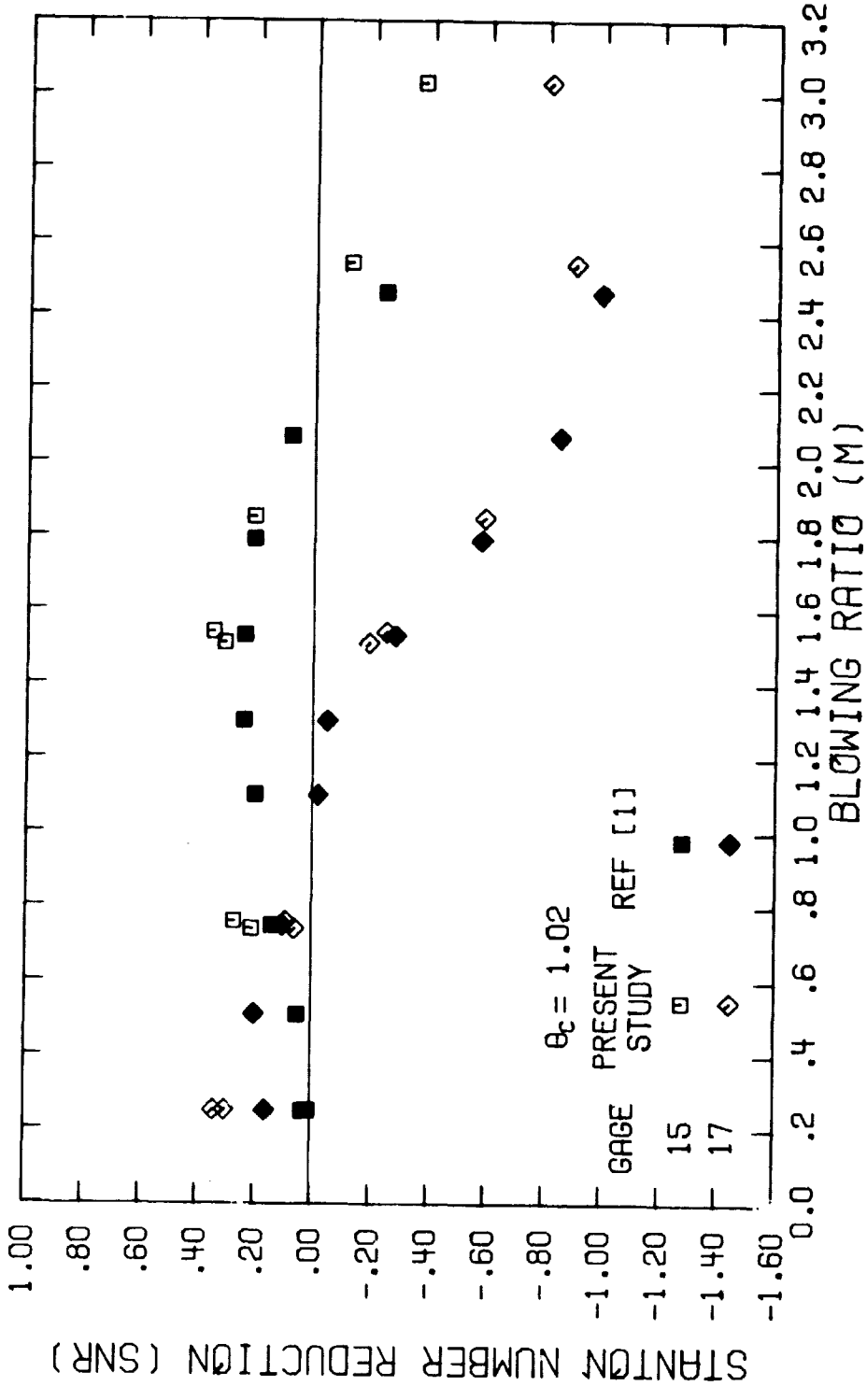

Figure A53. Comparison of Variation in Stanton Number Reduction with Blowing Ratio (Gages 15 and 17)

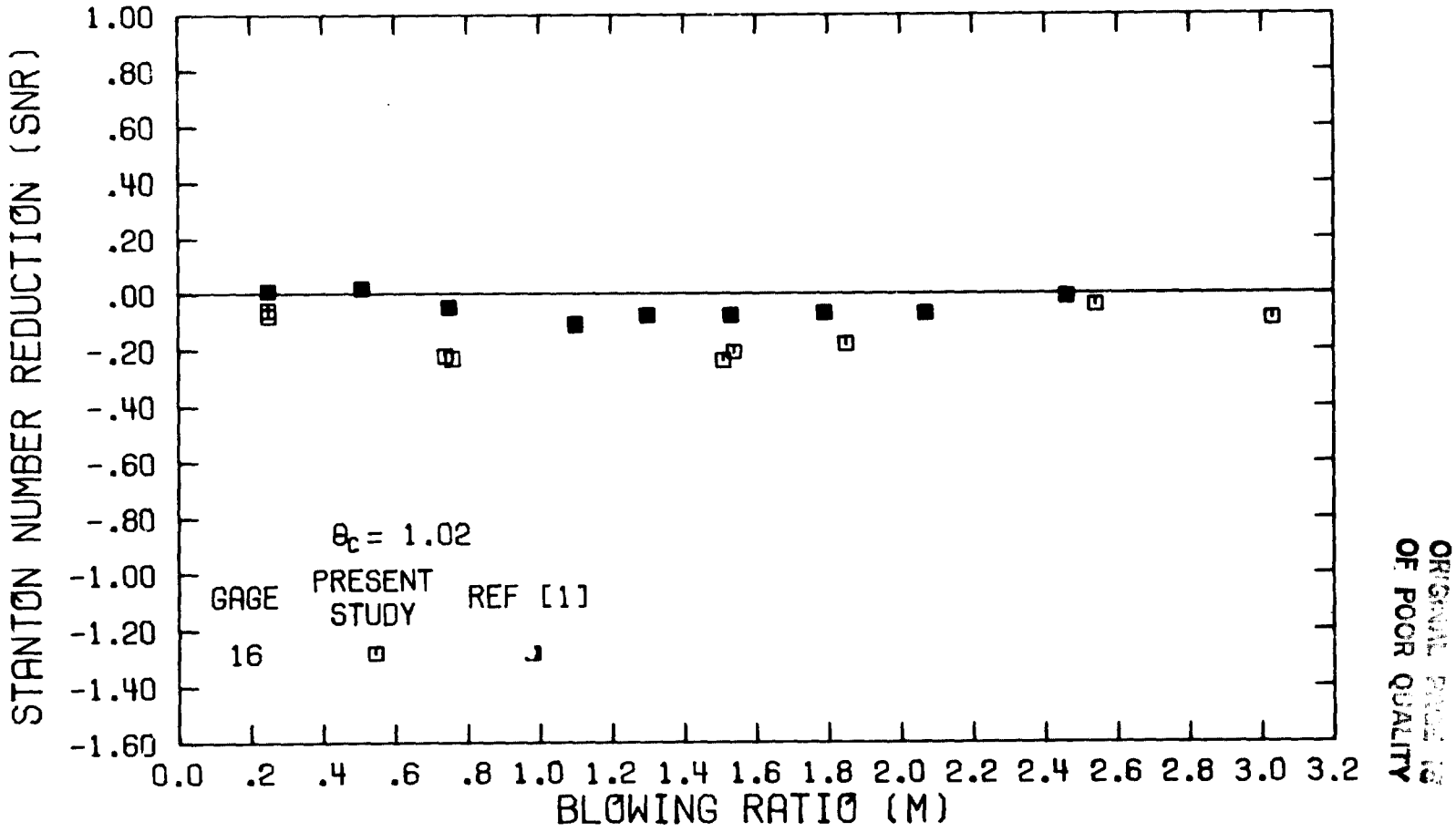

Figure A54. Comparison of Variation in Stanton Number Reduction with Blowing Ratio (Gage 16)

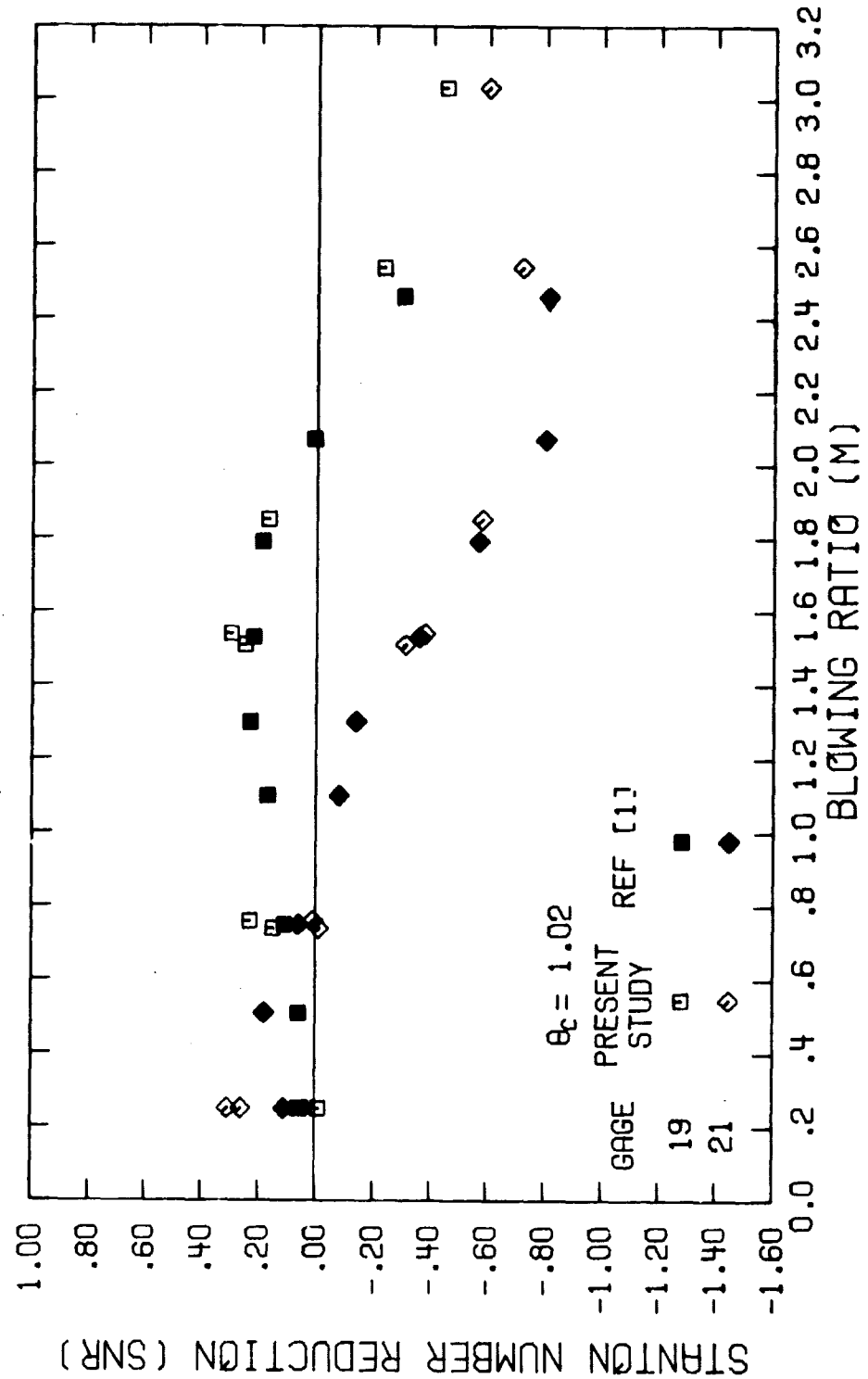

Figure A55. Comparison of Variation in Stanton Number Reduction with Blowing Ratio (Gages 19 and 21)

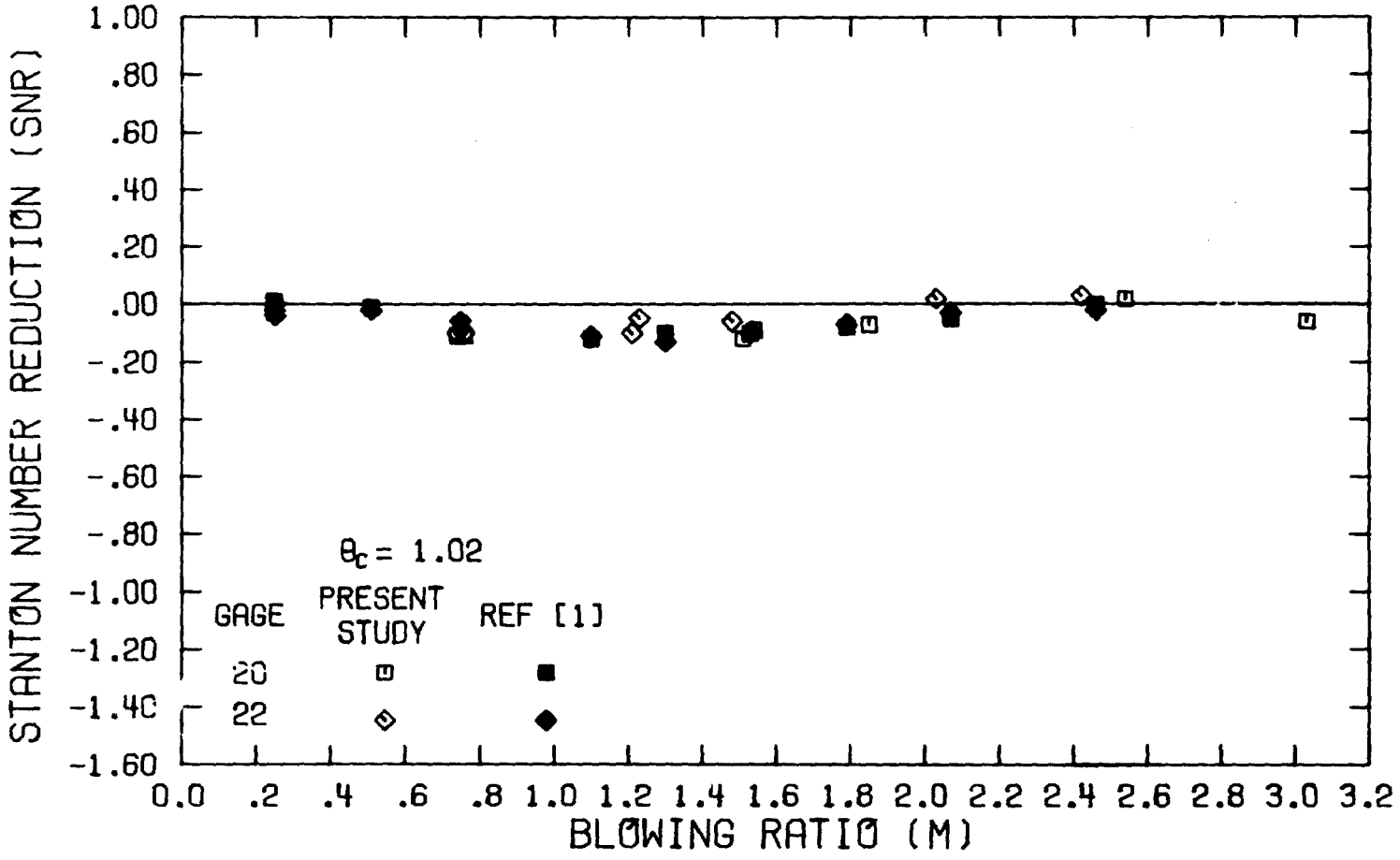

Figure A56. Comparison of Variation in Stanton Number Reduction with Blowing Ratio (Gages 20 and 22)

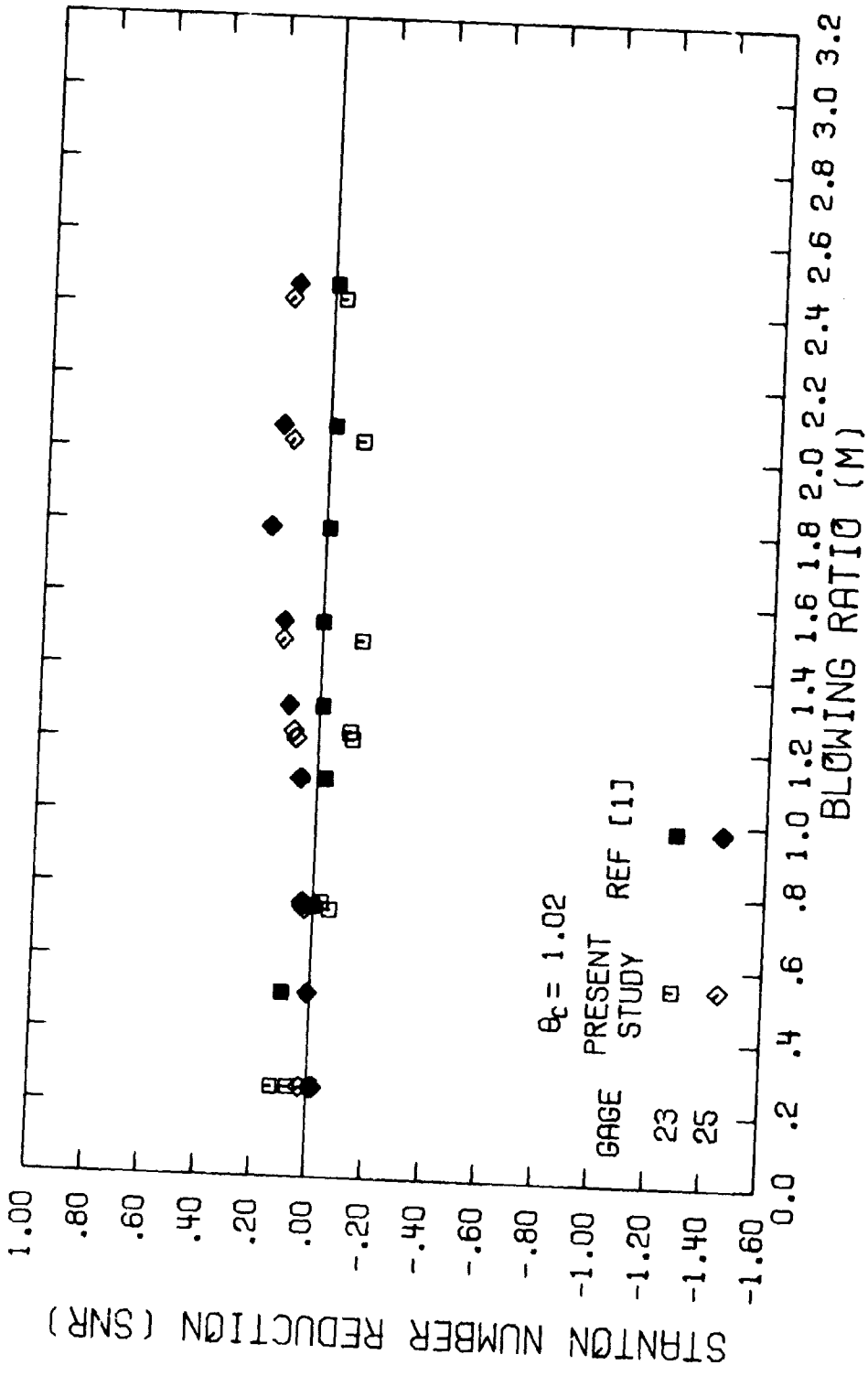

Figure A57. Comparison of Variation in Stanton Number Reduction with Blowing Ratio (Gages 23 and 25)

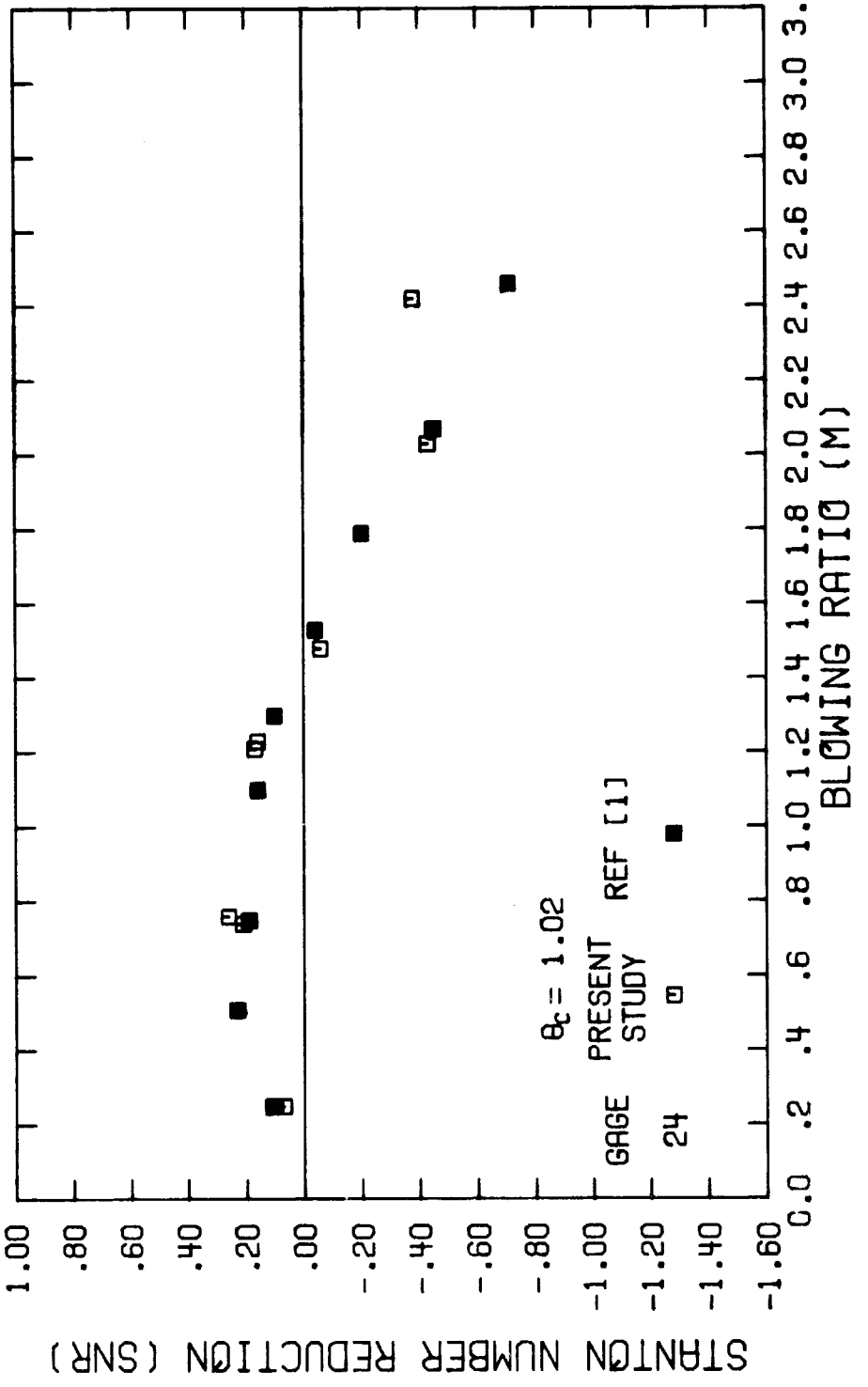

Figure A58. Comparison of Variation in Stanton Number Reduction with Blowing Ratio (Gage 24)